CHARACTERIZATION OF HEME OXYGENASE AND FERREDOXIN NADPH REDUCTASE: TWO REDOX PARTNER PROTEINS INVOLVED IN THE HEME-IRON ACQUISITION PATHWAY OF *PSEUDOMONAS AERUGINOSA*

by

An Wang

B.S., Chemistry, Jilin University, 2000, Jilin, P.R. China

Submitted to the Department of Chemistry and the
Graduate Faculty of the University of Kansas
in partial fulfillment of the requirements for the degree of
Doctor of Philosophy

Committee members:

Mario Rivera, Ph. D. (Chair)

Robert Dunn, Ph. D.

Heather Desaire, Ph. D.

Julian Limburg, Ph.D.

William Picking, Ph.D.

Date Defended: May 06, 2008

The Dissertation Committee for An Wang Certifies that This is the Approved Version of the Following Thesis:

CHARACTERIZATION OF HEME OXYGENASE AND FERREDOXIN NADPH REDUCTASE: TWO REDOX PARTNER PROTEINS INVOLVED IN THE HEME-IRON ACQUISITION PATHWAY OF *PSEUDOMONAS AERUGINOSA*

Committee members:

Mario Rivera, Ph. D. (Chair)

Robert Dunn, Ph. D.

Heather Desaire, Ph. D.

Julian Limburg, Ph.D.

William Picking, Ph.D.

Date Approved: _____

ABSTRACT

The infections from bacterial pathogen *Pseudomonas aerugionsa* are very difficult to cure and cause premature death of many patients with AIDs, cystic fibrosis and cancer. Bacteria need iron to infect an organism, but the concentration of free iron in mammals is very low (~10^{-9} M). Therefore, bacteria have developed sophisticated iron acquisition mechanisms, including the utilization of heme iron. Heme oxygenase is the only known protein used for heme degradation and iron release inside a cell. In *Pseudomonas aerugions*a, once heme is internalized to the cytoplasm, heme oxygenase (*pa*-HO) uses heme as a cofactor and substrate and degrades it into biliverdin and releases iron and CO. This heme degration process uses three oxygen molecules and seven electrons obtained from a novel redox partner protein: ferredoxin NADPH reductase (*pa*-FPR).

The unique heme degradation catalysis in *pa*-HO was studied from a global view by probing a series of hydrophobic phenylalanine (Phe) rings inside heme oxygenase. We probed the Phe rings *via* mutagenesis, fluorine labeling using reactivity assays and spectroscopic methods to understand the relationship of protein structure, dynamics and catalysis. The results show that the hydrophobic cluster not only maintains protein structure, but also fine-tunes protein dynamics to facilitate the channeled H-bonding network from the heme binding site to the protein periphery to sustain catalysis.

In bacteria, it is proposed that electrons from NADPH are transferred to ferredoxin reductase, then to ferredoxin, at last to heme oxygenase. In the study of *pa*-HO redox partner, we found a surprising result that *pa*-FPR by itself can donate all seven electrons to *pa*-HO for heme degradation and iron release. We studied *pa*-FPR by X-ray crystallography and spectroscopic methods in order to understand how *pa*-FPR interacts with *pa*-HO. *Pa*-FPR is a bacterial subclass I ferredoxin NADPH reductase (FNR) protein. In a study of $NADP^+$ coenzyme binding to *pa*-FPR, we obtained the NMR backbone resonance assignments for *pa*-FPR in solution, co-crystallized the *pa*-FPR-$NADP^+$ complex and obtained its crystal structure, which is the first example of a bacterial subclass FNR and second example in the whole FNR family. From this study, we proposed a novel stepwise $e^-/H^+/e^-$ hydride transfer mechanism for bacterial FNR rather than adopting the conventional direct hydride transfer mechanism for plastidic FNR. Furthermore, we studied the protein-protein interaction (PPI) between *pa*-FPR and *pa*-HO. The preliminary data suggests that this PPI is transient, ultra-weak and electrostatic and the interaction interface on *pa*-HO is around the heme binding site.

ACKNOWLEDGEMENTS

I would like to thank Dr. Mario Rivera for giving me the great chance to work with and learn from him in the process of getting a Ph.D. The most precious experience is gained from learning and improving from my own mistakes as well as searching for “the devils in the details”. I am deeply indebted to Professor Rivera for the opportunities to learn from him the good communication, dedication, commitment, and perseverance necessary not only for research but also for success in anything in life.

I am extremely thankful to my committee members: Dr. Robert Dunn, Dr. Heather Desaire, Dr. Julian Limburg and Dr. William Picking for kindly spending so much of their valuable time in helping me with my dissertation and for their wonderful advice to my dissertation.

I would like to extend my sincere and utmost gratitude to Dr. Juan Carlos Rodriguez and Dr. Huili Yao. I acquired huge amount of knowledge and training for my Ph.D. degree from Dr. Juan Carlos Rodriguez. And Dr. Huili Yao has been extremely helpful in giving me advice for my dissertation writing.

I would like to give my special thanks to the former members of the Rivera group: Dr. Adriana Altuve-Blanco, Dr. Christopher O. Damaso, Dr. Yuhong Zeng, Bailey Morgan and Veronica Rodríguez, as well as to the current members: Aileen Y. Alontaga, Saroja Weeratunga, Grace Jepkorir and James Brandon. Thank you for your consistent help, support and friendship. In addition, I would like to

acknowledge the help received from Lijun Wang from Dr. David Benson's group.

Special thanks to our collaborators: Dr. Ernst Schönbrunn and Dr. Huijong Han from H. Lee Moffitt Cancer Center & Research Institute for their marvelous X-ray crystallography skill and great support in Ferredoxin NAPDH Reductase protein study. Without them, we will not have our current progress. Also, we are very grateful for the highly professional and free high throughput screening service for protein crystallization condition offered by Hauptman-Woodward Institute HTS lab, and special thanks to Anne Kent for doing the service for us.

I also would like use this opportunity to express my gratitude to professors and friends at CEBC, who not only unconditionally taught and helped me but also made my time and life there very enjoyable and memorable. This work would not have been possible without the endless love, encouragement and support from my families: Jinyun Chen, Ping Wang and Tiaotiao Xie.

TABLE OF CONTENTS

X-RAY CRYSTALLOGRAPHIC AND SOLUTION STATE NMR SPECTROSCOPIC INVESTIGATIONS OF NADP$^+$ BINDING TO FERREDOXIN-NADP REDUCTASE (FPR) FROM *PSEUDOMONAS AERUGINOSA*

LIST OF FIGURES

CHAPTER I

CHAPTER II

CHAPTER III

CHAPTER IV

CHAPTER V

LIST OF SCHEMES

CHAPTER I

CHAPTER II

CHAPTER IV

LIST OF TABLES

CHAPTER I

CHAPTER II

CHAPTER III

CHAPTER IV

[c] *R*cryst) 100 * ∑|*F*obs - *F*model|/∑*F*obs, where *F*obs and *F*model are observed and calculated structure factor amplitudes, respectively.

[d] *R*free is the *R*cryst calculated for randomly chosen unique reflections, which were excluded from the refinement (1234 for FPR liganded with FAD)

ABBREVIATIONS

pa	*pseudomonas aeruginosa*
HO	heme oxygenase
***pa*-HO**	*P. aeruginosa* heme oxygenase
***cd*-HO**	*Corynebacterium diphtheriae* heme oxygenase
***nm*-HO**	*Neisseriae meningitidis* heme oxygenase
HO-1	heme oxygenase-1
h-HO-1	human heme oxygenase-1
FNR	ferredoxin NAD(P)H reductase
***pa*-FPR**	*P. aeruginosa* ferredoxin NADPH reductase
***Av*-FPR**	*Azotobacter* v*inelandii* ferredoxin reductase
***Ecl*-FldR**	*E. coli* flavodoxin reductase
Fd	ferredoxin
Bfd	Bacterioferritin-associated Ferredoxin
FAD	flavin adenine dinucleotide
FADH2	fully reduced flavin adenine dinucleotide
NAD(P)H	nicotinamide adenine dinucleotide (phosphate)
NAD(P)$^+$	oxidized nicotinamide adenine dinucleotide (phosphate)
ADP	adenosine 2', 5'-diphosphate
DMSO	dimethyl sulfoxide
EDTA	ethylenediaminetetraacetic acid
IPTG	Isopropyl-β-D-thiogalactopyranoside
PMSF	Phenylmethanesulfonyl fluoride
DTT	dithiothreitol
NMR	nuclear magnetic resonance
HSQC	Heteronuclear Single-Quantum Coherence Experiment
NOESY	Nuclear Overhause Effect Spectroscopy
MS	mass spectrometry
OD	Optical Density
cyt b$_5$	cytochrome b5
PCR	polymerase chain reaction
CD	circular dichroism
PDB	protein data bank
SDS PAGE	Sodium Dodecyl Sulfate Polyacrylamide Gel Electrophoresis
WT	wild type
o-^{19}F-Phe	ortho-^{19}F Phenylalanine labeling

CHAPTER I: INTRODUCTION

Pseudomonas aeruginosa, as an opportunistic pathogen, is well-known because it uses sophisticated virulence factors to infect many patients suffering from cystic fibrosis, AIDs and other diseases. It colonizes and damages the defense mechanism of its host and the infection is very difficult to cure and often leads to the death of the host [*1*]. With the available *Pseudomonas aeruginosa* genome: www.pseudomonas.com, many studies of this pathogen have become possible. One of the most interesting topics is how the bacterium acquires its nutrient, specifically iron from its host. Based on our previous study of heme containing proteins like cytochrome b5 and heme oxygenase, we are especially interested in identifying and studying the proteins involved in the heme-iron acquisition pathway in *Pseudomonas aeruginosa*. Through this pathway, well-designed by nature, the bacterium can successfully acquire heme-iron from the host for its own survival [*2*]. Understanding of this pathway can be used to discover novel treatments for infections with drug resistant *P. aeruginosa* strains. The importance of the iron acquisition has been recognized and acknowledged by more and more studies in recent years with the aid of fast developing biotechnologies, such as sequencing and high throughout screening etc.

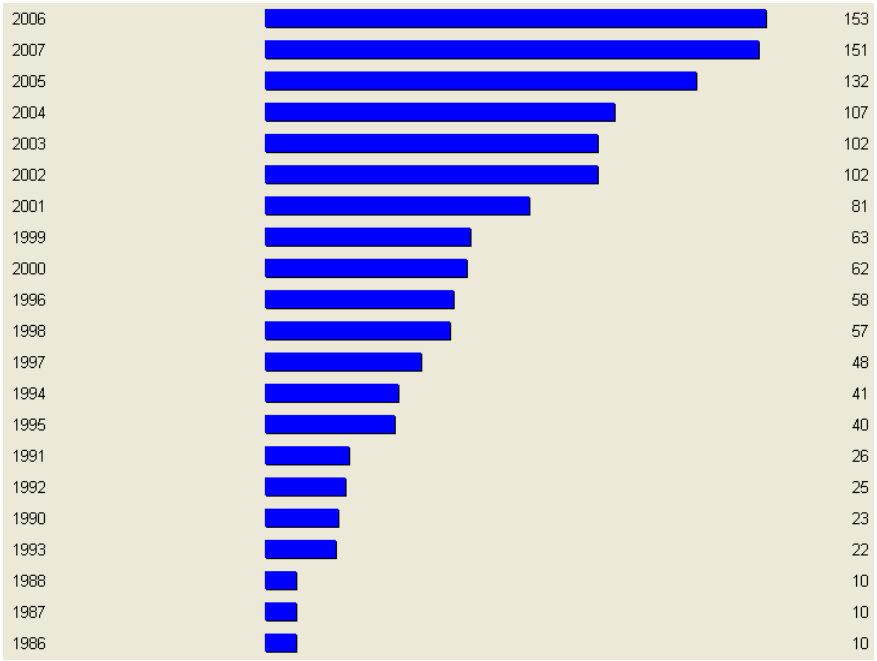

Figure 1-1. Result of searching "Iron Acquisition" in SciFinder 2007(done at 1/10/2008).

1. Background of Heme-Iron Acquisition in Pseudomonas aeruginosa

It is known that pathogenic bacteria need iron to colonize (infect) an organism. However, the concentration of free iron in mammals is typically very low (~10^{-9} M) because it is sequestered by iron-binding and iron-containing compounds such as transferrin, lactoferrin, heme, hemoglobin and ferritin [*3*]. In addition, mammals have evolved means to fight invading pathogens by making iron even less accessible by reducing levels of transferrin and by down-regulating the recycling of iron from macrophages [*4*]. It has also been shown that lipocalin 2, an iron-binding protein innate to the immune response sequesters iron from bacterial siderophores in the early stages of bacterial infection [*5*]. It is therefore not surprising that pathogens such as *Neisseriae meningitidis*, *Haemophilus influenzae*, *Shigella dysenteriae*, *Vibrio cholerae* and the opportunistic

Pseudomonas aeruginosa have evolved sophisticated mechanisms for iron acquisition, including the utilization of heme iron [*6, 7*]. Heme containing proteins and in particular hemoglobin constitute an important reservoir of iron given that more than two thirds of the total iron is chelated by heme and that ~ 95% of iron-bound heme is in the form of hemoglobin [*8*]. Consequently, many pathogenic bacteria have evolved specific heme uptake systems to acquire heme-iron from mammalian hosts. Although these systems are best understood in gram negative bacteria [*6, 7*], it has been recently shown that *Staphylococcus aureus* not only uses heme as an iron source but it prefers heme-iron in the initial stages of infection [*2*]. Heme uptake and utilization are also mechanisms used by the opportunistic pathogen *Pseudomonas aeruginosa*, which can deploy two operons regulated by Fur, the master **F**e **u**ptake **r**egulator [*9*]. The global iron response associated with Fur-regulated genes includes the heme uptake systems *phu* (***P****seudomonas* **h**eme **u**ptake) and *has* (**h**eme **a**cquisition **s**ystem). The *phu* locus consists of a receptor gene (*phuR*) and the *phuSTUVW* operon encoding a typical ABC transporter. The second uptake system, *has*, consists of a heme receptor (*hasR*) and a protein that binds heme with high affinity, also known as a hemophore [*6*]. Once internalized to the cytoplasm heme is delivered to heme oxygenase (*pa*-HO) for its degradation to biliverdin, thus facilitating release of the heme-iron for subsequent metabolic use [*10*].

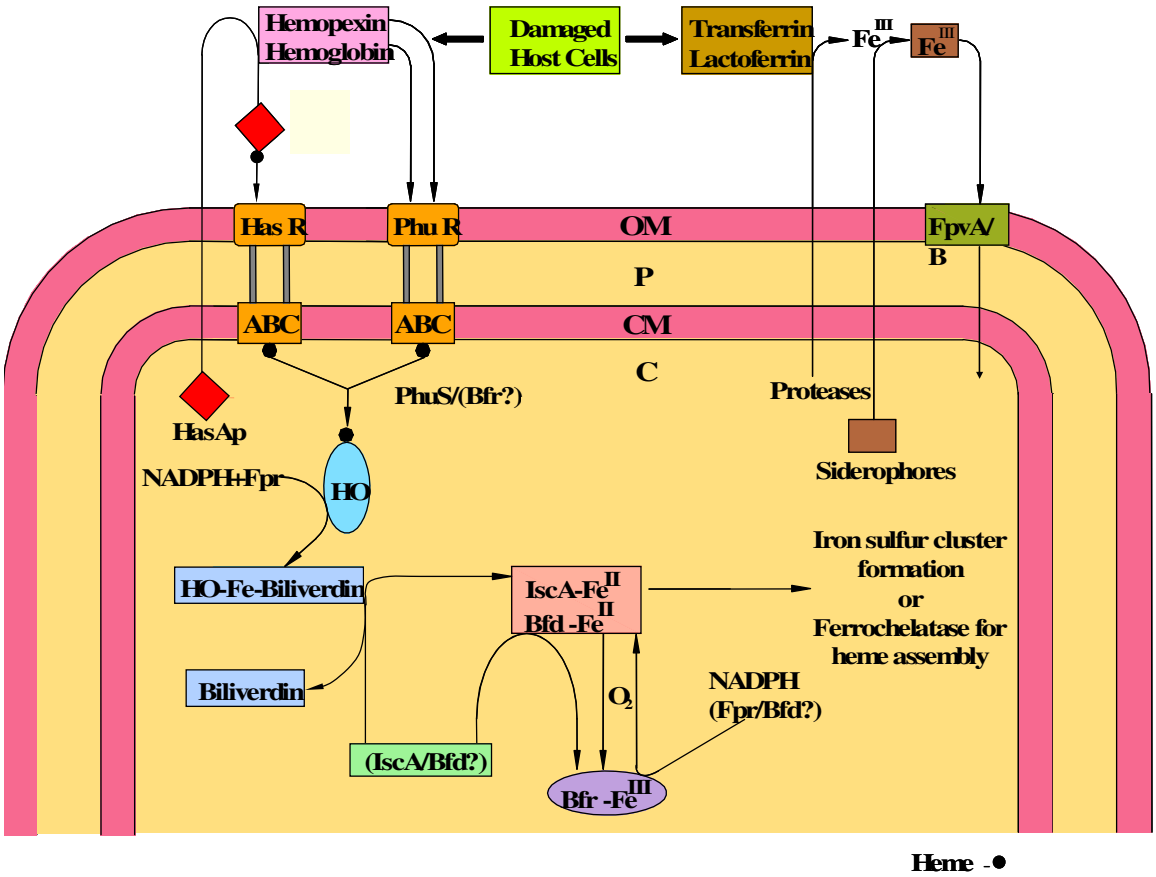

Figure 1-2. Proposed Heme-Iron Acquisition Pathway In *Pseudomonas aeruginosa* under iron-starvation [*11*] condition. (Courtesy of Saroja Weeratunga).

Release of heme-iron is accomplished by the breakdown of heme to biliverdin. This is a complex reaction requiring the input of 7 electrons and 3 molecules of O_2, which must be delivered to HO rapidly and efficiently in order to sustain catalytic activity (Figure 1-2). Heme breakdown starts with the one electron reduction of ferric HO (resting state) to the deoxyferrous state, followed by the rapid binding of dioxygen to form an oxyferrous complex (Fe^{II}-O_2) [*12*]. Injection of a second electron into the Fe^{II}-O_2 complex triggers electron rearrangement that leads to the formation of a ferric peroxide (Fe^{III}-OO^{-}) complex, which accepts a proton to form a ferric hydroperoxide (Fe^{III}-OOH) oxidizing

species [*13*]. Ring oxidation involves attack of the Fe^{III}-OOH intermediate on the aromatic macrocycle [*14*] to form a meso-hydroxyheme intermediate, which undergoes a subsequent O_2- and electron-dependent elimination of the hydroxylated meso carbon as CO, thus forming verdoheme. Verdoheme is then oxidized to Fe^{III}-biliverdin in a reaction that requires both O_2 and additional electrons [*15, 16*]. Fe^{III}-biliverdin must be reduced to Fe^{II}-biliverdin prior to the sequential release of Fe^{II} and biliverdin [*17*].

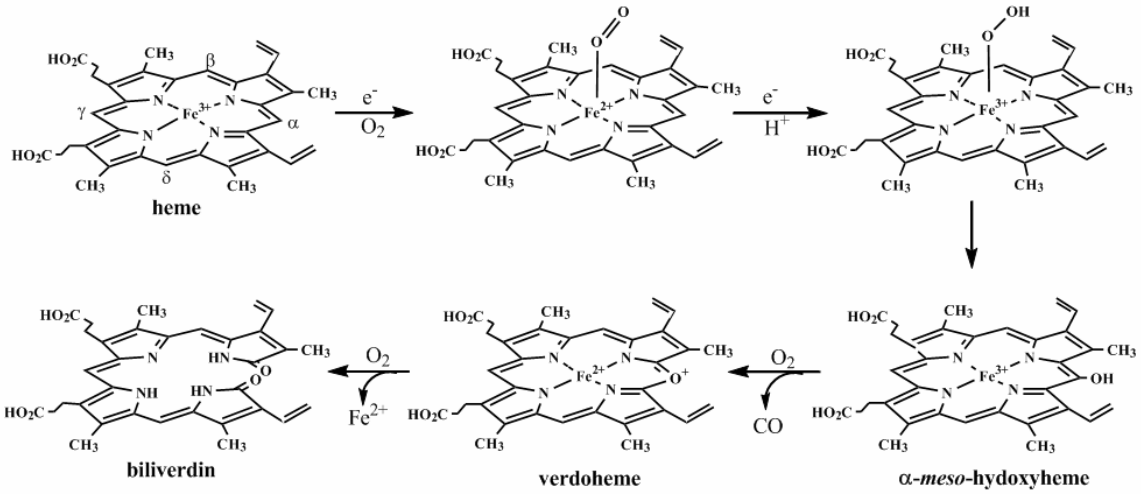

Scheme 1-1. Heme metabolism pathway in heme oxygenase.

Heme oxygenase is the only known enzyme to degrade heme and release iron inside a cell. The unique catalysis of its hydroxylation step (Scheme 1-1) that converts the ferric hydroperoxyl heme to α-meso-hydroxyheme is the most distinguishable step from all other heme-containing proteins. A unique phenylalanine ring cluster has been observed in several heme oxygenases. Intensive studies to this aromatic ring cluster in *Pseduomonas aeruginosa* heme

oxygenase (*pa*-HO) have been employed for understanding how protein structure and dynamics regulate this unique heme degradation catalysis in heme oxygenase. With the understanding of how heme oxygenase works, we further studied its potential redox partner proteins to reveal where and how *pa*-HO gets the seven electrons for heme degradation and iron releasing.

2. Dynamic structural regulation to functional catalysis --- Study of Heme Oxygenase Phenylalanine Ring Cluster

Heme oxygenase is well known for its distinctive catalytic cycle. Unlike other heme-containing proteins, heme is used as the substrate for not only electron transfer but also its own degradation. Previous intensive studies have revealed that there is a peculiar heme hydroxylation process which is extraordinary from all other heme-proteins [*10, 12, 14*]. The focus has been placed on the input of the first 2 electrons that are utilized by the enzyme to reduce coordinated O_2 at the active site. The resultant ferric hydroperoxide intermediate (Fe^{III}-OOH) reacts with the macrocycle to form meso-hydroxy heme, which in the presence of O_2 and five additional reducing equivalents is converted to biliverdin and free iron.

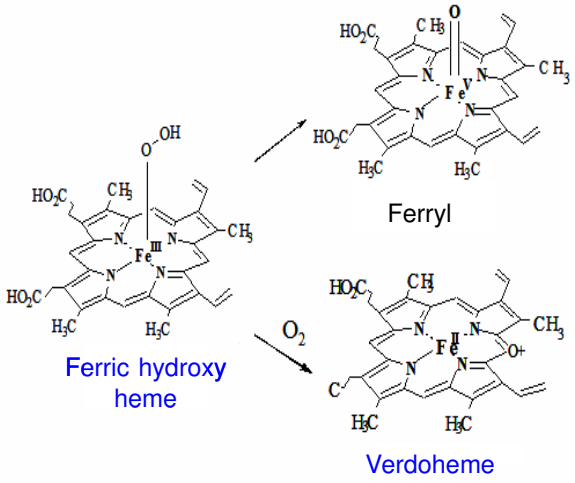

Figure 1-3. Obligated two heme hydroxylation paths.

The key in the heme degradation process is how nature tunes this enzyme to carry out the dioxygen activation toward heme oxygenation efficiently rather than taking the common alternative pathway for the formation of ferryl heme [*18*]. Observations made in our lab suggested that this heme hydroxylation is facilitated by the deformation of the heme that is regulated by the dynamic motion of protein structure [*19-21*]. From those studies, we can understand locally how heme interacts with the residues and the structural water inside the heme binding pocket. But how does the protein fulfill its specific catalysis function in a global fashion instead of the local view from the heme binding site? Also how do the hydrophobic cluster, H-bonding network and protein dynamics contribute to this unique catalysis? The answer is very limited and unexplored. Based on earlier findings, our target is to understand the protein structure-function from a global view.

Our entry point is originated from an intriguing observation that there is a cluster of conserved hydrophobic phenylalanine rings present in heme oxygenase, revealed by studies of protein crystal structures and structural alignment as shown below.

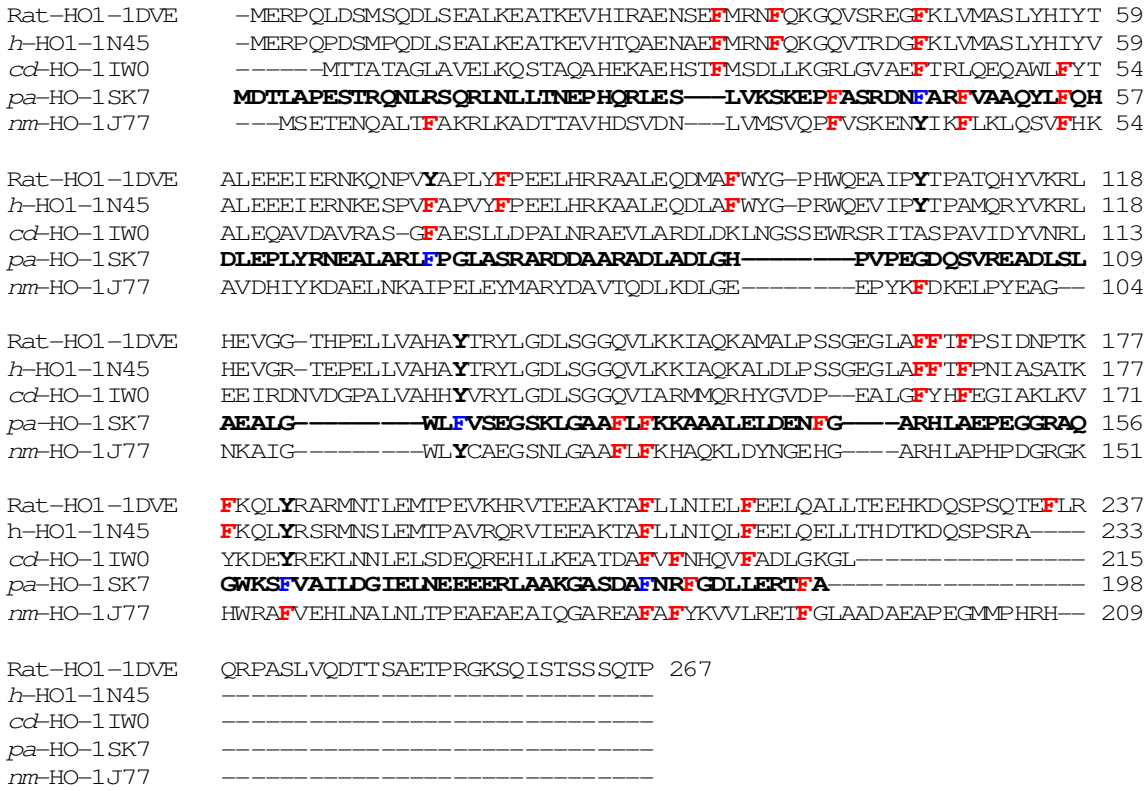

Figure 1-4. Phe rings in five heme oxygenases aligned by ClustalW. *Pa*-HO sequence is in bold. The possible conserved Phe rings are colored blue in *pa*-HO, the corresponding Phe residues are bold and colored red, and the corresponding Tyr residues are bold. Rat heme oxygenase 1 (Rat-HO1): 1DVE (pdb ID) [*22*], Human heme oxygenase 1 (*h*-HO1): 1N45 (pdb ID) [*23*], *Corynebacterium diphtheriae* heme oxygenase (*cd*-HO): 1IW0 (pdb ID) [*24*], *Pseudomonas aeruginosa* heme oxygenase (*pa*-HO): 1SK7 (pdb ID) [*25*], *Neisseria meningitidis* heme oxygenase (*nm*-HO): 1J77 (pdb ID) [*26*].

In the heme oxygenase protein sequence alignment shown in Figure 1-4 above, there is a series of Phe rings in all the heme oxygenases. In *pa*-HO, there are 13 of them. In other HOs, there is either Phe or Tyr in the corresponding or

similar locations in the protein sequence. For example, F45 and F186 in *pa*-HO are conserved, and F72, F117 and F161 in *pa*-HO are conserved as Phe or Tyr in the other four HOs. In human HO-1, the F166, F167 and F169 are not conserved in *pa*-HO but are conserved in rat and *Corynebacterium diphtheriae* heme oxygenases. By comparing the sequence of *pa*-HO with its equivalent HOs from other *Pseudomonas* strains, like *P. fluorescens* (PF), *P. syringae* (PS) and *P. putida* (PP), we found that most of the 13 Phe rings are reserved except F197, F72 and F130 and F197 is replaced with Tyr. Therefore, it is highly likely that these Phe rings are conserved. Next, we observed the Phe rings closely in the crystal structure of *pa*-HO.

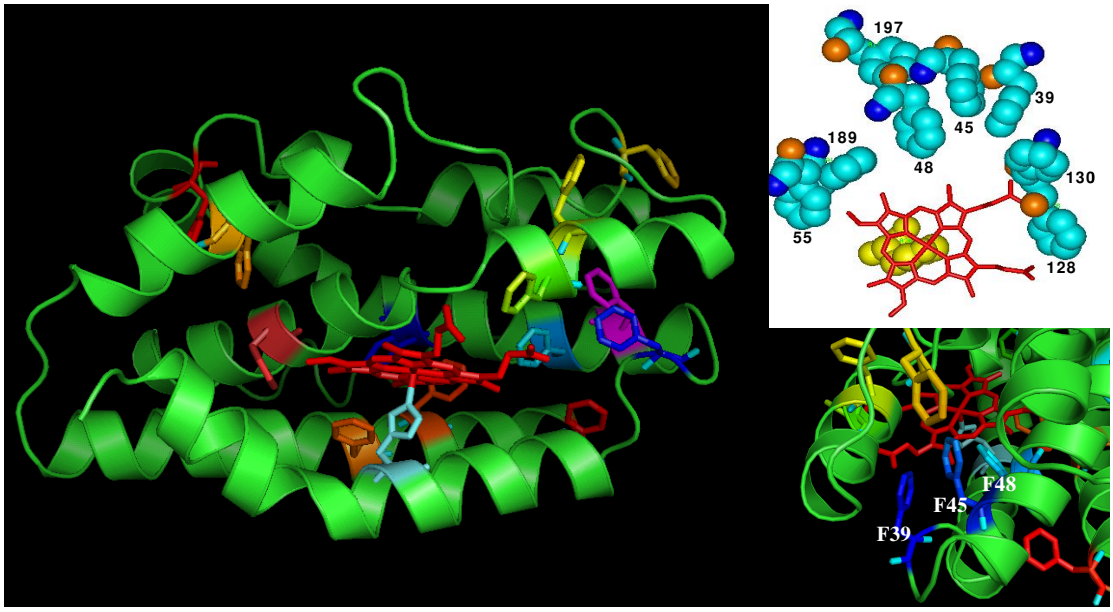

Figure 1-5. Target Phenyalanines of total 13 Phenyalanines in *pa*-HO (PDB: 1SK7).

As shown in Figure 1-5, most of the 13 Phe rings are located around the heme distal pocket. F55, F189, F197, F48, F45, F39, F130 and F128 can possibly

form a hydrophobic channel located around the heme pocket, especially F39, F45 and F48 are positioned so closely to each other. As shown in the "zoom-in" view of the three phenylalanine rings, one can predict that the rotation of F45 can possibly have a cooperative motion with F39 and F48.

In human HO-1, the rings of F47, 95, 166, and 167, Y58, and W96 are also close to one another spatially. Especially between F166 and Y58 and between F167 and F47, there are close interactions [*27*]. From the human HO-1 CN complex NMR studies done by La Mar and coworkers, they predicted two new water molecules in the empty space of the 1.5 Å h-HO-1 crystal structure, one is between the F167 ring and V42 based on the identified H-bond from F167 $C_{\xi}H$ to the hypothesized water molecule, and the other is between W96 and G163 based on the identified H-bond from W96 $N_{\varepsilon}H$ to the hypothesized water molecule [*27*]. Therefore, they suggested that the two proposed water molecules near the aromatic rings, together with other water molecules observed in the crystal structure, form a channel of water molecules that extends from the distal ligand to the surface of the protein on the opposite side of the heme binding pocket [*27*].

Phe is a hydrophobic residue; its ring rotation displaces about 80 cubic angstroms of volume. The cluster of Phe rings can possibly form a hydrophobic cluster and exclude water. The hydrophobic cluster is likely particularly important to protein folding, conformational changes and possibly protein dynamics [*28*].

By using mutagenesis and fluorine labeling of the Phe residues, we investigate the protein structure-function relationship *via* NMR and a reactivity assay simulating the heme oxygenase catalytic cycle (Scheme 1-1) in next chapter.

With the understanding of how *pa*-HO works in a global view, to probe this iron acquisition pathway in context with other partner proteins becomes important and urgent. In mammals, NADPH transfers electrons to cytochrome P450 reductase then to heme oxygenase [*29*], while heme oxygenase in plant or bacteria can obtain electrons from various redox partners to complete the heme degradation process [*30*].

3. Characterization of FPR as a novel redox partner of Heme Oxygenase

The identification and characterization of redox partners that deliver electrons to HO, as well as the characterization of protein-protein interactions that facilitate the vectorial electron flow from NAD(P)H to HO are important steps toward a molecular-level understanding of heme metabolism. Cytochrome P450 reductase supports the catalytic activity of mammalian HO-1 and HO-2 by donating all 7 electrons [*17*]. In comparison, current understanding regarding the nature of the redox partner(s) that support the catalytic activity of bacterial HO enzymes is significantly less developed. It is thought that cyanobacterial and eubacterial HOs are ferredoxin-dependent. However, it is noteworthy that the reports proposing this idea also state that HO activity in cell extracts containing reduced ferredoxin also requires the presence of a second (auxiliary) reductant,

such as trolox or ascorbate [*31-34*]. In fact, in the absence of such auxiliary reducing agents HO activity is very slow [*31, 33*] or is arrested at the oxyferrous heme stage [*32*]. It is also important to note that despite the widespread belief that bacterial HOs are ferredoxin-dependent the specific ferredoxins that support the activity of these HO enzymes are not yet known. We have recently observed a potentially important clue regarding the nature of the enzymes that transfer electrons to *P. aeruginosa* HO (*pa*-HO) under conditions of iron starvation. This indication comes from the analysis of relatively recent data on genes affected by the iron starvation response in *P. aeruginosa* [*35*], which revealed that the expression of 118 genes was increased at least 3-fold under iron-starvation conditions relative to iron-replete conditions. We noticed that among the 118 upregulated genes, the expression of a gene coding for a ferredoxin (*bfd*) is increased 203-fold and a gene coding for a ferredoxin reductase (*fpr*) is increased 3-fold. These observations suggested that the ferredoxin coded by the *bfd* gene may be the physiological reductant of *pa*-HO, a hypothesis that is in agreement with the fact that among the 118 genes upregulated by iron limitation, expression of the gene coding for *pa*-HO (*pigA*, or PA0672) is also increased 138-fold, and that there is no other upregulated gene coding for a ferredoxin or other classical electron transfer proteins. Moreover, the product of the *fpr* gene, a ferredoxin reductase (*pa*-FPR) is likely the enzyme that transfers electrons to *pa*-Bfd from NAD(P)H. Hence, the motivation of these studies was to probe a hypothesis that

the seven electrons needed by *pa*-HO to degrade heme and release iron in the cytosol of *P. aeruginosa* are shuttled from NAD(P)H to *pa*-FPR and subsequently to *pa*-Bfd, which in turn delivers them to *pa*-HO.

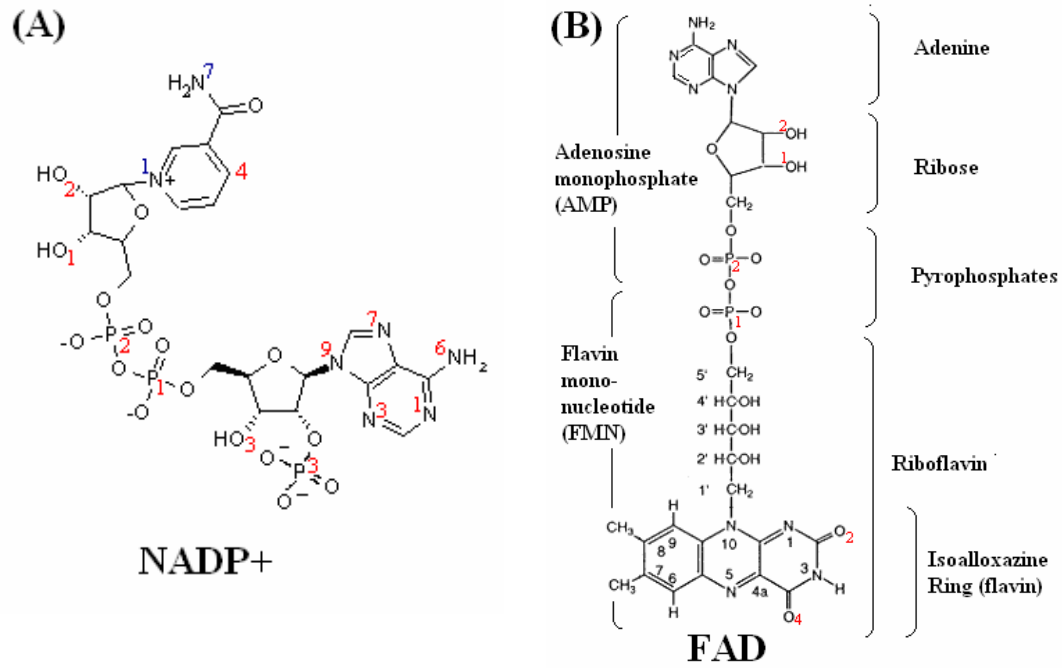

Figure 1-6. Structures of the *pa*-FPR cofactors: $NADP^+$ and FAD.
(A) Nicotinamide (Niacin) adenine dinucleotide phosphate ($NADP^+$), the nitrogen nomenclature adopts the same numbering system for NADP in protein crystal structure from Protein Data Bank (PDB), e.g. N9 is named as N9A (A stands for the adenine ring), the reactive site C4 is named as C4N (2^{nd} N stands for the nicotinamide ring). P3 phosphate group is the feature phosphate group different from NAD^+. The above figure is created and modified based on an original NADPH figure from http://www.uky.edu/ Pharmacy/ps/porter/ CPR_NADPH.gif, obtained at 2008/1/18.
(B) Flavin (Riboflavin) adenine dinucleotide (FAD) [*36*]. The numbering method is the same as above. FAD nomenclature breaks down into small groups; the same applies to $NADP^+$. N(5) and N(1) are the sequential active sites for accepting hydrides.

Biochemical and spectroscopic investigations demonstrated that the *bfd* gene encodes a 73-amino acid protein (*pa*-Bfd) that incorporates a $[2Fe\text{-}2S]^{2+/+}$

center, whereas the *fpr* gene encodes a 258-residue NADPH-dependent ferredoxin reductase (*pa*-FPR) that utilizes FAD as a cofactor. The structures of NADP(H) and FAD are illustrated in Figure 1-6. In vitro reconstitution of *pa*-HO catalytic activity with the newly characterized proteins (*pa*-FPR and *pa*-Bfd) led to the surprising observation that *pa*-FPR efficiently supports the catalytic cycle of *pa*-HO, without the need of a ferredoxin. In comparison, electron transfer from *pa*-Bfd to *pa*-HO is sluggish, which strongly argues against the possibility that the seven electrons needed by *pa*-HO to degrade biliverdin are transferred from NADPH to *pa*-HO in a ferredoxin (Bfd)-dependent manner. Given that *pa*-HO functions release iron from exogenous heme acquired under iron-starvation conditions, the use of a flavoenzyme rather than an iron-sulfur center containing protein to support heme degradation is an efficient use of resources in the cell. The crystal structure of *pa*-FPR (1.6 Å resolution) showed that its fold is comparable to that of the superfamily of ferredoxin reductases and most similar to the structure of *Azotobacter vinelandii* FPR and *E. coli* flavodoxin reductase. The latter two enzymes interact with distinct redox partners, a ferredoxin and a flavodoxin, respectively. Hence findings reported herein extend the range of redox partners recognized by the fold of *pa*-FPR to include a heme oxygenase (*pa*-HO).

Therefore, we propose the following electron transfer path.

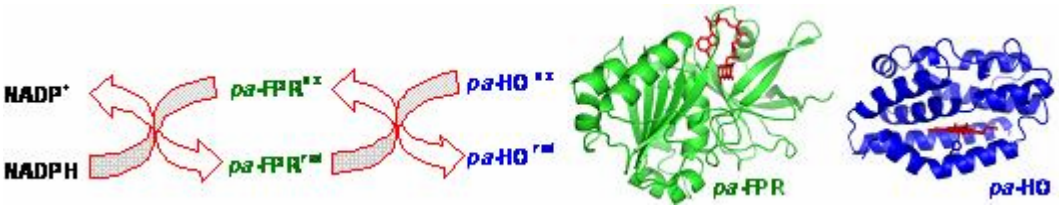

Scheme 1-2. Proposed electron transfer path from NADPH to *pa*-HO.

4. Characterization of FPR-NADP$^+$ complex and protein interaction with *pa*-HO

As shown in Scheme 1-2, NADPH first reduces the FAD in *pa*-FPR into its reduced form $FADH_2$ in *pa*-FPR. Then, the reduced *pa*-FPR can donate electron(s) to and reduce other proteins. The chemistry of the FAD reduction by NADPH inside ferredoxin NAD(P)H reductase protein(FNR) and subsequent electron transfer from FNR to other proteins is shown below:

$$NADPH + H^+ + FNRox\ (or\ FAD) \leftrightarrows NADP^+ + FNRH_2\ (or\ FADH_2) \quad (1\text{-}1)$$

$$FNRH_2\ (FADH_2) + n\ Protein_{ox} \rightarrow FNRox\ (or\ FAD) + n\ Protein_{red} \quad n=1 or\ 2 \quad (1\text{-}2)$$

The reaction in equation 1-1 is reversible for Plastidic FNRs, *i.e.*, enzymes from chloroplasts and cyanobacteria, and the backward reaction is dominant for producing NADPH for photosynthetic use [*37, 38*]. While for bacterial FNR, equation 1-1 is not reversible, the electron from NADPH is used in many oxidoreductive processes, according to equation 1-2 [*39-41*]. The electron transfer between NADPH and FAD is illustrated in Figure 1-7.

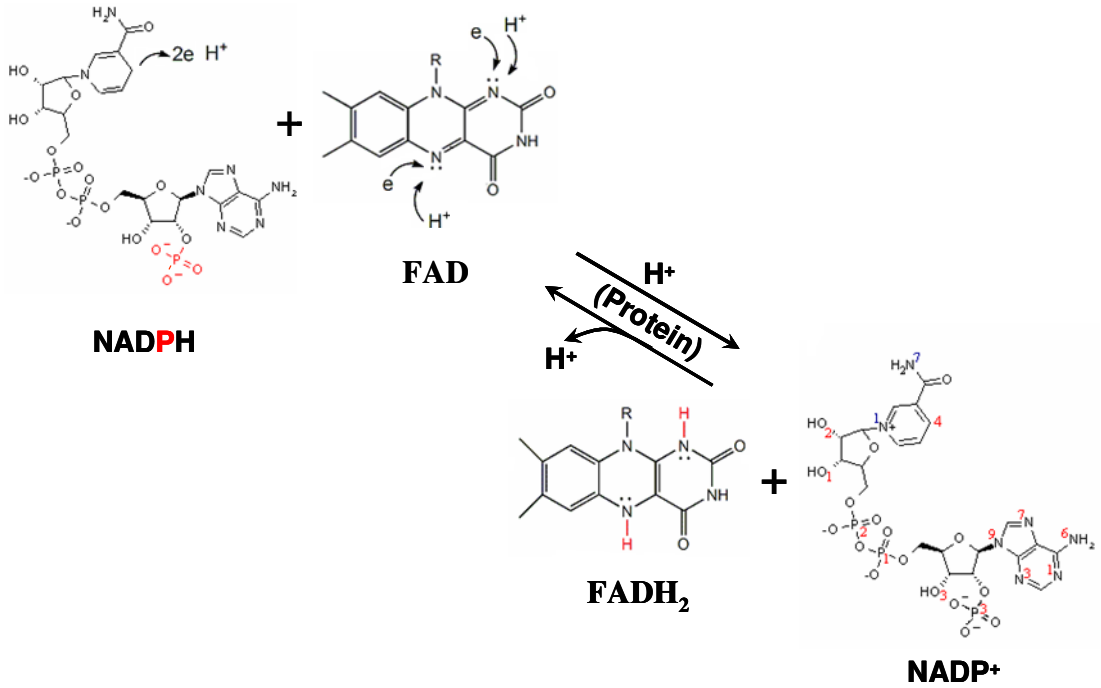

Figure 1-7. NADPH/FAD reaction in ferredoxin reductase protein. (NADP figures are created and modified based on an original NADPH figure from: http://www.uky.edu/Pharmacy/ps/porter/CPR_NADPH.gif at 2008/1/18, FAD figures are created and modified based on an original FAD figure from: http://www.gravitywaves.com/chemistry/CHE450/Images9-13/FAD.gif at 2008/1/18)

The study of electron transfer process between NAD(P)H and protein or NAD(P)$^+$ and protein is important and the first step that should be studied before further protein-protein interaction study. Therefore, the binding of NADP$^+$ to FNR has been studied intensively. Because FNR protein has large protein size (≥30kDa), it is difficult to obtain the 3D protein structure in solution phase using NMR. X-ray crystallography is the common method for obtaining protein 3D structure, however, it has been reported that the crystal of ferredoxin reductase in complex with its coenzyme NADP$^+$ can be very difficult to obtain in many cases, such as spinach-FNR [*42*] and Anabaena-FNR[*43-45*]. Also, as for the *pa*-FPR's

most similar homolog and the same bacterial subclass FNR proteins: *Azotobacter vinelandii* ferredoxin reductase (*Av*-FPR, 85% sequence identity to *pa*-FPR) and *E. coli* flavodoxin reductase (*Ecl*-FldR, 35% sequence identity to *pa*-FPR), there is no reported FNR crystal structure in complex with $NADP^+$.

Table 1-1. Homolog FNR protein comparison with *pa*-FPR. The FNR classification is based on protein sequence, phylogenic relationship as well as FAD conformation [*37*].

FNR Protein	pdb ID	C' Sequence	Sequence identity to *pa*-FPR	FNR Classification
***pa*-FPR**	2QDX	RAFVEK 258		Bacteria subclass I
A. vinelandii FPR	1A8P	RAFVEK 258	85%	Bacteria subclass I
Spinach FNR	1FNB	VY 314	11%	plastidic
Pea FNR	1QG0	VY 308	15%	plastidic
Anabaena FNR	1QUE	TY 303	17%	plastidic

$NADP^+$ binding is believed to be a two-step process: the first step has the strong interactions between the 2' adenosyl phosphate moiety and the FNR protein but the nicotinamide portion does not involve specific interactions with the enzyme, while in the second step the conserved C-terminal Tyr (shown in Table 1-1) moves away and allows the nicotinamide ring to stack parallel to the isoalloxazine ring, thus forming a transient but "productive" complex conducive to direct hydride transfer [*46*]. The reason for the difficulty in obtaining the FNR-$NADP^+$ complex protein crystal structure is likely due to the unfinished binding in

the nicotinamide ring portion of $NADP^+$ coenzyme. In the plastidic Pea, Spinach and Anabaena leaves FNRs, the conserved C-terminal Tyr is located between $NADP^+$ and FAD. The Tyr-Ser mutant of pea FNR in X-ray crystal structure complex with $NADP^+$ revealed that the mutation stabilizes the interaction between FAD and the nicotinamide ring of $NADP^+$, which leads to the proposal that the displacement of Tyr upon $NADP^+$ binding facilitates the direct hydride-transfer to FAD [*47*]. By soaking the FNR crystal in $NADP^+$ solution, crystals of Anabaena FNR and its $NADP^+$ complex were grown by Frey and coworkers in 1996 [*45*]. $NADP^+$ has only 80% occupancy in these crystals and only the ADP part of $NADP^+$ is bound; the nicotinamide tail points outwards. Next Medina and Carlos Gomez-Moreno *et al*. crystallized the Tyr303Ser mutant bound with $NADP^+$ and solved the structure at 3.0 Å resolution [*48*]. In those studies the crystal of mutant Tyr303Trp-$NADP^+$ was obtained by soaking crystal of the Tyr303Trp mutant in a solution of $NADP^+$ instead of co-crystallization method [*45*]. In 2002, the crystal structure of the Anabaena FNR-$NADP^+$ complex was solved by Medina and Carlos Gomez-Moreno *et al.* as the first co-crystallized native form FNR-$NADP^+$ complex [*49*]. Interestingly, Tyr303 is still stacked between FAD and $NADP^+$ instead of moving away to allow for a better $NADP^+$ FAD interaction. Also $NADP^+$ is in a long distant far from FAD for direct hydride transfer. Therefore, the authors concluded that a step-by-step reorganization of $NADP^+$ will eventually require the terminal Tyr to be pushed away, allowing closer contact between FAD

and $NADP^+$ [*50*]. How this putative displacement occurs is still unknown.

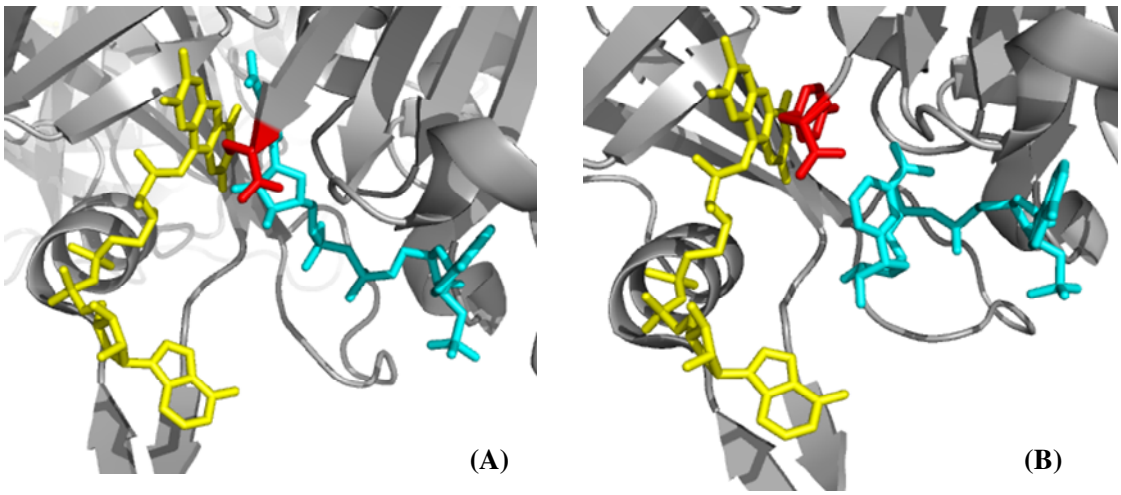

Figure 1-8. (A) *Pea* FNR Y308S-NADP+ (1QFY), (B) Anabaena-FNR-NADP+ (1GJR).

In the context of this general accepted direct hydride transfer mechanism for plastidic FNR proteins, we studied the X-ray crystal structure of the *pa*-FPR-$NADP^+$ complex. The complex crystal structure gives a first view of an extended network of interactions among FAD, $NADP^+$ and the C-terminal extension typical of bacterial subclass I enzymes (FPRs: the group of ferredoxin reductase protein with coding gene: *fpr*) [*37*]. Together with other in-depth comparative crystallography studies, the results suggest that the C-terminal extension will likely not be readily displaced to allow "productive" packing of the isoalloxazine and nicotinamide rings for direct hydride transfer. NMR has the obvious advantage in characterizing the protein-ligand or protein-protein interaction in solution phase. Thus, the NMR backbone assignment of *pa*-FPR was carried out by using protein labeling, TROSY-based NMR experiments as well as selective amino acid labeling. We obtained >95% of the possible assignments. Because

ferredoxin reductase protein has large protein size (≥30kD), until now there is only one NMR backbone assignment completed for Maize leaves FNR [*51*]. Here the NMR backbone assignment work for *pa*-FPR protein is the second example for ferredoxin reductase protein, and the first one for a bacterial FNR protein. The studies done with the aid of *pa*-FPR NMR backbone assignment in solution corroborate the crystal structure observation that the C-terminal tail is not dynamically active. These findings suggest that the direct hydride transfer mechanism as explained above is not applicable to *pa*-FPR and instead a concerted two electrons and one proton transfer, a multi-step hydride transfer is proposed.

5. Rationale of this research

Pseudomonas aeruginosa colonizes and damages the defense mechanism of its host; the infections of this microorganism can be very difficult to cure. This opportunistic pathogen infection in humans often leads to death of patients with diseases like cystic fibrosis or cancer, etc. [*52*]. It is found that these pathogenic bacteria need iron to colonize (infect) an organism. However, the concentration of free iron in mammals is typically very low (~10^{-9} M). Therefore, bacteria have developed sophisticated mechanisms for iron acquisition, including the utilization of heme iron [*53-55*]. In heme, iron is bound inside the porphyrin ring; it can be released after heme is broken. Heme oxygenase is the only known protein used

for heme degradation and iron release inside a cell. Therefore, in the quest to understand the iron acquisition pathway in *Pseudomonas aeruginosa* under iron-starvation conditions, this *Pseudomonas aeruginosa* heme oxgyenase is the key enzyme to study (Figure 1-2). We have carried out intensive protein structure, dynamics and catalysis studies for this *pa*-HO protein [*18-21*].

The in-depth understanding of structure-function relationships in HO is expected to benefit the future pharmaceutical study for selectively inhibiting the unique heme degradation process and stopping the heme-iron release by *pa*-HO. A cluster of Phe rings exists in HO, several of them are close to the heme distal pocket and are poised to interact with one another. Cooperative ring flipping may exist in this network of Phe. We studied this aromatic cluster in HO using *Pseudomonas aeruginosa* heme oxygenase as a model to understand its role in protein structure and function. This Phe ring cluster study is explained in chapter 2 with a large amount of experimental results discussed in detail.

As we know, heme oxygenase uses 3 O_2 and 7 electrons to degrade heme into biliverdin, releasing iron and CO. Therefore, in the context of the quest to understand the iron acquisition pathway in *Pseudomonas aeruginosa* under iron-starvation condition, the search for *pa*-HO redox partner proteins was carried out by studying two proteins: ferredoxin reductase (*pa*-FPR) and ferredoxin (*pa*-Bfd). The later was studied by Yuhong Zeng and Saroja Weeratunga; some of their findings are discussed in this dissertation for pedagogical reasons. The general

belief of ferredoxin being the redox partner of heme oxgyenase is challenged by our findings in the novel redox partnership between *pa*-FPR (ferredoxin reductase) and *pa*-HO. The crystal structure and biochemical characterization of *pa*-FPR as well as the surprising findings regarding the redox partnership study are discussed in detail in chapter 3. With this study, *pa*-FPR became the focus of our subsequent study in order to understand how and where these two novel redox partner proteins interact with each other.

Pa-FPR obtains electron from NADPH, its FAD cofactor is directly reduced into $FADH_2$ after coenzyme NADPH binding and the subsequent redox reaction inside the protein. The study of ligand binding and electron transfer inside the protein is a key in understanding how ferredoxin reductase carries out its redox reaction and interacts with other proteins. In general, a two-step $NADP^+$ binding and direct hydride transfer are accepted for the ferredoxin reductase protein family. As revealed in chapter 4, we examined the *pa*-FPR-$NADP^+$ complex by NMR and X-ray crystallography methods as the first study of a bacterial subclass I FNR complex. A novel FNR-$NADP^+$ binding as well as the multi-step two electrons and one proton hydride transfer mechanism was proposed based on careful data analysis.

With both a crystal structure and NMR protein backbone assignment in solution phase available for *pa*-FPR and *pa*-HO, investigation of their protein-protein interactions (PPI) was carried out in order to find whether the interaction

interface is located on each protein. The analysis of the two protein crystal structures suggests the potential interaction interface is located on the surface area of *pa*-HO, near the heme binding site, and at the concave bowl shape surface on top of isollaxazine ring's methyl group for *pa*-FPR. Preliminary NMR data suggests that PPI is an ultra-weak transient electrostatic interaction [*56, 57*] that can be detected only at the border of NMR detection limit. Also the NMR result corroborates the crystallography study. The proposed protein-protein interaction is discussed at the end of the chapter IV.

REFERENCES

[1] van Delden, C. (2004) Virulence factors in Pseudomonas aeruginosa. *Pseudomonas*, *2*, 3-45.

[2] Skaar, E. P.; Schneewind, O. (2004) Iron-regulated surface determinants (Isd) of *Staphylococcus aureus*: stealing iron from heme. *Microbes and Infection*, *6*, 390-397.

[3] Chipperfield, J. R.; Ratledge, C. (2000) Salicylic Acid is not a Bacterial Siderophore: A theoretical Study. *BioMetals*, *13*, 165-168.

[4] Ward, P. P.; Conneely, O. M. (2004) Lactoferrin: Role in Iron Homeostasis and Host Defense Against Microbial Infection. *BioMetals*, *17*, 203-208.

[5] Flo, T. H.; Smith, K. D.; Sato, S.; Rodriguez, D. J.; Holmes, M. A.; Strong, R. K.; Akira, S.; Aderem, A. (2004) Lipocalin 2 Mediates an Innate Immune Response to Bacterial Infection by Sequestering Iron. *Nature*, *432*, 917-921.

[6] Wandersman, C.; Delepelaire, P. (2004) Bacterial Iron Sources: From Siderophores to Hemophores. *Annual Review of Microbiology*, *58*, 611-647.

[7] Genco, C. A.; Dixon, D. W. (2001) Emerging Strategies in Microbial Haem Capture. *Molecular Microbiology*, *39*, 1-11.

[8] Otto, B. R.; Verweij-van Vught, A. M.; MacLaren, D. M. (1992) Transferrins and Heme-Compounds as Iron Sources of Pathogenic Bacteria. *Critical Reviews in Microbiology*, *18*, 217-233.

[9] Ochsner, U. A.; Johnson, Z.; Vasil, A. I. (2000) Genetics and Regulation of Two Distinct Haem-Uptake Systems, *phu* and *has*, in *Pseudomonas aeruginosa*. *Microbiology*, *146*, 185-198.

[10] Ratliff, M.; Zhu, W.; Deshmukh, R.; Wilks, A.; Stojiljkovic, I. (2001) Homologues of Nisserial Heme Oxygenase in Gram-Negative Bacteria: Degradation of Heme by the Product of the *pigA* Gene of *Pseudomonas aeruginosa*. *Journal of Bacteriology*, *183*, 6394-6403.

[11] Ravel, J.; Cornelis, P. (2003) Genomics of pyoverdine-mediated iron uptake in pseudomonads. *Trends in Microbiology*, *11*, 195-200.

[12] Yoshida, T.; Noguchi, M.; Kikuchi, G. (1980) Oxygenated Form of Heme-Heme Oxygenase Complex and Requirement for Second Electron to Initiate Heme Degradation from the Oxygenated Complex. *Journal of Biological Chemistry*, *255*, 4418-4420.

[13] Davydov, R. M.; Yoshida, T.; Ikeda-Saito, M.; Hoffman, B. M. (1999) Hydroperoxy-Heme Oxygenase Generated by Cryoreduction Catalyzes the Formation of meso-Hydroxyheme as Detected by EPR and ENDOR. *Journal of the American Chemical Society*, *121*, 10656-10657.

[14] Wilks, A.; Torpey, J.; Ortiz de Montellano, P. R. (1994) Heme Oxygenase (HO-1) Evidence for Electrophilic Oxygen Addition to the Porphyrin Ring in the Formation of α-meso-hydroxyheme. *Journal of Biological Chemistry*, *269*, 29553-29556.

[15] Yoshida, T.; Kikuchi, G. (1978) Features of the Reaction of Heme Degradation Catalyzed by the Reconstituted Microsomal Heme Oxygenase System. *Journal of Biological Chemistry*, *253*, 4230-4236.

[16] Yoshida, T.; Noguchi, M.; Kikuchi, G. (1980) A New Intermediate of Heme Degradation Catalyzed by the Heme Oxygenase System. *Journal of Biochemistry*, *88*, 557-563.

[17] Liu, Y.; Ortiz de Montellano, P. R. (2000) Reaction Intermediates and Single Turnover Rate Constants for the Oxidation of Heme by Human Heme Oxygenase-1. *Journal of Biological Chemistry*, *275*, 5297-5307.

[18] Rivera, M.; Zeng, Y. (2005) Heme oxygenase, steering dioxygen activation toward heme hydroxylation. *Journal of Biological Chemistry*, *99*, 337-354.

[19] Caignan, G. A.; Deshmukh, R.; Zeng, Y.; Wilks, A.; Bunce, R. A.; Rivera, M. (2003) The Hydroxide Complex of Pseudomonas aeruginosa Heme Oxygenase as a Model of the Low-Spin Iron(III) Hydroperoxide Intermediate in Heme Catabolism: 13C NMR Spectroscopic Studies Suggest the Active Participation of the Heme in Macrocycle Hydroxylation. *Journal of the American Chemical Society*, *125*, 11842-11852.

[20] Zeng, Y.; Caignan, G. A.; Bunce, R. A.; Rodriguez, J. C.; Wilks, A.; Rivera, M. (2005) Azide-Inhibited Bacterial Heme Oxygenases Exhibit an S = 3/2 (dxz,dyz)3(dxy)1(dz2)1 Spin State: Mechanistic Implications for Heme Oxidation. *Journal of the American Chemical Society*, *127*, 9794-9807.

[21] Zeng, Y.; Deshmukh, R.; Caignan, G. A.; Bunce, R. A.; Rivera, M.; Wilks, A. (2004) Mixed Regioselectivity in the Arg-177 Mutants of Corynebacterium diphtheriae Heme Oxygenase as a Consequence of in-Plane Heme Disorder. *Biochemistry*, *43*, 5222-5238.

[22] Sugishima, M.; Omata, Y.; Kakuta, Y.; Sakamoto, H.; Noguchi, M.; Fukuyama, K. (2000) Crystal Structure of Rat Heme Oxygenase-1 in Complex with Heme. *FEBS Letters*, *471*, 61-66.

[23] Lad, L.; Schuller, D. J.; Shimizu, H.; Friedman, J.; Li, H.; Ortiz de Montellano, P. R.; Poulos, T. L. (2003) Comparison of the Heme-free and-bound Crystal Structures of Human Heme Oxygenase-1. *Journal of Biological Chemistry*, *278*, 7834-7843.

[24] Hirotsu, S.; Chu, G. C.; Unno, M.; lee, D.-S.; Yoshida, T.; Park, S.-Y.; Shiro, Y.; Ikeda-Saito, M. (2004) The Crystal Structures of the Ferric and Ferrous Forms of the Heme Complex of HmuO, a Heme Oxyenase of *Corynebacterium diphtheriae*. *Journal of Biological Chemistry*, *279*, 11937-11947.

[25] Friedman, J.; Lad, L.; Li, H.; Wilks, A.; Poulos, T. L. (2004) Structural Basis for Novel δ-Regioselective Heme Oxygenation in the Opportunistic Pathogen *Pseudomonas aeruginosa*. *Biochemistry*, *43*, 5239-5245.

[26] Schuller, D. J.; Zhu, W.; Stojiljkovic, I.; Wilks, A.; Poulos, T. L. (2001) Crystal Structure of Heme Oxygenase from the Gram-Negative Pathogen *Neisseria meningitidis* and a Comparison with Mammalian Heme Oxygenase. *Biochemistry*, *40*, 11552-11558.

[27] Li, Y.; Syvitski, R. T.; Auclair, K.; Ortiz de Montellano, P. R.; La Mar, G. N. (2003) Solution ^{1}H, ^{15}N NMR Spectroscopic Characterization of Substrate-Bound, Cyanide-Inhibited Human Heme Oxygenase: Water Occupation of the Distal Cavity. *Journal of the American Chemical Society*, *125*, 13392-13403.

[28] Baldwin, R. L. (2002) PROTEIN FOLDING: Making a Network of Hydrophobic Clusters. *Science*, *295*, 1657-1658.

[29] Maines, M. D.; Gibbs, P. E. M. (2005) 30 some years of heme oxygenase: From a "molecular wrecking ball" to a "mesmerizing" trigger of cellular events. *Biochemical and Biophysical Research Communications*, *338*, 568-577.

[30] De Montellano, P. R. O.; Auclair, K. (2003) Heme oxygenase structure and mechanism. *Porphyrin Handbook*, *12*, 183-210.

[31] Cornejo, J.; Willows, R. D.; Beale, S. I. (1998) Phytobilin Biosynthesis: Cloning and Expression of a Gene Encoding Soluble Ferredoxin-Dependent Heme Oxygenase from *Synechocystis sp*. PCC6803. *The Plant Journal*, *15*, 99-107.

[32] Wegele, R.; Tasler, R.; Zeng, Y.; Rivera, M.; Frankenberg-Dinkel, N. (2004) The Heme Oxygenase(s)-Phytochrome System of *Pseudomonas aeruginosa*. *Journal of Biological Chemistry*, *279*, 45791-45802.

[33] Cornejo, J.; Beale, S. I. (1997) Phycobilin Biosynthetic Reactions in Extracts of Cyanobacteria. *Photosynthesis Research*, *51*, 223-230.

[34] Muramoto, T.; Tsurui, N.; Terry, M. J.; Yokota, A.; Kohchi, T. (2002) Expression and Biochemical Properties of a Ferredoxin-Dependent Heme Oxygenase Required for Phytochrome Chromophore Synthesis. *Plant Physiology*, *130*, 1958-1966.

[35] Ochsner, U. A.; Wilderman, P. J.; Vasil, A. I.; Vasil, M. L. (2002) GeneChip Expression Analysis of the Iron Starvation Response in *Pseudomonas Aeruginosa*: Identification of Novel Pyoverdine Biosynthesis Genes. *Molecular Microbiology*, *45*, 1277-1287.

[36] Macheroux, P. (1999) UV-visible spectroscopy as a tool to study flavoproteins, in *Methods in Molecular Biology (Totowa, New Jersey)* (Chapman, S. K., and Reid, G. A., Eds., Ed.), 1-7, Humana Press, Totowa, NJ.

[37] Ceccarelli, E. A.; Arakaki, A. K.; Cortez, N.; Carrilo, N. (2004) Functional Plasticity and Catalytic Efficiency in Plant and Bacterial Ferredoxin-(NADP(H) Reductases. *Biochimica et Biophysica Acta*, *1698*, 155-165.

[38] Shin, M.; Arnon, D. I. (1965) Enzymic Mechanisms of Pyridine Nucleotide Reduction in Chloroplasts. *Journal of Biological Chemistry*, *240*, 1405-1411.

[39] Liochev, S. I.; Hausladen, A.; Beyer, W. F. J.; Fridovich, I. (1994) NADPH:Ferredoxin Oxidoreductase Acts as a Paraquat Diaphorase and is

a Member of the *soxRS* Regulon. *Proceedings of the National Academy of Sciences*, *91*, 1328-1331.

[40] Yannone, S. M.; Burgess, B. K. (1998) The Seven-Iron Fdl from Azotobacter vinelandii Regulates the Expression of NADPH:Ferredoxin Reductase vian an Oxidative Stress Response. *Journal of Biological Inorganic Chemistry*, *3*, 253-258.

[41] Bittel, C.; Tabares, L. C.; Armesto, M.; Carrillo, N.; Cortez, N. (2003) The oxidant-Responsive Diaphorase of *Rhodobacter capsulatus* is a Ferredoxin (flavodoxin)-NADP(H) Reductase. *FEBS Letters*, *553*, 408-412.

[42] Bruns, C. M.; Karplus, P. A. (1995) Refined crystal structure of spinach ferredoxin reductase at 1.7 .ANG. resolution: oxidized, reduced and 2'-phospho-5'-AMP bound states. *Journal of Molecular Biology*, *247*, 125-145.

[43] Medina, M.; Martinez-Julve, M.; Hurley, J. K.; Tollin, G.; Gomez-Moreno, C. (1998) Involvement of glutamic acid 301 in the catalytic mechanism of ferredoxin-NADP+ reductase from Anabaena PCC 7119. *Biochemistry*, *37*, 2715-2728.

[44] Tejero, J.; Perez-Dorado, I.; Maya, C.; Martinez-Julvez, M.; Sanz-Aparicio, J.; Gomez-Moreno, C.; Hermoso, J. A.; Medina, M. (2005) C-Terminal Tyrosine of Ferredoxin-NADP+ Reductase in Hydride Transfer Processes with NAD(P)+/H. *Biochemistry*, *44*, 13477-13490.

[45] Serre, L.; Vellieux, F. M. D.; Medina, M.; Gomez-Moreno, C.; Fontecilla-Camps, J. C.; Frey, M. (1996) X-ray structure of the ferredoxin:NADP+ reductase from the cyanobacterium Anabaena PCC 7119 at 1.8 .ANG. resolution, and crystallographic studies of NADP+ binding at 2.25 .ANG. resolution. *Journal of Molecular Biology*, *263*, 20-39.

[46] Deng, Z.; Aliverti, A.; Zanetti, G.; Arakaki, A. K.; Ottado, J.; Orellano, E. G.; Calcaterra, N. B.; Ceccarelli, E. A.; Carrillo, N.; Karplus, P. A. (1999) A Productive NADP+ Binding Mode of Ferredoxin-NADP+ Reductase Revealed by Protein Engineering and Crystallographic Studies. *Nature Structural Biology*, *6*, 847-853.

[47] Deng, Z.; Aliverti, A.; Zanetti, G.; Arakaki, A. K.; Ottado, J.; Orellano, E. G.; Calcaterra, N. B.; Ceccarelli, E. A.; Carrillo, N.; Karplus, P. A. (1999) A productive NADP binding mode of ferredoxin- NADP reductase revealed by protein engineering and crystallographic studies. *Nature Structural Biology*, *6*, 847-853.

[48] Hurley, J. K.; Morales, R.; Martinez-Julvez, M.; Brodie, T. B.; Medina, M.; Gomez-Moreno, C.; Tollin, G. (2002) Structure-function relationships in Anabaena ferredoxin/ferredoxin:NADP+ reductase electron transfer: insights from site-directed mutagenesis, transient absorption spectroscopy and x-ray crystallography. *Biochimica et Biophysica Acta, Bioenergetics*, *1554*, 5-21.

[49] Hermoso, J. A.; Mayoral, T.; Faro, M.; Gomez-Moreno, C.; Sanz-Aparicio, J.; Medina, M. (2002) Mechanism of coenzyme recognition and binding revealed by crystal structure analysis of ferredoxin-NADP+ reductase complexed with NADP+. *Journal of Molecular Biology*, *319*, 1133-1142.

[50] Medina, M.; Gomez-Moreno, C. (2004) Interaction of ferredoxin-NADP+ reductase with its substrates: optimal interaction for efficient electron transfer. *Photosynthesis Research*, *79*, 113-131.

[51] Maeda, M.; Lee, Y. H.; Ikegami, T.; Tamura, K.; Hoshino, M.; Yamazaki, T.; Nakayama, M.; Hase, T.; Goto, Y. (2005) Identification of the N- and C-Terminal Substrate Binding Segments of Ferredoxin-NADP+ Reductase by NMR. *Biochemistry*, *44*, 10644-10653.

[52] Quinn, J. P. (1998) Clinical problems posed by multiresistant nonfermenting gram-negative pathogens. *Clinical Infectious Diseases*, *27*, S117-S124.

[53] Martinez, J. L.; Delgado-Iribarren, A.; Baquero, F. (1990) Mechanisms of iron acquisition and bacterial virulence. *FEMS Microbiology Reviews*, *75*, 45-56.

[54] Griffiths, E. (1991) Iron and bacterial virulence--a brief overview. *BioMetals*, *4*, 7-13.

[55] Berlutti, F.; Morea, C.; Battistoni, A.; Sarli, S.; Cipriani, P.; Superti, F.; Ammendolia, M. G.; Valenti, P. (2005) Iron availability influences aggregation, biofilm, adhesion and invasion of *Pseudomonas aeruginosa* and *Burkholderia cenocepacia*. *International Journal of Immunopathology & Pharmacology*, *18*, 661-670.

[56] Suh, J.-Y.; Tang, C.; Clore, G. M. (2007) Role of Electrostatic Interactions in Transient Encounter Complexes in Protein-Protein Association Investigated by Paramagnetic Relaxation Enhancement. *Journal of the American Chemical Society*, *129*, 12954-12955.

[57] Vaynberg, J.; Fukuda, T.; Chen, K.; Vinogradova, O.; Velyvis, A.; Tu, Y.; Ng, L.; Wu, C.; Qin, J. (2005) Structure of an Ultraweak Protein-Protein Complex and Its Crucial Role in Regulation of Cell Morphology and Motility. *Molecular Cell*, *17*, 513-523.

CHAPTER II: NMR STUDY OF PSEUDOMONAS AERUGINOSA HEME OXYGENASE VIA MUTATION AND ^{19}F-PHE LABELING

INTRODUCTION

Heme oxygenase (HO) is a distinctive heme containing protein. Heme in HO is used not only as a prosthetic group but also as a substrate. HO takes 7 electrons and 3 molecules of O_2 to catalytically degrade heme into biliverdin and release Fe^{II} and CO. It is the only known enzyme to degrade heme and release iron inside a cell. This enzyme exists in many organisms and plays a significant and diverse physiological role in nature. In mammals, recycled iron from heme is the major resource for daily iron needs in such a way that the produced CO is an important neural signal transmitter and the resulting biliverdin is further reduced to bilirubin, a powerful antioxidant [*1, 2*]. Human heme oxygenase-1 as an example has been intensively studied by Paul Oritz de Montelleano and co-workers [*3-6*]. In plants, HO is used to degrade heme to biliverdin, biliverdin is further used for synthesizing photosynthetic organisms as shown in an example of *Arabidopsis thaliana* Heme Oxygenase [*7*]. In bacteria and fungi, heme from a host is a major iron resource [*8*].

As mentioned before, heme oxygenase is different from all other heme-containing catalytic proteins, such as cytochrome P450, nitric oxide synthases,

peroxidases, and chloroperoxidase in its distinguishable catalytic pathway. As shown in Scheme 2-1, the release of heme-iron is accomplished by the breakdown of heme to biliverdin. This is a complex reaction requiring the input of 7 electrons and 3 molecules of O_2, which must be delivered to HO rapidly and efficiently in order to sustain catalytic activity. Heme breakdown starts with a single electron reduction of ferric HO (resting state) to the deoxyferrous state, followed by the rapid binding of dioxygen to form an oxyferrous complex (Fe^{II}-O_2) [*9*]. Injection of a second electron into the Fe^{II}-O_2 complex triggers the electron rearrangement that leads to the formation of a ferric peroxide (Fe^{III}-OO^{-}) complex, which accepts a proton to form a ferric hydroperoxide (Fe^{III}-OOH) oxidizing species [*10*]. The ring oxidation involves attack of the Fe^{III}-OOH intermediate on the aromatic macrocycle [*11*] to form a meso-hydroxyheme intermediate, which undergoes a subsequent O_2- and electron-dependent elimination of the hydroxylated meso carbon as CO, thus forming verdoheme. Verdoheme is then oxidized to Fe^{III}-biliverdin in a reaction that requires both O_2 and additional electrons [*12, 13*]. Fe^{III}-biliverdin must be reduced to Fe^{II}-biliverdin prior to the sequential release of Fe^{II} and biliverdin [*14*]. The peroxide shunt reaction (adding H_2O_2 in the presence of O_2 to initiate the reaction forms verdoheme) is a commonly used method for simulating the heme oxygenase metabolism pathway in vitro [*15-17*]. The highlighted hydroxylation step (blue box in Scheme 2-1) that converts the ferric hydroperoxyl heme to α-meso-hydroxyheme is the step that distinguishes it from all other heme-containing proteins.

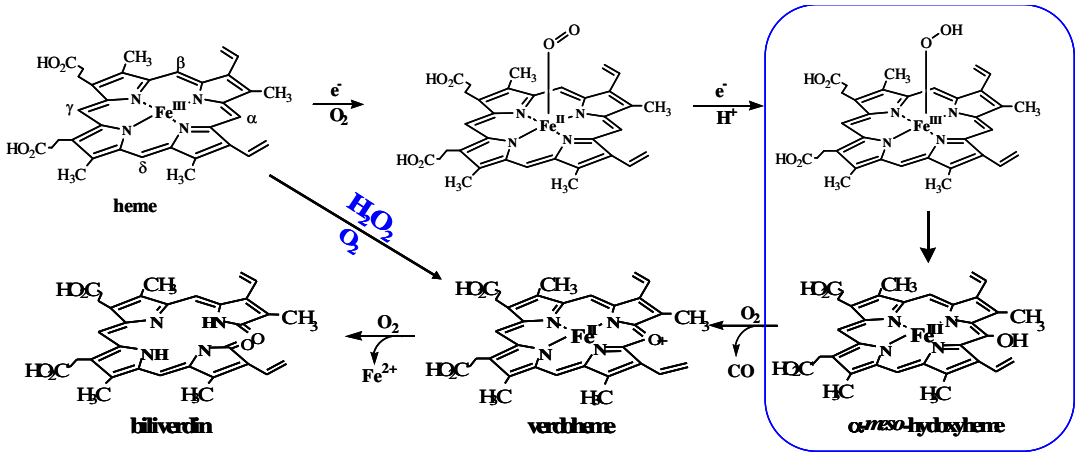

Scheme 2-1. Heme metabolism pathway of heme oxygenase.

As shown in the peroxide shunt reaction (Figure 2-1), H_2O_2 binds to the ferric heme to form an obligatory ferric hydroperoxyl heme intermediate. From there, there are two possible pathways. One pathway leads to the exclusive heme oxygenase metabolism. As mentioned above, the HOO^- group reacts with the heme *meso*-carbon to produce a *meso*-hydroxyheme intermediate, and then the subsequent reaction with O_2 leads to the release of CO and the formation of verdoheme. While the other pathway exists commonly in other heme-containing proteins like cytochrome P450 and peroxidase, the Fe^{III}-OOH intermediate undergoes auto-oxidation and forms ferryl heme. By monitoring the products of the peroxide shunt reaction, one can differentiate the heme oxygenase reactivity from the peroxidase reactivity.

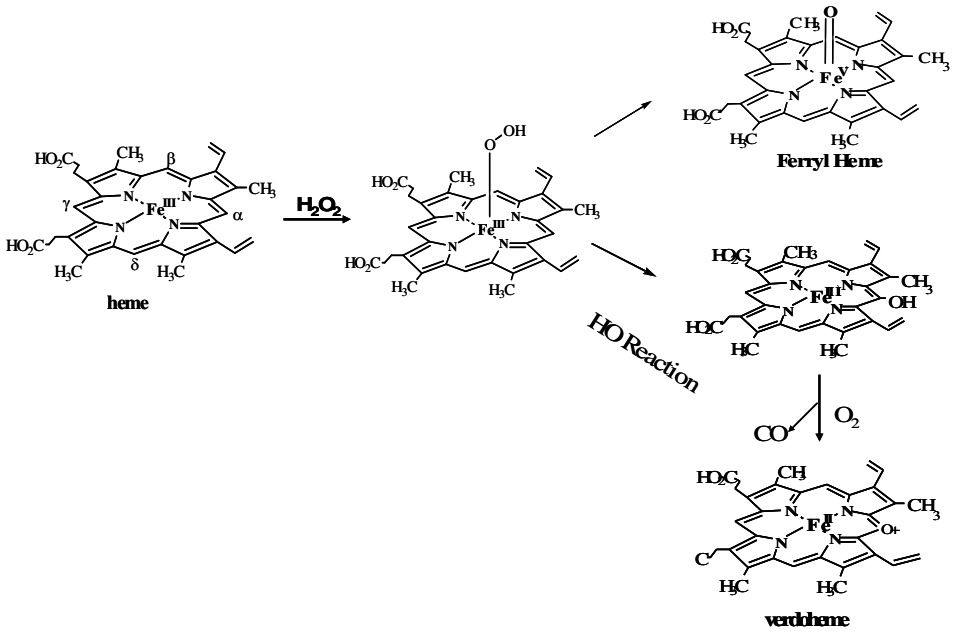

Figure 2-1. Obligatory heme hydroxylation in heme containing protein.

In order to answer the essential question of how nature tunes the catalytic mechanism of heme oxygenase, we have performed intensive studies aimed at understanding the structure-function relationships of this protein. From the past studies done in our lab, we observed that the deformation of heme from planarity facilitates heme hydroxylation by electronically activating the heme at the *meso*-carbon (Figure 2-2) [*18, 19*]. This activated electronic structure, likely linked to heme hydroxylation reactivity, is stabilized by the heme environment of the H-bonding network and the polypeptide dynamics [*19*]. Our previous protein dynamic studies [*20*] further confirmed that the unique heme oxygenase property is indeed linked with its protein structure and dynamics, involving H-bonding networks and polypeptide dynamics.

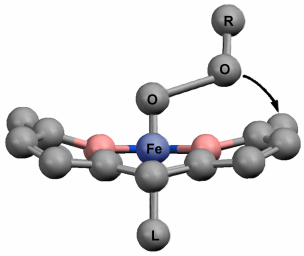

Figure 2-2. Proposed heme deformation in hydroxylation step, adapted from [*18, 19*].

During this study, we found a very interesting phenomenon when observing the protein 3D crystal structure. A cluster of Phe rings exists in HO, and several of them are close to the heme distal pocket and are poised to interact with one another (Figure 2-3). How does nature use this network of hydrophobic phenylalanines to fulfill heme oxygenase's versatile functions? We studied this cluster in HO from *Pseudomonas aeruginosa* heme oxygenase (*pa*-HO) using NMR by making comparisons among wild type (WT), mutants and ^{19}F-phenylalanine labeled WT proteins to understand its role in protein structure and function.

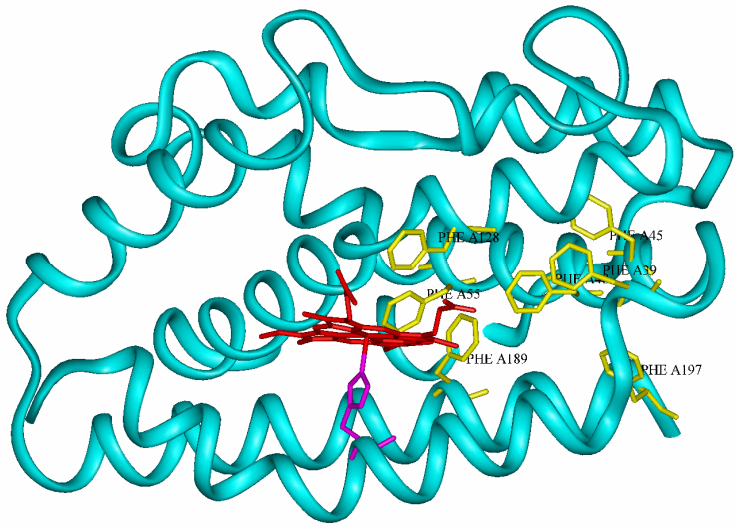

Figure 2-3. Structure of *Pseudomonas aeruginosa* heme oxygenase (PDB:1SK7). Heme is in red and the conserved aromatic rings are in yellow.

EXPERIMENTAL SECTION

i. Mutagenesis of *Pseudomonas aeruginosa* heme oxygenase

The wild-type *Pseudomonas aeruginosa* Heme Oxygenase gene on pET 21a plasmid was a generous gift from Dr. Angela Wilks at the University of Maryland. All F39L, F45L, F128L, F48L, F189L, F189V, F39/45L, F39/48L, F39/F128L, F45/128L, F39/189L and F45/189L *pa*-HO mutants were prepared using the Quickchange Mutagenesis Kit from Stratagene (La Jolla, CA) with oligonucleotides synthesized by the Biotechnology Support Facility, the University of Kansas Medical Center. After DNA sequencing and DNA plasmid were transformed into *E. coli*

BL21 (DE3) GOLD supercompetent cells, protein expression and purification were performed as described below.

ii. Protein expression and purification.

The wild type and mutant *pa*-HO proteins were purified as described below. A single colony of freshly transformed *E. Coli* BL21 Gold (DE3) *pigA* or its mutant cell was grown overnight in 10 ml of LB-media containing 100 μg/ml of ampicillin at 37 °C with a 225-240 rpm shaking speed. Then a 10 ml culture was transferred into LB-Ampicillin media (1 liter). After reaching mid-log phase, expression was induced by the addition of a final 1 mM concentration of IPTG (isopropyl-1-thiol-(D)-galactopyranoside). The cells were grown further for 4-5 hours at 30 °C and harvested by centrifugation (4500 rpm for 10-15 min). After stored overnight at -20 °C, cells were thawed at 4 °C and lysed in lysis buffer, lysozyme, phenylmethysulfonyl fluoride (PMSF), deoxycolic acid and DNase. After incubated for 20 minutes at 37 °C and stirred for one hour at room temperature, the cells were defragmented by sonication for 10 cycles of 1.5 mins each on ice. The cell suspension was then ultracentrifuged at 23,500g for 2 hrs. The clear supernatant was loaded onto a Sepharose-Q Fast Flow column (1.5 cm x 15 cm) previously equilibrated with 20 mM Tris-HCl (pH 7.6). After loading the sample, the column was equilibrated with one volume of 20 mM Tris-HCl (pH 7.6). The column was applied with NaCl linear gradient from 50 -500 mM. Protein eluted at about 200-250 mM. After run on SDS-PAGE and UV-vis, the *pa*-HO protein fractions were

collected and dialyzed against potassium phosphate (pH 7.0, u=0.1) (2 x 4 L) at 4 °C. The protein was either reconstituted with heme as described below or stored at -80 °C for later usage.

The ^{15}N labeled protein was expressed in a 1 liter minimal medium containing nutrients at natural isotopic abundance using the same protein expression procedures described above. After reaching mid-log phase, the cells were spun down and transferred to the same volume of the fresh minimal medium containing labeled material, for example, 1g $^{15}NH_4Cl$. The cells were grown further to O.D. = 0.6 ~ 0.7, then the temperature was lowered to 30 °C. Inducted with 1mM IPTG, the cells were harvested 5 hours later.

The ^{19}F-Phe protein was expressed as described in the study of Benjamin Schuler *et al.* [*21*]. Again, using a similar expression system as above, to a 1 liter minimal medium with all nutrients was added 1g of glyphosate (N-(phosphonomethyl)-glycine) and 50 mg of all amino acids except L-Phe; 5mg of this amino acid were added. The cell growth was monitored closely by measuring O.D. When O.D. reached ~1.1 at 550 nm, the cell growth went into lag phase due to the depletion of Phe. Then 200 mg (~1 mM) of ortho-, meta- or para-^{19}F-Phe (D-, L-) (purchased from MP Biomedicals Inc.) was added for labeling, at which point the temperature was lowered to 30 °C. IPTG was added 30 mins later. The cells were harvested after 5 h of growth following induction. The expressed protein contained in excess of 95% ^{19}F-Phe, as determined from mass spectrometer analysis.

The ^{15}N and ortho-^{19}F-Phe double labeled protein was expressed using a

similar method as for labeling protein with ^{15}N except that the second batch of minimal medium contains both 1 g $^{15}NH_4Cl$ and 600 mg (~3 mM) *ortho*-^{19}F-Phe (D-, L-).

iii. Reconstitution of the WT and mutant *pa*-HO proteins with heme

Hemin (aliquot of 5~50 µl of heme DMSO solution: 10 mg heme dissolved into 3 ml DMSO) was titrated into the purified HO protein solution (20~80ml 2~6 µmol protein in 20mM pH 7.6 Tris buffer) with moderate stirring. The titration is monitored by UV-vis spectrum until the absorbance ratio A_{280}/A_{405} reaches a maximum (0.4~0.5). Then the holo-form HO protein was concentrated into 1~3 ml volume and purified by size exclusion chromatography using a sephadex Gel-50 fine or superfine (for labeled protein) column (3.0 cm x 100 cm) pre-equilibrated with sodium phosphate (pH 7.0, u=0.1) (pH 7.0). The protein was then concentrated by Centricon tubes and stored at -80 °C.

iv. Extinction coefficient of *pa*-HO mutants

The millimolar extinction coefficient (Ω_{405nm}) of the heme-HO complex was determined *via* the pyridine hemochrome method [*22-24*]. The experiment was conducted with 900ul protein (concentration is adjusted to have UV-vis absorbance 1.089 at 405nm) in 50mM pH 7.0 sodium phosphate buffer inside a 1cm path length black quartz curvette. Then 100ul pyridine was added to coordinate the heme by displacing the heme out of heme protein pocket. Then heme was converted to the reduced ferrous pyridine hemochrome by reduction with excess sodium dithionite

(about several grains added). After mixing the solution with parafilm covering on top of the curvette, final UV-vis spectrum is taken. Then the concentration of the heme was calculated by Beer-Lambert Law using millimolar extinction coefficient values of 170, 17.5 and 34.4 at 418.5, 526, and 555 nm, respectively, for reduced ferrous pyridine-hemechrome [*18*]. The extinction coefficient for heme-HO complex (Ω_{405nm}) is then calculated based on the calculated heme concentration and previously measured absorbance. Three trials were taken for each sample.

v. Circular Dichroism Spectrophotometry of WT and mutant *pa*-HO

CD spectra were measured on a JASCO J-710 spectropolarimeter equipped with a Jasco PTC-4235 Peltier thermostated cell holder. Spectra were recorded in the far UV (190-250 nm) in a 2 mm flat cell at 25 °C in pH 7.0 KH_2PO_4 buffer (μ=0.1) with 4 sec response time, 50 nm/min scan rate and 5 times average. Three trials were taken for each sample. Baseline correction was carried out by subtracting averaged sample spectra from averaged buffer spectra recorded at the same conditions. The reading of molar ellipticity (degree cm^2 $dmol^{-1}$) was calculated by dividing the subtracted (protein – blank) spectra with protein concentration (about 3 μM).

vi. Thermal denaturation study of WT and mutant *pa*-HO

Thermal denaturation was measured on a Varian Carey 100 Bio UV/visible spectrophotometer equipped with a Peltier-thermostated cell holder. Sample concentration was about 3 μM in pH7 phosphate buffer (μ=0.1). Temperature increment is 2 °C; it was monitored by using a temperature probe ($\pm$0.1 °C). The

thermal denaturation temperature was averaged from the calculated first derivative values based on the three trial plots of soret absorbance (405 nm or so) vs. temperature.

vii. Hydrogen Peroxide Assay Study of the wild-type and *pa*-HO mutants

Reconstituted heme-*pa*HO complex (5 μM in 2 ml of phosphate buffer, μ=0.1, pH7) was placed in a 1.0 cm cell with moderate stirring at 25 °C. The soret absorbance was adjusted to 1.0 with Soret peak at ~405 nm. Reaction was initiated by titrating 1.0 equivalent of H_2O_2, and the spectra were monitored with respect to changes in time. Verdoheme formation, followed by increase in absorbance at 600 nm was plotted as a function of time, as a means to indicate heme oxygenase reactivity [*25, 26*].

Guaiacol assay was carried out under the same conditions as the above procedure with the following exceptions: 1.0 mM guaiacol was initially present and 100 equivalents of peroxide were added. The 470 nm peak formation of guaiacol oligomer with time was plotted as an indication of ferryl formation, which suggests peroxidase reactivity [*26, 27*].

viii. NMR Spectroscopy

NMR samples of *pa*-HO, *pa*-HO-N_3 and *pa*-HO-CN complexes contained 1.0~2.0 mM protein in 50 mM sodium phosphate, pH 7.0 and 5-10% D_2O [*19, 20*]. One-dimensional ^{1}H NMR spectra were acquired on a 600 MHz Varian Unity Inova

spectrometer equipped with a triple resonance triple-axis gradient probe. Spectra were referenced to the residual water peak at 4.8 ppm. One-dimensional ^{19}F NMR data were acquired with a 400 MHz Bruker Avance spectrometer equipped with a 5 mm inverse broad-band probe with the proton channel tuned to fluorine. Spectra were referenced to the CF_3COOH peak at -75.3 ppm at 37 °C, -75.6 ppm at 25 °C and -75.9 ppm at 5 °C.

Two- and three-dimensional NMR experiments (^{1}H-^{15}N-HSQC (Heteronuclear Single Quantum Coherence) and ^{1}H-^{15}N-NOESY-HSQC (Nuclear Overhauser Enhancement spectroscopy – HSQC) [*20*]) were acquired using a Bruker Avance 800 spectrometer equipped with a 5 mm TXI ^{1}H-^{13}C/^{15}/D xyz gradient probe. ^{1}H chemical shift was referenced to the proton resonance of DSS at 0 ppm, and ^{15}N and ^{13}C shifts were referenced indirectly to DSS using the ratios 0.101329118 and 0.251449530, respectively [*28*].

ix. NMR resonance assignments of F45L *pa*-HO-CN

The resonance assignments (Table S-2-1) for the F45L *pa*-HO-CN complex were obtained by comparing the HSQC spectrum of F45L *pa*-HO-CN with the HSQC spectrum WT *pa*-HO-CN and by identifying sequential amide HN to HN NOEs in a ^{1}H-^{15}N NOESY-HSQC spectrum, using the assignments of the wild type *pa*-HO-CN previously published [*20*]. If the peak in F45L *pa*-HO-CN has identical or very similar chemical shift as in WT *pa*-HO-CN HSQC spectra, a direct assignment transfer can be made. Most peaks in the spectrum of the single mutant

F45L *pa*-HO-CN have chemical shifts that are very similar to their counterparts in the spectrum of WT *pa*-HO-CN. Consequently, the sequential NOE connectivities obtained from 3D NOESY-HSQC experiment could be used to confirm the directly transferred assignments and assign the peaks that can not be assigned previously by comparing the HSQC spectra of F45L and WT *pa*-HO-CN complexes.

The 3D ^{15}N-edited NOESY experiment is composed of 2D ^{1}H-^{1}H NOESY and 2D ^{1}H-^{15}N HSQC. One can imagine the 3D ^{1}H-^{1}H-^{15}N NOESY experiment as the ^{1}H-^{1}H 2D NOESY with an extra extended dimension along the nitrogen frequency. The 3D ^{1}H-^{15}N NOESY-HSQC detects ^{1}H-^{1}H NOE correlations between amide hydrogen atoms located nearby in space. The NOE (Nuclear Overhauser Enhancement) correlation reveals the location and the specific interaction of amide hydrogen within its spatial environment, as shown below (modified and adapted from http://rmn.iqfr.csic.es/guide/man/3d/chap4-1.html).

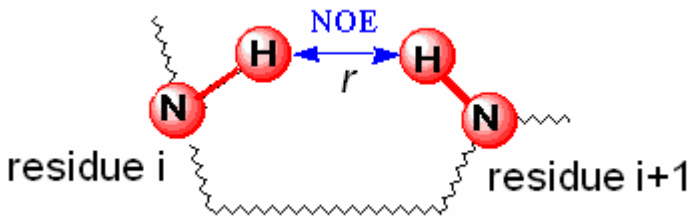

Figure 2-4. NOE correlation between amide protons in protein sequence.

NOE is a spatial phenomenon for two nuclei close in space. Transfer of spin polarization from one spin population to another is via dipolar cross-relaxation; the interaction is through space, not bonds [*29*]. The intensity of the NOE is related to the nuclear distance (e.g. usually for ^{1}H-^{1}H, distance $\leq$ 5 Å) and molecular motion:

$$I_{NOE} \propto f(\tau_C)*1/r^6 \qquad (2\text{-}1)$$

τ_C: rotational correlation time of a protein [*29*].

By measuring the intermolecular ^{1}H (amide hydrogen) -^{1}H (amide hydrogen) NOE, one can obtain the sequential connectivity for protein sequence. The NOE effect is distance dependent. The closer a hydrogen atom is to another hydrogen atom, the larger the enhancement for that hydrogen atom signal is.

Pa-HO polypeptide is highly helical. Therefore, in the NOESY-HSQC 3D experiments, the most intense signals are from the directly neighboring amide protons, e.g. ^{1}H- ^{1}H inter-residual NOE between amide hydrogen atoms from residue *i* and residue *i*+1 or *i*-1 (off diagonal cross peaks) and ^{1}H- ^{1}H intra-residual NOE between two amide hydrogen atoms from the same residue (diagonal cross peaks). The assignment of R47 in F45L *pa*-HO-CN is shown below as an example to demonstrate the assignment procedure.

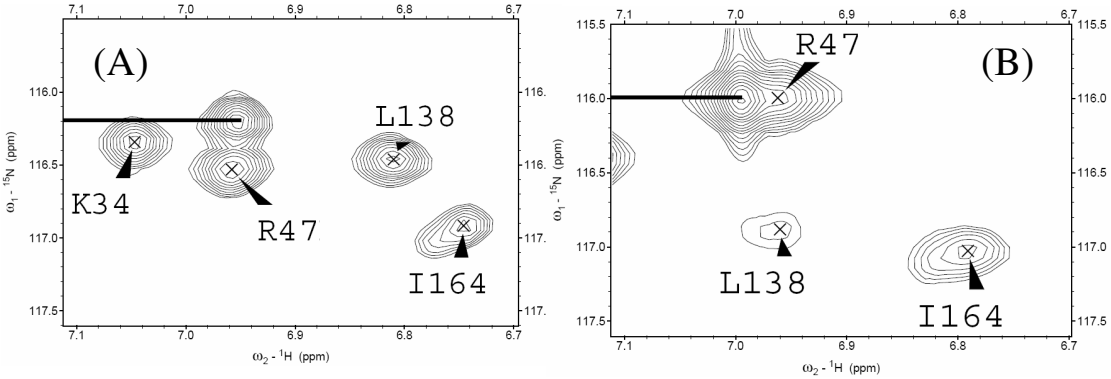

Figure 2-5. R47 amide peak comparison between WT *pa*-HO-CN (A) and F45L *pa*-HO-CN (B) HSQC spectra. Some peaks shifted, for example as shown above, R47 in WT (left) and F45L (right) NMR spectra. The black bar connects the side chain peaks which are not the

focus of our study. The K34 moved out of the selected spectrum window as shown in the case of the mutant F45L.

As shown in the above comparison for small areas of HSQCs from WT *pa*-HO (Figure 2-5 (A)) and F45L *pa*-HO (Figure 2-5 (B)), I164 does not move much. The other peaks are more difficult to assign by comparison. The black line connects the side chain peaks which are not the focus of this study. Although the side chain peak moved a little away from its position in WT for 0.2 ppm in the ^{15}N dimension, it superimposed even more severely with R47 in F45L than in WT. Also, there are other neighboring peaks that moved, for example, L138 and K34. The K34 moved out of the selected spectrum window as shown in the F45L spectrum. Due to all these complications, there is no simple way to assign R47 for 100% certainty by simply comparing the two HSQC spectra because the neighboring peaks of R47 also moved and one peak is partially superimposed with R47. Therefore, it is necessary to assign the R47 in the NOESY-HSQC spectra.

Shown in Figure 2-6 below, the left side shows the 2D ^{1}H-^{1}H plane of 3D NOESY-HSQC experiment with the specific nitrogen frequency of each target residue, and the right side shows the target residue in the 2D ^{1}H-^{15}N HSQC experiment. In Figure 2-6(A), residue A46 is the residue *i*-1 in reference to R47, the yellow cross lines locate the position of A46 in two 2D spectra, the yellow and white cross lines locate the position of A46 to R47 off-diagonal NOE peak. In Figure 2-6(B) showing residue R47, the white cross lines locate the position of A46, the white and yellow cross lines locate the position of R47 to A46 NOE peak and the white and red

cross lines locate the position of R47 to F48 NOE peak. In Figure 2-6(C), residue F48 is the residue *i*+1 to R47, the red cross lines locate the position of F48, and the red and white cross lines locate the position of F48 to R47 NOE peak.

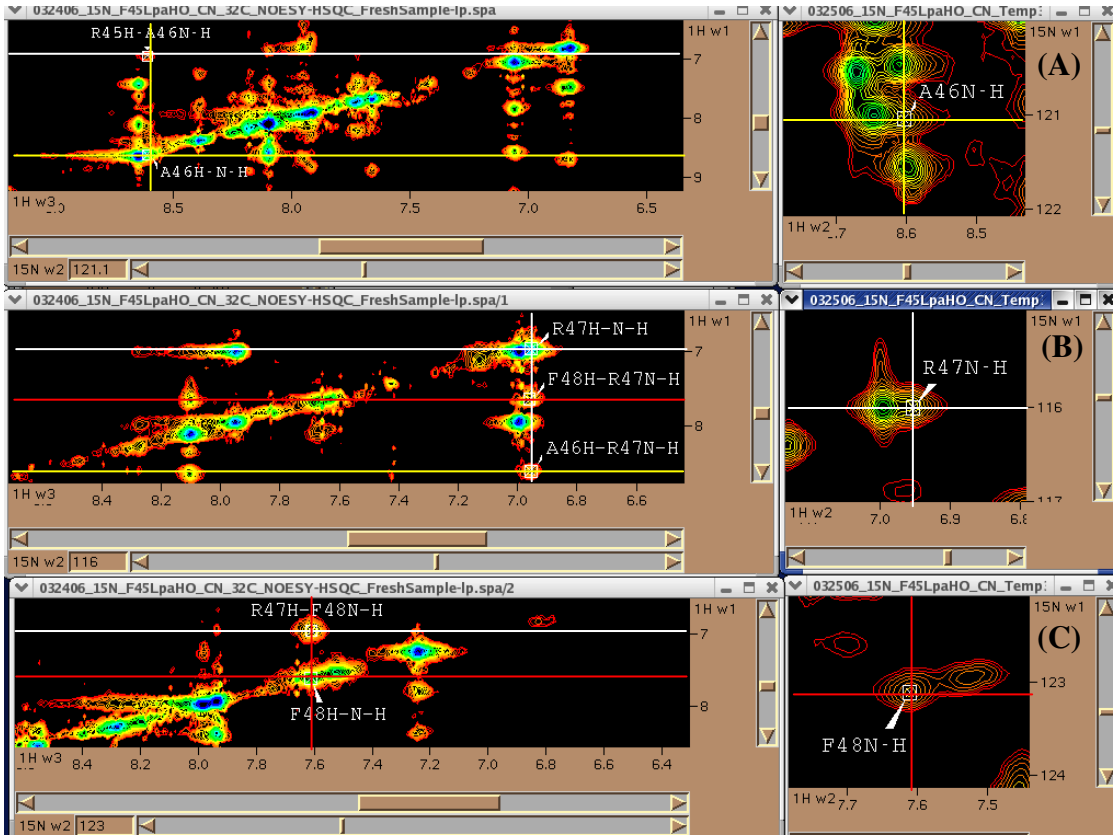

Figure 2-6. 3D NOESY-HSQC assignment using R47 as an example. The left side shows the 2D ^{1}H-^{1}H plane of 3D NOESY-HSQC experiment with the specific nitrogen frequency (value is shown at the bottom of the spectrum, as the 3rd dimension of the 3D experiment) of each target residue, and the right side shows the target residue in the 2D ^{1}H-^{15}N HSQC experiment. (A) Residue A46 as the *i*-1 residue to R47. The yellow cross lines locate the position of A46 in two 2D spectra, the yellow and white cross lines locate the position of A46 to R47 off-diagonal NOE peak; (B) Residue R47. The white cross lines locate the position of A46, the white and yellow cross lines locate the position of R47 to A46 NOE peak and the white and red cross lines locate the position of R47 to F48 NOE peak; (C) Residue F48 as the *i*+1 residue to R47. The red cross lines locate the position of F48, and the red and white cross lines locate the position of F48 to R47 NOE peak.

Therefore, the assignment of R47 is achieved by identifying and matching the NOE cross peaks with its two neighboring residues A46 and F48 on the protein

sequence. Other amino acids can be assigned using the same method.

x. H/D exchange experiments

A series of ^{1}H-^{15}N-HSQC experiments were measured at 37 °C on a Bruker Avance 800 spectrometer equipped with a 5 mm TXI ^{1}H-$^{13}C/^{15}N$/D xyz gradient probe using ^{15}N labeled WT or F45L *pa*-HO-CN complex NMR sample for H-D exchange NMR experiment. The 500 µl NMR samples contained 1.0-2.0 mM protein in 50 mM sodium phosphate, pH 7.0 and 5-10% D_2O. First, NMR samples were freeze-dried in a Savant® Speed Vac (Farmingdale, N.Y.) for about 6 hours to dry protein powder. Immediately before the NMR experiments, the sample was resuspended in 500 µL of D_2O together with 5~10 times pH 7 NaCN to compensate for the loss of CN^- during the freeze-drying process [*20*]. Then the first ^{1}H-^{15}N HSQC was taken with a 10-15 min dead time between the start of amide proton to amide deuterium (H_N-D_N) exchange upon adding D_2O into lyophilized protein and the start of data acquisition. Subsequently, a series of HSQC spectra were monitored as a function of time for the exchange process. The total acquisition time for each HSQC spectrum was 20 mins and the H-D exchange experiments were monitored for at least 24 hrs until the end of exchange event, indicated by no further peak intensity decrease observed in the ^{1}H-^{15}N HSQC spectrum. Spectra were acquired every 20 mins for the first 7-12 h; subsequently the time interval between spectra was increased to 1 h for the remaining time. These ^{1}H-^{15}N-HSQC spectra were collected over a 19.2 KHz (^{1}H) and 3 KHz (^{15}N) spectral widths, with 16 scans per increment and 2560 and 256

complex points for the ^{1}H- and ^{15}N- dimension. Spectra were processed using NMRPipe and analyzed using Sparky. Each spectrum was processed with a 90° shifted sine bell squared window function in each dimension and zero filled to twice the number of points. The per residue H/D exchange rate constant (k_{ex}) measured experimentally was calculated by fitting the time-dependent decay of peak intensities to a single-exponential decay of three parameters (Equation 2-2 and Figure 2-7) using Sigma Plot 2001 [*30, 31*].

$$I(t) = I_{\infty} + A^{(-k_{ex}\, t)} \qquad (2\text{-}2)$$

I_{∞} : the intensity at infinite time for each amide peak when reaching steady-state or equilibrium;

A : $I_0 - I_{\infty}$ (the total change in intensity from "zero time" to equilibrium);

k_{ex} : the experimentally observable rate of N-H exchange.

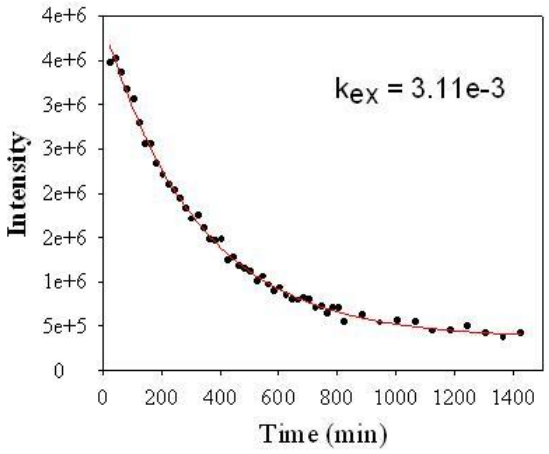

Figure 2-7. Proton-deuterium exchange rate constant determination for residue E194 in F45L *pa*-HO-CN complex at pD 7.03. The red line represents the fit of equation 1 to the experimental data.

One example is given in Figure 2-7 for fitting the experimental time dependent intensity to calculate intensity a rate constant. After the rate constants were obtained from the above fitting, the residue specific protection factors were calculated by following the same method reported by Englander *et al*. [*32, 33*]. First the values for sequence-specific intrinsic rate constants (k_{ch}) were calculated using the spreadsheet available from S. Englander's Web site at http://hx2.med.upenn.edu/download.html. Then the protection factors (P) were determined by the relation: $P = k_{ch}/k_{ex}$ [*32, 33*]. The pH value employed in the calculations was 7.03 for F45L *pa*-HO-CN complex. The pertinent data for the WT *pa*-HO-CN was obtained by Dr. Juan Carlos Rodriguez [*20*].

RESULTS AND DISCUSSION

1. Expression, Purification and Spectral Characterization of the WT, mutants and ^{19}F-Phenylalanine labeled *pa*-HO

The proteins were expressed and purified as described previously. After protein purification, the proteins were judged > 95% pure by SDS-PAGE (data not shown) as well as a UV-vis 280 nm/405 nm absorbance ratio (WT < 0.3, others < 0.35). Other than F128L *pa*-HO, all mutants show more yellowish and lighter greenish color than WT, which suggests that biliverdin is not as tightly bound to the expressed apo protein as in WT. While F128L shows strong greenish color, its UV spectrum suggests that it binds more biliverdin than WT apo protein during protein expression and purification. The changes in protein color and UV-vis spectra could

be due to the unique position of residue 128. F128 is located in between two heme propionate groups. Therefore, a F128L mutation possibly facilitates protein folding to bind biliverdin or heme (later incorporated after purification) more tightly. While the other *pa*-HO mutations likely weaken the cofactor-binding to differing extents.

The Soret maxima of the resting state (Fe^{III}) heme-*pa*-HO wild type and mutant proteins are very similar, ranging from 402 nm to 406 nm (Table 2-1). The extinction coefficients were measured using the pyridine hemochrome method [*34*]. The values vary from 113 $mM^{-1}\cdot cm^{-1}$ to 141 $mM^{-1}\cdot cm^{-1}$ for single mutation or *ortho*-^{19}F-phenylalanine labeling, and those of double mutations are between 76 $mM^{-1}\cdot cm^{-1}$ and 134 $mM^{-1}\cdot cm^{-1}$.

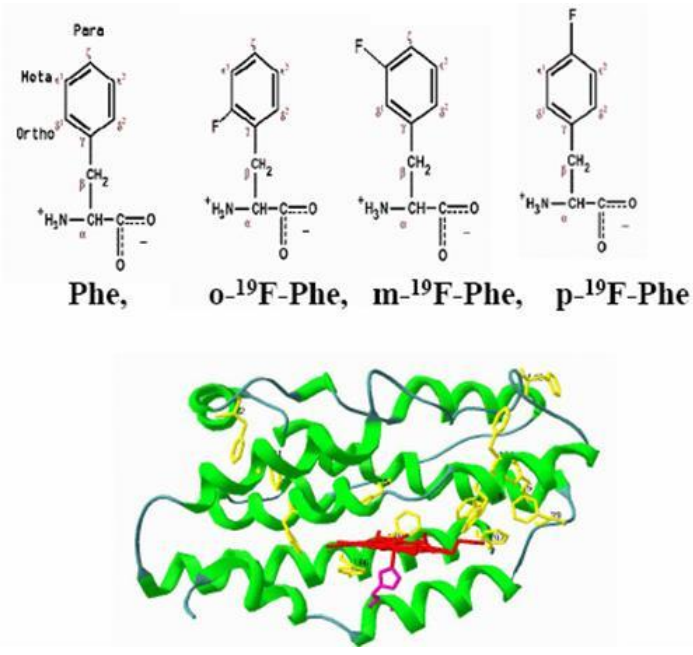

Figure 2-8. Illustration of *pa*-HO ^{19}F-phenylalanine labeling, the top is unlabeled, ortho-^{19}F labeled, meta-^{19}F labeled and para-^{19}F labeled phenylalanine, the bottom is the WT *pa*-HO with phenylalanines in yellow stick, heme in red stick and H26 in magenta stick.

Similar Soret bands show that the heme is still contained in the heme pocket, and it also suggests that the overall protein-heme structure is maintained. As for the change of extinction coefficient in double mutation or mutation with ^{19}F Phe labeling, it suggests that protein structure is slightly disrupted; it could be more manifested in the heme distal pocket. Protein structure characterization and enzyme properties are further tested by the following experiments.

Table 2-1. The soret maxima and extinction coefficients of the resting state (Fe^{III}) heme-*pa*-HO WT, mutant and ^{19}F-Phe labeled proteins.

	WT paHO	*F39L*	*F45L*	*F48L*	*F128L*	*F189L*	*o-^{19}F Phe*
Extinction Coefficient (ε ,$mM^{-1}cm^{-1}$)	129	129	101	117	140	113	141
UV Abs Peak(nm)	405	404	404	404	405	403	405
	F39/45L	*F39/48L*	*F39/128L*	*F45/128L*	*F39/189L*	*F45/189L*	*o-F45L*
Extinction Coefficient (ε ,mM-1cm-1)	108	96	124	134	80	76	99
UV Abs Peak(nm)	403	402	405	405	403	406	407

2. Protein secondary structure study by circular dichroism

Circular dichroism (CD) is a physical property of the absorption difference between left and right circularly polarized light. Because amino acids are enantiomers, different elements of secondary structures (like the alpha-helix, beta-sheet, beta-turn or random coil) have distinctive CD spectra. So CD spectroscopy is

commonly used to determine the secondary structure conformation changes in proteins [*25*]. The CD-spectra of the *pa*-HO wild type, F39L, F45L, F128L mutants and *ortho-, meta-, para-*^{19}F-phenylalanine labeled WT and ortho-F45L mutant are shown in Figure 2-9. As indicated by the crystal structure, *pa*-HO is mainly α-helical. These CD spectra show very similar α-helix content. This implies no major secondary structural perturbation occurred. It seems that the overall helical protein structure is still well maintained. In addition, the difference, as judged by the change of intensity at 194 nm, 208 nm and 224 nm, may suggest a slight change in α-helical content. F128L and *ortho*-WT have larger ellipticities, while F45L has the least between 200-240 nm (characteristic region for α-helix). This could mean that F128L and *ortho*-WT have more helical content than F45L. Further studies supporting this idea are discussed below.

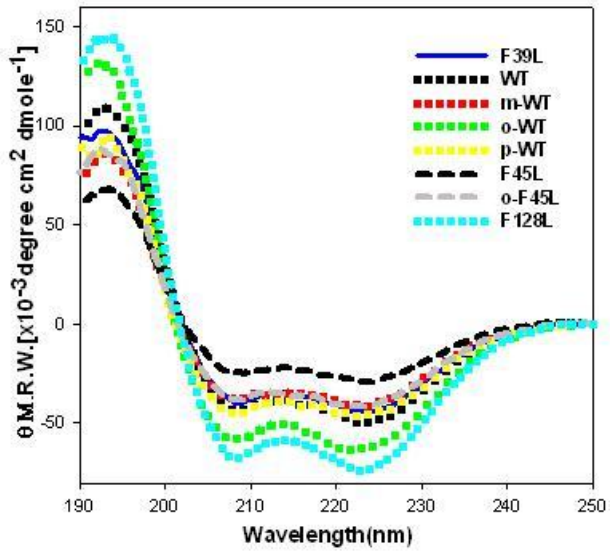

Figure 2-9. The superpositioned CD spectra of WT, mutant, ^{19}F-Phe labeled *pa*-HO proteins. The unit of CD spectrum is θ MRW (mean residue weight) (x10^{-3}degree cm^2 dmole^{-1}).

3. 1D proton NMR study of the heme distal pocket

Due to the paramagnetic influence from heme iron, the heme inside protein pocket is commonly studied by 1D proton NMR. The mutant and ^{19}F-Phe labeled *pa*-HO proteins have been studied by ^{1}H NMR spectroscopy and compared with WT *pa*-HO in the resting form, cyanide (CN^-) or azide (N_3^-) ligand bound forms. 1D ^{1}H NMR spectra of these proteins in their resting state are shown in Figure 2-10 (A), they are compared with the spectra of the same proteins in their CN^- bound forms in Figure 2-10(B). In the ^{1}H NMR spectra of Figure 2-10 (A), the broad resonances between 60 and 80 ppm from heme-methyl, indicate high-spin Fe^{III}-H_2O where the ferric ion is axially coordinated by a His and H_2O molecule [*25*]. While the sharp heme-methyl peaks near 20 ppm suggest the low-spin Fe^{III}-OH complex (OH is coordinated instead of H_2O) [*25*]. The WT resting state protein has mixtures of both high (above 40 ppm) and low spin (below 30 ppm) peaks in exchange [*25*]. The mutant proteins all have those low-spin and high-spin peaks as shown in WT spectra. But, the peaks in mutations are somewhat different in intensity, line width and peak area from those in WT. The difference between mutant and WT NMR spectra suggests that mutation costs a change in the heme distal pocket leading to different heme seating suggested by different isomer ratio and different proportion of high and low spins. F128L and F39L seem to possess more high spin features, and F45L has more low spin features; furthermore, the double mutants F39/128L and F45/128L *pa*-HO are showing the features in combination of both two single mutations.

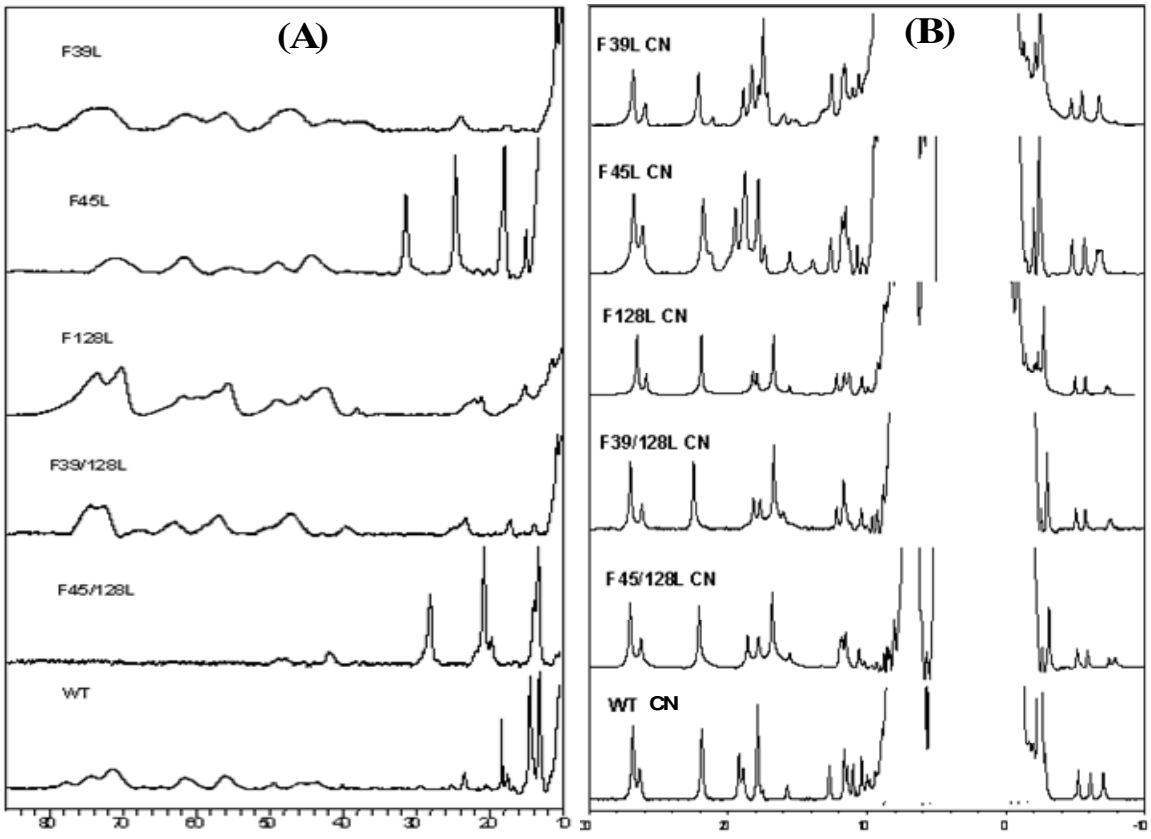

Figure 2-10. The 1D proton NMR spectra of (A) ligand free and (B) CN^- bound *pa*-HO proteins at 25 ℃, pH7 phosphate buffer. The bottom axis shows ^1H chemical shift in ppm.

As for the spectra of the ligand bound form shown in Figure 2-10 (B) and Figure 2-11, again the spectra from mutant proteins show major similarities to the spectra from the WT protein, except for the presence of several isomer peaks. Shown in Figure 2-10 (B), bound with CN^- ligand, F128L seems to be more similar to WT than F39L and F45L. As in the F39L and F45L mutants, the extra new peaks are likely suggestive of heme in-plane disorder [*35*]. Interestingly, the effect of F128L stabilizing the protein seems to be dominant in double mutants, F39/128L and F45/128L, as the two double mutants show a more similar pattern to WT than either

F39L or F45L. It may suggest that the F128L mutation indeed makes the protein folding of F39/128L and F45/128L similar to WT in the distal heme pocket environment. Also *ortho*-^{19}F labeled proteins show similar 1D NMR spectra as WT in both azide and CN^- inhibited (ligand bound) forms, as shown in Figure 2-11.

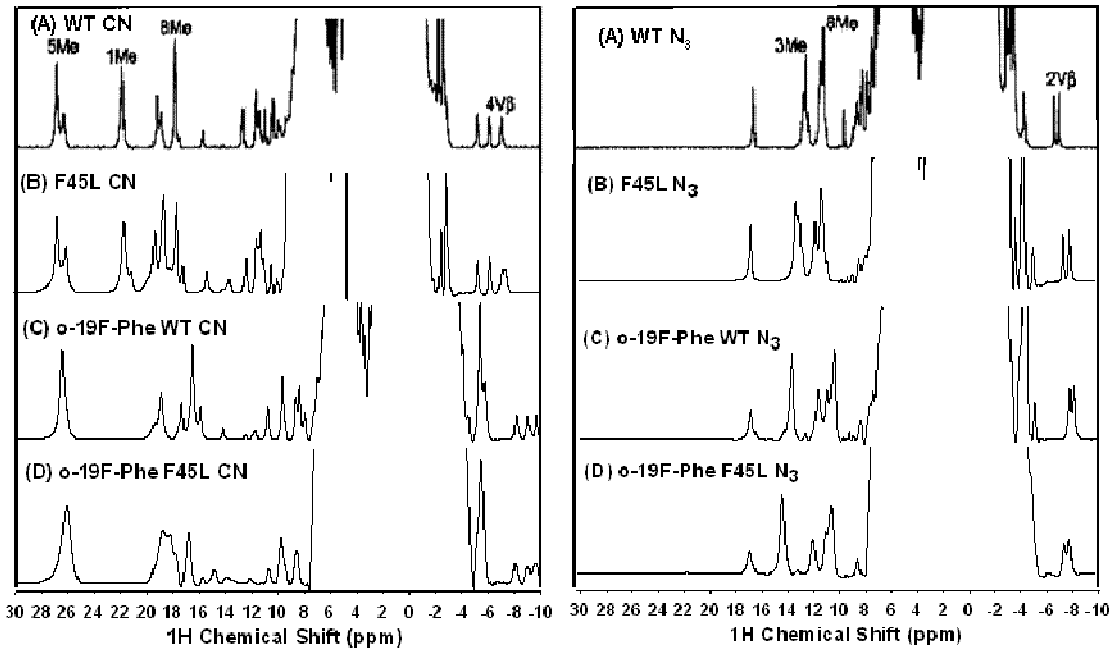

Figure 2-11. The 1D proton NMR spectra of (A) CN^- bound and (B) N_3^- bound *pa*-HO proteins at 25 ℃, pH7 phosphate buffer.

4. Protein conformational stability probed by thermal denaturation experiments

Assuming protein is experiencing two states: folded and unfolded in equilibrium, thermal unfolding of proteins is used to determine protein conformational stability. Study comparing WT and mutant proteins could give insights in the extent of protein structural disruption upon mutation. Thermal

denaturation curves comparing WT, mutant and ^{19}F-Phe labeled proteins are shown in Figure 2-12. The data in the Figure 2-12 (A) and (B) suggests that ^{19}F-Phe labeling does not change protein thermal stability much. During unfolding, all proteins experience overall similar temperature dependent conformational changes. In contrast, as shown in Figure 2-12 (C), mutant proteins not only have different T_m as reported in Table 2-2, but also unfold differently from low to high temperatures. These observations suggest that even at relatively low temperatures, the mutant proteins are exploring globally unfolding conformations, as compared to WT. It is interesting but not surprising that F128L has even higher T_m than WT, which again suggests that the F128L mutation makes the heme pocket more compact.

From the above observations, it is reasonable to assume that overall protein structure is well maintained with a single mutation or ^{19}F-labeling. The studies described below will reveal how these alterations to the protein affect the dynamics and function of *pa*-HO.

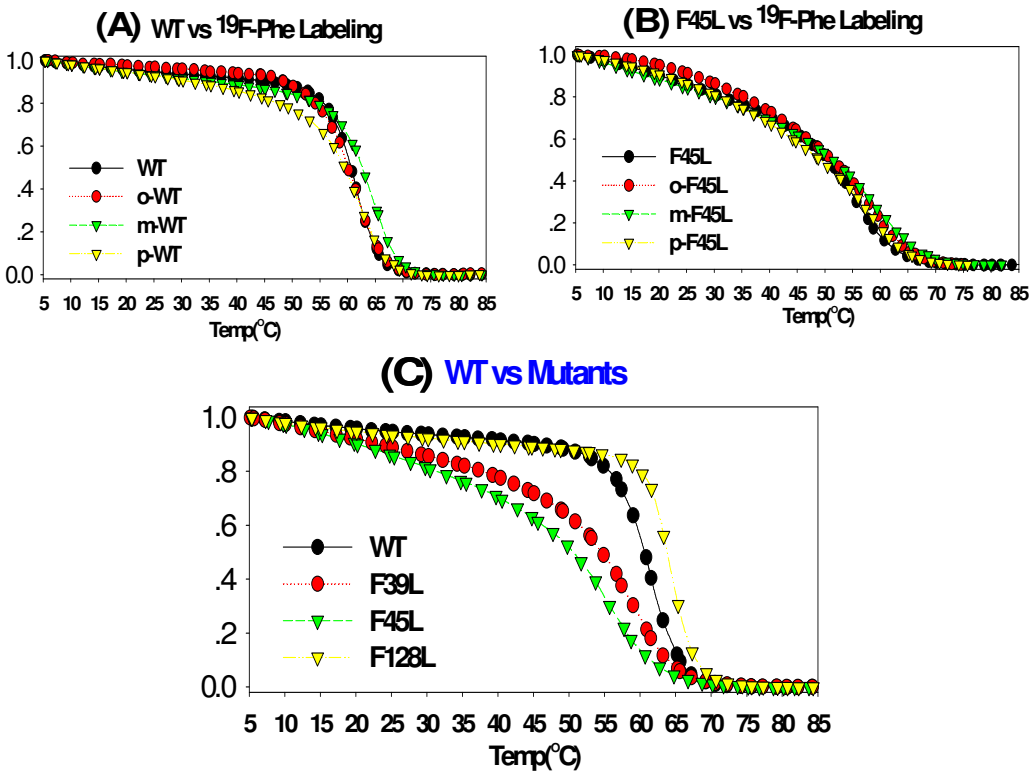

Figure 2-12. The comparison of the thermal denaturation curves in (A) WT vs ^{19}F-Phe labeling, (B) F45L vs ^{19}F-Phe labeling, and (C) WT vs Mutants. UV-vis absorbance normalized to 1.0.

Table 2-2. Thermal denaturation temperatures (T_m, ºC) derived from the above thermal denaturation curves. Left: WT vs ^{19}F-Phe labeling; middle: F45L vs ^{19}F-Phe labeling; right: WT vs Mutants. The largest T_m difference in each group is shown by maximum delta.

	Tm	Error(+/-)		Tm	Error(+/-)		Tm	Error(+/-)
WT	61.1	0.1	F45L	55.4	0.4	WT	61.1	0.1
oWT	60.6	0.1	oF45L	58.2	0.2	F39L	58.1	0.2
mWT	63.9	0.15	mF45L	59.5	0.2	F45L	55.4	0.4
pWT	61.4	0.2	pF45L	58	0.4	F128L	64.3	0.1
Max Delta	3.3		Max Delta	4.5		Max Delta	8.9	

5. Heme Oxygenase Reactivity Assay with Hydrogen Peroxide

The peroxide shunt reaction (Scheme 2-1) is commonly used to test heme oxygenase reactivity [*26*].

As shown earlier in Figure 2-1, once the hydroperoxyl group binds to heme iron, the ferric hydroperoxyl heme is obligated to two pathways: one goes to form ferryl as seen in cytochrome P450, peroxidase, etc; the other in the heme metabolism pathway forms verdoheme. It has been reported by Paul Ortiz De Montellano's human HO-1 study, that Asp-140 mutations can disrupt the hydrogen bond in heme distal pocket so that the human heme oxygenase-1 is converted into a peroxidase; in other words, the ferryl formation pathway is preferred [*26*]. Here we implement the peroxide shunt reaction to test the heme oxygenase reactivity change. The reaction is implemented with WT as control. Formation of verdoheme is indicative of the heme oxygenase reaction.

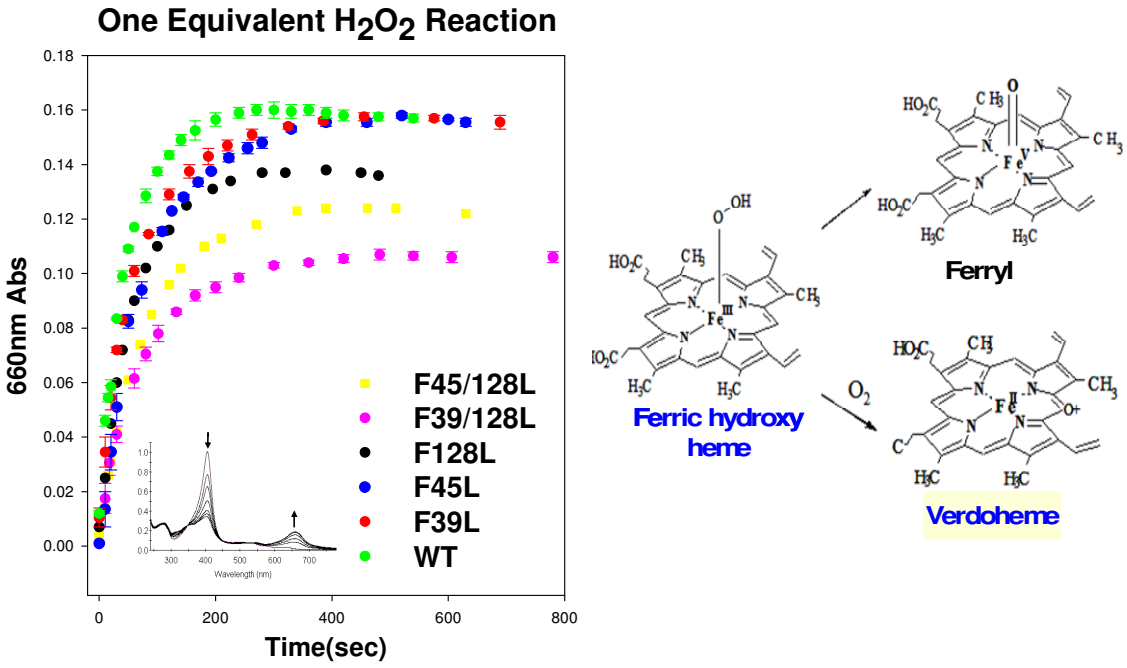

Figure 2-13. Heme oxygenase reactivity monitored by the peroxide shunt reaction. The reaction of *pa*-HO proteins with addition of one equivalent of peroxide is illustrated by the inset of UV-vis spectra changing with time at 25 ºC. The left plot shows the accumulation of verdoheme with time in *pa*-HO proteins. The right figure shows the heme hydroxylation pathway. Blue color highlights the heme oxygenase pathway.

As shown in above Figure 2-13, WT *pa*-HO produces the largest amount of verdoheme; formation of the latter is also faster relative to the mutant proteins, suggested by the slope of the plot. It is interesting that although F128L may facilitate a more stable *pa*-HO folding, the alteration increased stability of the distal pocket costs loss of heme oxygenase reactivity. Also it is clear that double mutants produce even less verdoheme. The plateau of each curve suggests the total amount of verdoheme formation. The difference between mutant and WT could be due to the ferric hydroperoxide accessing the alternative path in the right side of Figure 2-13. The formation of guaiacol is a very common assay to detect peroxidase reactivity [*4*].

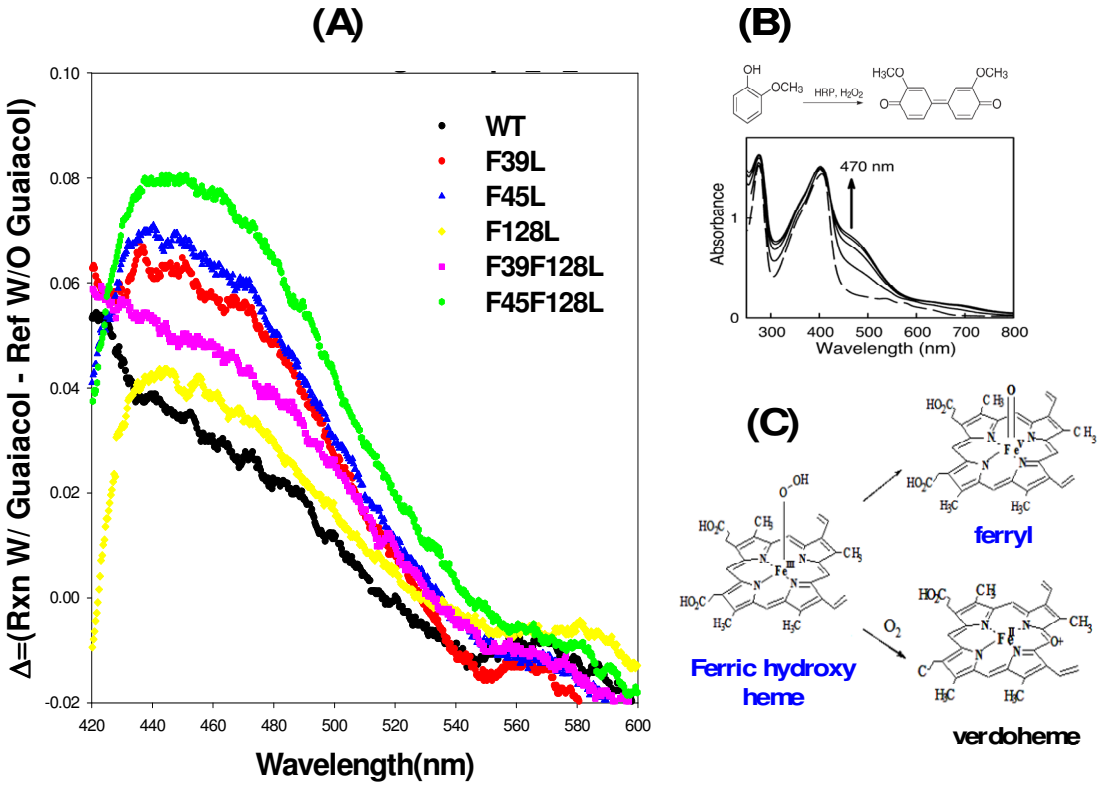

Figure 2-14. Peroxidase reactivity monitored by guaiacol formation assay. (A) The subtracted spectra of the peroxide protein guaiacol reaction after 300 sec from the peroxide protein control at 25 ºC. (B) The protein guaiacol peroxide assay for peroxidase reactivity test. The changing spectra after guaiacol reacting with ferryl heme to form guaiacol oligomer are adopted from [*4*]. (C) The heme hydroxylation pathway. The blue color highlights the taken pathway in this study.

Shown in Figure 2-14, the black dotted line for WT is located lowest in the plot. This pattern suggests WT forming the least amount of guaiacol which indicates that WT has the least ferryl formation, whereas the double mutant has the largest. Although the order is not exactly the same as what we would expect from the implication of Figure 2-13, this is likely due to the unpredictable protein intermediate degradation. The two assays show that the mutation has decreased heme oxygenase reactivity and correspondingly increased peroxidase reactivity. The *ortho*-^{19}F

labeling also had similar impact toward heme oxygenase reactivity, as shown in Figure 2-15.

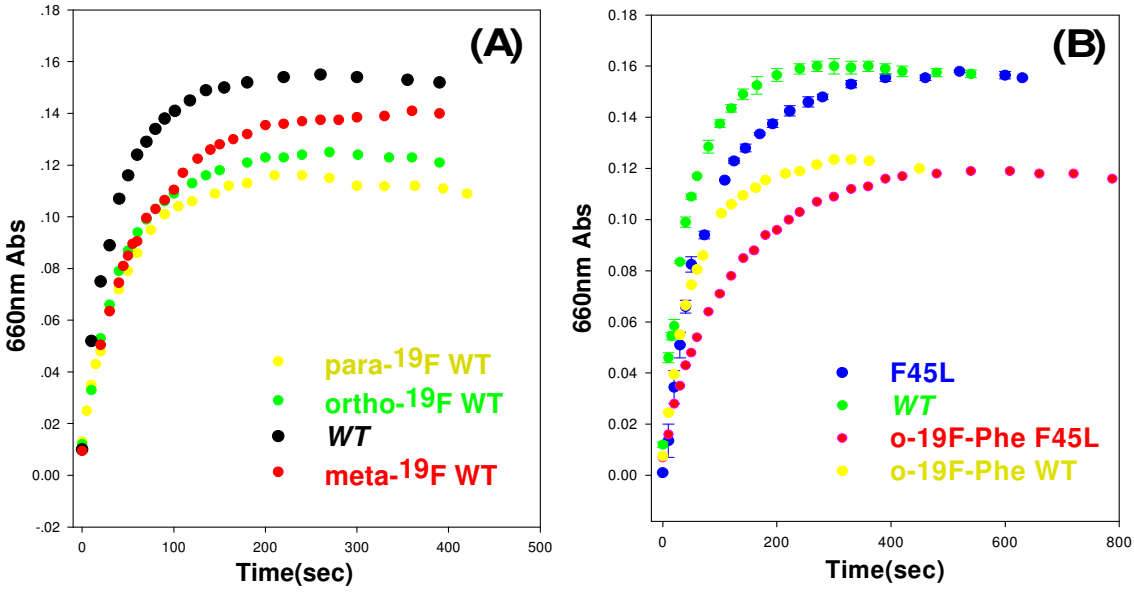

Figure 2-15. Heme oxygenase reactivity monitored by peroxide shunt reaction. The reaction of *pa*-HO proteins is initiated by addition of one equivalent of peroxide at 25 ºC. (A) Comparison between WT and ^{19}F-Phe labeling. (B) Comparison between WT and mutants.

The heme oxygenase reactivity is related to the protein structure and dynamics. NMR is a powerful tool to study both protein structure and dynamics as shown in the discussion below.

6. Study of Protein Structure and Dynamics by 1D ^{19}F NMR Spectroscopy

^{19}F NMR is a powerful tool for protein structure and dynamics study. It has several advantages: First, it is generally believed that ^{19}F-Phe labeling does little impact to overall protein stability, structure and function because it has similar atomic radius as H. Second, it is a very sensitive probe for NMR studies, comparable to ^{1}H.

Third, it can be used to probe the interior of proteins because the ^{19}F chemical shifts are very sensitive to chemical environment.

There are thirteen phenylalanines in *pa*-HO, as shown in the 3D protein crystal structure shown in Figure 2-16. Most of them are concentrated around the heme distal pocket. F128, as mentioned earlier, is pointing to the heme propionate groups. F39, F45 and F48 are very close to each other. Together, they form a well packed phenylalanine ring cluster. F39, F45 and F48L are so closely packed that rotation of the F45 side chain could affect the side chains of F39 and F48. Also, F161 is in proximity to F72 and F117. F117 could be connected to F189 and F55 by F186 in space. And F189 is close to F48, F128 is close to F130 which is also close to F39. F142 seems to be far from the other Phes, but it is located on top of the strand which is the most exposed to solvent. A hydrophobic channel (in a shape of long cylinder) seems to be crossing the protein at the back of the heme pocket.

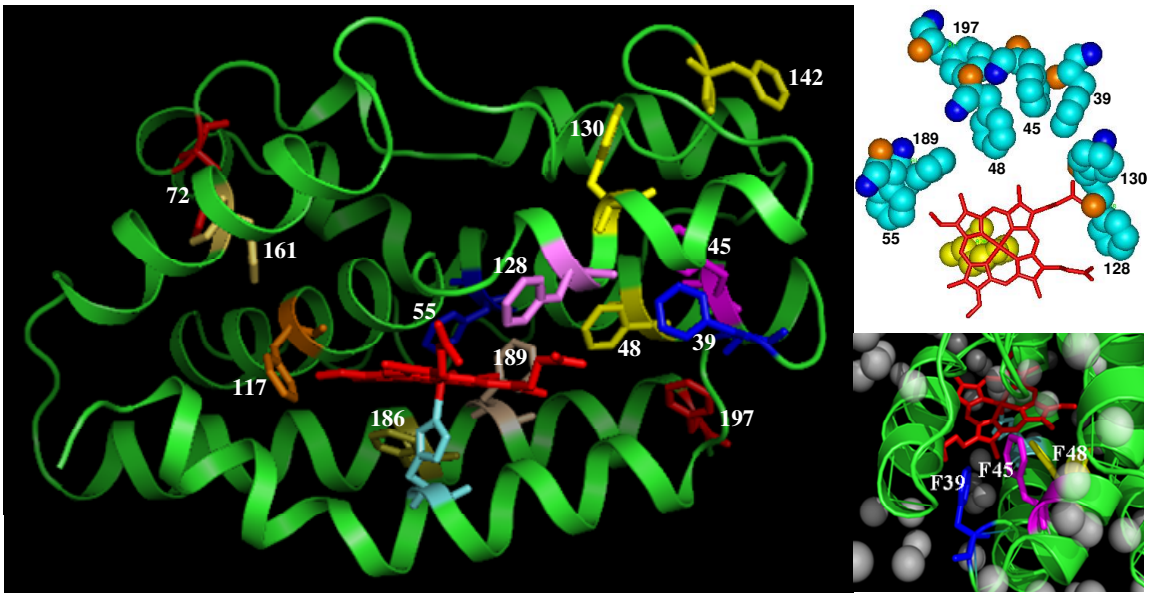

Figure 2-16. Target 13 phenyalanines in *pa*-HO (PDB: 1SK7) in the left figure. The top right figure shows the cluster of phenyalanines around heme in the heme pocket, the bottom right figure shows the compact cooperative packing of three phenyalanines: 39, 45 and 48.

After successful incorporation of ^{19}F-Phe into our target proteins, 1D ^{19}F NMR spectra were obtained in a 400 MHz Bruker NMR spectrometer. Chemical shift variation and temperature dependencies of ^{19}F-Phe peaks have been studied to compare WT with mutants in the absence and presence of protein ligand. The ligands are cyanide (CN^-) and azide (N_3^-).

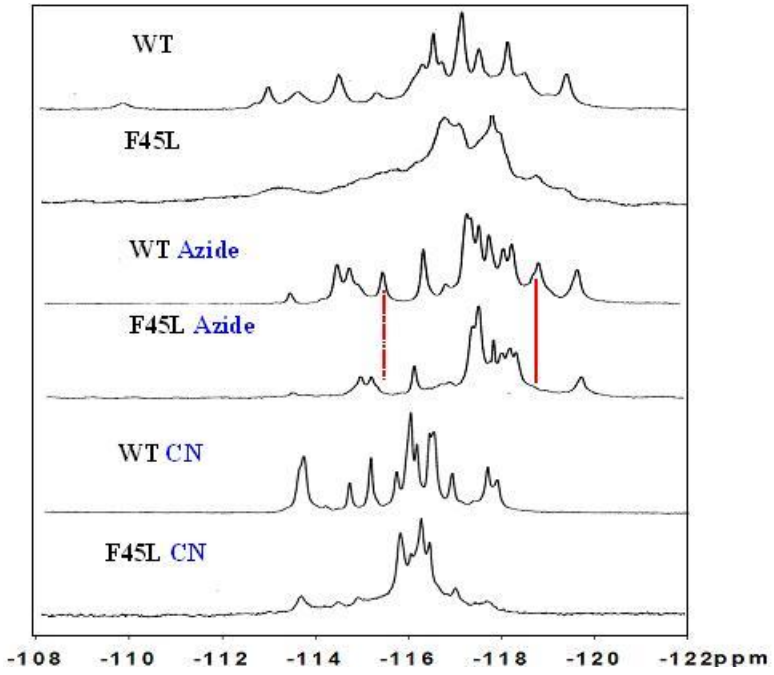

Figure 2-17. 1D ^{19}F NMR of WT and F45L *pa*-HOs in resting state, CN^- or Azide bound complex forms at 37 °C.

Figure 2-17 shows the comparison between WT and F45L mutant proteins in 3 states: resting state, azide bound and CN^- bound forms. It is obvious that ligand binding "cools down" protein motions, as suggested by the sharper line widths and resolved peaks. In the resting state, o-^{19}F Phe labeled F45L compared to o-^{19}F Phe labeled WT has 14 peaks detected. This suggests that at least one Phe has been detected to have more than one conformation, since there are 13 Phe residues in total. In comparison to the WT spectrum, the peaks in the F45L spectrum have much broader line widths. This suggests that the mutation disrupted the heme pocket and created conformational disorder. These observations match previous findings that the mutation disrupts the distal heme pocket.

In the spectra of F45L complexed with CN^- or N_3^-, there are two peaks missing. The disruption introduced by the side chain of ^{19}F-Phe is not only seen in the heme pocket environment but is also transferred to other Phe residues. Finally, when we compare the N_3^- set and the CN^- set, the F45L-N_3 complex looks more similar to the WT-N_3 complex than the F45L-CN complex to the WT-CN complex. It seems that binding of N_3^- does a better job in stabilizing the mutant protein than binding of CN^-.

The temperature dependence of the ^{19}F NMR spectra was tested with WT in resting state as well as with N_3^- or CN^- ligand bound forms; the spectra are shown in Figure 2-18, 2-19 and 2-20. Most of the resolved peaks exhibit a trend of line width broadening as the temperature decreases. Also there are fewer peaks at lower temperatures; which suggests that the system approaches from fast towards intermediate exchange as the temperature decreases.

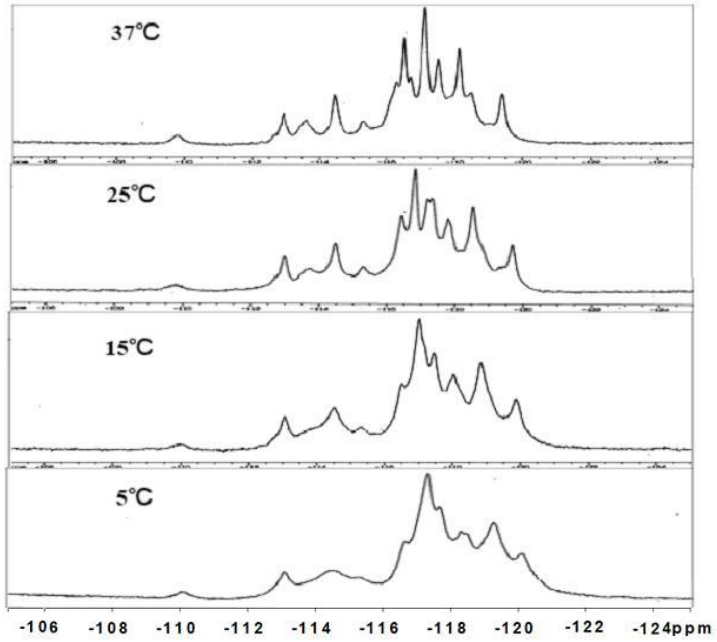

Figure 2-18. 1D ^{19}F NMR of o-^{19}F-Phe labeled *pa*-HO at resting state.

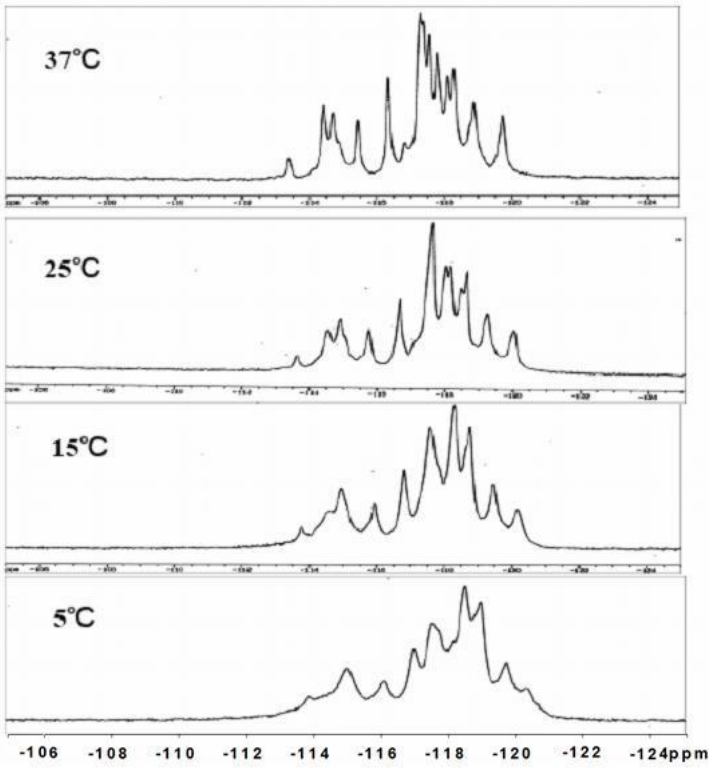

Figure 2-19. 1D ^{19}F NMR of o-^{19}F-Phe labeled *pa*-HO in complex with N_3^-.

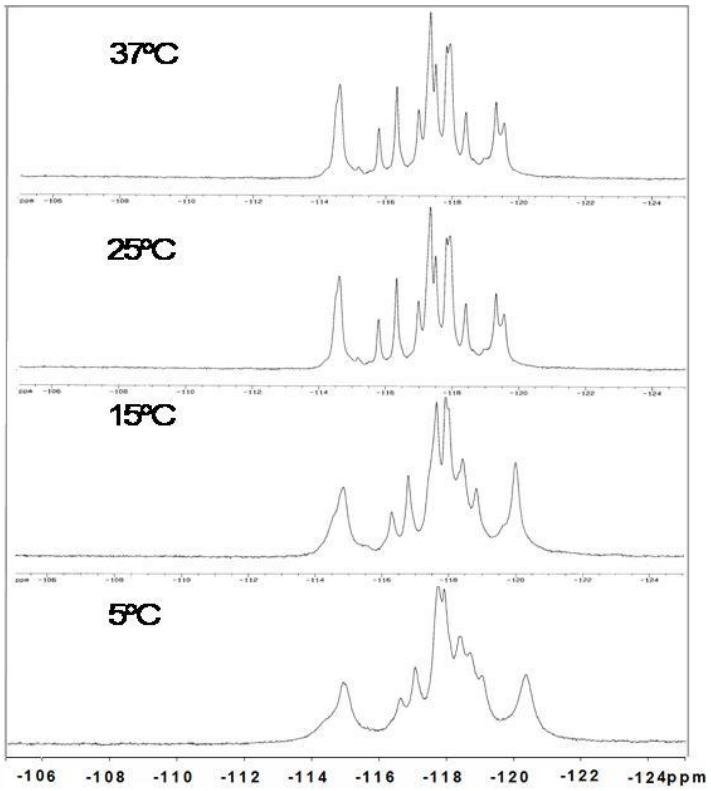

Figure 2-20. 1D ^{19}F NMR of o-^{19}F-Phe labeled *pa*-HO in complex with CN^-.

7. Protein Dynamics Probed by Amide H/D Exchange NMR Study

Using the sequential backbone NMR assignments of the WT protein obtained by Dr. Juan Carlos Rodriguez [*20, 36*], the assignments for F45L were achieved by comparing HSQC from F45L with HSQC from WT as well as finding NOEs between the sequential amide protons (H_N) in a ^1H-^{15}N NOESY-HSQC spectrum of F45L. With the available assignment of F45L, the H-D exchange experiments were carried out as described in Experimental Section. The 2D ^1H-^{15}N HSQC results are shown in Figure 2-21.

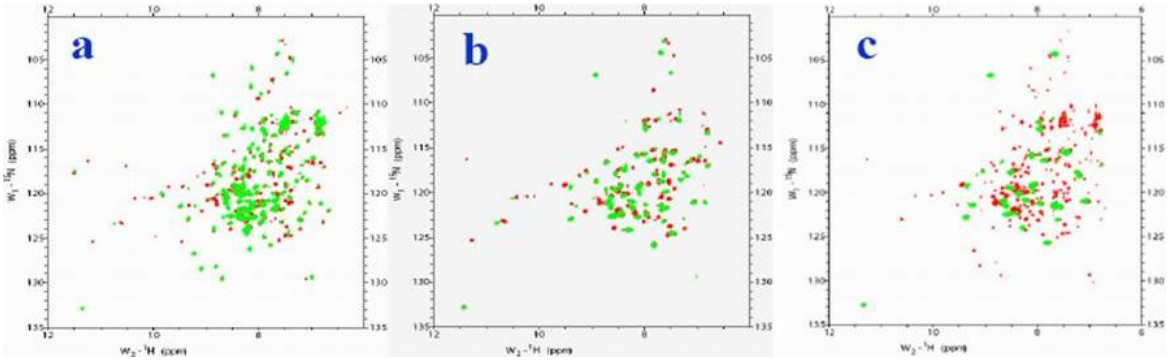

Figure 2-21. Superimposed H/D exchange 2D ^{1}H-^{15}N HSQC spectra of WT *pa*-HO-CN (red at bottom) and F45L *pa*-HO-CN (green on top). (a) 0 time in H/D exchange; (b) 1st H/D exchange HSQCs; (c) last H/D exchange HSQCs, after 24 hrs.

As shown in Figure 2-21 (a), overall, the HSQC spectrum of F45L *pa*-HO-CN is similar to the HSQC spectrum of WT, except that some peaks are shifted as indicated by the red peaks. These chemical shift changes indicate some structural changes in the protein. Figure 2-22 shows the mapped chemical shift changes between F45L and WT *pa*-HO-CN complexes.

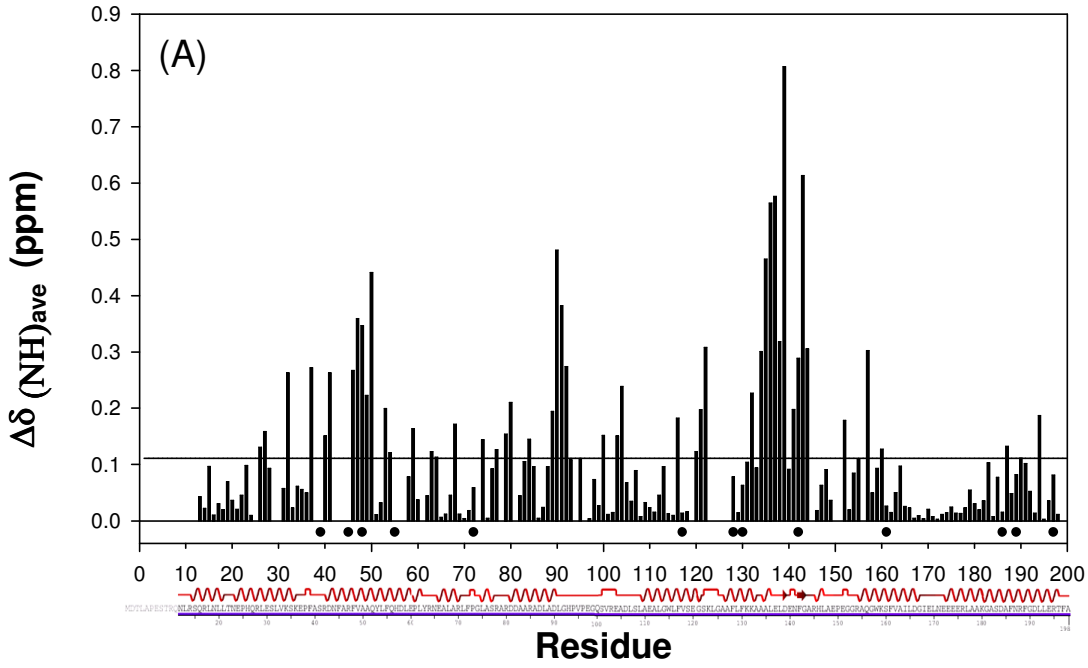

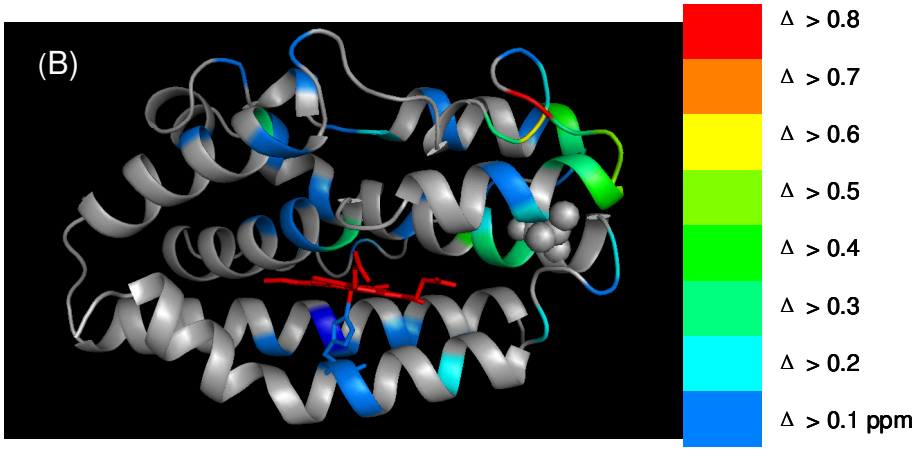

Figure 2-22. Chemical shift perturbation caused by the F45L mutation in the CN^- complex. (A) Chemical shift perturbation per residue plot. The weighted chemicals shift change Δδ is obtained by subtracting the ^1H and ^{15}N chemical shift of a residue in F45L *pa*-HO-CN from the corresponding shifts in WT *pa*-HO-CN, then the weighted average chemical shift change is calculated using the equation $\Delta\delta_{ave} = \sqrt{\frac{(\Delta\delta_{i_H})^2 + (\frac{\Delta\delta_{i_N}}{5})^2}{2}}$. The average difference of all residues (0.11) is indicated by a horizontal line. The dots above the residue axis indicate the location of phenylalanine residues. The secondary structure of *pa*-HO at the bottom of the plot was obtained from its 3D crystal structure (PDB: 1SK7) in DSSP view: Helix I (14-21), II(23-36), III(42-63), IV(66-71), V(75-78), VI(81-91), VII(109-121), VIII(126-133), IX(134-136), X(145-147), XI(154-167), XII(172-197). (B) Weighted average amide chemical shift differences mapped onto the crystal structure of resting state *pa*-HO. The F45L mutation is highlighted by ball and stick. The color coding follows the plotted Δδ using the colors demonstrated in the color gradient on the right side. The heme is shown in red. Both the heme and His26 are shown in sticks.

Herein, this chemical shift perturbation analysis is used to identify residues experiencing altered chemical properties as a result of the F45L mutation. The per residue change indicated by weighted average chemical shift difference of amide ^1H and ^{15}N nuclei is plotted in Figure 2-22 (A), and further mapped onto the 3D crystal structure of the *pa*-HO in the resting state (ligand free) in Figure 2-22 (B). The data show clear differences in amide chemical shifts between the mutant and WT in complex with CN^-. The overall chemical shift difference is relatively small. The

average chemical shift change is 0.11. It suggests that the overall protein structure is maintained. While some local regions are changed to a greater extent, as shown in Figure 2-22 (A), the largest change is located around the residues 135-145, 88-92 and the mutation site 45-50. Mapped onto 3D crystal structure in Figure 2-22 (B), the color gradient indicates that those regions experience the largest perturbation by the warmer color (red compared with blue). The weakly affected residues are located both on the bottom and on the top of the heme pocket. Largely affected residues are located on the helix III (42-63), VI (81-91) and IX (134-136). All Phe residues, as represented by dots underneath the *x* axis, have various chemical shift perturbations. F39, F45 and F55 are not included in the analysis because their resonances were not assigned. F48, F117 and F142 have larger than average chemical shift perturbation. And F72, F128, F130, F161, F186 and F189 and F197 are below average. As discussed in the introduction, F55, F189, F197, F48, F45, F39, F130 and F128 can possibly form a hydrophobic channel located around the heme pocket, especially because the F39, F45 and F48 are positioned so closely to each other (shown earlier in Figure 1-5 in Chapter I). Here the evidence from chemical shift perturbation suggests that the F45L mutation does change its local ring cluster so that F48 experiences large chemical shift perturbation. The influence of F45L mutation does not affect all the Phe residues in the hydrophobic channel, but it influences the residues nearby that make the heme distal pocket.

The local structural disruptions together with the small overall conformational difference suggest that the protein likely has a different dynamic behavior. This idea is confirmed by the results from H/D exchange studies discussed below.

There are three kinds of hydrogens in proteins: the hydrogen on the amino acid side chain that exchanges very rapidly and mostly can not be detected; the hydrogen covalently bonded to carbon does not exchange at all; and the hydrogen on the amino acid backbone amide is exchangeable and measurable. The protein backbone amide hydrogen-deuterium (H/D) exchange is a chemical reaction in which a covalently bonded hydrogen atom is exposed to the deuterated solvent and exchanging for a deuteron. Taking advantage of the magnetic property of proton and deuterium (deuterium is "invisible" for NMR detection), NMR amide H/D exchange studies monitored by 2D HSQC spectra give information regarding solvent accessibility to different parts of the protein. The largest advantage is that it produces specific information of each individual amino acid about whether the residue or region comprised of a group of residues is buried and therefore protected or exposed and prone to exchange. H/D exchange experiments were used to test the difference in protein conformational dynamics among the CN^- complexes of WT, F45L, *ortho*-^{19}F Phe labeled WT and *ortho*-^{19}F Phe labeled F45L *pa*-HO. Apparent rates of exchange were calculated from the time-dependent intensity changing plot of the HSQC amide cross peaks, as demonstrated in the Experimental Section. From the HSQC spectra obtained at different times of the H/D exchange experiment shown in Figure 2-21, it can be seen that the intensities of amide cross peaks decay with time. It is obvious

that at the end of the exchange, more green peaks (F45L) have disappeared than red peaks (WT). The faster intensity drop of F45L suggests the faster H/D exchange for F45L than WT. Detailed analysis of time-dependent intensity changes were used to calculate the protection factors, as demonstrated in Experimental Section [*32, 33*].

The calculated protection factors for F45L *pa*-HO-CN are compared with the corresponding values from WT *pa*-HO-CN in Figure 2-23 (a) and (c), and a per residue plot of protection factors (*P*), expressed as log *P*, is shown in Figure 2-23 (c) and (d) and mapped onto the 3D crystal structure in Figure 2-24. To compare F45L *pa*-HO-CN and WT *pa*-HO-CN, data from both complexes are included in the same plot, with red triangles representing values obtained from F45L *pa*-HO-CN and blue circles representing values obtained from WT *pa*-HO-CN. The values corresponding to WT *pa*-HO-CN was kindly provided by Dr. Juan Carlos Rodriguez in our lab [*20*]. The missing symbol in the plot indicates that the corresponding residues are either a proline or not assigned due to broad line width and low intensity of their cross-peaks in HSQC spectra [*20*]. The symbols with log $P > 2.0$ are for the residues exchanging at rates with practical measurement of k_{ex} [*20*]. The blue circles (WT *pa*-HO-CN) are all above the red triangles (F45L). This suggests that WT *pa*-HO-CN is less prone to H/D exchange than F45L mutant; thus WT is more protected than F45L. This difference, indicated by the H/D exchange study, is related to the altered dynamic behavior. In the context of relatively small changes in protein structure, the mutation makes the protein more dynamic in the time scales probed by H/D exchange experiments. The subtracted protection factors are plotted in Figure 2-23 (b) and (d),

and the corresponding residues are mapped onto the crystal structure in Figure 2-24.

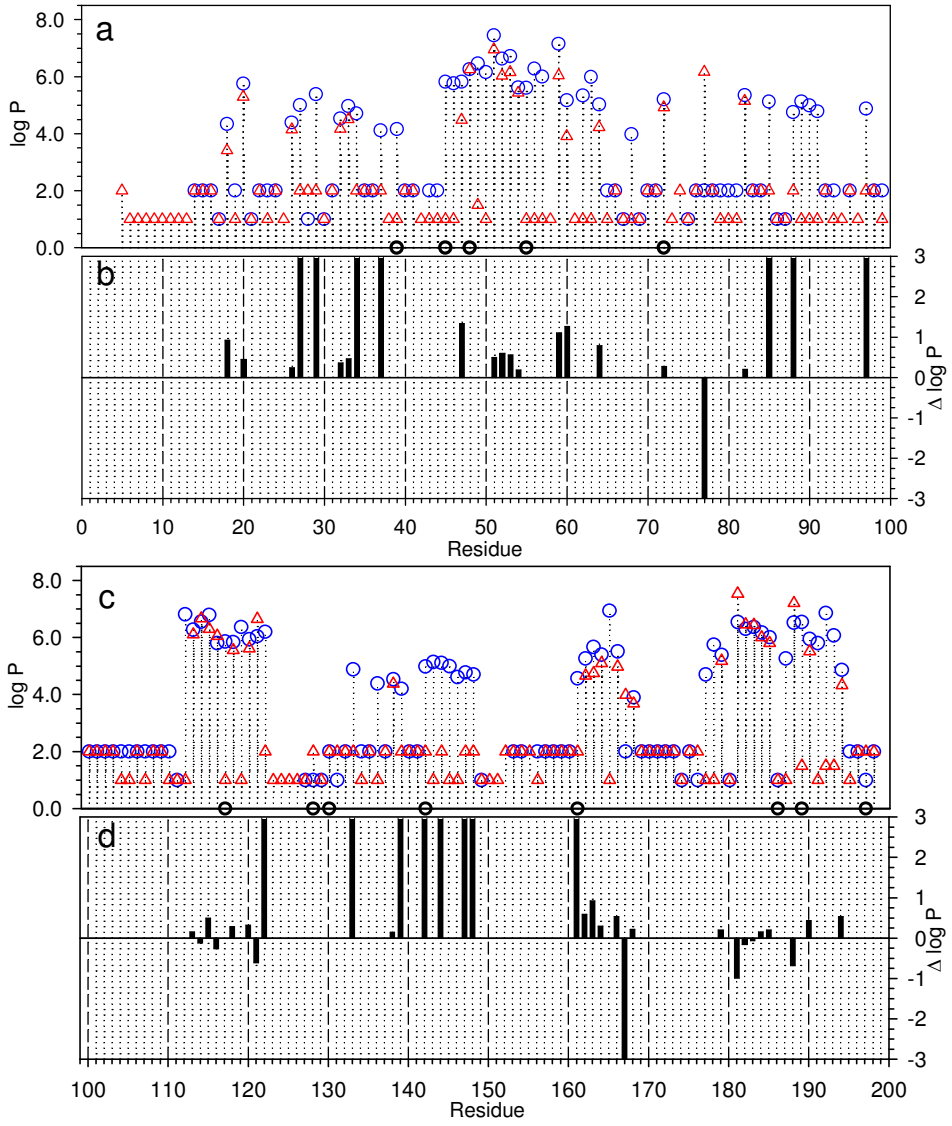

Figure 2-23. (a and c) Protection factors per residue plot obtained from amide H/D exchange experiments with F45L *pa*-HO-CN (red triangles) and WT *pa*-HO-CN (blue circles).

logP=2: exchange rates too fast to be measured (TFTM);
logP=1: Unassigned or superimposed or disappeared peaks.
logP=1.5: Exchange rates too slow to be measured (TSTM);
(b and d) Residue differences in protection factors ($\mathbf{logP} = \log P_{WT\text{-}CN} - \log P_{F45L\text{-}CN}$);
$\mathbf{logP}$ = -3: residue has TFTM in WT while measurable rate in F45L; logP = +3:

residue has TFTM in F45L while measurable rate in WT;
Phes are indicated by the empty circle in between two plots.

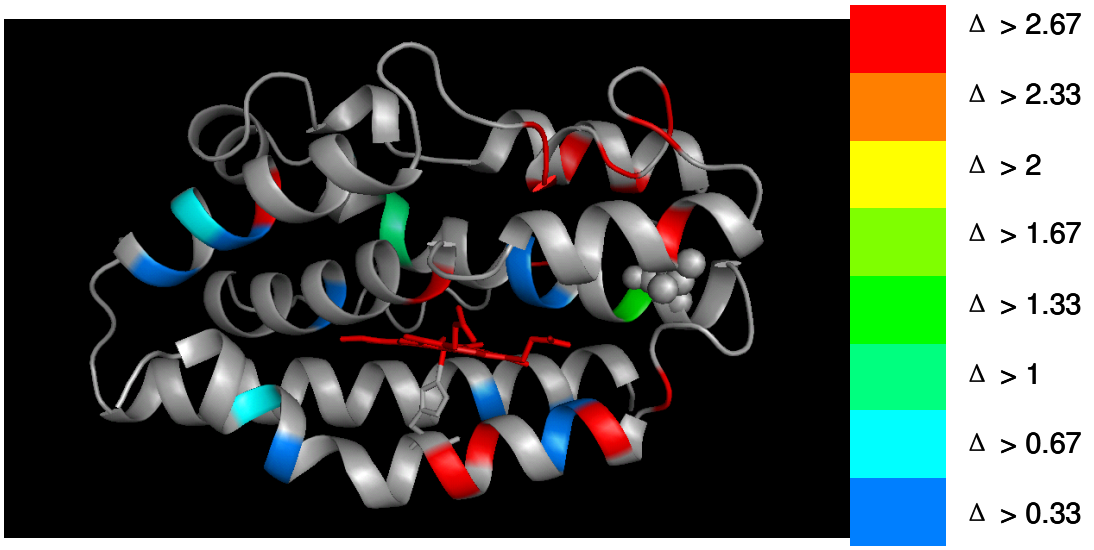

Figure 2-24. ΔlogP($logP_{WT-CN} - logP_{F45L-CN}$) plot mapped on to 3D crystal structure of *pa*-HO to highlight the regions in which WT *pa*-HO-CN exhibits enhanced protection to exchange relative to F45L *pa*-HO-CN. The color gradient is shown on the right side. The most pronounced differences in exchange behavior are shown by red color (0< Δ =< 3; 3 is TFTM in F45L but measurable in WT; gray is the amino acid that has no or smaller than 0.33 deltaLogP).

In Figure 2-24 the residues most protected in WT *pa*-HO-CN relative to F45L *pa*-HO-CN are colored red, and some of them are located closely to the mutation site. Residue 27, 29, 34 and 37 are located on helix II, close to the heme distal ligand H26. Residue 85 and 88 are located on helix VI. And residues 133, 139, 142, 144, 147 and 148 are located on helices VIII, IX and X. They are distant from the heme and the distal ligand. As suggested by the previous studies of the *pa*-HO-CN and *pa*-HO-N_3 by Juan Carlos Rodriguez and coworkers [*20, 36*] and the Human HO-1 by La Mar and coworkers [*5, 37*], most of the residues with distinct protection factors are likely to be involved in the hydrogen bonding network of the structural water molecules.

The single F45L mutation produces large protein dynamic change not only around its mutation site but also on the heme pocket as well as at the peripheral region on top of the heme pocket. This observation again supports that F45L mutation in the hydrophobic cluster composed of F39, F45 and F48 not only perturbs protein structure in different regions but also alters the overall protein dynamics, especially the regions that are structurally perturbed. Therefore, the phenylalanine rings not only function as an important structural component but also restrict the enzyme's plasticity for the specific catalytic requirement of heme oxygenase reactivity.

Next, we used the ortho-^{19}F-Phe labeling to study the Phe clusters. It is generally accepted that ^{19}F-Phe labeling is a good atomic level probe because it does not change protein stability, structure or dynamics. In order to evaluate the impact of *ortho*-^{19}F-Phe labeling in WT *pa*-HO, the chemical shift difference is acquired by comparing the same amino acid's HSQC peak in *ortho*-^{19}F-Phe labeled to WT paHO CN^- complexes. The result is shown in Figure 2-25. Inspecting the whole plot of Figure 2-25 (A), again the overall chemical shift difference is small which suggests that the protein structure is maintained. Similarly, some local regions exhibit larger changes, for example, in regions of helix II (bottom of heme pocket) and III (one side of heme pocket), and in regions of helix XIII (126-133) and IX (134-136), and the strand in-between and X (145-147) (these helices and neighboring loops are accessible to solvent). The regions perturbed by *ortho*-^{19}F-Phe labeling are different from those perturbed by the F45L mutation in the first two helix groups, and somewhat similar in the last three groups mentioned above. The 45 mutation site (45-

50) and the 88-92 regions are not much affected by the *ortho*-^{19}F-Phe labeling. All *ortho*-^{19}F labeled Phe residues, as represented by dots underneath the residue axis, have various degrees of chemical shift perturbations, for example, F48, F55, F130, F142 and F189 have chemical shift perturbation larger than the average. In the protein 3D crystal structure of resting state *pa*-HO, one can see that all these Phe residues seem to be randomly placed in the protein. By observing them closely, they fall into the proposed hydrophobic channel (F55, F189, F197, F48, F45, F39, F130 and F128 in the shape of a long cylinder that crosses the back of the heme pocket). The flexibility of the loop would possibly explain the large chemical shift perturbation. Again, the influence of ortho-^{19}F-Phe labeling does not channel through all the Phe candidates in the hydrophobic channel, and it affects the heme distal pocket to a larger extent than the F45L mutation.

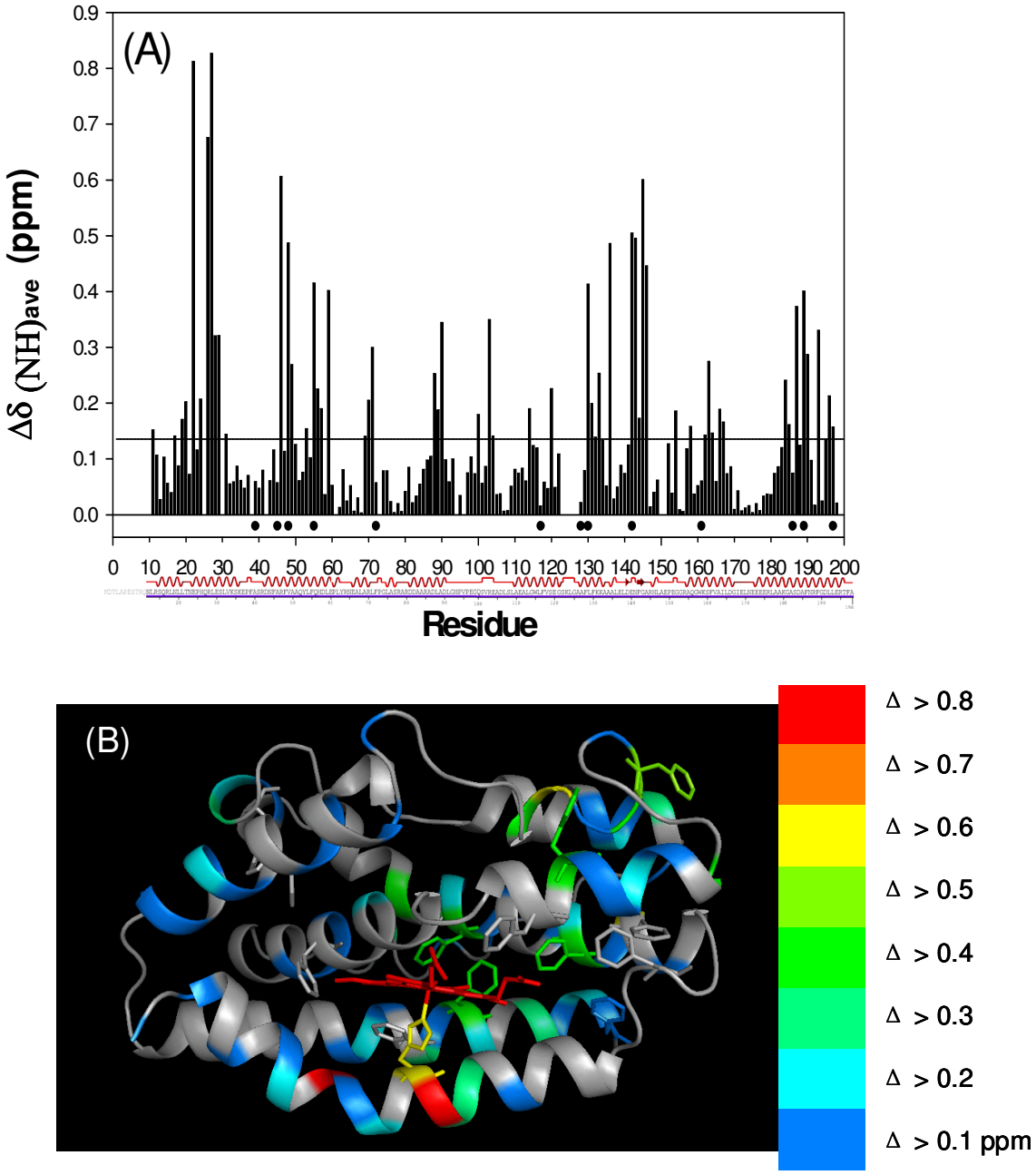

Figure 2-25. Chemical shift perturbations caused by ortho-^{19}F Phe labeling in the WT *pa*-HO-CN complex. (A) Chemical shift perturbation per residue plot, similarly presented as in Figure 2-22. The average 0.136 is shown by the horizontal line. (B) Weighted average amide chemical shift differences mapped onto the crystal structure of resting state *pa*-HO. The color coating follows the plotted Δδ using the colors demonstrated in the color gradient on the right side. The heme is shown in red. The heme, phenylalanines and His26 are shown in sticks.

Figure 2-25 (B) illustrates the chemical shift perturbations mapped onto the 3D crystal structure of *pa*-HO, with the warmer color representing larger chemical shift perturbations. Again, the distribution of the several warm colored Phes shows a clear pattern that the heme pocket and the loop on the right top of the structure have larger chemical shift perturbations. H26 and Q27 show the largest change, which suggests that there are possibly some disruptions to heme coordination in the heme pocket.

The H/D experiment was carried out with *ortho*-^{19}F-Phe *pa*-HO-CN as mentioned above. The calculated protection factors are compared with the corresponding values from WT *pa*-HO-CN in Figure 2-26 (a) and (c). The blue circles (WT for WT *pa*-HO-CN, CN^- here is the default binding ligand in this H/D exchange study) are all above the red triangles (o-WT for ortho-^{19}F-Phe labeled WT *pa*-HO-CN). It suggests that WT *pa*-HO-CN is less prone to H/D exchange than o-WT. This observation is similar that made in the comparison between WT and F45L. Here, *ortho*-^{19}F-Phe labeling also makes the protein more dynamic and more prone to the exchange compared with WT. The subtracted protection factors are plotted in Figure 2-26 (b) and (d), and the corresponding residues are mapped onto the 3D crystal structure in Figure 2-27. It is very surprising that a large influence on the flexibility of the protein occurs upon *ortho*-^{19}F-Phe labeling not only in the regions of the close proximity to the heme but also in the portions of the proteins that are far removed from the heme iron and distal ligand. Interestingly, the most affected

regions are similar like in the previous comparison between F45L mutant and WT *pa*-HO. The difference is that the previously affected residue 85 and 88 in the F45L mutant are not distinguishable between *ortho*-^{19}F-Phe labeling and WT. Yet the residue 20 and 21, as well as residues 110-120 seem to be more different here than in the comparison between mutation and WT. Overall, there are more residues prone to exchange found in the comparison between WT and ortho-^{19}F-Phe labeled *pa*-HO-CN than found in the comparison between WT and F45L mutation. Therefore it is not surprising that there are more Phe residues (indicated by a black circle in Figure 2-23 and 2-26) that are affected by *ortho*-^{19}F-Phe labeling than F45L mutation. This is because the *ortho*-^{19}F-Phe labeling that produces small but direct change in all total 13 Phe residues, but the F45L mutation only directly changes one Phe residue. All these differences suggest that the F45L mutation does not impact the protein dynamics as much as *ortho*-^{19}F-Phe labeling. Due to the limited data, protection factors for only a few Phe residues were calculated to compare with WT; F39, F128 and F161 seem to exhibit the most dramatic influence in protection factor. Although not all Phes in ortho-^{19}F-Phe labeled protein have dramatic change in protection factors, still most of them become more prone to exchange. Mapping $\Delta\log P$ on the structure of resting state *pa*-HO also reveals that sections of the protein remote from the heme-iron and distal ligand, where there is significantly less flexibility in *ortho*-^{19}F-Phe labeled *pa*-HO-CN relative to WT *pa*-HO-CN, appear to be in some kind of communication with the distal ligand *via* this hydrophobic channel formed by Phe residues. This observation in turn suggests that the hydrophobic cluster in the

structure plays an important role in maintaining protein tertiary structure and fine-tuning protein dynamics in heme oxygenase. Therefore, it again supports previous hypothesis that Phes not only function as an important structural component but also maintain the enzyme's plasticity for the specific catalytic requirement of unique heme oxygenase reactivity. By analyzing the residues showing the large change in both chemical shifts and protection factor in context of protein 3D crystal structure, the observation strongly suggests the possibility that hydrophobic channel (here proposed to be represented by a series of Phes forming a horizontal cylinder in this protein) inside the protein may function more importantly than is appreciated. It is easy to understand that the H-bonding network formed with structural water molecules plays a key role in protein structure and function. On the other hand, the hydrophobic channel (a hydrophobic core) may be as important to the integrity of the H-bonding network. Further detailed study is necessary to test this hypothesis.

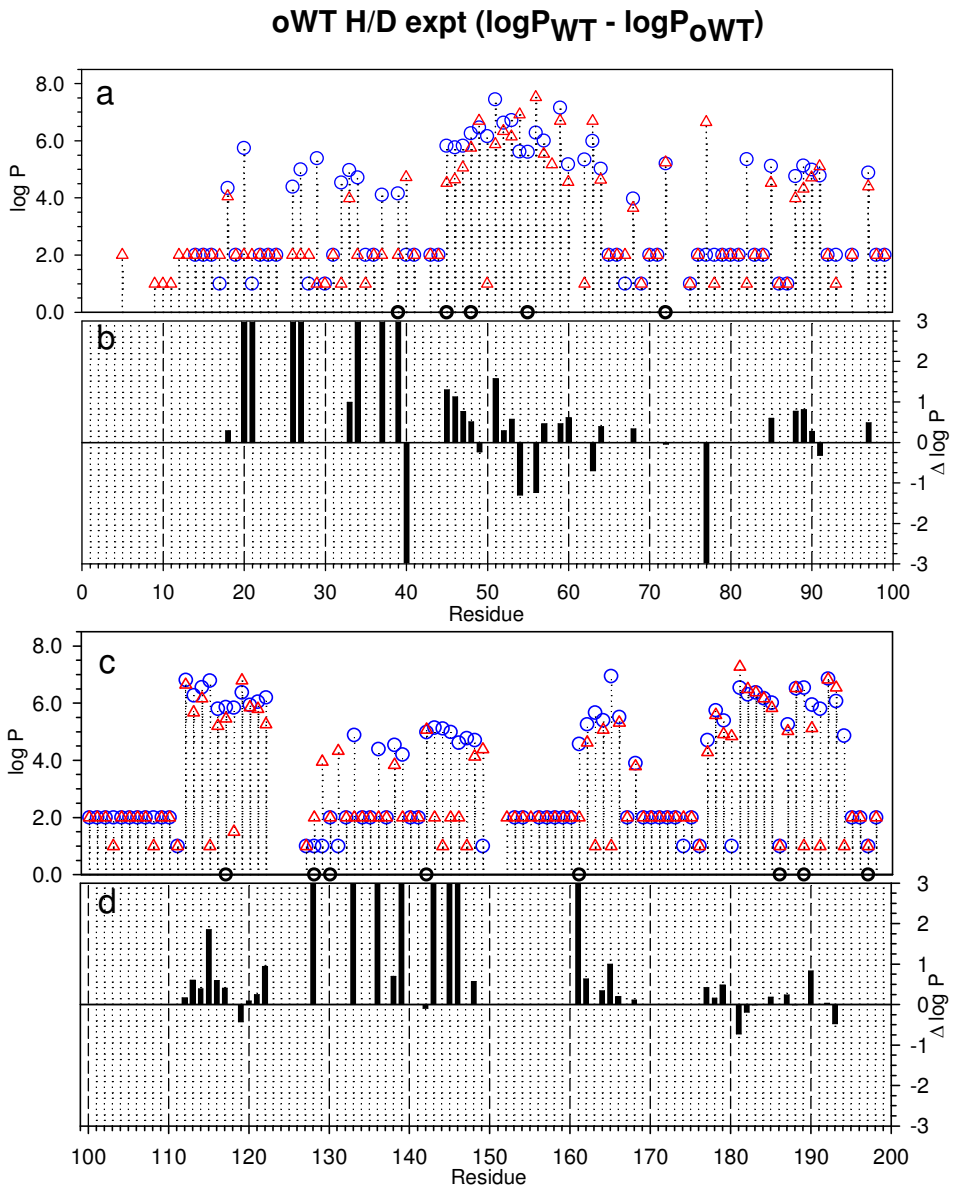

Figure 2-26. (a and c) Protection factors per residue plot obtained from amide H/D exchange experiments with o-^{19}F-Phe labeled *pa*-HO-CN (red triangles) and WT *pa*-HO-CN (blue circles).

logP=2: exchange rates too fast to be measured (TFTM);
logP=1: Unassigned or superimposed or disappeared peaks.
logP=1.5: Exchange rates too slow to be measured (TSTM);
(b and d) Residue differences in protection factors (ΔlogP =logP$_{WT\text{-}CN}$ – logP$_{o\text{-}19F\text{-}PheWT\text{-}CN}$);
ΔlogP = -3: residue has TFTM in WT while measurable rate in o-^{19}F-Phe-WT;

ΔlogP = +3: residue has TFTM in o-^{19}F-Phe-WT while measurable rate in WT;
Phes are indicated by the empty circle in between two plots

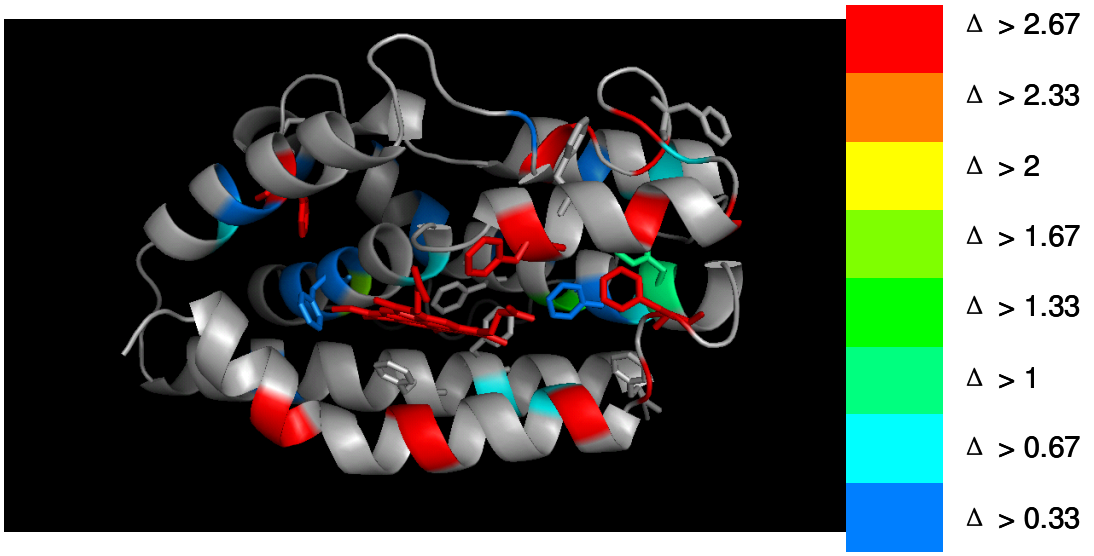

Figure 2-27. Mapping of ΔlogP($logP_{WT-CN} - logP_{o-WT-CN}$) plot on to 3D crystal structure of *pa*-HO to highlight the regions in which WT *pa*-HO-CN exhibits enhanced protection to exchange relative to o-WT *pa*-HO-CN. The color gradient is shown on the right side. The most pronounced differences in exchange behavior are shown by red color (0< Δ =< 3; 3 is TFTM in o-WT but measurable in WT; gray is the amino acid that has no or smaller than 0.33 deltaLogP).

A similar study was conducted by combining *ortho*-^{19}F-Phe labeling and the F45L mutation. The results are shown in Figure 2-28 and 2-29. Because of the aggravated change brought by mutation together with *ortho*-^{19}F-Phe labeling, many more residues were not assignable due to missing signals in the HSQC spectrum, due to broad line width and weak signal intensity caused by dynamic properties at 37 °C. Some of the signals reappear when the temperature is lowered. Thus, their assignments were achieved at lower temperatures. Those peaks with fast dynamics

are very prone to H/D exchange. Therefore, they are still included in the H/D exchange study as the least protected residues. From the chemical shift perturbation plot in Figure 2-28, it is clear that it has larger perturbation than either ortho-^{19}F-Phe labeling or F45L mutation, and the perturbed regions are the combination of both. Also, the average shift 0.14 is larger than either *ortho*-^{19}F-Phe labeling or F45L mutation. As shown in Figure 2-28 (B), the mapping suggests that the chemical shift change is spread around the whole protein.

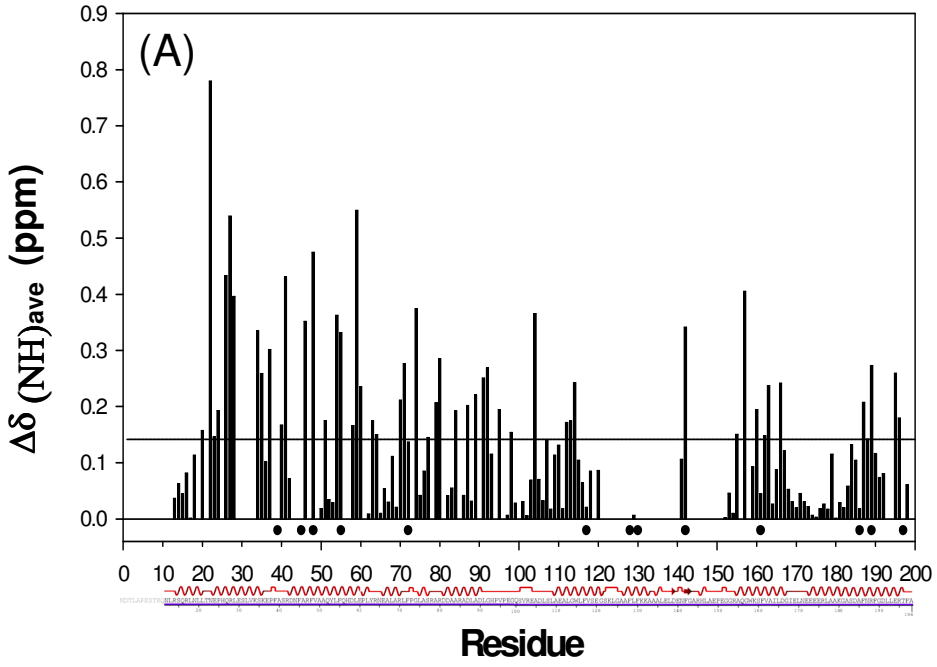

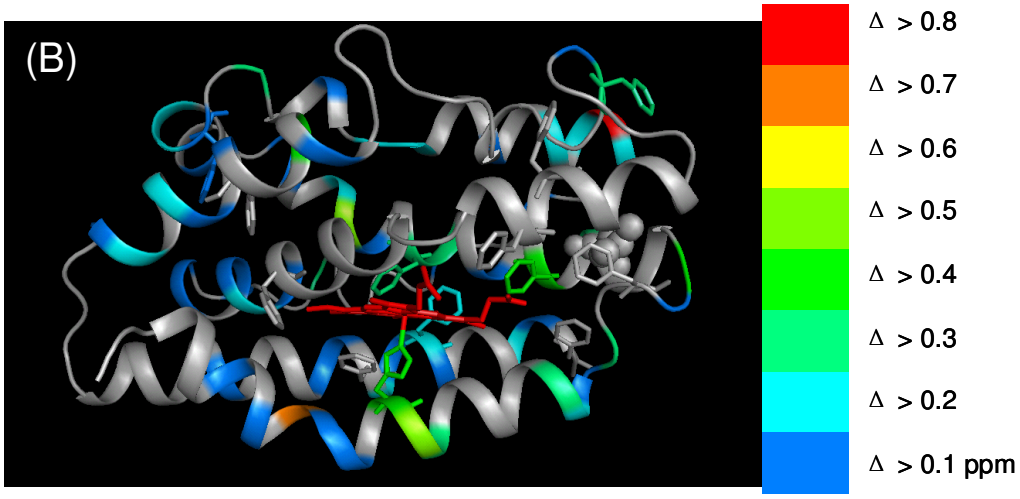

Figure 2-28. Chemical shift perturbation caused by both ortho-^{19}F Phe labeling and F45L mutation in WT *pa*-HO-CN complex. (A) Chemical shift perturbation per residue plot, similarly presented as in Figure 2-22. The average 0.14 is shown by the horizontal line. (B) Weighted average amide chemical shift differences mapped onto the crystal structure of resting state *pa*-HO. The color coating follows the plotted Δδ using the colors demonstrated in the color gradient on the right side. The heme is shown in red. The heme, phenylalanines and His26 are shown in sticks.

H/D experiments were also conducted with o-^{19}F-Phe F45L. The calculated protection factors again are compared with the corresponding values from WT *pa*-HO-CN in Figure 2-29. The blue circles (WT) are all above the red triangles (o-WT). Once again, these data suggest that WT *pa*-HO-CN is less prone to H/D exchange than o-F45L (o-F45L for ortho-^{19}F-Phe labeled F45L *pa*-HO-CN). Green diamond represents the new assignments achieved only at lower temperatures for the fast exchange residues. It is apparent that these green diamond symbolized residues are located in the regions that are more prone to H/D exchange in either *ortho*-^{19}F-Phe labeling or the F45L mutation compared with WT. Therefore, in the case of combining both *ortho*-^{19}F-Phe labeling and the F45L mutation, these residues are

even more dynamic than before. From temperature dependent experiments, these green diamond labeled residues were only detectable at lower temperatures. These observations confirm that the previous findings in *ortho*-^{19}F-Phe labeling or the F45L mutation were no coincidence. Again, Δlog *P* plot was mapped onto the 3D crystal structure in Figure 2-30. The regions with warmer color resemble the above mappings for F45L and ortho-^{19}F-Phe labeling H/D exchange studies.

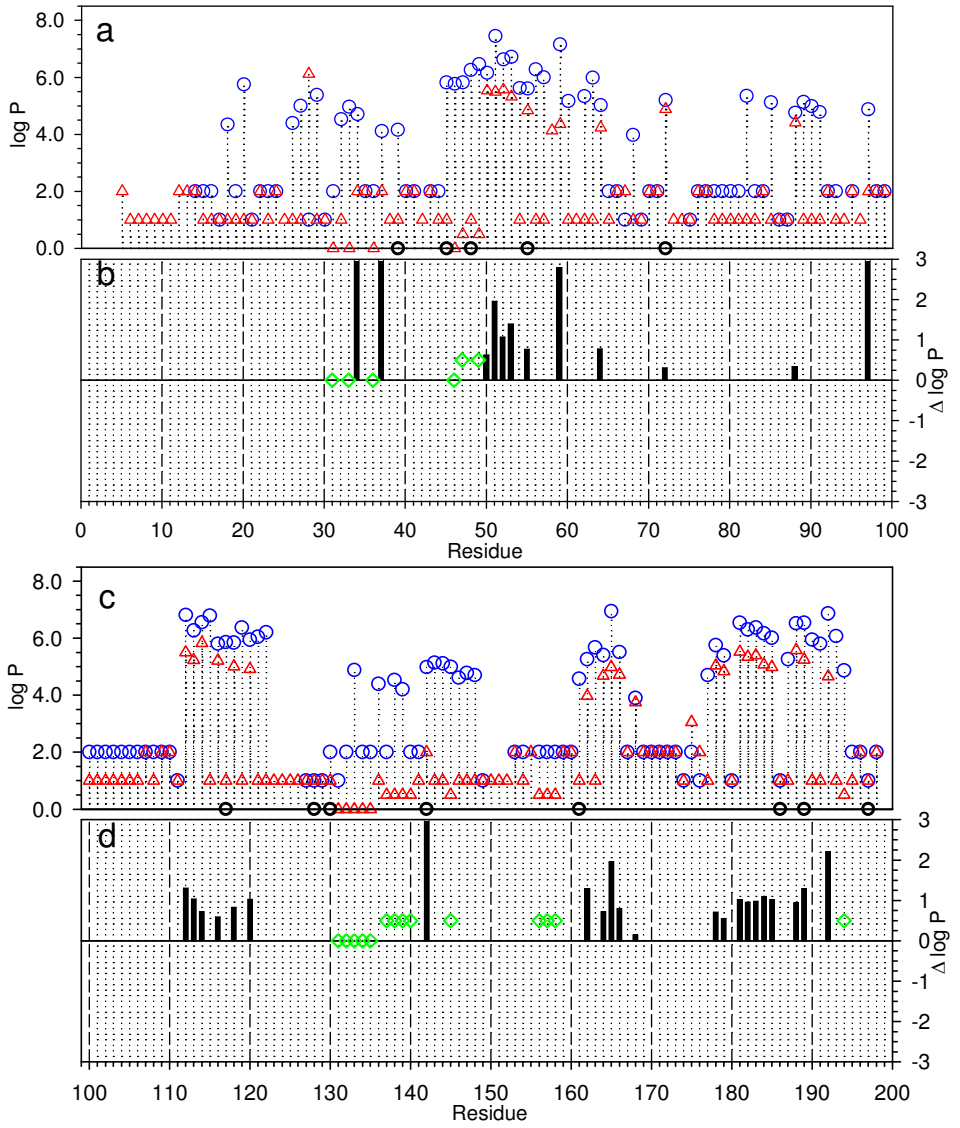

Figure 2-29. (a and c) Protection factors per residue plot obtained from amide H/D exchange experiments with o-^{19}F-Phe labeled F45L *pa*-HO-CN (red triangles) and WT *pa*-HO-CN (blue circles).

logP=2: exchange rates too fast to be measured (TFTM);
logP=1: Unassigned or superimposed or disappeared peaks.
logP=1.5: Exchange rates too slow to be measured (TSTM);
logP=0.5: Assigned at 15°C with assignment peak appearing or increasing intensity, shown by green diamond: sure assignments: 0.5, guessed assignments: 0.0.

(b and d) Residue differences in protection factors ($\Delta logP = logP_{WT\text{-}CN} - logP_{o\text{-}F45L\text{-}CN}$); $\Delta logP$ = -3: residue has TFTM in WT while measurable rate in o-^{19}F-Phe-F45L;

ΔlogP = +3: residue has TFTM in o-^{19}F-Phe-F45L while measurable rate in WT;
Phes are indicated by the empty circle in between two plots

Figure 2-30. ΔlogP($logP_{WT-CN} - logP_{o-F45L-CN}$) plot mapped on to 3D crystal structure of *pa*-HO to highlight the regions in which WT *pa*-HO-CN exhibits enhanced protection to exchange relative to o-F45L *pa*-HO-CN. The color gradient is shown on the right side. The most pronounced differences in exchange behavior are shown by red color (0< Δ =< 3; 3 is TFTM in o-F45L but measurable in WT; gray is the amino acid that has no or smaller than 0.33 deltaLogP).

CONCLUSION

Phe is a hydrophobic residue; its ring rotation displaces about 80 cubic angstroms volume. The cluster of Phe rings can possibly form a hydrophobic cluster and exclude water molecule. In a way it works like the "bank sides to river" to facilitate the internal structural water to form an H-bonding network with the protein side chain. Also the hydrophobic cluster is especially important in the protein folding and conformational changes in the protein dynamics [*38*].

By using mutagenesis and fluorine labeling to the Phe residues using *pa*-HO as a model, we investigated the observed Phe hydrophobic cluster inside heme oxygenase. Using *ortho*-^{19}F-Phe labeling and F45L etc mutations studied by NMR, UV-vis and CD, it is discovered that this Phe ring cluster not only functions to maintain protein structure but also fine-tunes the protein dynamic motion for this specific heme oxygenation catalysis.

Phe45 is the key residue in the hydrophobic Phe ring cluster inside *pa*-HO. F45L mutation causes certain disruptions in heme distal pocket and the loss of heme oxygenase reactivity while maintaining overall protein structure. It increases protein dynamic motion in the large (hrs-days) time scales detected by H/D exchange experiment.

Ortho-^{19}F-phenylalanine labeling in *pa*-HO decreases reactivity while maintaining the intact protein structure. Surprisingly contrary to general understanding that ^{19}F-Phe labeling will provide very little influence in protein structure and function. Again protein dynamic motion is altered. And with the combination of *ortho*-^{19}F-phenylalanine labeling and F45L mutation, the impact is enhanced on both reactivity and protein dynamics.

As shown in the studies of human HO-1[*5, 37*] and *pa*-HO [*20, 36*], a propagated water channel and H-bonding network exist for assisting protein catalysis. From this study of Phe ring cluster in *pa*-HO, we predicted that the H-bonding network in the heme binding pocket is likely altered during the protein mutation or/and the *ortho*-^{19}F-Phe labeling.

The understanding of how *pa*-HO possesses and carries out its unique catalysis gives us a solid foundation in searching and testing its redox partner proteins where *pa*-HO gets the seven electrons for heme degradation. The study of a novel *pa*-HO redox partner protein, ferredoxin NADPH reductase protein from *Pseudomoonas aeruginosa* will be discussed in next two chapters.

REFERENCES

[1] Maines, M. D. (2004) The Heme Oxygenase System: Past, Present, and Future. *Antioxidants & Redox Signaling*, *6*, 797-801.

[2] Maines, M. D.; Gibbs, P. E. M. (2005) 30 some years of heme oxygenase: From a "molecular wrecking ball" to a "mesmerizing" trigger of cellular events. *Biochemical and Biophysical Research Communications*, *338*, 568-577.

[3] Schuller, D. J.; Wilks, A.; De Montellano, P. R. O.; Poulos, T. L. (1999) Crystal structure of human heme oxygenase-1. *Nature Structural Biology*, *6*, 860-867.

[4] Liu, Y.; Lightning, L. K.; Huang, H.-W.; Moenne-Loccoz, P.; Schuller, D. J.; Poulos, T. L.; Loehr, T. M.; De Montellano, P. R. O. (2000) Replacement of the distal glycine 139 transforms human heme oxygenase-1 into a peroxidase. *Journal of Biological Chemistry*, *275*, 34501-34507.

[5] Syvitski, R. T.; Li, Y.; Auclair, K.; Ortiz de Montellano, P. R.; La Mar, G. N. (2002) 1H NMR Detection of Immobilized Water Molecules within a Strong Distal Hydrogen-Bonding Network of Substrate-Bound Human Heme Oxygenase-1. *Journal of the American Chemical Society*, *124*, 14296-14297.

[6] Lad, L.; Wang, J.; Li, H.; Friedman, J.; Bhaskar, B.; Ortiz de Montellano, P. R.; Poulos, T. L. (2003) Crystal structures of the ferric, ferrous, and ferrous-NO forms of the Asp140Ala mutant of human heme oxygenase-1: catalytic implications. *Journal of Molecular Biology*, *330*, 527-538.

[7] Davis, S. J.; Kurepa, J.; Vierstra, R. D. (1999) The Arabidopsis thaliana HY1 locus, required for phytochrome-chromophore biosynthesis, encodes a protein related to heme oxygenases. *Proceedings of the National Academy of Sciences of the United States of America*, *96*, 6541-6546.

[8] Frankenberg-Dinkel, N. (2004) Bacterial heme oxygenases. *Antioxidants & Redox Signaling*, *6*, 825-834.

[9] Yoshida, T.; Noguchi, M.; Kikuchi, G. (1980) Oxygenated Form of Heme-Heme Oxygenase Complex and Requirement for Second Electron to Initiate Heme Degradation from the Oxygenated Complex. *Journal of Biological Chemistry*, *255*, 4418-4420.

[10] Davydov, R. M.; Yoshida, T.; Ikeda-Saito, M.; Hoffman, B. M. (1999) Hydroperoxy-Heme Oxygenase Generated by Cryoreduction Catalyzes the Formation of α-meso-Hydroxyheme as Detected by EPR and ENDOR. *Journal of the American Chemical Society*, *121*, 10656-10657.

[11] Wilks, A.; Torpey, J.; Ortiz de Montellano, P. R. (1994) Heme Oxygenase (HO-1) Evidence for Electrophilic Oxygen Addition to the Porphyrin Ring in the Formation of α-meso-hydroxyheme. *Journal of Biological Chemistry*, *269*, 29553-29556.

[12] Yoshida, T.; Kikuchi, G. (1978) Features of the Reaction of Heme Degradation Catalyzed by the Reconstituted Microsomal Heme Oxygenase System. *Journal of Biological Chemistry*, *253*, 4230-4236.

[13] Yoshida, T.; Noguchi, M.; Kikuchi, G. (1980) A New Intermediate of Heme Degradation Catalyzed by the Heme Oxygenase System. *Journal of Biochemistry*, *88*, 557-563.

[14] Liu, Y.; Ortiz de Montellano, P. R. (2000) Reaction Intermediates and Single Turnover Rate Constants for the Oxidation of Heme by Human Heme Oxygenase-1. *Journal of Biological Chemistry*, *275*, 5297-5307.

[15] Wilks, A.; Ortiz de Montellano, P. R. (1993) Rat Liver Heme Oxygenase. *Journal of Biological Chemistry*, *268*, 22357-22362.

[16] Damaso, C. O.; Bunce, R. A.; Barybin, M. V.; Wilks, A.; Rivera, M. (2005) The Ferrous Verdoheme-Heme Oxygenase Complex is Six-Coordinate and Low-Spin. *Journal of the American Chemical Society*, *127*, 17852-17853.

[17] Damaso, C. O.; Rubie, N. D.; Moenne-Loccoz, P.; Rivera, M. (2004) Reduction of the Ferrous α-Verdoheme-Cytochrome b_5 Complex. *Inorganic Chemistry*, *43*, 8470-8478.

[18] Caignan, G. A.; Deshmukh, R.; Wilks, A.; Zeng, Y.; Huang, H.-w.; Moeenne-Loccoz, P.; Bunce, R. A.; Eastman, M. A.; Rivera, M. (2002) Oxidation of Heme to b- and d-Biliverdin by Pseudomonas aeruginosa Heme Oxygenase as a Consequence of an Unusual Seating of the Heme. *Journal of the American Chemical Society*, *124*, 14879-14892.

[19] Zeng, Y.; Caignan, G. A.; Bunce, R. A.; Rodriguez, J. C.; Wilks, A.; Rivera, M. (2005) Azide-Inhibited Bacterial Heme Oxygenases Exhibit an S = 3/2 (dxz,dyz)3(dxy)1(dz2)1 Spin State: Mechanistic Implications for Heme Oxidation. *Journal of the American Chemical Society*, *127*, 9794-9807.

[20] Rodriguez, J. C.; Wilks, A.; Rivera, M. (2006) Backbone NMR Assignments and H/D Exchange Studies on the Ferric Azide- and Cyanide-Inhibited Forms of Pseudomonas aeruginosa Heme Oxygenase. *Biochemistry*, *45*, 4578-4592.

[21] Schuler, B.; Kremer, W.; Kalbitzer, H. R.; Jaenicke, R. (2002) Role of Entropy in Protein Thermostability: Folding Kinetics of a Hyperthermophilic

Cold Shock Protein at High Temperatures Using 19F NMR. *Biochemistry*, *41*, 11670-11680.

[22] Berry, E. A.; Trumpower, B. L. (1987) Simultaneous determination of hemes a, b, and c from pyridine hemochrome spectra. *Analytical Biochemisry*, *161*, 1-15.

[23] Wilks, A. (2002) Heme Oxygenase: Evolution, Structure and Mechanism. *Antioxidants and Redox Signaling*, *4*, 603-614.

[24] Rivera, M.; Levine, D. J.; Aposhian, H. V.; Fernando, Q. (1991) Synthesis and properties of the monomethyl ester of meso-dimercaptosuccinic acid and its chelates of lead(II), cadmium(II), and mercury(II). *Chemical Research in Toxicology*, *4*, 107-114.

[25] Caignan, G. A.; Deshmukh, R.; Zeng, Y.; Wilks, A.; Bunce, R. A.; Rivera, M. (2003) The Hydroxide Complex of Pseudomonas aeruginosa Heme Oxygenase as a Model of the Low-Spin Iron(III) Hydroperoxide Intermediate in Heme Catabolism: 13C NMR Spectroscopic Studies Suggest the Active Participation of the Heme in Macrocycle Hydroxylation. *Journal of the American Chemical Society*, *125*, 11842-11852.

[26] Lightning, L. K.; Huang, H.-w.; Moenne-Loccoz, P.; Loehr, T. M.; Schuller, D. J.; Poulos, T. L.; de Montellano, P. R. O. (2001) Disruption of an Active Site Hydrogen Bond Converts Human Heme Oxygenase-1 into a Peroxidase. *Journal of Biological Chemistry*, *276*, 10612-10619.

[27] Tonami, H.; Uyama, H.; Nagahata, R.; Kobayashi, S. (2004) Guaiacol Oxidation Products in the Enzyme-Activity Assay Reaction by Horseradish Peroxidase Catalysis. *Chemistry letters*, *33*, 796-797.

[28] Wishart, D. S.; Bigam, C. G.; Yao, J.; Abildgaard, F.; Dyson, H. J.; Oldfield, E.; Markley, J. L.; Sykes, B. D. (1995) 1H, 13C and 15N chemical shift referencing in biomolecular NMR. *Journal of Biomolecular NMR*, *6*, 135-140.

[29] Otting, G. (1997) NMR studies of water bound to biological molecules. *Progress in Nuclear Magnetic Resonance Spectroscopy*, *31*, 259-285.

[30] Simeonov, M.; Altuve, A.; Massiah, M. A.; Wang, A.; Eastman, M. A.; Benson, D. R.; Rivera, M. (2005) Mitochondrial and microsomal ferric b5 cytochromes exhibit divergent conformational plasticity in the context of a common fold. *Biochemistry*, *44*, 9308-9319.

[31] Swint-Kruse, L.; Robertson, A. D. (1996) Temperature and pH dependences of hydrogen exchange and global stability for ovomucoid third domain. *Biochemistry*, *35*, 171-180.

[32] Hvidt, A.; Nielsen, S. O. (1966) Hydrogen Exchange in Proteins, in *Advances in Protein Chemistry* (Anfinsen, C. B.;Lanson, M. L.;Edsall, J. T.;Richards, F. M., Eds.), pp 288-380, Academic Press, New York.

[33] Bai, Y.; Milne, J. S.; Mayne, L.; Englander, S. W. (1994) Protein Stability Parameters Measured by Hydrogen Exchange. *Proteins: Struct. Funct. Genet.*, *20*, 4-14.

[34] Wegele, R.; Tasler, R.; Zeng, Y.; Rivera, M.; Frankenberg-Dinkel, N. (2004) The Heme Oxygenase (s)-Phytochrome System of Pseudomonas aeruginosa. *Journal of Biological Chemistry*, *279*, 45791.

[35] Zeng, Y.; Deshmukh, R.; Caignan, G. A.; Bunce, R. A.; Rivera, M.; Wilks, A. (2004) Mixed Regioselectivity in the Arg-177 Mutants of Corynebacterium diphtheriae Heme Oxygenase as a Consequence of in-Plane Heme Disorder. *Biochemistry*, *43*, 5222-5238.

[36] Rodriguez, J. C.; Zeng, Y.; Wilks, A.; Rivera, M. (2007) The Hydrogen-Bonding Network in Heme Oxygenase Also Functions as a Modulator of Enzyme Dynamics: Chaotic Motions upon Disrupting the H-Bond Network in Heme Oxygenase from Pseudomonas aeruginosa. *Journal of the American Chemical Societ.*, *129*, 11730-11742.

[37] Li, Y.; Syvitski, R. T.; Auclair, K.; Ortiz de Montellano, P. R.; La Mar, G. N. (2003) Solution ^{1}H, ^{15}N NMR Spectroscopic Characterization of Substrate-Bound, Cyanide-Inhibited Human Heme Oxygenase: Water Occupation of the Distal Cavity. *Journal of the American Chemical Society*, *125*, 13392-13403.

[38] Baldwin, R. L. (2002) PROTEIN FOLDING: Making a Network of Hydrophobic Clusters, pp 1657-1658.

APPENDIX

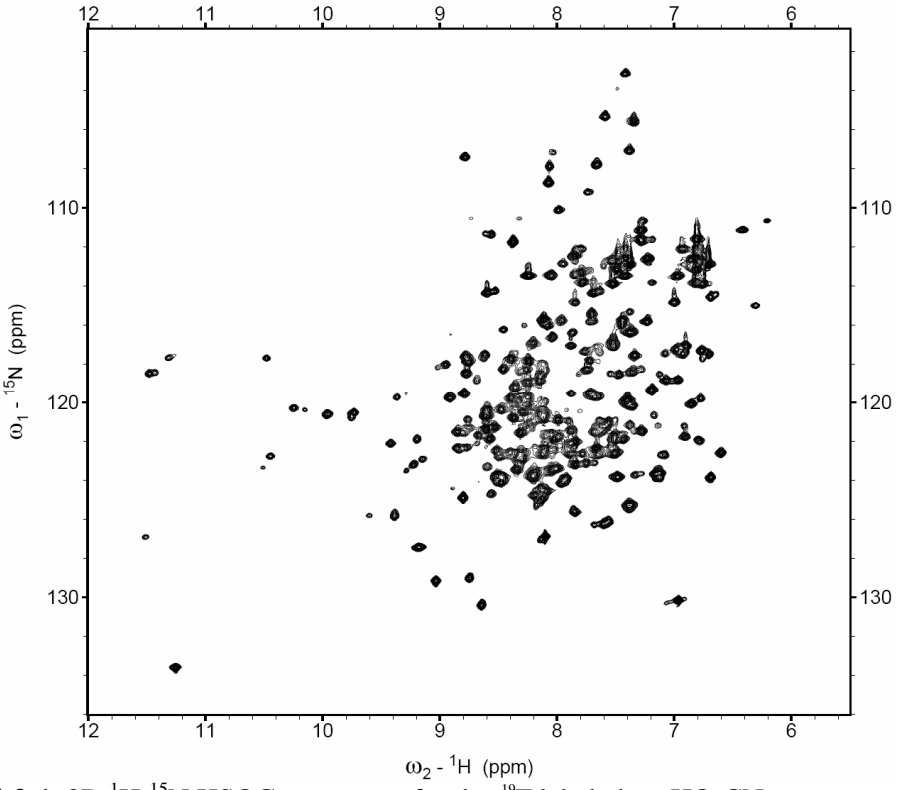

Figure S-2-1. 2D ^{1}H-^{15}N HSQC spectrum of ortho-^{19}F labeled *pa*-HO-CN.

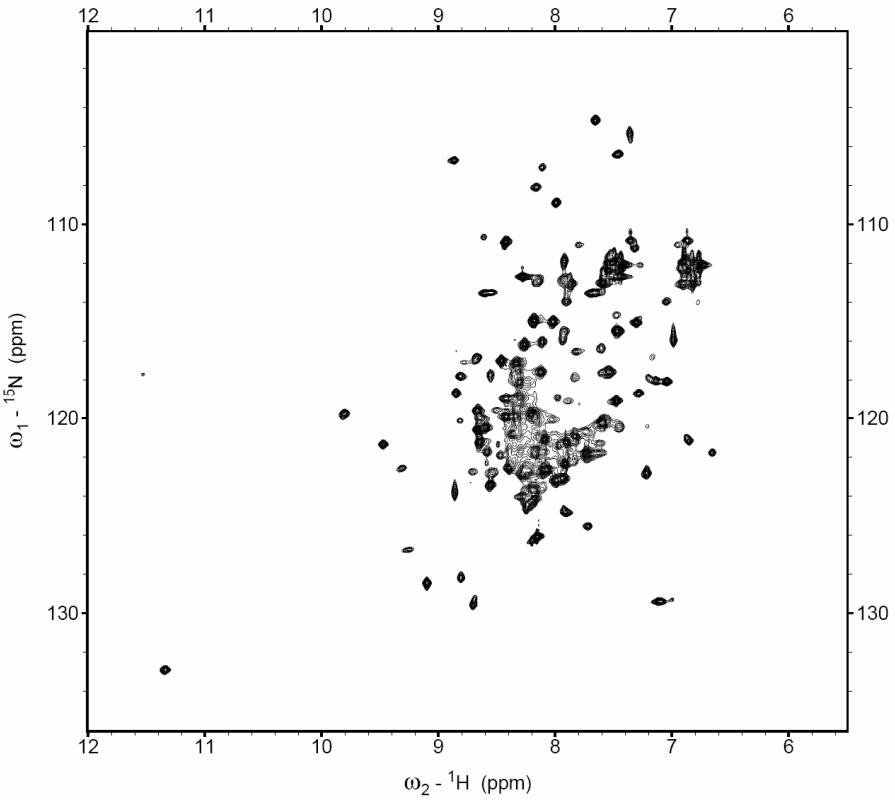

Figure S-2-2. 2D ^{1}H-^{15}N HSQC spectrum of ortho-^{19}F labeled F45L WT *pa*-HO-CN.

Table S-2-1. F45L *pa*-HO-CN 2D ^{1}H-^{15}N HSQC NMR assignments, chemical shifts are given in ppm.

Residue	No.	^{15}N	^{1}H
MET	1		
ASP	2		
THR	3		
LEU	4		
ALA	5		
PRO	6		
GLU	7		
SER	8		
THR	9		
ARG	10		
GLN	11		
ASN	12		
LEU	13	121.23	7.89
ARG	14	128.15	8.81

SER	15	117.50	11.49
GLN	16	121.88	6.65
ARG	17	121.73	8.16
LEU	18	118.84	8.85
ASN	19	120.83	7.98
LEU	20	119.79	8.02
LEU	21	119.39	8.36
THR	22	106.02	8.12
ASN	23	124.20	8.18
GLU	24	120.04	9.84
PRO	25		
HIS	26	120.64	10.46
GLN	27	123.37	10.73
ARG	28	120.59	8.93
LEU	29		
GLU	30		
SER	31	112.97	7.21
LEU	32	124.21	7.43
VAL	33	118.87	7.69
LYS	34	116.43	7.11
SER	35	114.98	7.48
LYS	36	119.17	6.85
GLU	37	111.17	7.28
PRO	38		
PHE	39		
ALA	40	120.90	7.70
SER	41	105.07	7.35
ARG	42		
ASP	43		
ASN	44		
PHE	45		
ALA	46	121.08	8.59
ARG	47	116.02	6.94
PHE	48	123.14	7.59
VAL	49	121.42	9.21
ALA	50	122.51	8.56
ALA	51	121.06	7.04
GLN	52	116.43	7.83
TYR	53	119.45	9.33
LEU	54	120.31	8.35
PHE	55		
GLN	56		
HIS	57		
ASP	58	122.21	7.92
LEU	59	113.45	6.77
GLU	60	124.53	7.43
PRO	61		

LEU	62	116.27	7.66
TYR	63	114.95	7.70
ARG	64	112.03	7.30
ASN	65	122.81	7.22
GLU	66	128.38	9.09
ALA	67	122.30	7.90
LEU	68	119.39	8.36
ALA	69	122.29	8.37
ARG	70	114.75	7.26
LEU	71	118.50	7.07
PHE	72	115.62	7.93
PRO	73		
GLY	74	115.61	8.96
LEU	75	123.24	7.96
ALA	76	117.81	8.76
SER	77	111.83	7.91
ARG	78		
ALA	79	122.86	6.79
LEU	80	117.77	7.80
ASP	81		
ASP	82	119.90	8.29
ALA	83	123.59	8.16
ALA	84	117.50	8.08
ARG	85	118.16	8.36
ALA	86	123.24	7.96
ASP	87	122.29	8.37
LEU	88	119.21	7.90
ALA	89	120.46	7.40
ASP	90	120.84	8.23
LEU	91	116.52	7.59
GLY	92	108.88	7.96
HIS	93	122.68	8.17
PRO	94		
VAL	95	123.93	8.84
PRO	96		
GLU	97	119.91	8.41
GLY	98	111.04	8.43
ASP	99	119.99	8.62
GLN	100	118.03	8.73
SER	101	117.03	8.77
VAL	102	122.86	8.26
ARG	103	121.82	8.29
GLU	104	114.80	7.79
ALA	105	122.81	7.22
ASP	106	120.89	8.36
LEU	107	121.75	7.73
SER	108	119.00	8.45

LEU	109	123.30	8.53
ALA	110	116.98	8.29
GLU	111	115.46	7.40
ALA	112	121.03	8.62
LEU	113	115.91	8.08
GLY	114	104.32	7.63
TRP	115	121.67	7.54
LEU	116	117.91	8.50
PHE	117	119.58	8.47
VAL	118	118.13	7.15
SER	119		
GLU	120	117.74	8.99
GLY	121	111.69	7.66
SER	122	113.94	6.37
LYS	123		
LEU	124		
GLY	125		
ALA	126		
ALA	127		
PHE	128	117.60	8.20
LEU	129	120.49	8.59
PHE	130	120.33	9.98
LYS	131	116.91	7.38
LYS	132	119.27	7.32
ALA	133	122.09	8.22
ALA	134	120.46	7.40
ALA	135	120.40	7.52
LEU	136	117.74	7.56
GLU	137	114.48	8.11
LEU	138	116.91	6.94
ASP	139	120.10	9.31
GLU	140	116.69	10.42
ASN	141	116.38	8.84
PHE	142	122.99	7.91
GLY	143	118.29	9.58
ALA	144	119.27	7.32
ARG	145		
HIS	146	116.29	11.28
LEU	147	120.56	7.64
ALA	148	122.98	7.50
GLU	149	122.62	8.38
PRO	150		
GLU	151		
GLY	152	113.56	9.09
GLY	153	108.04	8.14
ARG	154	125.19	9.46
ALA	155	122.68	8.68

GLN	156		
GLY	157	107.61	7.72
TRP	158	125.04	7.62
LYS	159	118.09	8.28
SER	160	112.80	8.12
PHE	161	123.84	7.22
VAL	162	117.31	8.35
ALA	163	119.82	7.51
ILE	164	117.05	6.77
LEU	165	121.23	7.89
ASP	166	116.51	8.63
GLY	167	106.53	7.46
ILE	168	121.12	6.80
GLU	169	129.51	8.69
LEU	170	124.86	7.90
ASN	171	121.39	9.47
GLU	172	116.94	8.45
GLU	173	121.07	8.08
GLU	174	120.49	8.59
GLU	175	119.67	8.66
ARG	176	119.05	7.46
LEU	177	122.62	8.05
ALA	178	124.06	8.25
ALA	179	118.59	7.27
LYS	180	121.73	8.16
GLY	181	106.77	8.86
ALA	182	121.31	7.64
SER	183	112.86	7.92
ASP	184	122.75	9.32
ALA	185	125.79	7.78
PHE	186	115.46	7.40
ASN	187	117.77	7.80
ARG	188	121.59	8.57
PHE	189	119.42	8.08
GLY	190	102.94	7.60
ASP	191	121.83	7.69
LEU	192	120.91	8.16
LEU	193	119.23	8.05
GLU	194	115.50	7.56
ARG	195	117.99	7.60
THR	196	110.95	8.70
PHE	197	120.06	7.70
ALA	198	129.33	6.99

Table S-2-2. ortho-^{19}F labeled *pa*-HO-CN 2D ^{1}H-^{15}N HSQC NMR assignments, chemical shifts are given in ppm.

Residue	No.	15N	1H
MET	1		
ASP	2		
THR	3		
LEU	4		
ALA	5		
PRO	6		
GLU	7		
SER	8		
THR	9		
ARG	10		
GLN	11	8.17	120.98
ASN	12	8.31	118.95
LEU	13	7.91	121.25
ARG	14	8.81	128.26
SER	15	11.54	117.72
GLN	16	6.67	121.82
ARG	17	8.19	121.88
LEU	18	8.86	118.74
ASN	19	8.04	120.98
LEU	20	8.05	120.13
LEU	21	8.32	119.31
THR	22	8.13	107.11
ASN	23	8.19	124.17
GLU	24	9.80	119.75
PRO	25		
HIS	26	10.31	119.51
GLN	27	10.51	121.99
ARG	28	8.73	120.91
LEU	29	8.58	122.99
GLU	30		
SER	31	7.03	112.70
LEU	32	7.45	124.50
VAL	33	7.74	118.92
LYS	34	7.04	116.47
SER	35	7.50	114.97
LYS	36	6.92	119.30
GLU	37	7.35	110.88
PRO	38		
PHE	39	7.80	108.43
ALA	40	7.72	120.75

SER	41	7.41	104.81
ARG	42		
ASP	43	8.22	118.07
ASN	44	7.95	120.68
PHE	45	8.63	123.93
ALA	46	8.92	121.57
ARG	47	6.99	116.69
PHE	48	7.40	122.94
VAL	49	8.84	121.55
ALA	50	8.40	122.07
ALA	51	6.97	120.99
GLN	52	7.83	116.58
TYR	53	9.43	118.95
LEU	54	8.30	120.28
PHE	55	8.46	121.79
GLN	56	8.52	115.46
HIS	57	9.21	122.14
ASP	58	7.81	122.34
LEU	59	6.75	113.79
GLU	60	7.45	124.50
PRO	61		
LEU	62	7.58	116.31
TYR	63	7.76	115.01
ARG	64	7.30	111.84
ASN	65	7.22	122.89
GLU	66	9.10	128.37
ALA	67	7.91	122.41
LEU	68	8.39	119.14
ALA	69	8.36	122.10
ARG	70	7.29	115.04
LEU	71	7.03	118.05
PHE	72	7.93	115.62
PRO	73		
GLY	74	8.97	115.70
LEU	75	7.98	123.12
ALA	76	8.84	117.70
SER	77	7.91	111.65
ARG	78	8.18	120.01
ALA	79	6.75	123.08
LEU	80	7.81	117.53
ASP	81	8.92	120.75
ASP	82	8.21	119.83
ALA	83	8.16	123.79
ALA	84	8.18	117.22
ARG	85	8.42	118.41
ALA	86	8.02	123.37
ASP	87	8.36	122.10

LEU	88	7.78	118.72
ALA	89	7.57	120.99
ASP	90	8.55	121.99
LEU	91	7.58	116.12
GLY	92	8.05	109.35
HIS	93	8.27	122.97
PRO	94		
VAL	95	8.86	124.13
PRO	96		
GLU	97	8.43	120.01
GLY	98	8.44	110.99
ASP	99	8.68	119.92
GLN	100	8.75	118.07
SER	101	8.82	117.12
VAL	102	8.27	122.97
ARG	103	8.36	122.10
GLU	104	7.77	114.66
ALA	105	7.19	122.85
ASP	106	8.37	120.79
LEU	107	7.73	121.61
SER	108	8.45	118.99
LEU	109	8.54	123.32
ALA	110	8.31	117.06
GLU	111	7.44	115.59
ALA	112	8.64	121.08
LEU	113	8.11	115.86
GLY	114	7.65	104.57
TRP	115	7.57	121.83
LEU	116	8.52	117.48
PHE	117	8.54	119.58
VAL	118	7.13	118.07
SER	119	8.01	112.09
GLU	120	9.02	117.25
GLY	121	7.59	111.93
SER	122	6.37	114.23
LYS	123		
LEU	124		
GLY	125		
ALA	126		
ALA	127		
PHE	128	8.19	117.74
LEU	129	8.82	120.51
PHE	130	10.03	119.84
LYS	131	7.40	116.77
LYS	132	7.43	119.40
ALA	133	7.95	121.87
ALA	134	7.35	120.69

ALA	135	7.50	121.12
LEU	136	7.42	117.63
GLU	137	8.15	115.25
LEU	138	6.83	116.53
ASP	139	9.26	121.12
GLU	140	10.54	116.92
ASN	141	8.85	116.84
PHE	142	7.85	121.87
GLY	143	10.03	119.84
ALA	144	7.46	119.09
ARG	145	11.58	126.14
HIS	146	11.38	116.90
LEU	147	7.66	120.45
ALA	148	7.55	123.05
GLU	149	8.41	122.66
PRO	150		
GLU	151		
GLY	152	9.14	113.99
GLY	153	8.13	107.95
ARG	154	9.45	125.05
ALA	155	8.66	122.54
GLN	156	8.98	118.97
GLY	157	7.72	107.01
TRP	158	7.63	125.33
LYS	159	8.31	118.17
SER	160	8.11	112.70
PHE	161	7.17	123.79
VAL	162	8.33	117.53
ALA	163	7.63	120.28
ILE	164	6.77	116.71
LEU	165	7.95	121.35
ASP	166	8.68	116.75
GLY	167	7.44	106.31
ILE	168	6.85	121.21
GLU	169	8.71	129.63
LEU	170	7.91	124.83
ASN	171	9.48	121.34
GLU	172	8.45	116.95
GLU	173	8.09	121.07
GLU	174	8.60	120.50
GLU	175	8.66	119.63
ARG	176	7.46	119.09
LEU	177	8.07	122.61
ALA	178	8.25	123.98
ALA	179	7.25	118.57
LYS	180	8.16	121.63
GLY	181	8.85	106.63

ALA	182	7.57	121.14
SER	183	7.86	112.54
ASP	184	9.29	122.40
ALA	185	7.67	125.46
PHE	186	7.44	115.59
ASN	187	7.79	117.06
ARG	188	8.58	121.70
PHE	189	7.94	118.74
GLY	190	7.48	102.37
ASP	191	7.57	121.83
LEU	192	8.12	120.85
LEU	193	7.94	118.74
GLU	194	7.51	115.21
ARG	195	7.53	117.79
THR	196	8.62	110.60
PHE	197	7.70	120.17
ALA	198	7.03	129.36

Table S-2-3. ortho-^{19}F labeled F45L *pa*-HO-CN 2D ^{1}H-^{15}N HSQC NMR assignments, chemical shifts are given in ppm.

Residue	No.	15N	1H
MET	1		
ASP	2		
THR	3		
LEU	4		
ALA	5		
PRO	6		
GLU	7		
SER	8		
THR	9		
ARG	10		
GLN	11		
ASN	12		
LEU	13	121.24	7.90
ARG	14	128.20	8.81
SER	15	117.70	11.53
GLN	16	121.76	6.65
ARG	17	121.68	8.16
LEU	18	118.70	8.85
ASN	19		
LEU	20	120.06	8.03

LEU	21		
THR	22	107.06	8.11
ASN	23	124.13	8.18
GLU	24	119.77	9.80
PRO	25		
HIS	26	119.85	10.37
GLN	27	122.39	10.64
ARG	28	121.02	8.86
LEU	29		
GLU	30		
SER	31		
LEU	32		
VAL	33		
LYS	34	116.81	7.17
SER	35	114.69	7.48
LYS	36	119.38	6.94
GLU	37	111.21	7.32
PRO	38		
PHE	39		
ALA	40	120.92	7.83
SER	41	105.31	7.36
ARG	42	118.09	8.23
ASP	43		
ASN	44		
PHE	45		
ALA	46	121.20	8.59
ARG	47		
PHE	48	122.96	7.54
VAL	49		
ALA	50	121.90	8.47
ALA	51	120.83	6.94
GLN	52	116.52	7.82
TYR	53	119.17	9.35
LEU	54	120.65	8.33
PHE	55	122.85	8.55
GLN	56		
HIS	57		
ASP	58	122.09	7.83
LEU	59	114.00	6.78
GLU	60	124.24	7.42
PRO	61		
LEU	62	116.34	7.60
TYR	63	114.88	7.73
ARG	64	112.08	7.27
ASN	65	122.81	7.22
GLU	66	128.44	9.10
ALA	67	122.32	7.91

LEU	68	118.99	8.42
ALA	69	122.27	8.36
ARG	70	115.05	7.30
LEU	71	118.08	7.04
PHE	72	115.51	7.92
PRO	73		
GLY	74	115.28	8.95
LEU	75	123.17	7.99
ALA	76	117.80	8.81
SER	77	111.85	7.92
ARG	78	119.89	8.18
ALA	79	122.79	6.79
LEU	80	117.88	7.84
ASP	81		
ASP	82	119.89	8.34
ALA	83	123.67	8.19
ALA	84	117.57	8.12
ARG	85		
ALA	86	123.17	7.99
ASP	87	122.54	8.39
LEU	88	119.12	7.88
ALA	89	120.42	7.45
ASP	90		
LEU	91	116.34	7.60
GLY	92	108.89	7.99
HIS	93	122.67	8.23
PRO	94		
VAL	95	123.81	8.86
PRO	96		
GLU	97	119.91	8.42
GLY	98	110.92	8.43
ASP	99	119.99	8.64
GLN	100		
SER	101	117.08	8.78
VAL	102	122.85	8.27
ARG	103	121.71	8.29
GLU	104	114.98	7.79
ALA	105	122.81	7.22
ASP	106	120.79	8.36
LEU	107	121.82	7.73
SER	108	118.99	8.42
LEU	109	123.41	8.55
ALA	110	117.13	8.33
GLU	111	115.49	7.46
ALA	112	121.21	8.64
LEU	113	116.03	8.11
GLY	114	104.65	7.65

TRP	115	121.80	7.63
LEU	116	117.73	8.56
PHE	117	119.60	8.50
VAL	118	118.03	7.14
SER	119		
GLU	120	117.45	9.02
GLY	121		
SER	122		
LYS	123		
LEU	124		
GLY	125		
ALA	126		
ALA	127		
PHE	128		
LEU	129	120.47	8.60
PHE	130		
LYS	131		
LYS	132		
ALA	133		
ALA	134		
ALA	135		
LEU	136		
GLU	137		
LEU	138		
ASP	139		
GLU	140		
ASN	141	116.51	8.85
PHE	142	123.07	7.94
GLY	143		
ALA	144		
ARG	145		
HIS	146		
LEU	147		
ALA	148		
GLU	149		
PRO	150		
GLU	151		
GLY	152	113.81	9.11
GLY	153	108.07	8.16
ARG	154	125.32	9.47
ALA	155	122.74	8.70
GLN	156		
GLY	157	107.75	7.75
TRP	158		
LYS	159	118.09	8.30
SER	160	112.90	8.14
PHE	161	123.94	7.22

VAL	162	117.54	8.31
ALA	163	120.23	7.59
ILE	164	116.90	6.82
LEU	165	121.39	7.96
ASP	166	116.82	8.67
GLY	167	106.37	7.45
ILE	168	121.18	6.85
GLU	169	129.55	8.70
LEU	170	124.81	7.91
ASN	171	121.33	9.47
GLU	172	116.98	8.46
GLU	173	121.09	8.09
GLU	174	120.47	8.60
GLU	175	119.63	8.66
ARG	176	119.09	7.47
LEU	177	122.64	8.07
ALA	178	124.01	8.27
ALA	179	118.68	7.28
LYS	180	121.68	8.16
GLY	181	106.70	8.86
ALA	182	121.29	7.62
SER	183	112.80	7.91
ASP	184	122.56	9.31
ALA	185	125.54	7.71
PHE	186	115.49	7.46
ASN	187	117.88	7.84
ARG	188	121.72	8.58
PHE	189	118.92	7.98
GLY	190	102.62	7.57
ASP	191	121.80	7.63
LEU	192	120.95	8.15
LEU	193		
GLU	194		
ARG	195	117.61	7.60
THR	196	110.64	8.61
PHE	197		
ALA	198	129.40	7.12

CHAPTER III: CHARACTERIZATION OF *PSEUDOMONAS AERUGIONSA* FPR: FERREDOXIN NADP$^+$ REDUCTASE: A KEY PROTEIN INVOLVED IN HEME-IRON ACQUISITION

INTRODUCTION

As discussed in previous chapters, the identification and characterization of redox partners that deliver electrons to HO, as well as the characterization of protein-protein interactions that facilitate the electron flow from NAD(P)H to HO are important steps toward a molecular-level understanding of heme metabolism. Thorough study of the novel protein ferredoxin-NADPH redutase from *Pseudomonas aeruginosa* (*pa*-FPR) in the proposed iron acquisition pathway (Figure 1-2 in Chapter I) is very important and has been carried out in our lab. The interesting findings will be shown both in this and the next chapters.

Pa-FPR belongs to the flavoprotein family, one of the most abundant protein families. In human there are 361 flavoproteins; in *E. Coli* there are 205 flavoproteins [*1*]. In *Pseudomonas aeruginosa* genome PA01 (http://www.pseudomonas.com), there are 79 hits of flavoproteins. It is well known that flavoprotein has enormous metabolic versatility, and most of flavoproteins function as electron transfer redox proteins in mammal, bacteria, plant, etc many organisms [*1-4*]. One unique example of flavoprotein's versatility in nature is shown by a novel kind of cytochrome P450 reductase found in *Ralstonia, Burkholderia and Rhodococcus* bacteria. This

flavoprotein has three components: 2Fe-2S ferredoxin domain, FMN-dependent NADP(H) reductase domain and cytochrome P450 domain[*1*]. Nature fused the three different proteins into one to conduct the same catalysis function done by the three individual proteins all together.

Ferredoxin(flavodoxin)–NAD(P)H reductase (FNR) is one of the most important and well-studied flavoproteins [*2, 3, 5*]. In plastids, mitochondira, bacteria and parasite, it transfers electrons either from NAD(P)H to its redox partner protein ferredoxin/flavodoxin or from redox partner protein to $NAD(P)^+$ [*5-17*]. When FNR receives electron from reduced partner protein and transfers hydride to $NADP^+$, this reaction is so called the photosynthetic path, a reversible process shown below in Equation 3-1 [*2, 3*]. And in the nonphotosynthetic path, it receives two electrons and a proton or a hydride (H:) from NADPH and delivers electrons to the oxidized partner protein, shown in Equation 3-2 [*2, 3*]. As will be mentioned in this study, the Maize, Pea, Spinach leaves and *Anabaena* FNRs are following the photosynthetic pathway, while *E. coli* and *Azotobacter vinelandii* FNR, same as our *pa*-FPR are following the nonphotosynthetic pathway.

$$2Fd(Fe^{II})/2Fld(FMNH\cdot) + NADP^+ + H^+ \leftrightarrow 2Fd(Fe^{III})/2Fld(FMN) + NADPH \qquad (3\text{-}1)$$

$$NADPH + H^+ + FNRox \leftrightarrow NADP^+ + FNRH_2,$$

$$FNRH_2 + n\ Protein_{ox} \rightarrow FNRox + n\ Protein_{red} \qquad n = 1 \text{ or } 2 \qquad (3\text{-}2)$$

These reactions are by no means limited to protein redox partner, and FNR can readily react with many molecules, e.g. ferredoxin, flavodoxin, ferricynaide, heme, phenol for different purposes *in vivo* [*5*]. Interestingly enough, there is very high similarity between NAD(P)H and $NAD(P)^+$ binding domains in many examples [*5, 14, 18-22*]. And from the phylogenetic study done by E. Ceccarelli and coworkers, they found that the photosynthetic and nonphotosynthetic FNR groups share the same ancestor; the functional difference is most likely the evolution result of different metabolic pressure [*2*].

Structural characterization of FNR proteins is done mainly by crystallography. FNR structure is highly conserved. The protein is composed of two binding domains, the N-terminal beta barrel which binds FAD, connected by one alpha helix with C-terminal alpha-beta sandwich adopting altered Rossmann fold (composed of six parallel β-strands intervened with α-helices, one half β1α1β2α2β3 binds cofactor as the N-terminal domain, the other half β4α4β5α5β6 binds the NADH as the C-terminal domain, connected by α3 in dehydrogenase [*23*]) to bind NAD(P)H[*24*]. And the FAD and NAD(P)H are placed in close proximity to each other in space, the common protein binding site is the concave region of FAD binding domain. The FAD cofactor adopts bend (in *Azotobacter vinelandii* FNR, pdb:1A8P [*25*]) or extended form (in Spinach FNR, pdb: 1FDR [*6*] and NADPH-P450 reductase, pdb: 1AMO [*26*]). Either in bend or extended form, the isoalloxazine ring of FAD is inserted into the protein, while the $NAD(P)^+$ binding site varies in different proteins [*24*]. FNR proteins have characteristic conserved sequence motifs which are different from other flavoproteins,

like, glutathione reductase (GR), pyruvate oxidase (PO) etc; the sequence motifs are RxYS(T) (the Arg binds FAD's negative pyrophosphate oxygen atom: Op_1 or Op_2, and the Tyr H-bonds to ribityl 4' hydroxyl O_4 and forms extensive van der Waals interaction with FAD), GxxS(T)xxL$(x)_5$G$(x)_7$PxG (well known phosphate binding motif, Ser or Thr is able to H-bond to Op_2 or Op_1 in FAD), and MxxxGT(S)G(A)IxP (the βαβ motif binds $NAD(P)^+$) [*24*].

The spinach FNR is the first crystallized FNR protein by Shin *et al*. in 1963 [*27*]. Its high resolution crystal structure was solved by Karplus and coworkers in 1991 [*18*]. Nowadays spinach FNR is commercially available from Sigma-Aldrich. In its structure, FAD's isoalloxazine ring is stacked in between Tyr96 on si- face and Tyr314 on re- face. Tyr314 is close to the NADPH binding site. This Tyr at C-terminal as a key structural feature is conserved in many FNRs. Its unique location has been studied intensively and will be described later in this and the next chapter. Since 1991, many other FNR protein structures have been solved under different conditions, e.g. containing oxidized FAD, containing reduced $FADH_2$, NAD(P)H or $NAD(P)^+$ bound, NAD(P)H analog bound forms [*6, 18, 28-31*]. Also, the detailed studies of NAD(P)H binding, structure-catalysis relationship and electron transfer have been carried out with the aid of site-directed mutagenesis, X-ray diffraction, NMR protein titration and protein-protein interaction techniques.

By searching *Pseuodomonas areuginosa* genome PA01, it is found that there are two plant-type FNRs (bacterial subclass I and II) and a mitochondrial-type FNR which is very unique comparing to most organism only having one FNR form [*2*].

Unfortunately, there is no study to differentiate the functions of these three FNRs yet. Our interested protein *pa*-FPR(PA3397, gene *fpr*) is the bacterial subclass I FNR[*2*]. It has two most similar (>30%) homolog proteins: *Av*-FPR(98%) and *Ec*-FldR(35%) with crystal structure available. The other FNRs with crystal structure available have less than 20% similarity, e.g. *Anabaena* FNR (17%) and *spinach* FNR (11%).

Under the context of the redox partner proteins study in search for iron acquisition pathway of pathogenic bacterium *Pseudomonas aeruginosa* under iron-starvation condition, the key protein *pa*-FPR is crucial in mediating electron transfer in the process of heme degradation and iron release. The structural and biochemical studies of *pa*-FPR described below have proved the previous finding about FPR being a 98% sequence identical homolog protein as *Av*-FPR. From the crystal structure of *pa*-FPR, indeed it is highly similar to *Av*-FPR in which both have the unique Ala instead of the "common" Tyr at the end of C-terminus. In general, ferredoxin (Fd) or/and flavodoxin (Fld) is considered to be the physiological redox partner(s) of the FNR , like in the case of *Anabaena*, Pea, Spinach FNR and *Av*-FPR proteins.

Therefore, our initial proposed electron transfer path from NADPH to ferredoxin to ferrdoxin reductase and at last to heme oxygenase is a conventional opinion. Interestingly, *pa*-FPR is able to transfer electrons to not only its proposed physiological partner protein: *pa*-Bfd (ferredoxin protein in *Pseudomonas aerguniosa*) but also proteins like *pa*-HO and *pa*-Bfr (bacteria ferritin in *Pseudomonas aerguniosa*). Surprisingly, studies done by Yuhong Zeng and Saroja Weerutunga reveal that in the NADPH initiated protein reduction assays, *pa*-FPR as

the redox partner can donate all seven electrons to *pa*-HO and reduce it in a much faster rate than *pa*-Bfd. This novel redox partnership between *pa*-Fpr and *pa*-HO has never been found before. Also, the versatile redox partnership between *pa*-FPR and other proteins in the heme-iron acquisition pathway in *Pseudomonas aerguniosa* indicates that *pa*-FPR is a key protein with profound physiological functions.

EXPERIMENTAL SECTION

i. Cloning and expression of pa-FPR

The genes encoding for *pa*-FPR (PA3397) was synthesized and subcloned into the pET11a vector, GeneScript Corporation (Piscataway, NJ). The genes were engineered with silent mutations introducing codons favored by *E. coli* [*32*] and with *Nde* I and a *Bam*H I restriction enzyme sites at 5' and 3' ends, respectively, for subcloning into the pET11a vector. The above work is accomplished by previous lab member Bailey Morgan (Figures S1/S2). The pET11a vector harboring the *fpr* gene was transformed into *E. coli* ArcticExpress^{TM} RIL Competent Cells (Stratagene), in order to overcome protein misfolding and insolubility issues observed with BL21 Gold (DE3) cells. To express *pa*-FPR a single colony of ArcticExpress^{TM} RIL cells was introduced into 10 mL of an LB medium containing ampicillin as above and cultured at 37 °C and 220 rpm overnight. The cell suspension was transferred into a 1 L LB-ampicillin medium and further cultured at 37 °C (4-5 hrs) to an OD of approximately 0.7. At this point the cells were transferred to another shaker incubator (Barnstead) pre-equilibrated at 10 °C and cultured for an additional 30 min.

Protein expression was then induced by addition of IPTG to a final concentration of 0.3 mM and the cells were subsequently cultured for approximately 14 hrs before they were harvested by centrifugation (4000 rpm for 10 min) and stored at – 20 °C.

ii. Purification of pa-FPR

Cells were resuspended in 3 mL lysis buffer, stirred for 20 min at 4 °C, incubated at 37 °C for 20 min, stirred at ambient temperature for one hour and then sonicated at 4 °C. The lysed cells were centrifuged at 35,000 rpm for 2 hrs to sediment cell debris and the supernatant dialyzed against 4 L of 20 mM Tris-HCl (pH 7.5, 4 °C) with at least three buffer changes over a period of approximately 16 hrs. The resultant solution was applied to a Q-Sepharose Fast Flow column (10 cm × 2.5 cm i.d.) previously equilibrated with 20 mM Tris-HCl (pH 7.5, 4 °C). The column was washed with 3 volumes of 20 mM Tris-HCl (pH 7.5) containing 50 mM NaCl and the protein eluted in the same buffer with a linear gradient (50 mM to 500 mM) of NaCl. Fractions containing FPR (yellow) were pooled, concentrated and then loaded onto a Sephadex-G50 column (3.0 cm x 100 cm) pre-equilibrated and eluted with phosphate buffer (μ = 0.1, pH 7.0) at 4 °C. Fractions with absorbance ratio A_{280}/A_{450} less than 8 were pooled and *pa*-FPR was determined to be homogeneous by SDS-PAGE and mass spectrometry. To improve stability during storage (-80 °C) the solutions were made either 0.3 M in NaCl or 10% in glycerol before they were frozen and stored.

iii. Protein Extinction Coefficient Measurement

The extinction coefficient of the flavin in *pa*-FPR was determined spectrophotometrically using a previously established protocol [*33*]. Flavin in the protein was first released and quantified by the trichloroacetic acid method. Then the extinction coefficient of the flavoprotein is calculated to be 11.5±0.1 $mM^{-1} \cdot cm^{-1}$ by using the following relationship:

$\varepsilon_{unknown} = \varepsilon_{FAD} * (Abs_{450nm}Flavoprotein / Abs_{450nm}FreeFAD)$,

and $\varepsilon_{FAD} = 11.3\ mM^{-1} \cdot cm^{-1}$. [*33*]

iv. Characterization of pa-FPR FAD/FMN cofactor

The flavin cofactor was released from *pa*-FPR by addition of trichloroacetic acid, as has been described earlier [*34*]. Denatured protein was removed by centrifugation and the yellow supernatant was analyzed by mass spectrometry (MS/MS), which was performed using a Q-Tof-2 hybrid mass spectrometer (Micromass, Manchester, UK) housed in the Protein Mass Spectrometry Laboratory at the University of Kansas. The instrument was operated for maximum sensitivity with all lenses optimized while infusing a sample of lysozyme. The cone voltage was 45eV and Ar was admitted to the collision cell. Spectra were acquired at 11,364 Hz pusher frequency, covering a mass range 800 to 3000 amu and accumulating data for 5 seconds per cycle. Time to mass calibration was made with CsI cluster ions analyzed under the same conditions. Samples (500 μg) were desalted on a short column (3 cm x 1 mm ID) of polymeric HPLC resin (Hamilton PRP1, Reno Nevada)

by loading the protein dissolved in a solution of 1% HOAc and eluting the column directly into the source at 25 μL/min with 95% MeOH, 0.08% formic acid.

v. Protein Substrate NADPH/NADH Determination

Pa-FPR is a ferredoxin-NAD(P)$^+$ reductase protein. The protein binds either NADP+ or NAD+ specifically. Parallel Fpr-NADH and NADPH reduction experiments were taken place under the same conditions in aerobic and anaerobic environments. The experiments were conducted in 800ul 50mM Na_2Pi (pH 7.0) containing 70 μM *pa*-FPR (UV-vis absorbance is 0.8 at 450nm). The reactions were initiated by the addition of 2 equivalents amount of NADPH or NADH. The NADH and NADPH concentrations were determined by UV-vis using the same extinction coefficient of 6.22$mM^{-1}\cdot cm^{-1}$ [*35*] at 340nm after making fresh solutions in 50 mM Na_2Pi (pH 7.0) either inside glove box (coy) or at aerobic condition. The reactions were monitored using UV-Vis S2000 spectrophotometer (Ocean Optics, Dunedin, FL).

vi. X-ray crystallography

Crystal growing conditions were identified in the High Throughput Screening Laboratory of the Hauptman Woodward Medical Research Institute, Buffalo, New York [*36*]. X-ray-quality single crystals of *pa*-FPR were grown using the hanging drop vapor diffusion method by mixing 2 μL of *pa*-FPR (18 mg/mL) dissolved in 20 mM Tris, pH 7.6 with 2 μL of a solution consisting of 125 mM sodium cacodylate, 200 mM ammonium sulfate and 20% (w/v) PEG- 8000 acetate, pH 6.5. Diffraction

data were recorded at –180 °C using the rotation method on a single flash-frozen crystal [Detector: R-axis IV^{++} image plate; X-rays: CuKα, focused by mirror optics; Generator: Rigaku RU300 (MSC, The Woodlands, TX, USA)]. The cryoprotectant was 20 % ethylene glycol. X-ray data were reduced with XDS [*37*]; the program package CNS [*38*] was employed for phasing and refinement; model building was performed with *O [39]*. The structure was solved by molecular replacement using the coordinates of ferredoxin oxidoreductase from *Azotobacter vinelandii* (PDB entry 1A8P) as search model, stripped of solvent molecules and ligands. Refinement was performed using data to the highest resolution with no sigma cut-off applied. Several rounds of minimization, simulated annealing (2500 K starting temperature) and restrained individual B-factor refinement were implemented. Data collection and refinement statistics are summarized in Table 3-1.

Table 3-1. Summary of data collection and structure refinement[a].

Data set	FPr liganded with FAD
Space group	$P2_12_12$
Unit cell dimensions (Å)	a=68.7 b=74.9 c=52.8 α=β=γ=90º
Protein atoms	2071 [average B-factor = 11.6 Å^2]
Ligand	FAD (53 atoms) [average B-factor = 8.1 Å^2]
Solvent molecules	385 [average B-factor = 25.2 Å^2]
rmsd[b] bonds (Å)	0.01
rmsd[b] angles (°)	1.54
Resolution range	15-1.55 (1.6-1.55)
Unique reflections	40,269 (3,620)

Completeness (%)	98.9 (95.6)
I/σI	26.4 (9.9)
R_{merge} (%)	3.6 (9.9)
R_{cryst} [c] (%)	15.8
R_{free} [d] (%)	19.0

[a] Values in parentheses refer to the highest-resolution shell.
[b] Rootmean-square deviation from ideal values.
[c] *R*cryst) 100 * ∑|*F*obs - *F*model|/∑*F*obs, where *F*obs and *F*model are observed and calculated structure factor amplitudes, respectively.
[d] *R*free is the *R*cryst calculated for randomly chosen unique reflections, which were excluded from the refinement (1234 for FPR liganded with FAD).

vii. Electronic absorption spectrophotometry

NADPH-*cytochrome C reduction* activity is commonly used to study the activity of the ferredoxin reductase in complex with ferredoxin [*40-44*]. In order to study the electron transfer from *pa*-FPR to ferredoxin, a modified activity assay [*43*] was used for *pa*-FPR in complex with spinach ferredoxin (Sigma-Aldrich, St. Louis, MO) in the presence of cytochrome C (Sigma-Aldrich, St. Louis, MO). The reactions were performed in the anaerobic condition inside a glove box (Coy) and monitored by Ocean Optics 2000 spectrophotometers (Dunedin, FLA) equipped with fiber optics. The 1 cm cuvette was filled with 2 mL (final volume) of 20 mM Tris-HCl Buffer (pH7.5), followed by the addition of 3.5 μM *pa*-FPR (100μl *pa*-FPR stock solution giving 0.04 absorbance at 450nm), 12.5 μM cytochrome c (50 ul 0.5mM stock, protein purified by Gel-50 size exclusion chromatography column), 2.5 μM spinach ferredoxin (5ul of 1mM stock solution); then the reaction is initiated by the addition of 200 μM NADPH and the increase in absorbance at 550 nm was monitored.

Catalase (0.1 mg/mL final concentration) was used as a H_2O_2 scavenger. The reaction is under constant stirring condition with speed 4 using Corning^{TM} stirring plate. The similar reaction of *pa*-FPR complex with spinach ferredoxin was repeated in air under the following conditions: 7.5 μM cytochrome c, 3.5 μM *pa*-Fpr, 2.5 μM spinach ferredoxin, then add 0.2 mM NADPH to initial reaction in 2 mL 20mM Tris-HCl Buffer (pH 7.6).

The following electron transfer reactions done by electron transfer reactions from NADPH to *pa*-HO using different redox protein mediators were carried out with *pa*-Bfd, *pa*-FPR, spinach ferredoxin and spinach ferredoxin reductase (Sigma-Aldrich, St. Louis, MO), using a previously reported method with modifications [*45*]. The reactions are done by Yuhong Zeng and Saroja Weerutunga in our lab. The reactions were taken place either in a glove box (Coy) under O_2-free conditions or in air, in a 1 cm path-length cuvette, and monitored by electronic absorption spectroscopy using diode array Ocean Optics 2000 spectrophotometers (Dunedin, FLA) equipped with fiber optics. For each reaction the cuvette was filled with 2 mL of 25 mM HEPES-KOH (pH7.5), followed by the addition of a few μL of stock solutions of the enzymes and proteins to be tested. In typical experiments the final concentration of resting state *pa*-HO was 10 μM and the concentrations of *pa*-Bfd, *pa*-FPR, spinach ferredoxin and spinach ferredoxin reductase were 10 μM, 8 μM, 5 μM and 0.05 U/mL, respectively. Catalase (0.1 mg/mL final concentration) was used as a H_2O_2 scavenger. The electron transfer reactions were initiated by the addition of a stock solution of NADPH to give a final concentration of 200 μM. The expression

system for *pa*-HO [*46*] was a gift from Dr. Angela Wilks (the University of Maryland) and the protocols for expression and purification of this enzyme have been reported previously [*47*].

RESULTS AND DISCUSSION

1. Expression and purification of pa-FPR

Protein is expressed from DNA listed below, initially by previous lab member Bailey Morgan in an LB medium [*48*].

5' ***Nde* I**

GGGCATATG AGC AAC CTG TAT ACC GAA CGT GTG CTG AGC GTG CAT CAT TGG AAC GAT ACC

M S N L Y T E R V L S V H H W N D T

CTG TTT AGC TTT AAA ACC ACC CGT AAC CCG GGC CTG CGT TTT AAA ACC GGC CAG TTT GTG

L F S F K T T R N P G L R F K T G Q F V

ATG ATT GGC CTG GAA GTG GAT GGC CGT CCG CTG ATG CGT GCG TAT AGC ATT GCG AGC CCG

M I G L E V D G R P L M R A Y S I A S P

AAC TAT GAA GAA CAT CTG GAA TTT TTT AGC ATT AAA GTG CCG GAT GGC CCG CTG ACC TCT

N Y E E H L E F F S I K V P D G P L T S

CGT CTG CAG CAT CTG AAA GAA GGC GAT GAA CTG ATG GTG AGC CGT AAA CCG ACC GGC ACC

R L Q H L K E G D E L M V S R K P T G T

CTG GTG CAT GAT GAT CTG CTG CCG GGC AAA CAT CTG TAT CTG CTG AGC ACC GGC ACC GGC

L V H D D L L P G K H L Y L L S T G T G

ATG GCG CCG TTT CTG AGC GTG ATT CAG GAC CCG GAA ACC TAT GAA CGT TAT GAA AAA GTG

M A P F L S V I Q D P E T Y E R Y E K V

ATT CTG GTG CAT GGC GTG CGT TGG GTG AGC GAA CTG GCG TAT GCG GAT TTT ATT ACC AAA

I L V H G V R W V S E L A Y A D F I T K

GTG CTG CCG GAA CAT GAA TAT TTT GGC GAT CAG GTG AAA GAA AAA CTG ATT TAT TAT CCG

V L P E H E Y F G D Q V K E K L I Y Y P

CTG GTG ACC CGT GAA CCG TTT CGT AAC CAG GGC CGT CAG ACC GAT CTG ATG CGT AGC GGC

L V T R E P F R N Q G R Q T D L M R S G

AAA CTG TTT GAA GAT ATT GGC CTG CCG CCG ATG AAC CCG CAG GAT GAT CGT GCG ATG ATT

K L F E D I G L P P M N P Q D D R A M I

TGC GGC AGC CCG AGC ATG CTG GAA GAA ACC AGC GCG GTG CTG GAT AGC TTT GGC CTG AAA

C G S P S M L E E T S A V L D S F G L K

ATT AGC CCG CGT ATG GGC GAA CCG GGC GAT TAT CTG ATT GAA CGT GCG TTT GTG GAA AAA

I S P R M G E P G D Y L I E R A F V E K

***BamH* I** **3'**

TAA GGATCCGGG

Figure 3-1. DNA sequence of *fpr* (PA3997) from *P. aeruginosa* (PA01 genome) and the corresponding amino acid sequence. A *Nde* I and a *Bam*H I restriction endonuclease sites were constructed at the 5' and 3' ends for subcloning.

The *pa*-FPR enzyme was purified to homogeneity, as judged by the presence of a single band in SDS-PAGE gels (Figure 3-2).

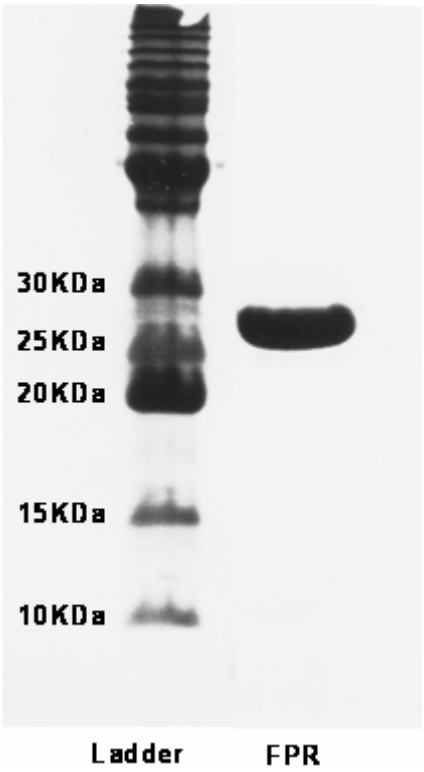

Figure 3-2. SDS PAGE obtained from homogeneous solutions of *pa*-FPR.

Pa-FPR's theoretical pI is 5.65 (calculated via pI tool from http://ca.expasy.org/tools/pi_tool.html), and protein is purified and stable around neutral pH. The protein is prone to precipitate under high protein concentration (> 1.5 mM). As for short term storage (less than a week), low temperature (0~4 °C) and high ionic strength (50 mM Na_2Pi pH7) will help preventing it from denaturation,

aggregation and precipitation. As for long-term storage, the protein coming out of -20 °C or -80 °C freezer will form large percent (30~50%) of precipitation during thawing on ice. Shaking and thawing under higher temperature (37 °C) will slightly decrease the amount of precipitated protein. From SDS-PAGE and UV-vis absorption studies, *pa*-FPR loses activity and partially dimerizes during precipitation process. It is critical to search for the optimal storage conditions for FPR. The similar phenomenon is discovered for *Av*-FNR by Burgess group [*49*]. They use 0.3 M NaCl to stabilize *Av*-FNR at low temperatures for the long-term storage [*49*]. It is proved to work for our low temperature storage as well. Also, some additives like 10-15% glycerol or 50 mM L-Arg [*50*] also stabilize the protein as 0.3 M NaCl.

2. Identification of co-expressed substrate FAD/FMN in pa-FPR

The molecular weight of *pa*-FPR measured by ESI-MS is 29,386 Da, a value that is in good agreement with the molecular weight of the enzyme calculated from the sequence, not including the initiator methionine (29,387). Solutions containing *pa*-FPR are yellow, which is consistent with the presence of a flavoprotein. Indeed, the electronic absorption spectrum of oxidized *pa*-FPR (Figure 3-3(A)) is typical of flavin containing proteins, with bands at 370 nm, 450 nm and 475 nm; these bands lose their intensity and almost disappear when a solution of NADPH is added to a solution of *pa*-FPR under anerobic conditions, a spectroscopic property typically observed upon reduction of flavin containing proteins [*33*].

The nature of the cofactor in *pa*-FPR (FAD or FMN) was determined to be FAD using mass spectrometry by previous lab member Bailey Morgan [*51*],

following its extraction from the enzyme into an aqueous solution. The mass spectrum of the *pa*-FPR cofactor (Figure 3-3(B)) exhibits a parent ion peak (X_0) at *m/z* = 788.41 Da, which corresponds to the calculated mass of FAD + $3H^+$. Fragmentation of this peak in an MS/MS experiment renders peaks at m/z 439.12, 348.10 and 136.07. The peak at *m/z* = 439.12 (X_1) corresponds to the FMN + $2H^+$ fragment, the peak at *m/z* = 348.10 (X_2) corresponds to the AMP + H^+ fragment and the peak at 136.07 *m/z* (X_3) corresponds to the adenine fragment + 2 H^+. This fragmentation pattern together with the fact that the mass spectrum of an FAD standard is identical to that of Figure 3-4(B) indicates that the cofactor in *pa*-FPR is FAD. The nature of the electron donor to FAD, NADH, or NADPH, was addressed next.

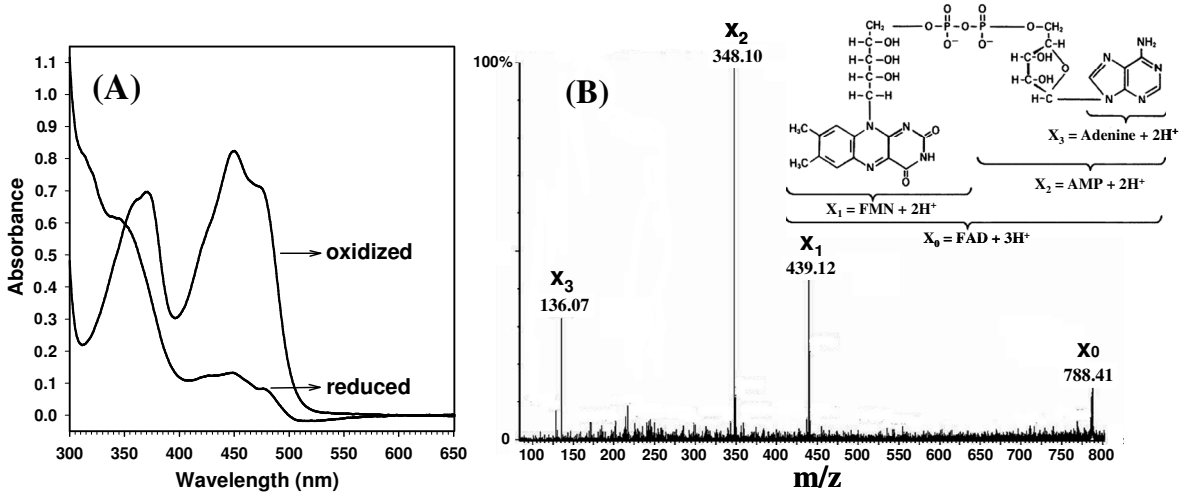

Figure 3-3. (A) Electronic absorption spectra of *pa*-FPR in oxidized and reduced form. (B) MS/MS spectrum of the cofactor extracted from *pa*-FPR. The fragmentation pattern unequivocally identifies the cofactor as FAD.

3. Protein Substrate NADPH/NADH Determination

By adding the same equivalent of NADPH or NADH into the same amount of FPR proteins under either aerobic or anaerobic conditions, the reduction of protein is monitored by UV-vis with respect to time. After adding the colorless NADPH into the yellowish protein solution, the mixture solution color changes from yellow into pale green quickly. It is known that oxidized FAD is yellowish, while FAD semiquinone (FADH: one electron reduction of FAD) is blue, and fully reduced FAD is colorless. The light green color suggests that the reduction is not 100% fully toward reduced FAD; the small amount of residual yellow oxidized FAD and blue semiquinone together might contribute to the light green color. As for the reaction with NADH which has no absorbance above 400 nm, the yellow color of the protein and NADH mixture does not change even with more access of NADH or at longer incubation time.

The results show that NADPH reduces FPR in a much faster and more efficient way than NADH. It suggests that NADPH indeed is the physiological coenzyme for FPR. The same reactions under both aerobic and anaerobic conditions show the same results. The anaerobic reactions are shown below in Figure 3-4. Also, FPR-$NADP^+$ crystal has been successfully achieved, the detailed discussion about *pa*-FPR-$NADP^+$ complex and the reason for this coenzyme specificity are explained in next chapter.

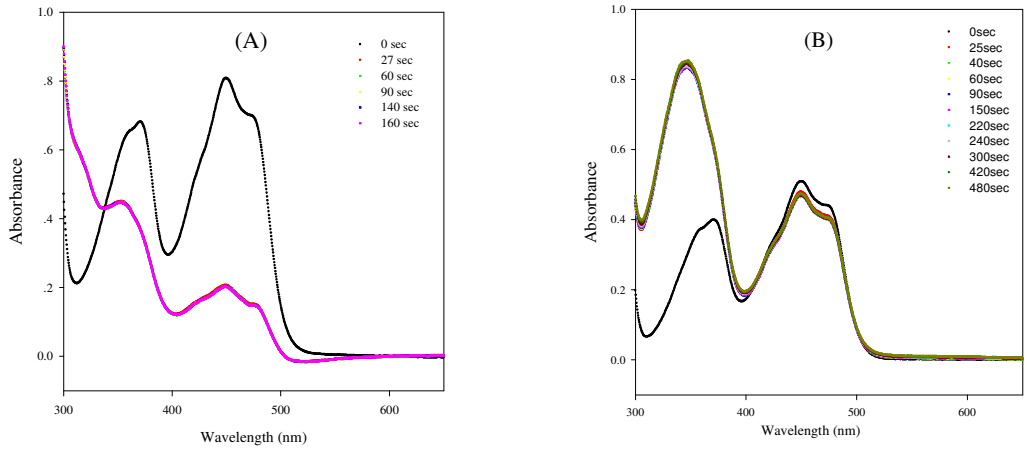

Figure 3-4. *pa*-FPR physiological substrate determination: (A) reduction test by titrating 2 units (1 equivalent) of NADPH into 1unit *pa*-FPR; (B) reduction test by titrating 2 units (1 equivalent) of NADH into 1unit *pa*-FPR.

4. The structure of pa-FPR

The polypeptide in *pa*-FPR folds into the classical two-domain structure of ferredoxin NAD(P)H reductases (Figure 3-5(A)), which includes spinach FNR. The N-terminal domain, residues 1-87, comprise an anti-parallel β-barrel (β1-β6) capped by helix α1, where FAD binds near the N-terminal end of α1 and the carboxy ends of β4 and β5. The C-terminal domain, residues 104-258 fold into the typical nucleotide binding fold comprised of a five-stranded parallel β-sheet (order β9, β8, β7, β10, β11) that is surrounded by nine α-helices (α2 – α10). The $NADP^+$ domain in ferredoxin reductases of known structures is across the carboxy-terminal domain of the β-sheet encompassing β7, β10, the loop connecting β7 to α3 and the N-terminal residues of α3. The $NADP^+$ and FAD binding domains are joined mainly by α3, α6 and to a certain extent by α5 and by the loops preceding and succeeding it. This interface produces a deep cleft where the FAD and $NADP^+$ cofactors reside in close proximity

to one another. Finally, the two domains are linked by residues 88 to 103, which comprise elements of secondary structure β6-loop-α2.

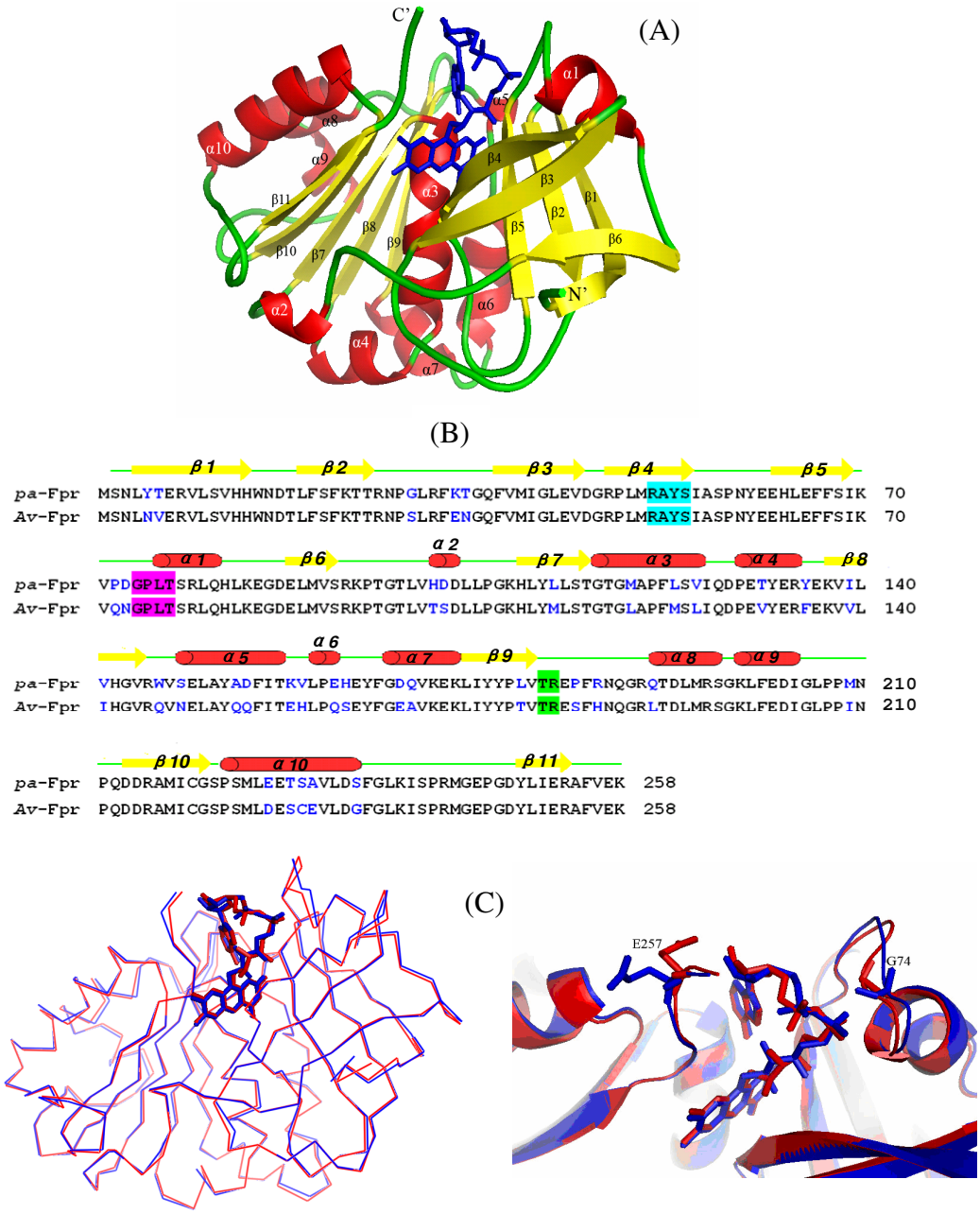

Figure 3-5. (A) View of *pa*-FPR depicting the two domains and the bound FAD. (B) Amino acid sequence alignment of *pa*-FPR and *Av*-FPR using ClustalW (http://www.ebi.ac.uk).

Residues distinct among the two enzymes are shown in blue. The conserved sites for binding the isoalloxazine ring of FAD, as well as phosphates P_1 of FAD and the feature phosphate group of NADP are highlighted by cyan, magenta and green, respectively. (C) Left: superposition of *Av*-FPR (blue) and *pa*-FPR (red) obtained using the Protein3Dfit server shows a C_α RMSD of 0.416 Å. The view is as shown in (A).

The structure of *pa*-FPR is very similar to the characteristic of the superfamily of NAD(P)H reductases and most similar to the structure of NADPH ferredoxin reductase from *Azotobacter vinelandii* (*Av*-FPR) [*52*]. The latter is perhaps not surprising, given the 85% amino acid identity and 91% similarity between the two enzymes (see Figure 3-5(B)). The high degree of structural identity can be seen in the superposition (RMSD C_α = 0.42 Å) of *pa*-FPR (red) and *Av*-FPR (blue) shown in Figure 3-5(C), in a view identical to that of Figure 3-5(A). Only a few amino acids differ in the position of their C_α carbons; these are Ser2, Gly74, Arg186 and Glu257. The position of Ser2 in the amino terminal sequence is expected to impart it with a large B factor, which is likely the reason for the discrepancy in the C_α position of this residue in the two structures. R186 is located in the middle of the loop connecting β9 with α8, thus it would also be expected to experience conformational flexibility. This leaves Gly74 and Glu257, which are located in the FAD binding domain, where the largest differences in structure are observed between *pa*- and *Av*-FPR. In both crystal structures the B-factors exhibited by these residues are very close to the average B-factor for each structure, which suggests that Gly74 and Glu257 have low conformational flexibility. Consequently, the differences in the crystal structures likely represent subtle differences in the way in which each of the enzymes interacts with their FAD cofactors.

The FAD cofactor binds to *pa*-FPR using contacts that are typical of the superfamily of NAD(P)H reductases; these conserved sequences have been highlighted in Figure 3-5(B). Among residues in the R^{51}xYS/T motif in strand β4, the side chain of R51 hydrogen bonds the phosphate in the FMN moiety, the carbonyl oxygen of A52 accepts a hydrogen bond from the ribityl C2' hydroxyl, the hydroxyl group in Y53 hydrogen bonds with the ribityl C4' hydroxyl and the aromatic side chain in the same residue π-stacks against the isoalloxazine ring (see Figure 3-6).

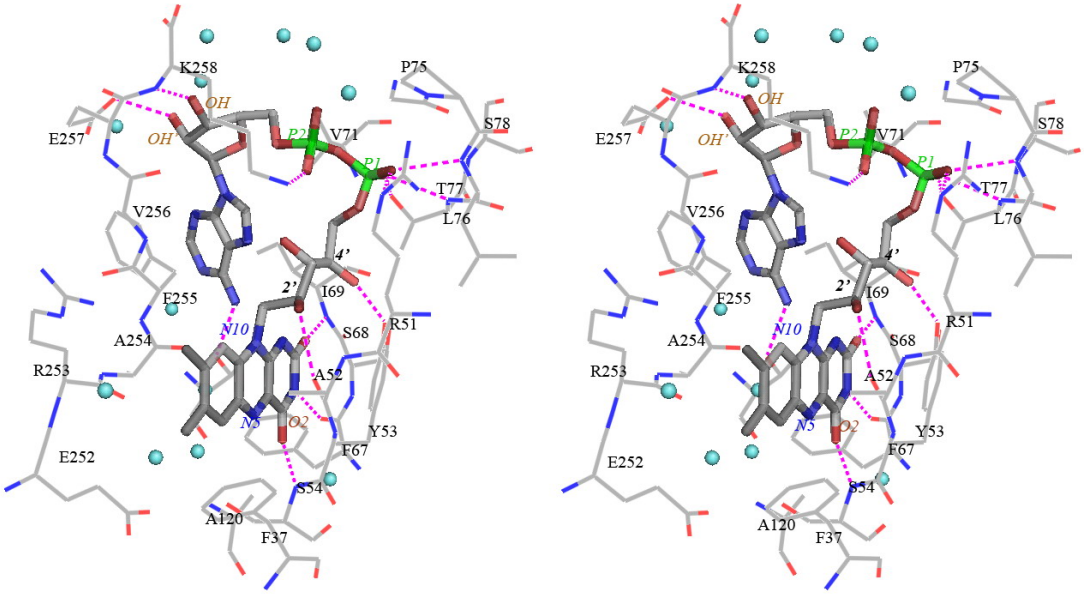

Figure 3-6. Stereo view of the FAD binding site in *pa*-FPR.

The phosphate in the FMN portion of the cofactor is stabilized by hydrogen bonding interactions to the amides of L76 and T77, which are part of the G^{74}xxT/S motif near the amino terminal section of helix α1. The FAD cofactor in *pa*-FPR adopts a conformation that places the isoalloxazine and adenine rings in close proximity. This conformation is similar to that adopted by the FAD cofactor in *Av*-

FPR [*49, 52*] and *E. coli* flavodoxin reductase (*Ec*FldR) [*53*] but distinct from that seen in spinach FNR [*54*] and other members of the reductase family [*55*], where an extended cofactor places the adenine ring distant from the isoalloxazine moiety. As is the case in the structures of *Av*-FPR and *Ec*FldR, the adenine ring in the cofactor of *pa*-FPR π-stacks with the aromatic side chain of F255; this residue is F255 in *Av*-FPR and W255 in *Ec*FldR. Hence, the observations made in the crystal structure of *pa*-FPR support the idea that the conformation of FAD in *Av*-FPR, *Ec*FldR and now *pa*-FPR, is driven by stabilizing π-stacking interactions [*52*]. In comparison the adenine ring in spinach FNR is extended into the surface of the protein, where it π-stacks with the side chain of Y120. It is also worth noting that similar to the structure of *Av*-FPR, the structure of *pa*-FPR lacks an aromatic side chain on the face of the isoalloxazine ring, opposite to the side that interacts with Y53 of the R^{51}xYS/T motif on β4. Instead, the fold of *Av*-FPR and *pa*-FPR place A254 at the equivalent position, where the side chain of A254 is directed away from the isoalloxazine ring. It has been pointed out in the context of the structure of *Av*-FPR that the carbonyl oxygen of A254 and its negatively charged dipole may alter the electronic structure of the isoalloxazine ring, which may account for the absence of a stable semiquinone state in this enzyme [*52*]. It is therefore interesting that a stable semiquinone state is also not observed in *pa*-FPR because it suggests that the electronic structure of the isoalloxazine ring in this enzyme is similar to that of *Av*-FPR and distinct from other reductases. An additional difference pointed out between *Av*-FPR and other reductases in the superfamily [*52*] is the three amino acid carboxy terminal extension,

which includes K258 as the terminal residue. The side chain of this residue together with the side chain of R51 in the R^{51}xYS/T motif interacts electrostatically with the two phosphate groups of FAD. A similar electrostatic interaction between K258 and one of the phosphate groups in the FAD cofactor is also present in the structure of *pa*-FPR (Figure 3-6), which also has the three amino acid carboxy-terminal extensions in its sequence. Hence, it appears that the microenvironment of FAD in *pa*-FPR is very similar to that of FAD in *Av*-FPR but distinct from that observed in other enzymes from the ferredoxin reductase family. How these subtle differences affect reactivity and perhaps redox complementarity with physiologic partners remains to be investigated.

5. NADPH cytochrome c reduction assay for Ferredoxin Reductase reactivity

The NADPH cytochrome c reduction assay is commonly used to measure the ferredoxin dependent cytochrome c reduction activity by monitoring the reduction of cytochrome c [*43, 56*]. In this assay, cytochrome c is reduced by the mediated electron transferred from NADPH to ferredoxin reductase to ferredoxin then to cytochrome c, as illustrated below.

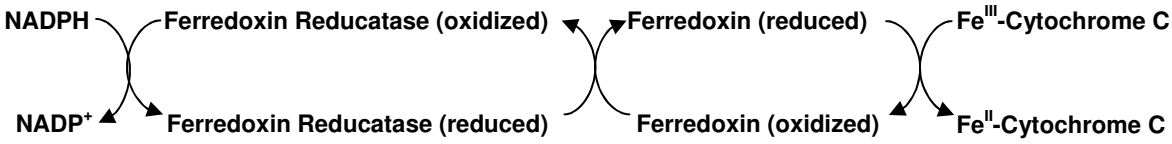

Figure 3-7. Electron transfer pathway in cytochrome c reduction assay.

The UV-vis absorption spectrum of cytochrome c has distinguished soret band and charge transfer band in its oxidized and reduced forms, as exhibited in Figure 3-8. Upon reduction, a sharp absorption peak is observed at 550 nm. Thus, the reduction of cytochrome c is monitored by the increase of 550 nm absorbance with time.

Aerobic:Fpr + Fdl (Spinach) + Cytochrome C + NADPH

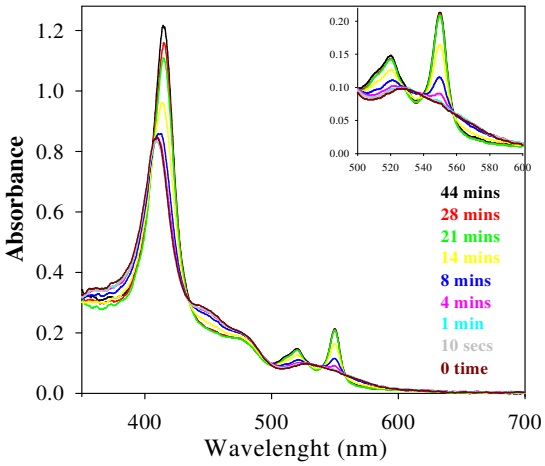

Figure 3-8. Cytochrome c reduction assay in aerobic condition.

Anaerobic*: *Fpr + Fdl (Spinach) + Cytochrome C + NADPH

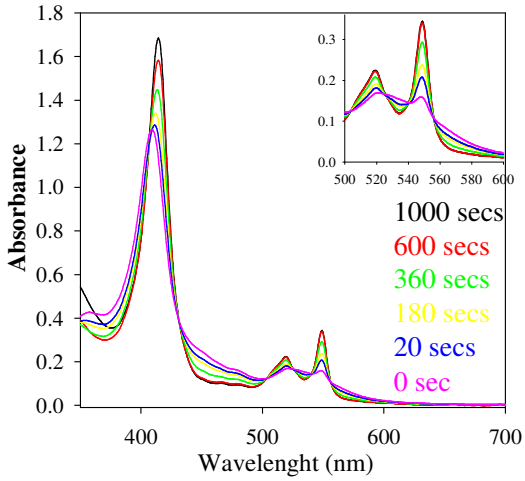

Figure 3-9. Cytochrome c reduction assay in anaerobic condition.

The above two similar experiments are done at either an anaerobic or aerobic condition. The results are similar except that the reaction is slower in the aerobic condition. It is likely due to the oxygen in air that oxidation of the reduced proteins is toward the opposite direction of cytochrome c direction. These experiments suggest no surprise but *pa*-FPR indeed is a typical ferredoxin reductase that can reduce common ferredoxin protein like Spinach ferreodoxin. However, a surprising result is revealed by further redox reactions tested with *Pseudomonas aeruginosa* ferredoxin (*pa*-Bfd), the predicted physiological partner protein executed by Dr. Yuhong Zeng initially and Saroja Weeratunga later from our lab.

6. *Pa*-FPR is a ferredoxin reductase $NADP^+$ protein

The crystal structure of *pa*-FPR revealed a fold typical of the ferredoxin reductase superfamily and provided unequivocal corroboration to biochemical observations described herein, indicating that the flavin cofactor is FAD. Structural comparisons indicate that the structure of *pa*-FPR is almost identical to that of *Av*-FPR and very similar to that of *E. coli* flavodoxin reductase. The function of the latter two enzymes has been proposed to be their participation in a putative redox pathway leading to protection against oxidative stress, which is carried out by performing the reductive repair of O_2^--damaged hydroxylases, such as the [Fe-S] containing aconitase [*57, 58*]. Additional studies suggest that a function of *Av*-FPR and *Ec*FldR is to maintain tolerable levels of NADPH during oxidative stress, thereby preventing reduction or iron and other transition metals that catalyze the formation of highly toxic hydroxyl radicals via Fenton-type chemistry [*58*]. It is therefore

remarkable that although the structures of *Av*-FPR and *Ec*FldR are nearly identical, each utilizes a different type of redox partner; *Av*-FPR interacts specifically with FdI, a protein containing a $[3Fe\text{-}4S]^{+/0}$ and a $[4Fe\text{-}4S]^{2+/+}$ clusters [*59*], whereas *Ec*FldR interacts with a flavodoxin [*60*]. Our findings extend the range of possible redox partners for the same fold (*pa*-FPR) to include a bacterial heme oxygenase (*pa*-HO) which metabolizes heme in the cytosol of *P. aeruginosa*. This notion is supported by the fact that some bacteria and algae possess flavodoxins capable of efficiently replacing ferredoxins as electron transfer proteins and that the expression of these proteins is induced under conditions of iron starvation, which limits the biosynthesis of [Fe-S] clusters and thus the assembly of electron transfer ferredoxins [*55, 61*].

7. *Pa*-FPR and not *pa*-Bfd is the electron donor to *pa*-HO

The proposed physiological redox partner protein *pa*-Bfd was synthesized and over-expressed by Yuhong Zeng in our lab [*31*]. *Pa*-FPR was given to her first and later to Weeratunga, Saroja for the electron transfer assay study using *pa*-FPR, *pa*-Bfd and *pa*-HO in a similar procedure as the above cytochrome c assay in the anaerobic condition inside glove box [*31*]. A surprising result was observed by them, as shown in Figure 3-10.

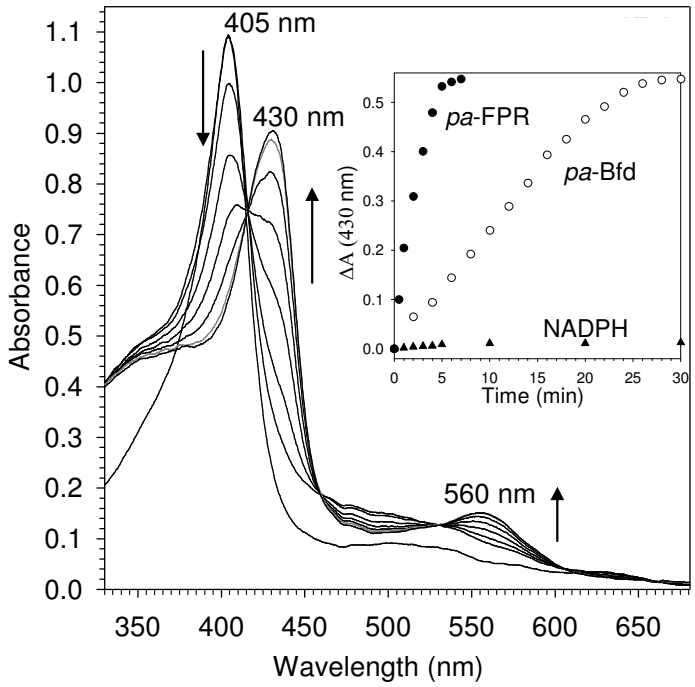

Figure 3-10. Spectral changes taking place upon the addition of reduced *pa*-FPR (8 μM) to resting state *pa*-HO (8 μM) under the anaerobic conditions. The appearance and growth of a band at 430 nm is diagnostic of the formation and accumulation of deoxyferrous *pa*-HO. Inset: time dependent plot of the formation of deoxyferrous *pa*-HO (430 nm) upon the addition of reduced *pa*-FPR (●) and upon the addition of reduced pa-Bfd (○) to resting state *pa*-HO. All experiments were carried out at 25 °C in the presence of catalase. Concentrations in parenthesis correspond to solutions in the cuvette (final concentration) [*31*]. (Courtesy of Yuhong Zeng and Saroja Weeratunga)

In the above reaction, the reduced *pa*-FPR or *pa*-Bfd was initially made by one equivalent NADPH reduction under the anaerobic condition inside glove box. Then direct *pa*-HO one electron reduction initiated by adding equivalent amount of reduced *pa*-FPR or reduced *pa*-Bfd was carried out under the same conditions. The change of *pa*-HO UV-vis absorbance spectrum was monitored with time. It was surprising that electron transfer from *pa*-Bfd to *pa*-HO is a slow process compared with the electron transfer from *pa*-FPR to *pa*-HO, as revealed in the inset in the above

figure. Together with other experiments, it is found that *pa*-Bfd is not required to support the catalytic activity of *pa*-HO and *pa*-FPR by itself can donate all the seven electrons needed for heme degradation in *pa*-HO [*31*].

8. *Pa*-FPR supports the efficient degradation of heme by *pa*-HO

Previous reports suggested that HOs in cyanobacteria and eubacteria are ferredoxin-dependent and thus are thought to receive electrons from NAD(P)H via ferredoxin reductase and ferredoxin. It is interesting; however, that the rates of heme degradation observed in the presence of ferredoxin are typically slow, unless a second reducing agent such as ascorbate, iso-ascorbate or trolox is added to the system [*62-65*]. In this context, it should be pointed out that ascorbate or other similar reducing agents causes heme degradation by two chemically distinct processes, heme oxygenation (as seen in the normal catalytic cycle of HO) and coupled oxidation [*66-68*]. The process of heme oxygenation occurs as outlined in Heme Oxygenase Metabolism Scheme 1, where O_2 coordinated to iron is reduced to HOO^-, in order to form the ferric hydroperoxide (Fe^{III}-OOH) intermediate within the active site of heme oxygenase; and Fe^{III}-OOH adds an OH group to the macrocycle to form meso-hydroxyheme. In contrast, in the coupled oxidation process non-coordinated O_2 is reduced to H_2O_2 by the reducing agent (*i.e.*, ascorbate) outside the enzyme [*68*]. Once formed, H_2O_2 can diffuse into the active site and react with *ferrous* heme to form meso hydroxyheme, which is then channeled to iron biliverdin using additional electrons from ascorbate. Thus the processes of heme oxygenation and coupled oxidation differ fundamentally in the form in which O_2 is reduced to H_2O_2 [*68*]. In

addition, it is also important to consider that resting state (ferric) HO can bind exogenous H_2O_2 to form the Fe^{III}-OOH intermediate, which decays into meso-hydroxyheme [*69, 70*]. Because exogenous H_2O_2 is readily formed when dissolved O_2 reacts with electron donors such as NADPH, ascorbate, hydrazine, etc., it is important that assays of HO activity include catalase to destroy exogenous H_2O_2, thus preventing the oxidation of heme by paths other than the catalytic cycle of heme oxygenase. In this context, it is important to note that with only one exception, assays to determine the activity of "ferredoxin-dependent" HOs do not include catalase [*62-65*]. Interestingly, the study that reports on the inclusion of catalase in the heme degradation assays found that the oxyferrous complex is formed readily; decay of this complex into iron-biliverdin, however, is a very slow process [*63*]. In contrast, when ascorbate was added as the auxiliary electron donor in addition to ferredoxin, the oxyferrous complex decayed rapidly to biliverdin even if catalase was present [*63*]. Consequently, it was suggested that in addition to ferredoxin, an auxiliary electron donor is necessary to carry out the catalytic activity of bacterial HOs. It is therefore significant that findings reported herein demonstrate that when *pa*-FPR is the redox partner of *pa*-HO the degradation of heme to iron biliverdin occurs rapidly and efficiently in the *absence* of an auxiliary electron donor, despite the fact that all assays were carried out in the presence of catalase [*31*].

In order to understand the structure, catalysis and physiological meanings behind this novel redox partnership, further studies of *pa*-FPR protein in complex with its coenzyme $NADP^+$ are discussed in next chapter. The study of the *pa*-FPR

and *pa*-HO protein-protein interaction will be facilitated by the analysis of the available crystal structures for *pa*-HO [*71*] and *pa*-FPR-$NADP^+$ complex, as well as by the availability of sequential backbone NMR assignments for *pa*-FPR. This information will make it possible to carry out chemical shift perturbation experiments [*72*] aimed at experimentally defining the inter-protein interface once the sequential assignments of *pa*-FPR have been obtained.

REFERENCES

[1] Reid, G. A. (2002) Flavins, flavoproteins and flavoproteomics. *Flavins and Flavoproteins 2002, Proceedings of the International Symposium, 14th, Cambridge, United Kingdom, July 14-18, 2002*, 3-10.

[2] Ceccarelli, E. A.; Arakaki, A. K.; Cortez, N.; Carrillo, N. (2004) Functional plasticity and catalytic efficiency in plant and bacterial ferredoxin-NADP(H) reductases. *Biochimica et Biophysica Acta, Proteins and Proteomics*, *1698*, 155-165.

[3] Arakaki, A. K.; Ceccarelli, E. A.; Carrillo, N. (1997) Plant-type ferredoxin-NADP+ reductases: A basal structrual framework and a multiplicity of functions. *The FASEB journal*, *11*, 133-140.

[4] Xu, F.; Scientist, S. (2005) Applications of oxidoreductases: Recent progress. *Ind Biotechnol*, *1*, 38-50.

[5] Carrillo, N.; Ceccarelli, E. A. (2003) Open questions in ferredoxin-NADP+ reductase catalytic mechanism. *European Journal of Biochemistry*, *270*, 1900-1915.

[6] Bruns, C. M.; Karplus, P. A. (1995) Refined crystal structure of spinach ferredoxin reductase at 1.7 .ANG. resolution: oxidized, reduced and 2'-phospho-5'-AMP bound states. *Journal of Molecular Biology*, *247*, 125-145.

[7] Serre, L.; Vellieux, F. M. D.; Medina, M.; Gomez-Moreno, C.; Fontecilla-Camps, J. C.; Frey, M. (1996) X-ray structure of the ferredoxin:NADP+ reductase from the cyanobacterium Anabaena PCC 7119 at 1.8 .ANG. resolution, and crystallographic studies of NADP+ binding at 2.25 .ANG. resolution. *Journal of Molecular Biology*, *263*, 20-39.

[8] Ingelman, M.; Bianchi, V.; Eklund, H. (1997) The three-dimensional structure of flavodoxin reductase from Escherichia coli at 1.7 .ANG. resolution. *Journal of Molecular Biology*, *268*, 147-157.

[9] Kurisu, G.; Kusunoki, M.; Katoh, E.; Yamazaki, T.; Teshima, K.; Onda, Y.; Kimata-Ariga, Y.; Hase, T. (2001) Structure of the electron transfer complex between ferredoxin and ferredoxin-NADP reductase. *Nature Structural Biology*, *8*, 117-121.

[10] Hurley, J. K.; Morales, R.; Martinez-Julvez, M.; Brodie, T. B.; Medina, M.; Gomez-Moreno, C.; Tollin, G. (2002) Structure-function relationships in Anabaena ferredoxin/ferredoxin:NADP+ reductase electron transfer: insights from site-directed mutagenesis, transient absorption spectroscopy and x-ray crystallography. *Biochimica et Biophysica Acta, Bioenergetics*, *1554*, 5-21.

[11] Maeda, M.; Lee, Y. H.; Ikegami, T.; Tamura, K.; Hoshino, M.; Yamazaki, T.; Nakayama, M.; Hase, T.; Goto, Y. (2005) Identification of the N- and C-Terminal Substrate Binding Segments of Ferredoxin-NADP+ Reductase by NMR. *Biochemistry*, *44*, 10644-10653.

[12] Mayoral, T.; Martinez-Julvez, M.; Perez-Dorado, I.; Sanz-Aparicio, J.; Gomez-Moreno, C.; Medina, M.; Hermoso, J. A. (2005) Structural analysis of interactions for complex formation between ferredoxin-NADP+ reductase and

its protein partners. *PROTEINS: Structure, Function, and Bioinformatics*, *59*, 592-602.

[13] Mayoral, T.; Martinlvez, M.; Perez-Dorado, I.; Sanz-Aparicio, J.; Gomez-Moreno, C.; Medina, M.; Hermoso, J. A. (2005) Structural Analysis of Interactions for Complex Formation between Ferredoxin-NADP Reductase and Its Protein Partners. *PROTEINS: Structure, Function, and Bioinformatics*, *59*, 592-602.

[14] Tejero, J.; Perez-Dorado, I.; Maya, C.; Martinez-Julvez, M.; Sanz-Aparicio, J.; Gomez-Moreno, C.; Hermoso, J. A.; Medina, M. (2005) C-Terminal Tyrosine of Ferredoxin-NADP+ Reductase in Hydride Transfer Processes with NAD(P)+/H. *Biochemistry*, *44*, 13477-13490.

[15] Reipa, V.; Holden, M. J.; Vilker, V. L. (2007) Association and Redox Properties of the Putidaredoxin Reductase-Nicotinamide Adenine Dinucleotide Complex. *Biochemistry*, *46*, 13235-13244.

[16] Roehrich, R. C.; Englert, N.; Troschke, K.; Reichenberg, A.; Hintz, M.; Seeber, F.; Balconi, E.; Aliverti, A.; Zanetti, G.; Koehler, U.; Pfeiffer, M.; Beck, E.; Jomaa, H.; Wiesner, J. (2005) Reconstitution of an apicoplast-localised electron transfer pathway involved in the isoprenoid biosynthesis of Plasmodium falciparum. *FEBS Letters*, *579*, 6433-6438.

[17] Seeber, F.; Aliverti, A.; Zanetti, G. (2005) The plant-type ferredoxin-NADP+ reductase/ferredoxin redox system as a possible drug target against Apicomplexan human parasites. *Current Pharmaceutical Design*, *11*, 3159-3172.

[18] Karplus, P. A.; Daniels, M. J.; Herriott, J. R. (1991) Atomic structure of ferredoxin-NADP+ reductase: prototype for a structurally novel flavoenzyme family. *Science (Washington, DC, United States)*, *251*, 60-66.

[19] Medina, M.; Martinez-Julve, M.; Hurley, J. K.; Tollin, G.; Gomez-Moreno, C. (1998) Involvement of glutamic acid 301 in the catalytic mechanism of ferredoxin-NADP+ reductase from Anabaena PCC 7119. *Biochemistry*, *37*, 2715-2728.

[20] Ziegler, G. A.; Schulz, G. E. (2000) Crystal structures of adrenodoxin reductase in complex with NADP and NADPH suggesting a mechanism for the electron transfer of an enzyme family. *Biochemistry*, *39*, 10986-10995.

[21] Medina, M.; Luquita, A.; Tejero, J.; Hermoso, J.; Mayoral, T.; Sanz-Aparicio, J.; Grever, K.; Gomez-Moreno, C. (2001) Probing the determinants of coenzyme specificity in ferredoxin-NADP+ reductase by site-directed mutagenesis. *Journal of Biological Chemistry*, *276*, 11902-11912.

[22] Martinez-Julvez, M.; Hermoso, J.; Hurley, J. K.; Mayoral, T.; Sanz-Aparicio, J.; Tollin, G.; Gomez-Moreno, C.; Medina, M. (1998) Role of Arg100 and Arg264 from Anabaena PCC 7119 ferredoxin-NADP+ reductase for optimal NADP+ binding and electron transfer. *Biochemistry*, *37*, 17680-17691.

[23] Rossmann, M. G.; Moras, D.; Olsen, K. W. (1974) Chemical and biological evolution of a nucleotide-binding protein. *Nature*, *250*, 194-199.

[24] Dym, O.; Eisenberg, D. (2001) Sequence-structure analysis of FAD-containing proteins. *Protein Science*, *10*, 1712.

[25] Prasad, G. S.; Kresge, N.; Muhlberg, A. B.; Shaw, A.; Jung, Y. S.; Burgess, B. K.; Stout, C. D. (1998) The crystal structure of NADPH:ferredoxin reductase from Azotobacter vinelandii. *Protein Science*, *7*, 2541-2549.

[26] Wang, M.; Roberts, D. L.; Paschke, R.; Shea, T. M.; Masters, B. S. S.; Kim, J. J. P. (1997) Three-Dimensional Structure of NADPH-Cytochrome P450 Reductase: Prototype for FMN-and FAD-Containing Enzymes. *Proceedings of the National Academy of Sciences*, *94*, 8411-8416.

[27] Shin, M.; Tagawa, K.; Arnon, D. I. (1963) CRYSTALLIZATION OF FERREDOXIN-TPN REDUCTASE AND ITS ROLE IN THE PHOTOSYNTHETIC APPARATUS OF CHLOROPLASTS. *Biochem Z*, *338*, 84-96.

[28] Bruns, C. M.; Karplus, P. A. (1994) Refined crystal structures of native, complexed and reduced forms of spinach ferredoxin reductase, pp 443-446.

[29] Nascimento, A. S.; Ferrarezi, T.; Catalano-Dupuy, D. L.; Ceccarelli, E. A.; Polikarpov, I. (2006) Crystallization and preliminary x-ray diffraction studies of ferredoxin reductase from Leptospira interrogans. *Acta Crystallographica, Section F: Structural Biology and Crystallization Communications*, *F62*, 662-664.

[30] Hermoso, J. A.; Mayoral, T.; Faro, M.; Gomez-Moreno, C.; Sanz-Aparicio, J.; Medina, M. (2002) Mechanism of coenzyme recognition and binding revealed by crystal structure analysis of ferredoxin-NADP+ reductase complexed with NADP+. *Journal of Molecular Biology*, *319*, 1133-1142.

[31] Wang, A.; Zeng, Y.; Han, H.; Weeratunga, S.; Morgan, B. N.; Moeenne-Loccoz, P.; Schoenbrunn, E.; Rivera, M. (2007) Biochemical and Structural Characterization of Pseudomonas aeruginosa Bfd and FPR: Ferredoxin NADP+ Reductase and Not Ferredoxin Is the Redox Partner of Heme Oxygenase under Iron-Starvation Conditions. *Biochemistry*, *46*, 12198-12211.

[32] Ikemura, T. (1985) Codon Usage and tRNA Content in Unicellular and Multicellular Organisms. *Mol. Biol. Evol.*, *2*, 13-34.

[33] Macheroux, P. (1999) UV-Visible Spectroscopy as a Tool to Study Flavoproteins, in *Methods in Molecular Biology* (Chapman, S. K.;Reid, G. A., Eds.), pp 1-7, Humana Press, Totowa, New Jersey.

[34] Aliverti, A.; Curti, B.; Vanoni, M. A. (1999) Identifying and Quantitating FAD and FMN in Simple and in Iron-Sulfur-Containing Flavoproteins, in *Methods in Molecular Biology* (Chapman, S. K.;Reid, G. A., Eds.), pp 9-23, Humana Press, Totowa, New Jersey.

[35] Wang, G.; Maier, R. J. (2004) An NADPH Quinone Reductase of Helicobacter pylori Plays an Important Role in Oxidative Stress Resistance and Host Colonization. *Infection and Immunity*, *72*, 1391.

[36] Luft, J. R.; Collins, R. J.; Fehrman, N. A.; Lauricella, A. M.; Veatch, C. K.; DeTitta, G. T. (2003) A Deliberate Approach to Screening for Initial Crystallization Conditions of Biological Macromolecules. *Journal of Structural Biology*, *142*, 170-179.

[37] Kabsch, W. (1993) Automatic Processing of Rotation Diffraction Data from Crystals of Initially Unknown Symmetry and Cell Constraints. *Journal of Applied Crystallography*, *26*, 795-800.

[38] Brunger, A. T.; Adams, P. D.; Clore, G. M.; DeLano, W. L.; Gros, P.; Grosse-Kunstleve, R. W.; Jiang, J. S.; Kuszewski, J.; Nilges, M.; Pannu, N. S.; Read, R. J.; Rice, L. M.; Simonson, T.; Warren, G. L. (1998) Crystallography & NMR System: A New Software Suite for Macromolecular Structure Determination. *Acta Crystallographica*, *D54*, 905-921.

[39] Jones, T. A.; Zhou, J. Y. (1991) Improved Methods for Binding Protein Models in Electron Density Maps and the Location of Errors in These Models. *Acta Crystallographica Section A: Foundations of Crystallography*, *A47*, 110-119.

[40] Wan, J. T.; Jarrett, J. T. (2002) Electron acceptor specificity of ferredoxin (flavodoxin):NADP+ oxidoreductase from Escherichia coli. *Archives of Biochemistry and Biophysics*, *406*, 116-126.

[41] Regnstrom, K.; Sauge-Merle, S.; Chen, K.; Burgess, B. K. (1999) In Azotobacter vinelandii, the E1 subunit of the pyruvate dehydrogenase complex binds fpr promoter region DNA and ferredoxin I. *Proceedings of the National Academy of Sciences of the United States of America*, *96*, 12389-12393.

[42] Pueyo, J. J.; Gomez-Moreno, C.; Mayhew, S. G. (1991) Oxidation-reduction potentials of ferredoxin-NADP+ reductase and flavodoxin from Anabaena PCC7119 and their electrostatic and covalent complexes. *European Journal of Biochemistry*, *202*, 1065-1071.

[43] Jung, Y.-S.; Roberts, V. A.; Stout, C. D.; Burgess, B. K. (1999) Complex formation between Azotobacter vinelandii ferredoxin I and its physiological electron donor NADPH-ferredoxin reductase. *Journal of Biological Chemistry*, *274*, 2978-2987.

[44] Hasumi, H.; Nakamura, S.; Koga, K.; Yoshizumi, H.; Parcells, J. H.; Kimura, T. (1982) Further physicochemical studies on the complex formation between iron-sulfur proteins and flavoproteins from spinach chloroplast and beef

adrenal cortex electron-transfer systems. *Journal of Biochemistry (Tokyo, Japan)*, *91*, 135-141.

[45] Deshmukh, R.; Zeng, Y.; Furci, L. M.; Huang, H.-w.; Morgan, B. N.; Sander, S.; Alontaga, A.; Bunce, R. A.; Moënne-Loccoz, P.; Rivera, M.; Wilks, A. (2005) Heme Oxidation in a Chimeric Protein of the α-Selective Neisseriae meningitidis Heme Oxygenase with the Distal Helix of the δ-Selective Pseudomonas aeruginosa. *Biochemistry*, *44*, 13713-13723.

[46] Ratliff, M.; Zhu, W.; Deshmukh, R.; Wilks, A.; Stojiljkovic, I. (2001) Homologues of Neisserial Heme Oxygenase in Gram-Negative Bacteria: Degradation of Heme by the Product of the *pigA* Gene of *Pseudomonas aeruginosa*. *Journal of Bacteriology*, *183*, 6394-6403.

[47] Caignan, G. A.; Deshmukh, R.; Wilks, A.; Zeng, Y.; Huang, H.; Moënne-Loccoz, P.; Bunce, R. A.; Eastman, M. A.; Rivera, M. (2002) Oxidation of Heme to ß- and δ-biliverdin by *Pseudomonas aeruginosa* Heme Oxygenase as a Consequence of an Unusual Seating of the Heme. *Journal of the American Chemical Society*, *124*, 14879-14892.

[48] Morgan, B. N. (2006) Determinants of regioselectivity and electron transfer in the process of heme degradation carried out by the enzyme heme oxygenase in *Pseudomonas aeruginosa*. *Master Dissertation*, 48-51.

[49] Isas, J. M.; Burgess, B. K. (1994) Purification and characterization of a NADP+/NADPH-specific flavoprotein that is overexpressed in FdI- strains of Azotobacter vinelandii. *Journal of Biological Chemistry*, *269*, 19404-19409.

[50] Blobel, J.; Schmidl, S.; Vidal, D.; Nisius, L.; Bernad, P.; Millet, O.; Brunner, E.; Pons, M. (2007) Protein Tyrosine Phosphatase Oligomerization Studied by a Combination of 15 N NMR Relaxation and 129 Xe NMR. Effect of Buffer Containing Arginine and Glutamic Acid. *Journal of the American Chemical Society*, *129*, 5946-5953.

[51] Morgan, B. N. (2006) Determinants of regioselectivity and electron transfer in the process of heme degradation carried out by the enzyme heme oxygenase in *Pseudomonas aeruginosa*. *Master Dissertation*, 62-67.

[52] Prasad, G. S.; Kresge, N.; Muhlberg, A. B.; Shaw, A.; Jung, Y. S.; Burgess, B. K.; Stout, C. D. (1998) The Crystal Structure of NADPH:Ferredoxin Reductase from *Azotobacter vinelandii*. *Protein Science*, *7*, 2541-2549.

[53] Ingelman, M.; Bianchi, V.; Eklund, H. (1997) The Three-Dimensional Structure of Flavodoxin Reductase from *Escherichia coli* at 1.7 A Resolution. *Journal of Molecular Biology*, *268*, 147-157.

[54] Karplus, P. A.; Daniels, M. J.; Herriott, D. J. R. (1991) Atomic Structure of Ferredoxin-$NADP^+$ Reductase: Prototype for a Structurally Novel Flavoenzyme Family. *Science*, *251*, 60-66.

[55] Carrillo, N.; Ceccarelli, E. A. (2003) Open Questions in Ferredoxin-$NADP^+$ Reductase Catalytic Mechanism. *European Journal of Biochemistry*, *270*, 1900-1915.

[56] Isas, J. M.; Yannone, S. M.; Burgess, B. K. (1995) Azotobacter vinelandii NADPH:ferredoxin reductase cloning, sequencing, and overexpression. *Journal of Biological Chemistry*, *270*, 21258-21263.

[57] Bianchi, V.; Haggard-Ljungquist, E.; Pontis, E.; Reichard, P. (1995) Interruption of the Ferredoxin (Flavodoxin) $NADP^+$ Oxidureductase Gene in *Escherichia coli* Does Not Affect Anaerobic Growth but Increases Sensitivity to Paraquat. *Journal of Bacteriology*, *177*, 4528-4531.

[58] Krapp, A. R.; Rodriguez, R. E.; Poli, H. O.; Paladini, D. H.; Platnik, J. F.; Carrillo, N. (2002) The Flavoenzyme Ferredoxin (Flavodoxin)-NADP(H) Reductase Modulates NADP(H) Homeostasis During the *soxRS* Response in *Escherichia coli*. *Journal of Bacteriology*, *184*, 1474-1480.

[59] Isas, J. M.; Burgess, B. K. (1994) Purification and Characterization of $NADP^+$/NADPH-Specific Flavoprotein That is Overexpressed in FdI^- Strains of *Azotobacter vinelandii*. *Journal of Biological Chemistry*, *269*, 19404-19409.

[60] Bianchi, V.; Reichard, P.; Eliasson, R.; Pontis, E.; Krook, M.; Jornvall, H.; Haggard-Ljungquist, E. (1993) *Escherichia coli* Ferredoxin $NADP^+$

Reductase: Activation of *E. coli* Anaerobic Ribonucleotide Reduction, Cloning of the Gene (*fpr*), and Overexpression of the Protein. *Journal of Bacteriology*, *175*, 1590-1595.

[61] Razquin, P.; Fillat, M. F.; Schmitz, S.; Bohme, H.; Gomez-Moreno, C.; Peleato, M. L. (1996) Expression of Ferredoxin-$NADP^+$ Reductase in Hetocysts from *Anabaena sp*. *Biochemical Journal*, *316*, 157-160.

[62] Cornejo, J.; Willows, R. D.; Beale, S. I. (1998) Phytobilin Biosynthesis: Cloning and Expression of a Gene Encoding Soluble Ferredoxin-Dependent Heme Oxygenase from *Synechocystis sp*. PCC6803. *Plant Journal*, *15*, 99-107.

[63] Wegele, R.; Tasler, R.; Zeng, Y.; Rivera, M.; Frankenberg-Dinkel, N. (2004) The Heme Oxygenase(s)-Phytochrome System of *Pseudomonas aeruginosa*. *Journal of Biological Chemistry*, *279*, 45791-45802.

[64] Cornejo, J.; Beale, S. I. (1997) Phycobilin Biosynthetic Reactions in Extracts of Cyanobacteria. *Photosynthesis Research*, *51*, 223-230.

[65] Muramoto, T.; Tsurui, N.; Terry, M. J.; Yokota, A.; Kohchi, T. (2002) Expression and Biochemical Properties of a Ferredoxin-Dependent Heme Oxygenase Required for Phytochrome Chromophore Synthesis. *Plant Physiology*, *130*, 1958-1966.

[66] Avila, L.; Huang, H.-w.; Rodríguez, J. C.; Moënne-Loccoz, P.; Rivera, M. (2000) Oxygen Activation by Axial Ligand Mutants of Mitochondrial Cytochrome b_5: Oxidation of Heme to Verdoheme and Biliverdin. *Journal of the American Chemical Society*, *122*, 7618-7619.

[67] Sigman, J. A.; Wang, X.; Lu, Y. (2001) Coupled Oxidation of Heme by Myoglobin is Mediated by Exogenous Peroxide. *Journal of the American Chemical Society*, *123*, 6945-6946.

[68] Avila, L.; Huang, H.; Damaso, C. O.; Lu, S.; Moënne-Loccoz, P.; Rivera, M. (2003) Coupled Oxidation vs Heme Oxygenation: Insights from Axial Ligand

Mutants of Mitochondrial Cytochrome b_5. *Journal of the American Chemical Society*, *125*, 4103-4110.

[69] Wilks, A.; Torpey, J.; Ortiz de Montellano, P. R. (1994) Heme Oxygenase (HO-1) Evidence for Electrophilic Oxygen Addition to the Porphyrin Ring in the Formation of α-meso-hydroxyheme. *Journal of Biological Chemistry*, *269*, 29553-29556.

[70] Damaso, C. O.; Bunce, R. A.; Barybin, M. V.; Wilks, A.; Rivera, M. (2005) The Ferrous Verdoheme-Heme Oxygenase Complex is Six-Coordinate and Low-Spin. *Journal of the American Chemical Society*, *127*, 17852-17853.

[71] Friedman, J.; Lad, L.; Li, H.; Wilks, A.; Poulos, T. L. (2004) Structural Basis for Novel δ-Regioselective Heme Oxygenation in the Opportunistic Pathogen *Pseudomonas aeruginosa*. *Biochemistry*, *43*, 5239-5245.

[72] Zuiderweg, E. R. P. (2002) Mapping Protein-Protein Interactions in Solution by NMR Spectroscopy. *Biochemistry*, *41*, 1-7.

CHAPTER IV: X-RAY CRYSTALLOGRAPHIC AND SOLUTION STATE NMR SPECTROSCOPIC INVESTIGATIONS OF $NADP^+$ BINDING TO FERREDOXIN-NADP REDUCTASE (FPR) FROM *PSEUDOMONAS AERUGINOSA*

INTRODUCTION

Ferredoxin $NADP^+$ reductases (FNRs), which catalyze the reversible electron transfer between NADP(H) and their cognate ferredoxin or flavodoxin partners, are found in plastids, phototropic and heterotropic bacteria and in mitochondria [*1*]. One of the best characterized enzymes is FNR from the spinach leafs, which is typical of FNRs found in plastids, where the reducing power of electromagnetic radiation is used by these reductases to reduce $NADP^+$, thus producing the NADPH needed for the subsequent photosynthetic paths [*2*]. In contrast, bacterial ferredoxin reductases displace the equilibrium toward the oxidation of the NADPH pool, in order to use this reducing potential in a large number of oxidoreductive processes. For instance, *E. coli* flavodoxin reductase functions in the reduction of flavodoxin for the activation of anaerobic enzymes and in the oxidation of NADPH as a mechanism of protection against oxidative stress [*3-5*]. In *R. capsulatus* [*5*], *A. vinelandii* [*4*] and *E coli* [*3*] the gene *fpr* encodes a **f**erredoxin (**f**lavodoxin) nicotinamide adenine dinucleotide **p**hosphate **r**eductase (FPR) that functions in the oxidation of NADPH as a

mechanism of defense against oxidative stress. A similar FPR (*pa*-FPR) in *P. aeruginosa* has been characterized as a 258-residue long NADPH-dependent enzyme that uses FAD as cofactor [*6*]. Although it is possible that *pa*-FPR also functions in mitigating oxidative stress [*4*], it has been shown that under iron starvation conditions *pa*-FPR functions by shuttling electrons from NADPH to a heme oxygenase, thus supporting the process of releasing iron from exogenously acquired heme for subsequent metabolic use [*6*].

The crystal structure of *pa*-FPR [*6*] revealed a fold very similar to the characteristics of the FNR superfamily and is almost identical to the structure of FPR from *A. vinelandii* (*Av*-FPR) [*7*] and *E. coli* flavodoxin reductase [*8*]. The comparative analysis of the X-ray crystal structures of ferredoxin reductases uncovered some interesting differences in the context of a similar fold. These differences led to the classification of these enzymes into reductases of the plastidic class, *i.e*., enzymes from chloroplasts and cyanobacteria, and enzymes of the bacterial class, which are further subdivided into proteobacterial subclass I enzymes (*A. vinelandii, R. capsulatus*, *P. aeruginosa*) and proteobacterial subclass II reductases (*E. coli* flavodoxin reductase) [*9*]. The structures showed that plastidic FNRs and bacterial FPRs differ in the conformation and chemical environment of the FAD cofactor. In the plastidic enzymes the FAD is bound in an extended conformation, which is stabilized by specific interactions with residues in a sheet-loop-sheet motif (green in Figure 4-1(A)). These encompass π-stack the adenine ring with the conserved aromatic side chain of Tyr120 and the hydrogen bonding interactions

involving the 2'-P AMP moiety. In comparison, bacterial FPRs lack the sheet-loop-sheet motif that stabilizes the extended FAD conformation, thus the cofactor adopts a bent conformation at which the adenine ring π-stacks with the conserved aromatic side chain of residue 255 (Figure 4-1(B)). The FMN portion of FAD in plastidic and bacterial reductases exhibits very similar conformations and chemical environments. Additional important differences occur in the carboxyl terminal domains, which are typically thought to be involved in NADP(H) binding. Whereas in plastidic FNRs the carboxyl terminal Tyr (Y314 in spinach FNR, Y308 in pea FNR and Y303 in *Anabaena* FNR) π-stacks against the isoalloxazine ring of FAD [*10, 11*] (see Figure 4-1(A)). In subclass I bacterial FPRs this residue is replaced by Ala254, which is followed by a $FVEK^{258}$ terminal sequence (Figure 4-1(B)). In the structures of *pa*-FPR and *Av*-FPR the carbonyl oxygen of Ala254 packs against the isoalloxazine ring, replacing the conserved π-stacking interaction between the carboxyl terminal Tyr ring and the isoalloxazine ring seen in the plastidic FNRs. In subclass II bacterial enzymes, a conserved terminal Trp is found immediately after the position is occupied by the terminal Tyr in the plastidic enzymes, thus extending the carboxy terminal domain by only one residue. In these enzymes FAD also adopts a bent conformation.

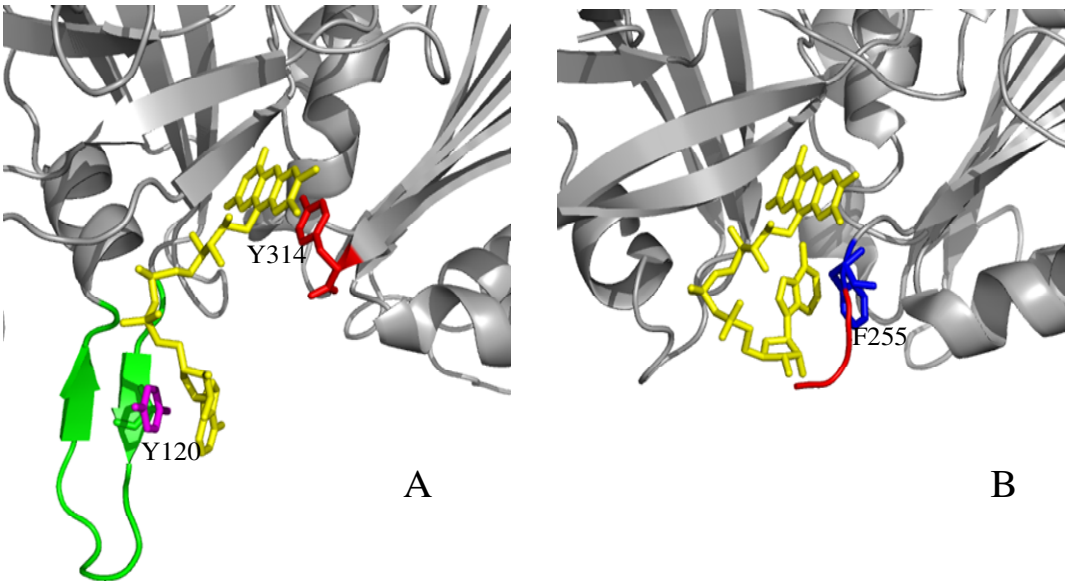

Figure 4-1. (A) The fold of plastidic FNRs exhibits a conserved sheet-loop sheet motif (green) that contributes to stabilizing the extended FAD (yellow) conformation characteristic of these enzymes. (B) The fold of bacterial FPRs, which is devoid of the sheet-loop-sheet motif, exhibits a characteristically bent FAD conformation.

The binding of $NADP^+$ to FNRs has been the subject of intense investigations. Cocrystallization of *Anabaena* FNR [*12*] with $NADP^+$ revealed a complex in which the 2'P AMP portion of the cofactor is stabilized in a manner identical to that observed in the $NADP^+$ complex obtained by soaking crystals of the *Anabaena* enzyme in $NADP^+$ solution [*13*]. The conformation of the nicotinamide portion of the cofactor, however, is different in the two structures. The structure of *Anabaena* FNR obtained from the crystals soaked in $NADP^+$ solutions of the nicotinamide ring extends toward the surface of the protein and away from the isoalloxazine ring, whereas in the structure obtained from the co-crystallization with $NADP^+$, the side chain of the carboxyl terminal Tyr (Y303) is stacked between the nicotinamide and

isoalloxazine rings. The latter structure resembles more "productive" interactions seen in other flavoenzyme families that are structurally and functionally different from FNRs (*i.e.* glutathione reductase), at which the nicotinamide and iosalloxazine rings stack parallel and adjacent to one another [*14, 15*]. Nevertheless, the side chain of Tyr303 is not displaced to allow direct overlap of the cofactor rings, as would be expected in a "productive" complex that facilitates direct hydride transfer. A "productive" complex was observed only in Y308 mutants (the C'-terminal residue) of pea-FNR, where the $NADP^+$ nicotinamide ring is nearly parallel and adjacent to the FAD isoalloxazine ring [*16*].

These observations have led to the conclusion that $NADP^+$ binding to FNRs is a two-step process with nearly independent binding of the two halves of the cofactor [*16*]. In the first step the 2'-P-AMP moiety binds tightly and anchors the cofactor, whereas the niconinamide portion is disordered. In the second step, the enzyme-cofactor complex is expected to sample a set of "productive" conformations in which the side chain of the C'-terminal Tyr is displaced, thus allowing overlap of the nicotinamide and isoalloxazine rings to facilitate hydride transfer. In the context of this mechanism, it is significant that in the structures of FPRs from *A. vinelandii* and *P. aeruginosa* the terminal Tyr is replaced by Ala254, which is followed by a C'-terminal extension ($AFVEK^{258}$). This extension of the sequence, in principle, can be expected to slow the rate of conformational rearrangements needed to access the "productive" conformation of the cofactors thought to facilitate direct hydride transfer, assuming that the binding of $NADP^+$ is similar in FNRs and FPRs.

Nevertheless, nothing is known about the structural properties of the NADP(H) complex of FPRs, and the functional role, if any, played by the C'-terminal extension characteristic of these enzymes has so far been elusive. In this report we present the X-ray crystal structure of the *pa*-FPR-NADP complex, which shows an extensive network of the interactions among FAD, $NADP^+$ and the C'-terminal extension. The complementary observations made with the aid of NMR spectroscopy in the solution support the notion inferred from the analysis of the network of interactions in the crystal structure that the C'-terminal tail is not dynamically active, even upon $NADP^+$ binding. These findings, which suggest that the C'-terminal extension will likely not be readily displaced to allow "productive" packing of the isoalloxazine and nicotinamide rings for direct hydride transfer, are discussed in the context of a possible multi-step hydride transfer operative in the oxidation of NADPH by FPR enzymes.

Based on the insights from the biochemical and structural studies of *pa*-FPR and *pa*-HO proteins, we further investigated the protein-protein interaction between *pa*-FPR and *pa*-HO using the available protein crystal structures and NMR backbone assignments in the solution phase. As discussed in chapter 3, *pa*-HO is a novel redox partner protein of *pa*-FPR. *Pa*-FPR is a ferredoxin reductase protein. It is generally known that ferredoxin reductase forms electrostatic complex with its redox partner proteins and the interaction interface is most likely located around the active site to facilitate efficient electron transfer [*17-21*]. Also, the NMR method is a highly sensitive approach in detecting ultra-weak protein-protein interactions (PPIs) and

identifying the interaction interface. The chemical shift perturbation study using one [U-^{15}N] protein titrated by the other unlabeled protein is carried out with ^{1}H-^{15}N HSQC experiment. By following the chemical shift perturbed residues and mapping them onto protein 3D crystal structure, the protein interaction interface can be obtained for the weak PPI with Kd > 10^{-4} M [*22*].

By using the two proteins' crystal structure, the interaction interfaces are predicted to be the area around the heme binding pocket for *pa*-HO and the concave bowl-shaped surface area on top of the FAD isoallaxozine ring. The chemical shift perturbation studies by titrating unlabeled *pa*-FPR into ^{15}N labeled *pa*-HO produced very small but consistent chemical shift changes for the residues located around the heme binding pocket. This result matches with the predicted protein interaction interface for *pa*-HO from the crystallography study. The chemical shift perturbation studies by titrating unlabeled *pa*-HO into ^{15}N labeled *pa*-FPR did not produce obvious chemical shift changes, likely due to the larger protein size of *pa*-FPR compared with *pa*-HO. This interesting observation of trivia chemical shift perturbation from protein titration experiments likely suggests that the complex is indeed ultra weak and the PPI is transient.

EXPERIMENTAL SECTION

i. Expression of labeled *pa*-FPR for NMR Studies

Pa-FPR was expressed and purified following previously reported protocols [*6*]. For the expression of ^{15}N labeled *pa*-FPR 1.0 L-cultures were incubated at 37 °C in a medium containing non-labeled nutrients. Upon reaching mid-log phase the cells were centrifuged and transferred to the same volume of a fresh minimal medium containing labeled $^{15}NH_4Cl$ (1.0 g/L) and cultured to an optical density at 600 nm (OD_{600}) of approximately 0.7. The culture was then transferred to a shaker incubator pre-equilibrated at 10 °C at which the cells were cultured for 30 min to allow for the thermal equilibrium. Protein expression was then induced by the addition of IPTG (0.3 mM final concentration), followed by culturing at 10 °C for approximately 14 hrs before harvesting by centrifugation. Uniformly ^{13}C and ^{15}N-labeled *pa*-FPR, [U-^{13}C, ^{15}N]-*pa*-FPR was expressed in a similar manner, except that the cells centrifuged after reaching mid-log phase were resuspended in a minimal medium containing $^{15}NH_4Cl$ (1.0 g/L) and $^{13}C_6$-D-glucose (2.0 g/L). Uniformly ^{2}H, ^{13}C and ^{15}N-labeled *pa*-FPR, [^{2}H, ^{13}C, ^{15}N]-*pa*-FPR was expressed using similar protocols, modified to meet the requirements for protein perdeuteration [*23-25*]. Prior to the expression, the ArcticExpress™ RIL cells harboring the recombinant plasmid containing the *pa-fpr* gene were adapted to grow in D_2O using a protocol similar to that reported for the expression of deuterated proteins in *P. pastoris* [*23*]. In short, cells were plated on an LB-ampicillin plate and grown at 37 °C for 16 hrs. An isolated colony from this plate was transferred to 10 mL of an LB-ampicillin medium containing 25% D_2O (v/v) and the cells were grown at 37 °C overnight. The resultant cell suspension was used to

plate LB-agar containing 25% D_2O and the cells were grown at 37 °C for 16 hrs. An isolated colony from this plate was transferred to 10 mL of an LB-Amp medium (50% D_2O v/v) to start a new cycle of adaptation. Subsequent cycles were carried out similarly and included the adaptation at 75% and 95 % D_2O. Cells grown in 95% D_2O were used to make a glycerol stab culture stock. A single colony of cells grown in an LB-amp plate made with 95% D_2O was transferred to 10 mL of LB-Amp (99.9% D_2O) and cultured at 37 °C and 220 rpm overnight. This culture was used to inoculate 100 mL (99.9% D_2O) M9 medium containing $^{15}NH_4Cl$ (1.0 g/L) and $^{3}C_6$-D-glucose (2.0 g/L) and the cells were grown at 37 °C to an OD_{600} of ~ 0.7. Fifty mL from this culture were used to inoculate 1.0 L of M9 medium (99.9% D_2O) containing $^{15}NH_4Cl$ (1.0 g/L) and $^{13}C_6$-D-glucose (2.0 g/L), and the cells were grown to an OD_{600} of ~ 0.7 at 37 °C. The culture was then equilibrated at 10 °C, followed by the induction of protein expression by the addition of IPTG (0.2 mM final concentration) and cultured at 10 °C for 30 hrs. Cell harvesting, cell lysis and enzyme purification were carried out as described previously [*27*]. Amide and side chain deuterons were exchanged for hydrogen as follows**:** pure protein was dissolved in 50 mM sodium phosphate buffer (pH 7.0) containing 8 M urea, 100 mM NaCl, and 0.1 mM FAD to a final concentration of ~ 8 μM and incubated at 37 °C for 3 hrs. This solution was dialyzed extensively against 50 mM sodium phosphate (pH 7.0) containing 100 mM NaCl, 10% (v/v) glycerol, 0.1 mM EDTA, and 5 mM DTT at 4 °C. The resultant solution was concentrated by ultrafiltration (Centricon **-**10, MW cutoff 10 kDa) to 1.0

mL and loaded onto a Sephadex G-50 column (100 cm × 1.6 cm) to remove free FAD and eluted with 50 mM sodium phosphate buffer (pH 7.0).

Selective amino acid labeling [*24-26*] of *pa*-FPR was carried out following a protocol reported previously [*27*] with some modifications [*28*]. The minimal medium used to obtain uniformly labeled protein was supplemented with the following amino acids (g/L): *L*-Ala (0.5), *L*-Arg (0.4), *L*-Asp (0.4), *L*-Asn (0.4), *L*-Cys (0.05), *L*-Gln (0.4), *L*-Glu (0.65), Gly (0.55), *L*-His (0.1), *L*-Ile (0.23), *L*-Leu (0.23), *L*-Lys hydrochloride (0.42), *L*-Met (0.25), *L*-Phe (0.13), *L*-Pro (0.1), *L*-Ser (2.10), *L*-Thr (0.23), *L*-Tyr (0.17), *L*-Val (0.23), and *L*-Trp (0.05). All amino acids except *L*-Trp and the ^{15}N-enriched amino acid were added in solid form to the media prior to autoclaving. ^{15}N-Trp was filter sterilized and added prior to inoculation. For the preparation of [^{15}N-Leu]-*pa*-FPR, 10 mL of an LB medium was inoculated with a single colony and grown overnight at 37 °C. The overnight culture was used to inoculate 1.0 L of the M9 medium supplemented as above, but not containing *L*-Leu. The cells were grown at 37 °C to an OD_{600} of ~ 0.7, equilibrated at 10 °C and supplemented with ^{15}N-*L*-Leu prior to the induction of protein expression by the addition of IPTG (of 0.2 mM final concentration)and cultured for 12~15 hrs. The same process was used to prepare *pa*-FPR labeled selectively with ^{15}N-Val, ^{15}N-Glu, ^{15}N-Phe and ^{15}N-Asp. A slight modification was needed to prepare enzyme labeled with ^{15}N-Tyr, ^{15}N-Phe and ^{15}N-Thr. In the preparation of [^{15}N-Tyr]-*pa*-FPR and [^{15}N-Phe]-*pa*-FPR, 0.25 g of glyphosate (N-phosphonomethyl-glycine) was added together with the ^{15}N-labeled amino acid to minimize isotope scrambling via aromatic amino

acid metabolism [*24*]. In the preparation of [^{15}N-Thr]-*pa*-FPR, additional 0.23 g/L of *L*-Ile and 0.115 g/L of *L*-Val were added together with the ^{15}N-Thr to minimize isotope scrambling to Ile or Val [*25*]. In the preparation of [^{15}N-Gly]-*pa*-FPR, the relatively minor scrambling from ^{15}N-Gly to ^{15}N-Ser was intentionally preserved because it was useful in the identification of cross-peaks originating from Ser residues in *pa*-FPR. Cell harvesting, cell lysis and enzyme purification were carried out as described previously [*29*].

ii. NMR Sample Preparation

Protein concentrations were determined by measuring the absorption of *pa*-FPR solutions at 450 nm (ε_{450} = 11.5 mM^{-1} cm^{-1}) [*27*]. NMR samples typically containe 0.1 - 1.2 mM *pa*-FPR, 5 - 10 % D_2O in 50 mM sodium phosphate buffer (pH = 7.0). The details of experimental conditions used for specific NMR experiments are shown in the appropriate figure captions.

iii. NMR Spectroscopy and Backbone Resonance Assignments

NMR experiments were carried out in a Bruker Avance 800 spectrometer equipped with a 5 mm TXI ^{1}H-^{13}C/^{15}N/D_{xyz} gradient probe. Two- and three-dimensional NMR experiments (^{1}H-^{15}N-HSQC, ^{1}H-^{15}N-TROSY-HSQC, HNCA, HN(CO)CA, TROSY-HNCACB, TROSY-HN(CO)CACB, TROSY-HN(CA)CO, and TROSY-HNCO) for NMR assignment were conducted at 25 °C. Amino acid selective ^{15}N-labeled *pa*-FPR: [^{15}N-Gly]-*pa*-FPR, [^{15}N-Leu]-*pa*-FPR, [^{15}N-Val]-*pa*-FPR, [^{15}N-Glu]-*pa*-FPR, [^{15}N-Phe]-*pa*-FPR, [^{15}N-Asp]-*pa*-FPR, [^{15}N-Tyr]-*pa*-FPR

and [^{15}N-Thr]-*pa*-FPR were used to acquire ^{1}H-^{15}N HSQC spectra. Two- and three-dimensional NMR spectra were processed using NMR Pipe [*30*] and analyzed with Sparky [*31*]. ^{1}H chemical shifts were referenced to the proton resonance of DSS at 0 ppm, while ^{15}N and ^{13}C shifts were referenced indirectly using the ratios 0.101329118 and 0.251449530, respectively [*32*].

a) Protein Sequential Backbone Assignment Methodology

NMR spectroscopy and X-ray crystallography are two well-developed methods capable of determining protein structure at the atomic resolution. NMR can be used to obtain protein structure in the solution phase. Because the crystal structure of *pa*-FPR has been solved (chapter III), NMR backbone assignments are capable of giving protein structure in the solution phase in context with its crystal structure. If the target protein has no available crystal structure, there are two additional steps in protein structure determination by NMR: the first uses backbone chemical shift information to predict the secondary structure (so called chemical shift indexing, CSI), and the second is the 3D structure calculation.

For each resonance signal (cross peak, or simply stated as peak) of each nucleus, the NMR spectroscopy detects three types of information: chemical environment (via chemical shift), through-bond (via scalar coupling) and through-space (via dipolar coupling) interactions. Therefore, a sequential assignment can be made from N-terminus to C-terminus for all backbone amide peaks originating from the amino acids in the protein. The strategy employed for resonance assignments

depends on the properties of the protein, for example, size, stability, secondary structure, etc.

A ^{15}N isotopically labeled NMR sample is used to acquire two dimensional (2D) ^{1}H-^{15}N Heteronuclear Single Quantum Coherence (HSQC) experiment for the purpose of evaluating the feasibility on carrying out NMR spectroscopic studies. When a protein is large in size (>20kDa), the spectrum will be crowded. Furthermore, if the protein contains a large percentage of alpha-helix secondary structure or it forms dimer or multimer in solution, the spectrum can be clustered as well. Consequently, the assignment work can be very challenging. The three dimensional NMR experiments can be used to separate the clustered signals by adding another extra dimension. A ^{13}C and ^{15}N doubly labeled protein is needed to acquire three dimensional (3D) ^{1}H-^{15}N-^{13}C heteronuclear correlation spectra and to facilitate the NMR assignments. As for the large proteins, the serious problem in the 3D NMR spectra is that many signals are very weak and broad due to either very short magnetization relaxation time or fast relaxation rate caused by slower protein tumbling from larger protein size.

There are two commonly used techniques to solve this problem: (i) protein deuteration and (ii) the transverse relaxation-optimized spectroscopy (TROSY) [*33, 34*].

The advantage of deuteration lies in the different relaxation properties of the proton and deuteron. As mentioned earlier, the NMR signal sensitivity relates to the dipole-dipole interaction between nuclei. And the dipole-dipole relaxation of nucleus

X (such as ^{1}H or D) and nucleus Y (such as ^{13}C) is related to their gyromagetic ratios (γ) and the spin quantum number (S) shown by following equation (4-1).

$$Em = -\gamma * Iz * Bo \qquad (4\text{-}1)$$

Where γ: gyromagnetic ratio, *Iz:* angular momentum quantum number, *Bo:* magnetic field vector [*35*].

The gyromagnetic ratio of deuterium (γ_D) is 4.107×10^{7} $T^{-1}s^{-1}$ and that for proton (γ_H) is 6.5 times larger (2.6752×10^{8} $T^{-1}s^{-1}$). Also, for deuterium, the spin quantum number is 1, and the number for proton is 1/2. Therefore, the total reduction of the dipolar relaxation for a deuterated sample is much higher than that for a non-deuterated sample. So the deuterated sample gives stronger and more resolved carbon signals compared with the non-deuterated sample in the 3D experiments [*36, 37*].

The transverse relaxation-optimized spectroscopy (TROSY) is a method developed by Wüthrich for the suppression of transverse relaxation (T_2) in multidimensional NMR experiments [*33*]. The rate of the transverse spin-relaxation is mainly related with the dipole–dipole coupling of the observed spin (nucleus) with other nearby spins (nuclei), and the chemical shift anisotropy (CSA). These two interactions are directly affected by the protein rotational motions in solution. Larger proteins rotate more slowly. And as a result, they have higher rates of transverse relaxation. To overcome this disadvantage, TROSY uses the CSA-relaxation at high fields to cancel the dipolar relaxation [*33*] and to cause longer T_2 values or slower

relaxation rate, therefore, to get the better signal resolution for the previous weak and broad cross-peaks.

Again sometimes even with the help of above two techniques, some signals may still be weak for some amino acids due to their dynamic properties, which also enhance relaxation rates, for example, residues located on a floppy loop or on a ligand binding site. Protein-selective amino acid labeling has also been found to be a very helpful and practical technique to advance and complement the assignment work. *Pa*-FPR has a 30 kDa molecular weight, therefore, we used above three strategies for our *pa*-FPR backbone assignment work and results are shown below.

b) 3D NMR Experiments and Data Processing Overview

As mentioned above, either ^{1}H, ^{13}C, ^{15}N triple resonance 3D experiments for ^{13}C, ^{15}N doubly labeled *pa*-FPR, or ^{2}H, ^{13}C, ^{15}N-Trosy version triple resonance 3D experiments for ^{2}H, ^{13}C, ^{15}N triply labeled *pa*-FPR are carried out under the guidance from Dr. Juan Carlos Rodriguez. The 3D experiments detect the nuclei with specific sequential correlations between intra- or inter-residual nuclei.

As shown in Figure 4-2, there are through-bond correlations via scalar coupling (in the form of magnetization transfer in the NMR experiment) from one backbone atom to another. As shown by the arrows, the amide nitrogen of residue i can correlate to neighboring carbons or protons by transferring magnetization to them; and all the different correlations can be selectively and specifically detected by different NMR experiments. Because these correlations are dominated by protein sequence, therefore they can give us sequential connectivities between amino acids

(from residue i-1, to i, to i+1, …) for backbone assignment, somewhat like "walking down" the protein sequence.

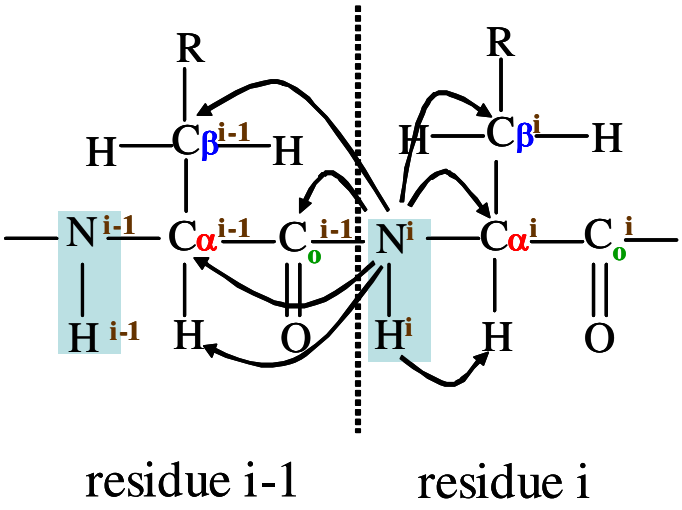

Figure 4-2. Magnetization transfer from backbone N_H of residue i to residue i-1 through bonds.

There are many 3D NMR experiments for detecting the correlation information. At least six 3D experiments are needed for accomplishing backbone assignment work: HNCA, HN(CO)CA, HNCACB, HN(CO)CACB (or CBCA(CO)NH), HNCO and HN(CA)CO. Each experiment is designed to detect the correlations between the specific carbon (C_α ,C_β and C_o or CA, CB and CO as in the 3D experiment title) and its neighboring nuclei. The HNCA experiment can detect C_α of residue i and i-1, while the HN(CO)CA can detect only C_α of residue i-1. By pairing information obtained from both experiments, one can tell the C_α cross-peak of residue i aparts from that corresponding to C_α of residue i-1. The same idea applies to other paired 3D experiments. HNCACB and HN(CO)CACB can be used to assign C_α

and C_β: HNCACB can detect both residue i and i-1, while HN(CO)CACB can only detect residue i. HNCO and HN(CA)CO are for C_o. HNCO can detect C_o of residue i and i-1 and HN(CA)CO can only detect residue i. The parenthesis in the 3D experiments suggests that the included carbon can not be detected. Because all these 3D triple resonance experiments share the same ^1H,^{15}N chemical shifts, they have the same ^1H,^{15}N HSQC spectra. Therefore, they can all be connected by the same amide peak in ^1H,^{15}N HSQC. As mentioned before, the amide strip plots of the residues can be sequentially aligned for the assignment, as shown in the illustration.

In Figures 4-3(A) and 4-3(B), the path of magnetization transfer in 3D HNCA and HN(CO)CA experiments, respectively, is illustrated. The HNCA experiment correlates the amide proton (H), the ^{15}N spin (N) and the $^{13}C_\alpha$ of residues i and i-1 (CA) into a three dimensional spectrum. The HN(CO)CA experiment detects the correlation between the ^1H and ^{15}N spins of residue i with the $^{13}C_\alpha$ spin of residue (i-1). The HN(CO)CA spectrum shows cross-peaks with coordinates ($^1H^N_i$, $^{15}N_i$, $^{13}C_\alpha$ (i-1)). The HNCA spectrum shows the same cross-peaks, but also the intra-residue ($^1H^N_i$, $^{15}N_i$, $^{13}C_\alpha$ (i)) cross-peaks. The signal containing $^{13}C_\alpha$ (i) is stronger than the signal containing $^{13}C_\alpha$ (i-1). In the HN(CO)CA, the Co frequency of residue i-1 is not measured; instead, the Co only helps in transferring magnetization. By aligning the strip plots (as shown in Scheme 4-1) of both HNCA and HN(CO)CA, we can identify the signals from C_α. Examples will be given in the later discussion.

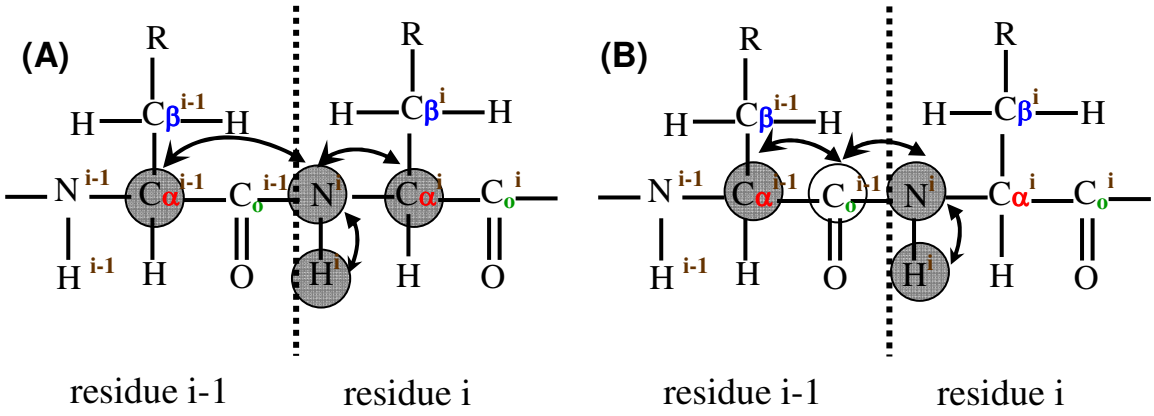

Figure 4-3. Magnetization transfer in (A) 3D HNCA and (B) 3D HN(CO)CA experiment. The gray circles show the nuclei whose chemical shifts are measured. The arrows show the transfer of magnetization. The open circle indicates that the magnetization is transferred through this nucleus, but the chemical shift is not measured.

In Figure 4-4, the magnetization transfer in 3D HNCACB and HN(CO)CACB (or CBCA(CO)NH) experiments is illustrated. The HNCACB experiment correlates both intra-residue C_α and C_β of residue i, and sequentially correlates to the C_α and C_β of residue i-1. The HN(CO)CACB (or CBCA(CO)NH) experiment only detects the sequential C_α and C_β correlation of residue i-1. The sequential connection can then be made using both the C_α and C_β chemical shifts. Together with above HNCA and HN(CO)CA, we can assign all C_α and C_β from four experiments.

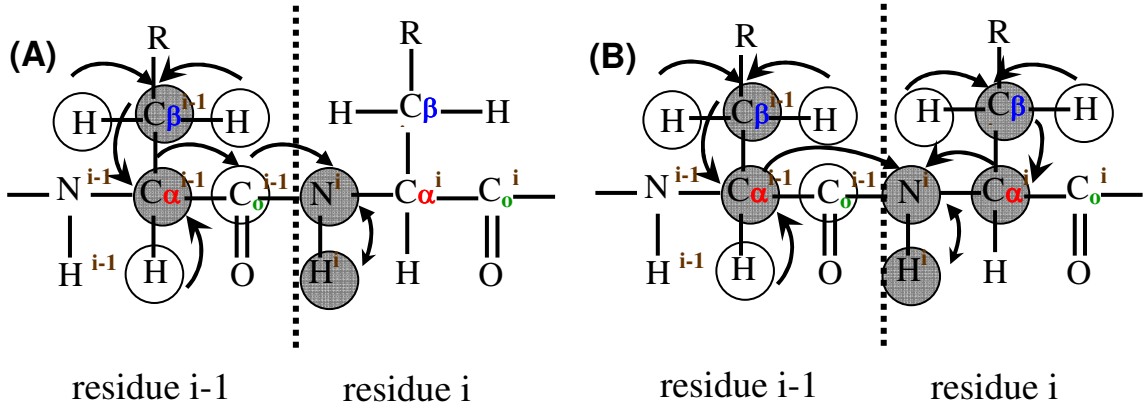

Figure 4-4. Magnetization transfer in (A) HN(CO)CACB (or CBCA(CO)NH) (B) HNCACB (or CBCANH) experiments. The gray circles show the nuclei whose chemical shifts are measured. The arrows show the transfer of magnetization. The open circle indicates that the magnetization is transferred through this nucleus, but the chemical shift is not measured.

Shown in Figure 4-5, the HNCO and HN(CA)CO experiments detect the signal from Co. HNCO experiment detects Co of residue i-1, and HN(CA)CO detects both Co of residue i-1 and Co of residue i. Like the other two experiment pairs, the pair of HNCO and HN(CA)CO experiments can give sequential connectivity for the carbonyl Co and the carbonyl Co assignment can be done by aligning the amide strips from both experiments in sequence.

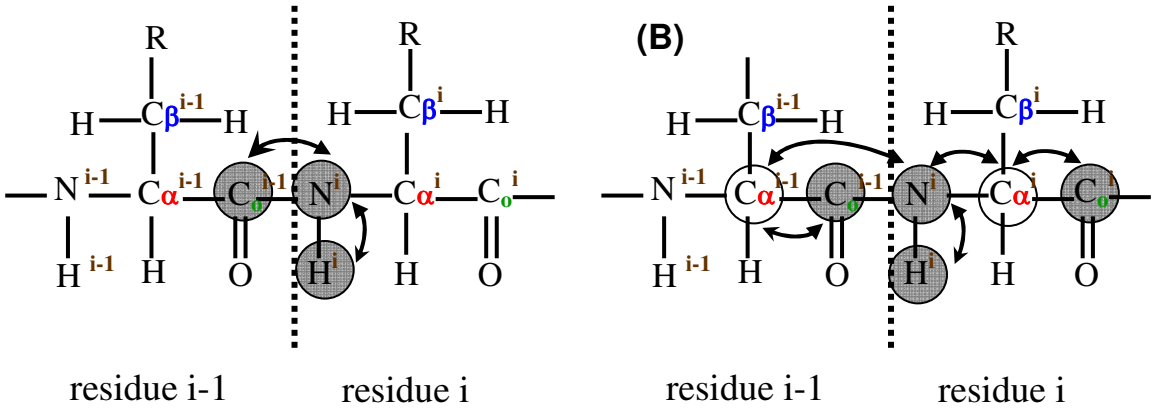

Figure 4-5. Magnetization transfer in (A) HNCO and (B) HN(CA)CO experiments. The gray circles show the nuclei whose chemical shifts are measured. The arrows show the transfer of magnetization. The open circle indicates that the magnetization is transferred through this nucleus, but the chemical shift is not measured.

Therefore, with all above three pairs of 3D experiments, all the backbone chemical shifts (H of N_H, N_H, C , C and Co) can be assigned sequentially. The procedure of doing backbone assignment is summarized in the following scheme.

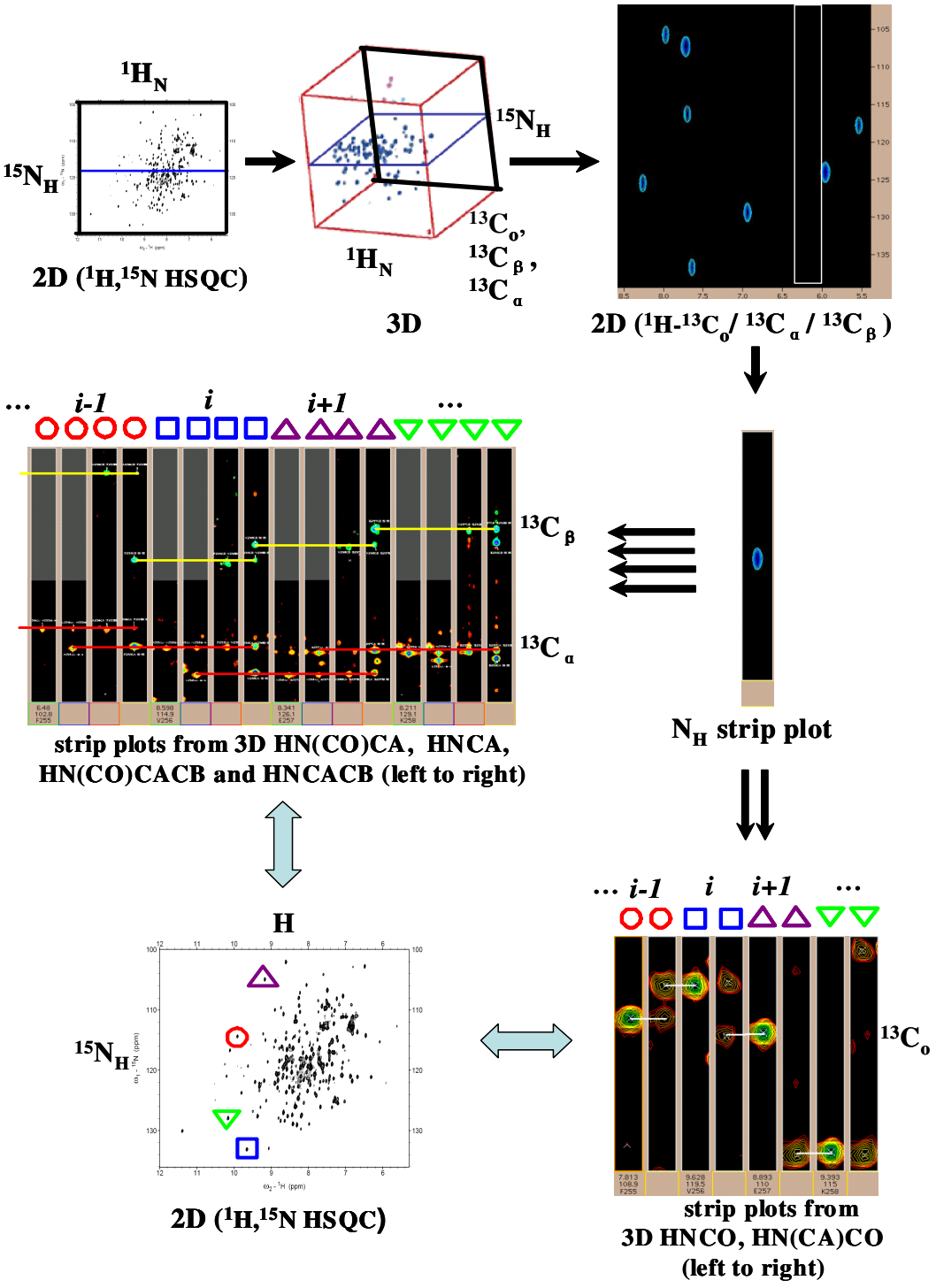

Scheme 4-1. 3D NMR Sequential backbone assignment using C-terminal F255, V256, E257 and K258 as a model (data is processed by NMR pipe and Sparky).

As shown on the 3D NMR sequential backbone assignment illustrated in Scheme 4-1, all the signals are contained in a cube instead of a plane. The 3D experiment can be viewed as the combination of a series of 2D experiments. Each 2D plane cutout along ^{15}N dimension has much less signals compared with the 2D ^{1}H, ^{15}N HSQC containing all amide peaks. Subsequently one or a few peaks can be selected out and put into a strip (usually called amide strip, as a strip of the 2D ^{1}H-$^{13}C_o$/ ^{13}C / ^{13}C cutout plane along the amide nitrogen dimension in 3D experiments, shown in Scheme 4-1). Each amide strip of the amino acid from each 3D experiment can then be aligned side by side and viewed together with other amino acids by following the protein sequence for sequential assignment. The four c-terminal residues F255, V256, E257 and K258 are given as a model to illustrate how the assignment is done. In the strip plots from 3D HN(CO)CA, HNCA, HN(CO)CACB and HNCACB (from left to right) shown in Scheme 4-1, each four strips are from one residue, and each four strips are aligned by protein sequence: residue i-1, I, i+1, …. The C_α signal of the current residue i (i is the arbitrary assignment for the residue we are currently viewing) is only seen as one peak in the HNCA and HNCACB. Its correlation to next residue i+1 is seen in all the four 3D experiments as a C_α peak with the same carbon frequency in each strip. All the six C_α peaks from the same carbon are connected by red lines. And so forth, i+1 can go to next residue. Here, taking the example of V256, it is the current residue i if we have not got the assignment yet. It has four C_α signals connected with two C_α signals at the same frequency from the previous residue i-1. Because all the C_α signals are originated from the previous C_α

of F255, this peak is assigned as ($^{1}H^{N}_{i}$, $^{15}N_{i}$, $^{13}C_{\alpha}$ (i-1)) in reference to V256. This correlation from F255 to V256 is called intra-residual correlation. An assignment note is made in white color to the peak. There is another C_{α} peak in the HNCA and HNCACB strip plots of V256, seen at a little bit lower position. That signal is originated from the C_{α} of V256. This correlation is called inter-residual correlation. Therefore, connectivity as shown in the red line is made from F255 to V256. By doing the same thing to next residue, connectivity is continued in protein sequence. That is why the assignment method is generally called the sequential assignment. The green peaks are ^{13}C peaks. They are only shown in HN(CO)CACB and HNCACB. The connectivity is made in the same way as for C_{α}. In residue i: V256, one green peak exists in HN(CO)CACB, as the same peak in HNCACB. That peak is originated from residue i-1 or F255 in this case. There is another green peak C in HNCACB strip of V256. Using the same logic, this peak can be assigned as $^{1}H^{N}_{i}$, $^{15}N_{i}$, ^{13}C (i)). The connectivity is demonstrated by the yellow line connecting the same C . Therefore, the information for C_{α} and C for these four residues is obtained. As we discussed earlier, the 3D experiment can be seen as the combination of a series of 2D experiments. Each peak in 3D experiment has chemical shifts in a format of (^{1}H, ^{15}N, ^{13}C). Therefore, each peak in 3D experiment is corresponding to a peak in 2D experiment, as shown in Scheme 4-1 by the red circle, blue square, magenta and green triangles. The chemical shift of ^{1}H and ^{15}N for each residue can be achieved as well. The last one C_{o} is detected in the other two 3D experiments: HNCO and HN(CA)CO. In residue i: V256, the white line connects the peak ($^{1}H^{N}_{i}$, $^{15}N_{i}$, $^{13}C_{o}$ (i-

1)) (the left HNCO strip plot of V256 in the scheme 1) with the peak ($^{1}H^{N}_{i}$, $^{15}N_{i}$, $^{13}C_{o}$ (i)) (the right HN(CA)CO strip plot of F255 in the scheme 1) in the 3D experiments. And in the right HN(CA)CO strip plot of V256, the same peak is seen in much weaker intensity. And a new peak at a little lower position is originated from ($^{1}H^{N}_{i}$, $^{15}N_{i}$, $^{13}C_{o}$ (i)) or V256. Its connectivity to next residue i+1(or E257) is shown by the white line. Also, the same relationship between 3D and 2D experiments applies here. Therefore, we can achieve all the chemical shift assignments (H of N_H, N_H, C_α, C_β and Co) for all the residues in protein sequence by using the same strategy. In reality, even in 3D experiments, cross-peaks can still be overlapped due to the similar chemical shifts in many cases. Also, as discussed previously, large protein size and extremely weak or broad signals from dynamic protein regions can complicate the assignment work as well. Some examples will be given in the results and discussion part.

iv. Chemical Shift Perturbation Experiments

^{1}H-^{15}N HSQC spectra were recorded at 25 °C using Varian Unity Inova 600 MHz and Bruker Avance 800 MHz spectrometers. [^{15}N]-*pa*-FPR (500 μL, 0.25 mM) in 50 mM sodium phosphate (pH 7.0, 10 % D_2O) contained in a 5 mm diameter NMR tube was titrated with a stock solution of $NADP^+$ (39 mM) dissolved in the same buffer. Titrations were carried out by the addition of 0.05, 0.10, 0.20, 0.30, 0.40, 0.50, 0.75, 1.0, 1.5, 2.0, 3.5, 5.0, 7.5, 10, 15, 20 and 25 equivalents of $NADP^+$ relative to *pa*-FPR. The pH of the solution after the addition of each aliquot of $NADP^+$ was adjusted to 7.0 prior to recording the corresponding ^{1}H-^{15}N HSQC spectrum. The

spectra were acquired at 25 °C using Varian Unity Inova 600 MHz. For the protein-protein interaction study, [^{15}N]-*pa*-HO (500 μL, 0.2 mM) in 50 mM sodium phosphate (pH 7.0, 10 % D_2O) with 2 mM NaCN contained in a 5 mm diameter NMR tube was titrated with a stock solution of *pa*-FPR protein (2 mM) dissolved in the same buffer. Titrations were carried out by the addition of 6, 12 equivalents of *pa*-FPR relative to *pa*-HO. The data were processed using NMRpipe [*30*] and analyzed using Sparky [*31*]. Similar experiments were carried out with adenosine 2'5'-diphosphate (ADP), a competitive inhibitor of ferredoxin reductase enzymes.

v. X-ray crystallography

X-ray-quality single crystals of *pa*-FPR in complex with NADP+ were grown using the hanging drop vapor diffusion method by mixing 2 μL of *pa*-FPR (20 mg/mL) dissolved in 20 mM Tris (pH 7.6) containing 10 mM $NADP^+$ with 2 μL of a solution consisting of 200 mM ammonium acetate, 100 mM sodium citrate tribasic dihydrate and 25% PEG-4000 (pH 5.6). Diffraction data were recorded at –180 °C using the rotation method on a single flash-frozen crystal [Detector: R-axis IV^{++} image plate; X-rays: CuKα, focused by mirror optics; Generator: Rigaku RU300 (MSC, The Woodlands, TX, USA)]. The cryoprotectant was 20 % ethylene glycol. X-ray data were reduced with XDS [*38*]; the program package CNS [*39*] was employed for phasing and refinement; and model building was performed with *O* [*40*]. The structure was solved by molecular replacement using the coordinates of ferredoxin oxidoreductase from *pa*-FPR (PDB entry 2QDX) as search model, stripped

of solvent molecules and ligands. Refinement was performed using data to the highest resolution with no sigma cut-off applied. Several rounds of minimization simulated annealing (2500 K starting temperature) and restrained individual B-factor refinement were carried out. Data collection and refinement statistics are summarized in Table 4-1.

Table 4-1. Summary of data collection and structure refinement[a].

Data set	FPR(FAD) – $NADP^+$ complex
Space group	$P2_12_12$
Unit cell dimensions (Å)	a=67.14 b=73.49 c=51.54 $\alpha=\beta=\gamma=90º$
Protein atoms	2037 [average B-factor = 22.5 $Å^2$]
Ligands	FAD and $NADP^+$ (101 atoms) [average FAD B-factor = 19.4 $Å^2$] [average $NADP^+$ B-factor = 24.4 $Å^2$]
Solvent molecules	288 [average B-factor = 33.1 $Å^2$]
rmsd[b] bonds (Å)	0.01
rmsd[b] angles (°)	1.7
Resolution range	20-1.90 (1.95-1.90)
Unique reflections	20561 (2895)
Completeness (%)	99.7 (99.4)
I/σI	28.45 (8.44)
R_{merge} (%)	3.8 (15.7)
R_{cryst}[c] (%)	18.1
R_{free}[d] (%)	21.8

[a] Values in parentheses refer to the highest-resolution shell.
[b] Rootmean-square deviation from ideal values.
[c] *R*cryst) 100 * ∑|*F*obs - *F*modell/∑*F*obs, where *F*obs and *F*model are observed and calculated structure factor amplitudes, respectively.
[d] *R*free is the *R*cryst calculated for randomly chosen unique reflections, which were excluded from the refinement (1234 for FPR liganded with FAD).

RESULTS AND DISCUSSION

Precedents guiding current views of hydride transfer between flavin and nicotinamide are grounded on observations made with the structure of glutathione reductase, a flavoenzyme that is functionally and structurally different from FNR [*14, 15*]. The structure of glutathione reductase shows the nicotinamide ring parallel and adjacent to the isoalloxazine ring; this relative orientation, which likely facilitates direct hydride ion transfer, is viewed as a "productive" complex. In the structures of plastidic FNRs, however, the side chain of the C'-terminal Tyr lies parallel to the flavin isoalloxazine ring, thus occupying the place that would be taken by the nicotinamide ring in a "productive" complex. Work aimed at explaining these structural observations led to the hypothesis that $NADP^+$ binding to plastidic FNRs is a two step process; with the first step involving strong interactions between the 2' adenosyl phosphate moiety and FNR, whereas the nicotinamide portion undergoes less specific interactions with the enzyme. In the second step the side chain of the terminal Tyr moves and allows the nicotinamide ring to stack parallel to the isoalloxazine ring, thus forming a transient but "productive" complex conducive to the direct hydride transfer [*16*].

In comparison, previous to this report, virtually nothing was known regarding the binding of $NADP^+$ to bacterial FPRs. Amino acid sequence alignments and the structures of *Av*- and *pa*-FPRs had demonstrated that the position occupied by the terminal Tyr in FNRs is occupied by Ala in the bacterial enzymes (A254 in *pa*-FPR), where the carbonyl oxygen of this residue stacks against the isoalloxazine ring of FAD [*6, 7*]. In addition, FPR enzymes possess a characteristic C'-terminal extension

following A254 ($AFVEK^{258}$). The effect of $NADP^+$ binding on the interaction between A254 and FAD and on the conformation of the C'-terminal extension, however, was difficult to predict. The structure of the *pa*-FPR-NADP complex reported herein provides a first view of the interactions between $NADP^+$ and *pa*-FPR. As will be shown below, analysis of the structure shows a vast network of stabilizing interactions between FAD, $NADP^+$ and the C'-terminal extension, which suggests that the gross conformational rearrangements that would be needed for placing the nicotinamide and isoalloxazine rings parallel and adjacent is not likely to occur. These observations are discussed in the context of a putative mechanism where the oxidation of NADPH by FPRs may occur via a stepwise rather than direct hydride transfer.

1. The Crystal Structure of pa-FPR-NADP shows a network of interactions encompassing FAD, $NADP^+$ and the C'-Terminal Extension

The recently reported crystal structure of *pa*-FPR [*6*] showed that the enzyme folds into a two-domain structure, typical of the ferredoxin $NADP^+$ reductase superfamily. The FAD cofactor binds in the N-terminal domain (residues 1-87), comprised of an antiparallel β-barrel (β1-β6) capped by helix α1. The stabilizing interactions between FAD and *pa*-FPR have been described in detail [*6*]; these interactions remain largely unchanged in the structure of the *pa*-FPR-NADP complex, which shows that $NADP^+$ binds in the C'-terminal domain of the β-sheet, comprised of β7, β10, the loop connecting β7 to α3, the N-terminal residues of α3 and the carboxy terminal residues $AFVEK^{258}$ (Figure 4-6).

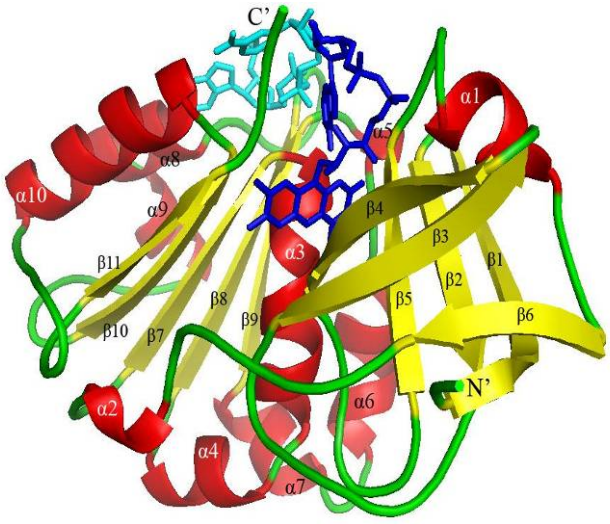

Figure 4-6. View of the structure of the *pa*-FRP bound to $NADP^+$. FAD is shown in blue, $NADP^+$ in cyan, α-helices in red, β-sheets in yellow and loops in green.

There are several stabilizing interactions between the polypeptide and the cofactor (Figure 4-7): starting at the adenine end of the $NADP^+$ molecule, the NH_2 nitrogen in this ring is within hydrogen bonding distance of the hydroxyl oxygen in Ser223 and the carboxylate group of Glu227. The 2'-phosphate (2'-P) is anchored to the enzyme via H-bonds and salt bridges to the hydroxyl oxygen of Thr181, the guanidinium NH and NH_2^+ groups in the side chain of Arg182 and the guanidinium NH group of Arg190. A salt bridge between the negatively charged oxygen in the pyrophosphate P1 group of $NADP^+$ and the guanidinium NH_2^+ group of Arg145, and a hydrogen bond between the NH group of the same side chain and the neutral oxygen in P1 stabilize this portion of the cofactor. The 1'- and 2'-hydroxyl groups in the nicotinamide ribose ring of $NADP^+$ are engaged in hydrogen bonding interactions with the adenine 3N atom and with the ribose 2-hydroxyl groups of FAD,

respectively. It is important to point out that despite the proximity suggested by these interactions, the isoalloxazine and nicotinamide rings of FAD and $NADP^+$ are separated by the C'-terminal residues. This network is expanded by π-stacking interactions between the adenine ring in FAD and the aromatic side chain of Phe255; the latter is also T-stacked against the nicotinamide ring of $NADP^+$. The nicotinamide amide NH and cabonyl groups are within hydrogen bonding distance of the carboxylate group in Glu257 and the backbone N-H of Ser 223, respectively. The carboxylate group of Glu257 expands the network by hydrogen bonding with the 1-hydroxyl group in the AMP portion of FAD. Lys258 complements the network with the electrostatic and hydrogen bonding interactions with FAD that involve the side chain NH_3^+ with the 2 pyrophosphate group and the terminal carboxylate with the 2'ribityl hydroxyl, respectively.

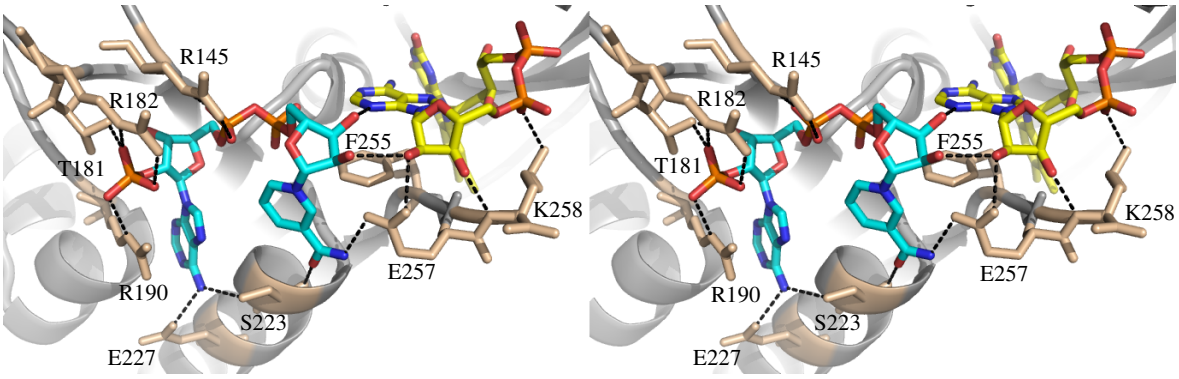

Figure 4-7. Stereoview of a portion of the structure of *pa*-FPR-NADP, highlighting the network of stabilizing interactions between the C'-terminal extension ($AFVEK^{258}$) and the cofactors. FAD is shown in yellow and $NADP^+$ in cyan, with their N, O and P atoms in blue, red and orange, respectively.

Three important observations emerge from this analysis: (1) Residues in the $AFVEK^{258}$ extension form an integral part of a complex network of interactions that

associate the FAD and $NADP^+$ cofactors with the enzyme. (2) The C'-terminal extension would have to undergo extensive conformational rearrangements to permit the formation of a "productive" complex with the nicotinamide and isoalloxazine rings stacked parallel and adjacent to one another. (3) Parallel stacking of these rings would also acquire large conformational changes in FAD, which would have to change from its bent conformation to perhaps the extended conformation characteristic of plastidic FNRs. This is unlikely because the bent conformation of FAD is stabilized by the network of interactions with $NADP^+$ and the C'-terminal extension and because the absence of a sheet-loop-sheet motif in FPRs renders the enzyme incapable of stabilizing FAD in its extended conformation.

Consequently, in the context of current models for $NADP^+$ binding to plastidic FNR enzymes, it seems unlikely that binding of the cofactor to *pa*-FPR would trigger the gross conformational rearrangement needed to allow parallel and adjacent placement of the nicotinamide and isoalloxazine rings in the *pa*-FPR-NADP complex. This in turn suggests that formation of a "productive" complex, in the sense of $NADP^+$ binding to plastidic FNR, is not likely to occur with a frequency (μs-ms) conducive to catalytical competence.

2. The Structure of pa-FPR Harbors a Pre-Formed $NADP^+$ Binding Pocket

The binding of $NADP^+$ brings about relatively minor structural changes to *pa*-FPR, as can be seen in the per-residue plot of ΔC_α (4-8(A)), obtained by aligning the structures of *pa*-FPR and *pa*-FPR-NADP. The largest differences in C_α position, taken as $\Delta C_\alpha > 1.5$ times the average rmsd (0.47 Å) obtained from the alignment, are

localized in the N-terminal of helix α10 (residues 221-225), the middle of the loop connecting α10 to β11 (residues 242-244) and the carboxy terminal Lys 258. Among the affected amino acids, residues 221-225 and 258 are located in close proximity to the bound $NADP^+$, whereas residues 242-244 are distant; the differences in C_α position seen for the latter are likely a consequence of the higher than average B-factors exhibited by these residues. Figures 4-8(B) and 4-8(C) illustrate a portion of the surface of *pa*-FPR and *pa*-FPR-NADP, respectively. The side-by-side comparison reveals that the surface of *pa*-FPR has a pre-formed cavity where the $NADP^+$ cofactor binds to form the *pa*-FPR-NADP complex with minimal perturbation of the *pa*-FPR structure.

It is well known that $NADP^+$-dependent enzymes can't substitute this cofactor for NAD^+, a fact that is also evident in the negligible catalytic activity observed with *pa*-FPR when NADPH is replaced with NADH [*6*]. Site directed mutagenesis studies indicated that stabilization of the 2'-P in $NADP^+$ contributes significantly to the mechanism whereby NADP(H) dependent FNR enzymes discriminate against NAD(H) [*41, 42*]. In this context, it is interesting that in the crystal structure of *pa*-FPR a sulfate anion (from the crystallization solution) is nearly isostructural with the 2'-P group of $NADP^+$ in the crystal structure of the *pa*-FPR-NADP complex. This is illustrated in Figure 4-8, where the sulfate in the structure of *pa*-FPR (Figure 4-8(D)) exhibits interactions nearly identical to those shown by the 2'P group in the structure of the *pa*-FPR-NADP complex (Figure 4-8(E)). These observations are in good agreement with the idea that the structure of *pa*-FPR harbors a pre-formed binding

pocket, where residues involved in important contacts with the 2'P group of $NADP^+$ require little or no rearrangement to accommodate the cofactor. Among these residues, R182 and R190 are conserved in bacterial subclass II reductases, Thr181 is conserved in bacterial subclass I enzymes and substituted for Ser in plant reductases (Ser223 in spinach FNR) and R182 is conserved in all enzymes with known sequence.

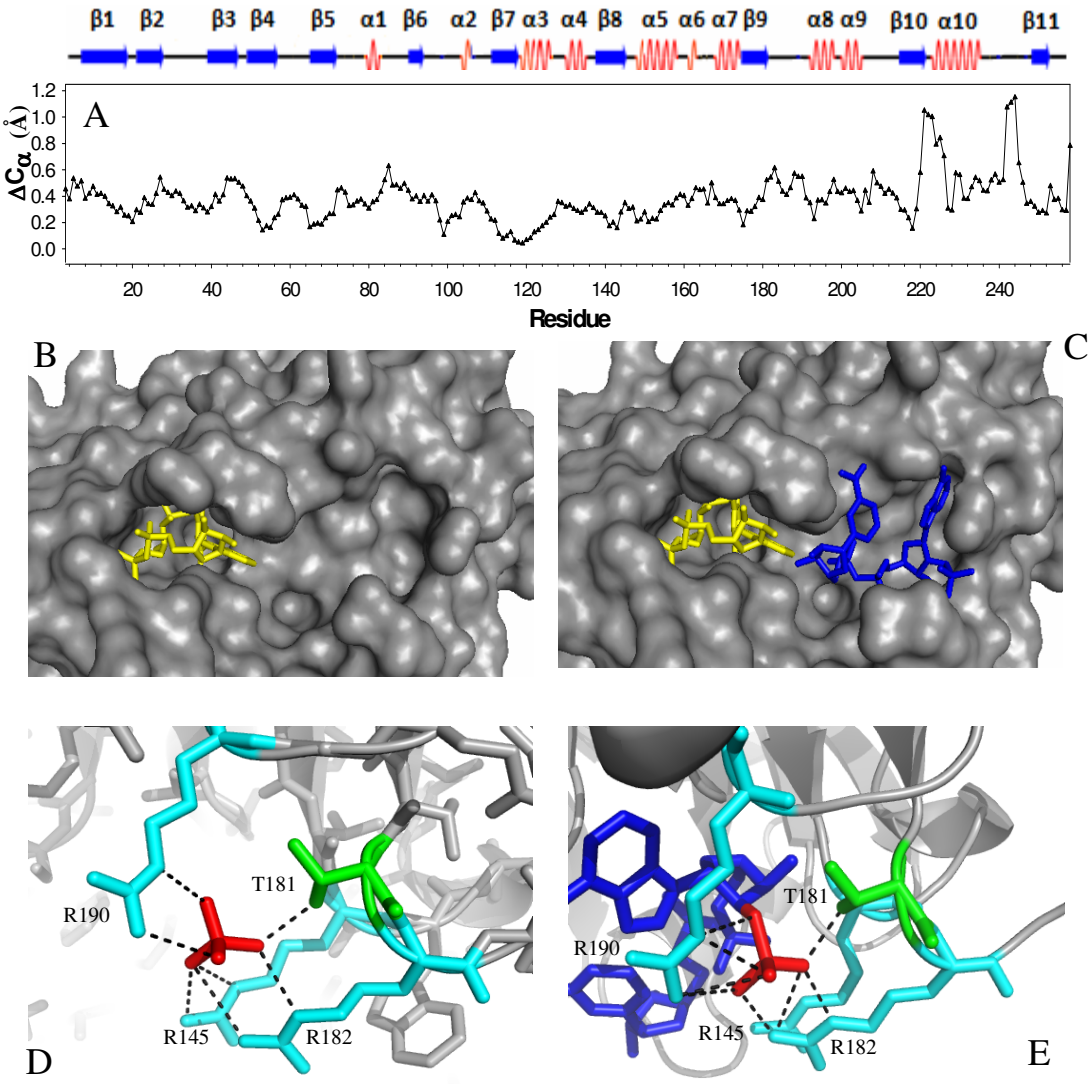

Figure 4-8. (A) Per residue plot of the difference in the position of alpha carbons (ΔC_α) obtained upon aligning the structures of *pa*-FPR and that of its $NADP^+$ complex. The average RMSD is 0.47 Å. (B) Close-up view of the empty "NADP-binding pocket" on the surface of *pa*-FPR; the FAD is rendered in yellow sticks. (C) Equivalent view, obtained from the structure of the *pa*-FPR-NADP complex, highlighting $NADP^+$ (blue sticks) lodged in its binding pocket. (D) The structure of pa-FPR displays a sulfate ion (red) from the crystallization buffer that occupies the position of the 2'-phosphate group in the *pa*-FPR-NADP complex (E). Note that the interactions exhibited by the phosphate and sulfate ions are nearly identical.

3. Assignment of Amide Backbone Resonances from pa-FPR

NMR spectroscopy studies were carried out to obtain complementary information in solution regarding the binding of $NADP^+$ to *pa*-FPR. Before these investigations could begin, however, it was necessary to obtain sequential backbone resonance assignments. The relatively large molecular weight of the enzyme (29,518 Da) posed some challenges. These were overcome with the strategy described below. The ^1H-^{15}N HSQC spectrum of *pa*-FPR acquired at 25 °C from a 1.2 mM solution of *pa*-FPR in 50 mM sodium phosphate buffer, pH 7.0 is shown in Figure 4-9(A). These conditions were chosen for the NMR spectroscopic studies because they completely eliminate the slow precipitation of the enzyme when its concentration exceeds 1.5 mM or when the samples are exposed to temperatures above 25 °C for 24 hrs or longer. The spectrum exhibits relatively well dispersed cross-peaks, despite the relatively large molecular weight of the enzyme. Conventional heteronuclear 2D and 3D NMR experiments (see Experimental) carried out with a sample of *pa*-FPR uniformly labeled with ^{13}C and ^{15}N did not yield enough information to permit full sequential assignments. This is mostly because many residues exhibited weak or absent beta carbon (C_β) correlations in TROSY-HNCACB and TROSY-CBCA(CO)NH experiments, which is attributed to efficient transverse relaxation brought about by the dipolar interactions between carbons and their attached protons [*43*]. This problem was circumvented by preparing a sample of [U-^2H, ^{13}C, ^{15}N]-*pa*-FPR, which was used to acquire TROSY-HNCACB and TROSY-CBCA(CO)NH experiments for subsequent use with the data obtained from the suite of experiments

obtained with [U-^{13}C, ^{15}N]-*pa*-FPR. This approach allowed us to assign approximately 85% of the non-proline residues in the enzyme. With respect to [U-^{2}H, ^{13}C, ^{15}N]-*pa*-FPR, it should be noted that although most of the exchangeable deuterons exchanged for protons during their purification, several residues are clearly protected from exchange because a number of cross-peaks displayed low-intensity or were absent when the HSQC spectrum of [U-^{2}H, ^{13}C, ^{15}N]-*pa*-FPR was compared with that obtained from a sample of [U-^{15}N, ^{13}C]-*pa*-FPR. Deuterons protected from exchange under native conditions were exchanged by dissolving the triply labeled sample in a urea containing solution, followed by dialysis in the presence of FAD. This unfolding/refolding procedure resulted in complete replacement of exchangeable deuterons for protons, as indicated by the fact that the TROSY-HSQC spectrum of the resultant enzyme is identical to that obtained with doubly labeled *pa*-FPR.

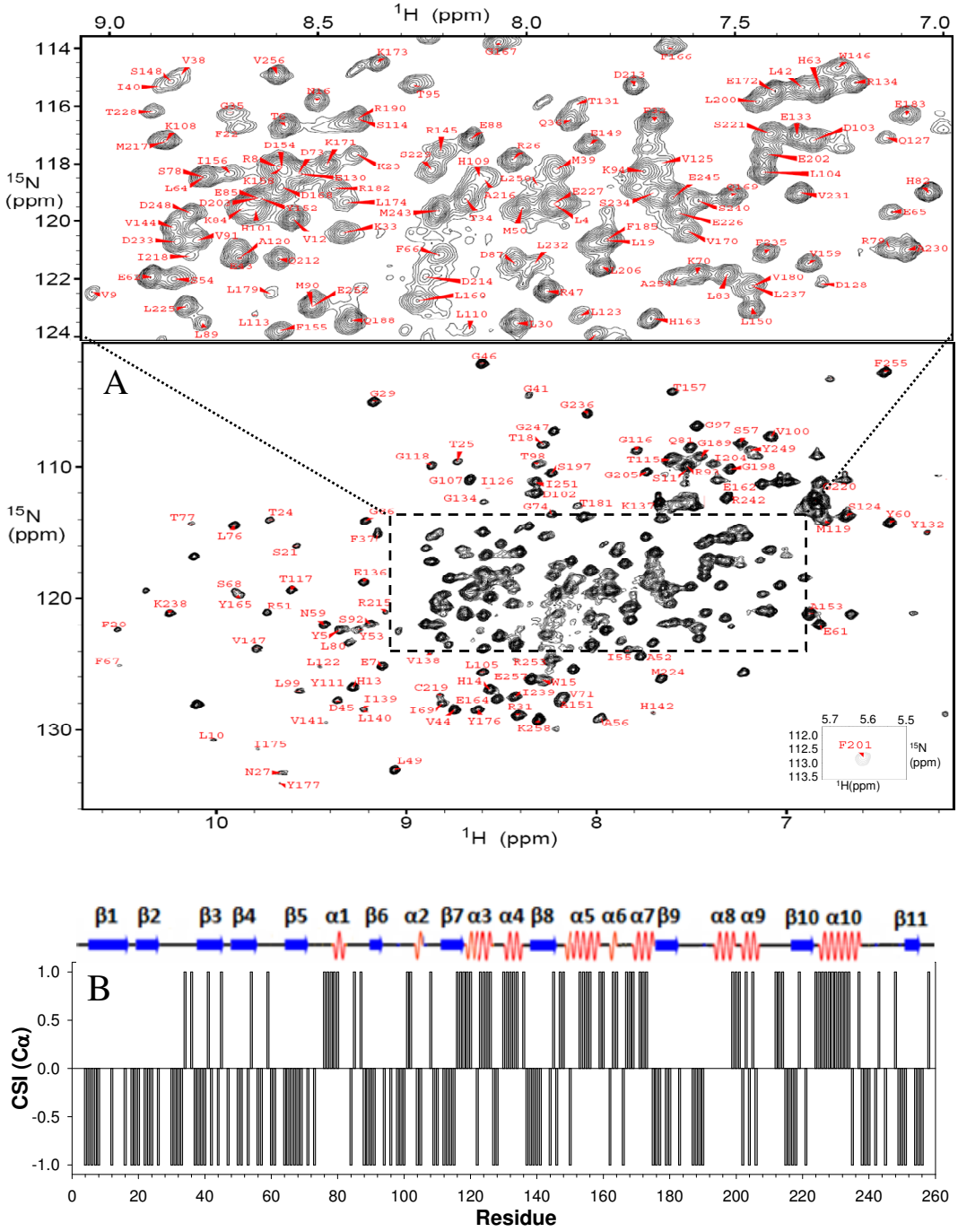

Figure 4-9. (A) ^{1}H-^{15}N HSQC of 1.5 mM [U-^{13}C,^{15}N]-*pa*-FPR in 50 mM sodium phosphate, pH 7.0, and 6% D_2O, obtained at 25 °C using a Bruker Avance800 NMR spectrometer. Complex points, 256 (^{1}H) x 2048 (^{15}N); spectral width, 14.4 kHz (^{1}H) and 3.3 kHz (^{15}N); 4 scans per increment, recycle delay 0.8s. (B) Secondary structure in *pa*-FPR inferred from chemical shift indexing (C_α), which can be compared to secondary structure inferred from the X-ray crystal structure (top).

Additional assignments were obtained by incorporating amino acid-selective ^{15}N labeling into *pa*-FPR. This strategy has been successfully utilized in our laboratories to complete the sequential backbone resonance assignments of a paramagnetic, highly helical heme oxygenase from *P. aeruginosa* [*44*]. In the context of assigning the backbone resonances from *pa*-FPR, selective labeling was important in our strategy for two main reasons. (1) Because isotopic scrambling was virtually undetectable, the amino acid identity corresponding to well-resolved cross peaks in the HSQC spectrum of each selectively labeled protein could be readily established in the HSQC spectrum obtained with [U-^{15}N]-labeled enzyme by simple comparison. This information was subsequently used in conjunction with the backbone connectivities derived from the suite of three-dimensional experiments described above in order to make the sequential assignment. This approach was essential to assign stretches in a sequence where spin systems of key residues within a segment could not be identified due to poor detection of C resonances. (2) The simplicity of HSQC spectra obtained from amino acid-selective ^{15}N-*pa*-FPR allows identification of cross-peaks that can be easily overlooked in the spectrum of [U-^{15}N]-labeled samples, because of overlap with other resonances or due to relative low intensity. For instance, in the HSQC spectrum of ^{15}N-Gly-*pa*-FPR the cross-peak in red corresponds to G205 (Figure 4-10). The same cross-peak is located in a crowded section of the spectrum obtained with [U-^{15}N]-labeled enzyme and thus it had been overlooked. Its definitive identification in the spectrum of the ^{15}N-Gly-*pa*-FPR allowed its subsequent sequential assignment with the aid of the suite of three-dimensional experiments described above. In the end, the combined strategies

allowed us to make 95% of backbone assignments in *pa*-FPR, not counting Pro; these assignments are summarized in Table S4-1.

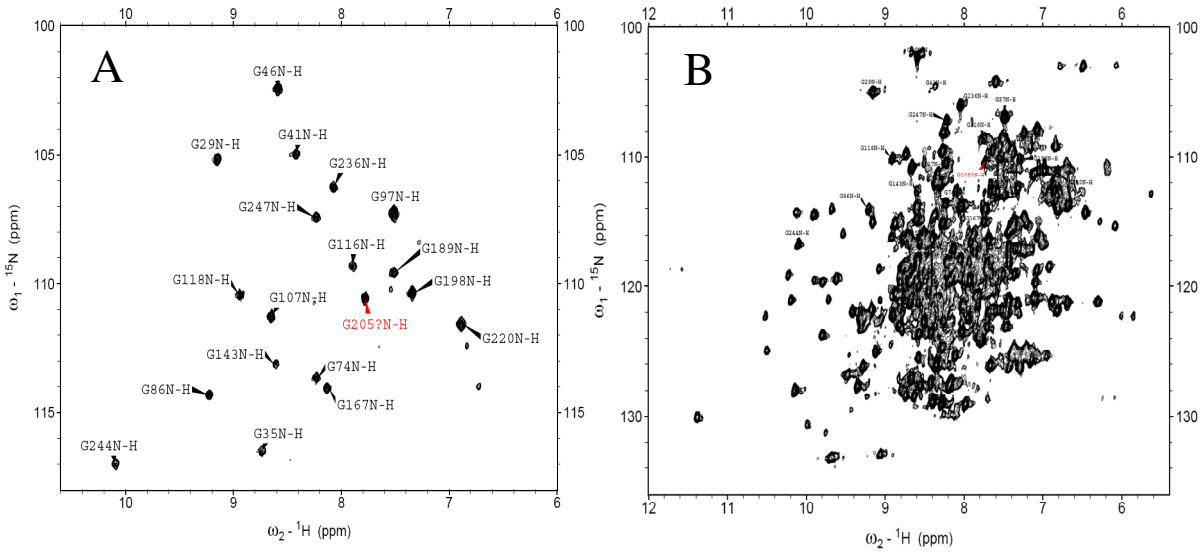

Figure 4-10. [^{1}H-^{15}N]-HSQC of ^{15}N-Gly selectively labeled *pa*-FPR in (A) compared with fully [^{1}H-^{15}N]-HSQC of [U-^{15}N] -labeled *pa*-FPR in (B). The labels are only for Gly.

Once assigned, the backbone chemical shifts were used to identify elements of secondary structure in solution by chemical shift indexing (CSI) [*45, 46*]. Results obtained from this process carried out with C chemical shifts have been plotted per residue in Figure 4-9(B), where they are compared with elements of secondary structure obtained from the crystal structure of *pa*-FPR using the program DSSP (http://swift.cmbi.ru.nl/gv/dssp/) [*38*]. It is apparent that secondary structure identified with the aid of NMR spectroscopic studies in solution is consistent with secondary structure obtained from the enzyme in crystal form. The most significant differences are in residues 191-197 (8) and residues 199-204 (9). The backbone resonances of residues in 8 were not assigned, most likely because the NH cross-

peaks of these residues are very weak or unobservable in HSQC spectra, due to line broadening brought about by segmental dynamic behavior. Cross-peaks from residues 199-204, although observable, are significantly less intense than average, suggesting that these residues are also affected by dynamic conformational exchange. Hence, it is likely that this segment of the structure in solution is conformationally averaged between helical and disordered states; the fact that 8 and 9 are flanked by loops likely facilitates this segmental dynamic behavior. Interestingly, the crystal structure of the *pa*-FPR-NADP complex shows that 8 and 9 are in close proximity to the $NADP^+$ binding site, which suggests the possibility that local conformational plasticity prepares the enzyme to bind the NADP(H) cofactor.

4. Probing the Binding of $NADP^+$ to pa-FPR in Solution by NMR Chemical Shift Perturbations

The binding of $NADP^+$ to *pa*-FPR was studied by titrating $NADP^+$ into a solution containing ^{15}N-labeled *pa*-FPR, while monitoring induced chemical shift perturbations of amide ^1H and ^{15}N resonances with the aid of ^1H-^{15}N-HSQC spectra. The titration induced chemical shift perturbations larger than two times the average of the weighted chemical shift perturbation (0.12 ppm) in 22 cross-peaks, a characteristic that identifies the corresponding residues as potential sites of interaction with $NADP^+$. The $NADP^+$-dependent gradual shift of cross-peaks indicates that interconversion between $NADP^+$-bound and free forms of the enzyme is fast relative to the NMR timescale (*i.e.* fast exchange). The titration also caused the disappearance of 18 cross-peaks, which is likely a consequence of exchange between

bound and free forms at rates approximately equal to the chemical shift timescale (*i.e.* intermediate exchange). Cross-peaks exhibiting gradual chemical shift perturbations have been plotted per-residue (black in Figure 4-11(A)), together with cross-peaks that disappear upon the addition of $NADP^+$ (red in Figure 4-11(A)). The plot makes it evident that those residues whose chemical shifts exhibit gradual chemical shift perturbations (fast exchange) are clustered with residues whose chemical shifts disappear during the titration, which strongly suggests that line broadening of the latter is a consequence of binding interactions that trigger dynamic events taking place in the intermediate exchange regime. The $NADP^+$-dependent chemical shift perturbation of cross-peaks in fast exchange has been plotted for several representative amino acids (V144, W146 and V147) in Figure 4-12 and the curve fitted to a model where one molecule of *pa*-FPR binds one molecule of $NADP^+$. This analysis reveals an average dissociation constant (K_d) of 24 μM, a value similar to that reported for the binding of $NADP^+$ to spinach FNR (14 μM) at lower ionic strength [*47*].

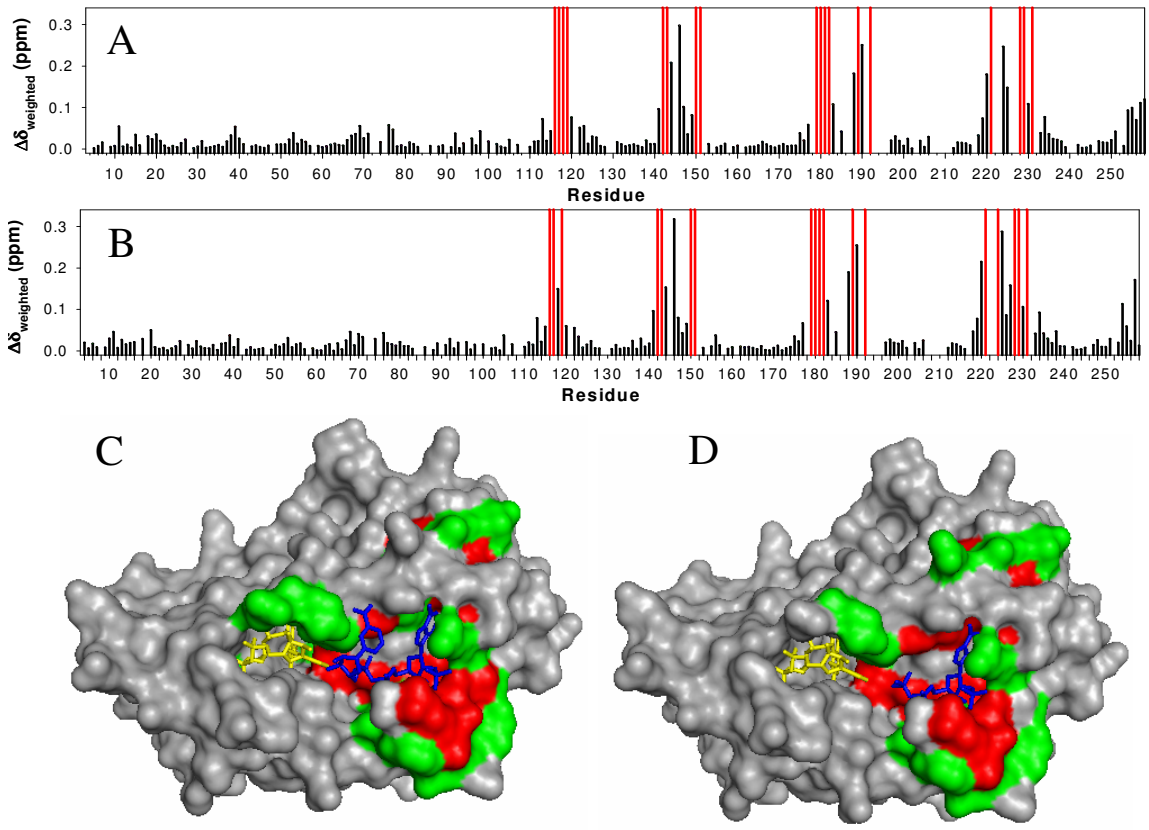

Figure 4-11. (A) Per-residue plot of weighted chemical shift perturbations (black lines) obtained upon titration of a solution of *pa*-FPR with a solution of $NADP^+$ (A) and with a solution of ADP (B). The weighted values of chemical shift perturbations were obtained from $\Delta\delta_{weighted} = \sqrt{[(\Delta\delta N/5)^2 + \Delta\delta H^2]/2}$ [*48*]. The red lines in the plot correspond to residues whose corresponding cross-peaks decreased in intensity and disappeared during the titration. (C) Residues whose corresponding cross-peaks exhibited gradual chemical shift perturbations during the titration with $NADP^+$ are highlighted green on the surface of the *pa*-FPR-NADP complex, whereas those residues whose cross-peaks decreased in intensity and disappeared during the titration are highlighted in red. FAD and $NADP^+$ are rendered in yellow and in blue sticks, respectively. (D) Residues whose cross peaks were affected during the titration of *pa*-FPR with ADP have been highlighted as in (C).

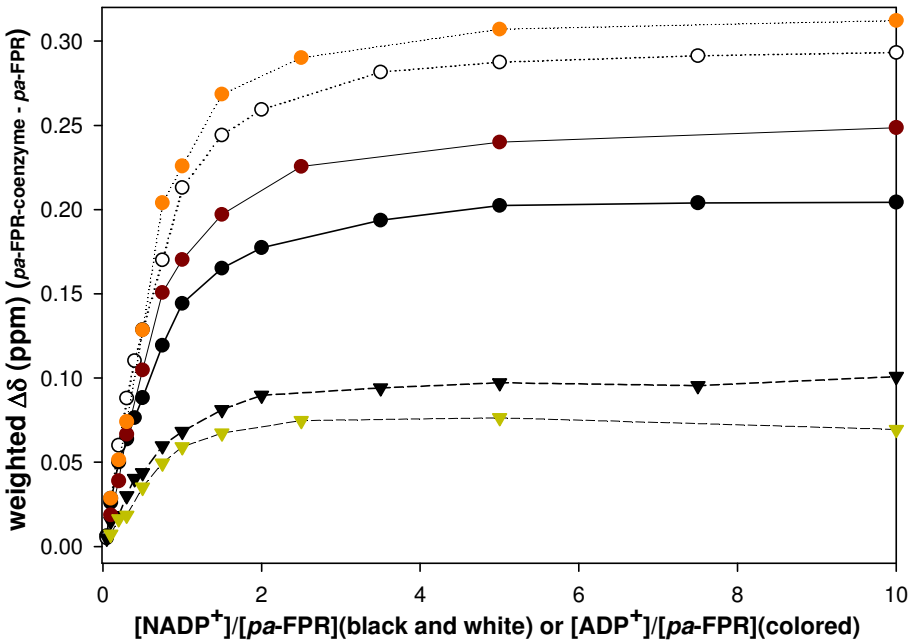

Figure 4-12. Chemical shift perturbations observed upon titrating [15N]-*pa*-FPRP with $NADP^+$ and with ADP. The plots represent W146, V144 and V147, from top to bottom. These three are used to estimate the *pa*-FPR coenzyme dissociation constant. (24±3μM for $NADP^+$), (32±3μM for ADP).

Residues whose N-H cross-peaks exhibit weighted chemical shift perturbations larger than (0.08 ppm) upon titrating *pa*-FPR with $NADP^+$ are highlighted in green on the X-ray crystal structure of the *pa*-FPR-NADP complex (Figure 4-11(C)), whereas residues whose N-H cross-peaks disappear are highlighted in red. It is reassuring that the chemical shifts of amide cross-peaks corresponding to residues identified in the crystal structure as being in close proximity to $NADP^+$ are perturbed by the presence of $NADP^+$. Amongst these, cross-peaks from residues interacting with the 2'-P group of $NADP^+$, Thr181, Arg182 and Arg190 (see Figure 4-7), are broadened and disappear due to exchange in the intermediate regime, whereas the cross-peak originating from Glu257, which interacts with the amide NH_2

group of the nicotinamide ring exhibits perturbations in the fast exchange regime. Cross peaks for Arg145 and Ser223, which interact with the pyrophosphate group P1, and with both the nicotinamide amide and the 2'P groups of $NADP^+$, respectively, have not been assigned. A comparison of the X-ray crystal structures of *pa*-FPR and *pa*-FPR-NADP has been made in Figures 4-8(B) and 4-8(C), which shows that the structure of *pa*-FPR has a pre-formed "$NADP^+$ binding pocket" where the cofactor binds with minimal perturbations on the structure of the enzyme. In Figure 4-11(C), the cofactors have been rendered in sticks to illustrate the fact that residues comprising the "internal walls" of the "$NADP^+$ binding pocket" are highlighted in red and green. This observation indicates that the surface of interaction in the structure of $NADP^+$ includes the "internal walls" of the "$NADP^+$ binding pocket", and demonstrates that the chemical shift perturbations and line broadening effects brought about by the binding of $NADP^+$ in solution delineate a binding surface highly consistent with that observed in the crystal structure. Hence, observations made with the enzyme in solution also indicate that the structure of *pa*-FPR harbors a pre-formed "$NADP^+$ binding pocket".

Current models of NADP(H) binding to plastidic FNRs propose that parallel stacking of the nicotinamide ring onto the isoalloxazine ring to form a "productive" complex for direct hydride transfer requires displacement of the side chain from the terminal Tyr. Equilibrium binding studies conducted with spinach FNR revealed that its binding affinity for $NADP^+$ is approximately seven times lower than its affinity for adenonsine 2',5'-diphosphate (ADP) [*47*], which lacks the nicotinamide nucleotide

moiety. These observations have been interpreted in the context of the binding model to support the idea that NADP(H) binding to plastidic FNRs is a two-step process, with the first step involving strong interactions between the 2'adenosyl phosphate and FNR, and the second step requiring displacement of the terminal Tyr to allow the nicotinamide ring to stack parallel to the isoalloxazine ring of FAD. In this model, the second step, which is thought to be energetically costly, has been invoked to explain the higher affinity of FNR for ADP relative to $NADP^+$ [*16, 49*]. It was therefore of interest to examine the binding of ADP to *pa*-FPR and compare the results with those described above for the binding of $NADP^+$. Hence, ADP was titrated into a solution containing ^{15}N-labeled *pa*-FPR, while monitoring induced chemical shift perturbations in ^1H-^{15}N-HSQC spectra. Remarkably, titration with ADP revealed a pattern of perturbed residues (Figure 4-11(B)) nearly identical to the pattern obtained upon binding of $NADP^+$ to *pa*-FPR (Figure 4-11(A)). This fact is also evident in the corresponding color coded representation obtained by mapping residues whose cross-peaks exhibit chemical shift perturbations (green) and line broadening effects (red) on the structure of *pa*-FPR-NADP (Figure 4-11(D)). Chemical shift perturbations induced by addition of ADP to *pa*-FPR for several representative amino acids (V144, W146 and V147) have been plotted and fitted to a simple one site saturation ligand binding equation using software SigmaPlot 9.0. This process reveals an average K_d of 32 μM, a value that is slightly larger than that measured for the *pa*-FPR-NADP complex (see above). The similarity in the magnitudes of K_d obtained for the binding of $NADP^+$ and the competitive inhibitor

ADP indicates that stabilization of the *pa*-FPR-NADP complex is derived mainly from interactions between the polypeptide and the adenosine 2', 5'-diphosphate moiety in $NADP^+$. In contrast to observations made with spinach FNR, however, the binding affinity of *pa*-FPR for $NADP^+$ is slightly larger than its affinity for ADP, which indicates that the nicotinamide nucleotide moiety does not undergo destabilizing interactions with the enzyme, as is thought to be the case in the binding of $NADP^+$ to plastidic FNRs. It is therefore likely that $NADP^+$ binding to *pa*-FPR occurs in one step, rather than two, as is thought to be the case when it binds to FNRs.

As pointed out above, the X-ray crystal structure of *pa*-FRP revealed a network of interactions involving the C'-terminal extension and the two cofactors, strongly suggesting that the C'-terminal sequence of *pa*-FPR is not likely to be displaced readily in order to allow parallel stacking of the nicotinamide and isoalloxazine rings. This notion was probed in solution by acquiring ^1H-^{15}N-HSQC spectra of *pa*-FPR, *pa*-FPR-NADP and *pa*-FPR-ADP at different temperatures (35 °C, 25 °C and 15 °C). Cross-peaks corresponding to the $AFVEK^{258}$ sequence exhibit ^1H linewidths very similar to the average ^1H linewidth at each of the temperatures in all spectra, suggesting that the C'-terminal extension is unlikely to undergo significant conformational changes, in the presence or in the absence of $NADP^+$.

5. Potential Implications to the Mechanism of NADPH Oxidation by FPRs

The above-described observations suggest that conformational reorganization of the C'-terminal peptide and of the $NADP^+$ and FAD cofactors to allow formation of a "productive" complex for direct hydride transfer is unlikely to take place in the

pa-FPR-NADP complex. In this context, it is important to consider that extensive fundamental investigations of the mechanism of NAD(P)H oxidation have demonstrated that hydride transfer can also occur in a stepwise manner by sequential electron-proton-electron transfer [*50-59*] (Equation 4-2). These investigations documented the formation of radical cations and radicals of NAD(P)H and its

$$\mathrm{NAD(P)H + A \rightarrow NAD(P)H^{\bullet+} \cdots A^{\bullet} \rightarrow NAD(P)^{\bullet} \cdots AH^{\bullet+} \rightarrow NAD(P)^{+} + HA} \qquad (4\text{-}2)$$

analogues similar to the middle two species in Equation 4-1, which have been characterized with the aid of electronic absorption and EPR spectroscopic methods. The formation and detection of these reactive species indicated that the oxidation of NAD(P)H and its analogues can occur stepwise via electron-proton-electron transfer of hydride, if the acceptor is also capable of undergoing a stepwise two electron reduction. This point has been recently underscored with the EPR and electronic absorption spectroscopic detection of a radical cation of an NADH analogue in the thermal two-electron reduction of a quinone [*50*]. Moreover, it has also been demonstrated that in the absence of H_2O_2, the oxidation of NADH by native horseradish peroxidase (HRP) begins with single-electron transfer from NADH to ferric HRP to form the $NADH^{\bullet+}$ radical cation and ferrous peroxidase [*54*]. A similar stepwise oxidation of NADPH is thought to be operative in the rescue of inactive catalase [*60*]. Hence, under appropriate circumstances the oxidation of NAD(P)H by sequential electron-proton-electron transfer of hydride is a viable alternative mechanistic path to the well-known direct mechanism involving synchronous transfer of a proton and two electrons.

It has also been established that long-range (up to 30 Å) electron transfer through proteins occurs via tunneling pathways, which involve dominant bonding and nonbonding interactions coupling donor and acceptor. Coupling through covalent and hydrogen bonds is stronger than coupling through van der Waals gaps [*61-63*], and these differences in the details of specific paths involved in distinct systems account for the dependence of electron transfer rates on the particular aspects of the protein structure that mediate coupling of donor and acceptor [*63*]. In this frame it is interesting that the structure of the *pa*-FPR-NADP complex places C4 of the nicotinamide ring 14.5 Å away from C5 of the isoalloxazine ring. Further inspection of the structure suggests a "tunneling pathway" connecting the nicotinamide ring in NADP(H) with the isoalloxazine ring in FAD. This putative path (Figure 4-13(A)) can be thought to start with the T-stacking of the nicotinamide and Phe255 rings, continue along Phe255 into Ala254 across the peptide bond and finally communicate with the isoalloxazine ring via the Ala254 carbonyl oxygen, which is 2.93 Å from the N10 and 3.93 Å from the N5 atom in the isoalloxazine ring. In this putative mechanism, electron tunneling from the nicotinamide to the isoalloxazine ring would form an NADPH cation radical analogous that shown in Equation 4-2. Radical cations of NADH model compounds are known to be significantly more acidic than their neutral precursors [*57*], thus, the NADPH cation radical formed upon tunneling of one electron would be expected to lose a proton thereby forming an NADPH radical similar, as shown in Equation 4-2. Tunneling of a second electron from the latter would form the

closed shell $NADP^+$. Accordingly, the electron acceptor, FAD, can be reduced in two sequential one-electron and one proton transfer reactions [*64, 65*]. In the context of a stepwise, electron-proton-electron, hydride transfer, it is also interesting to note a network of structural water molecules which may facilitate proton translocation from NADPH to FAD (Figure 4-13(B)).

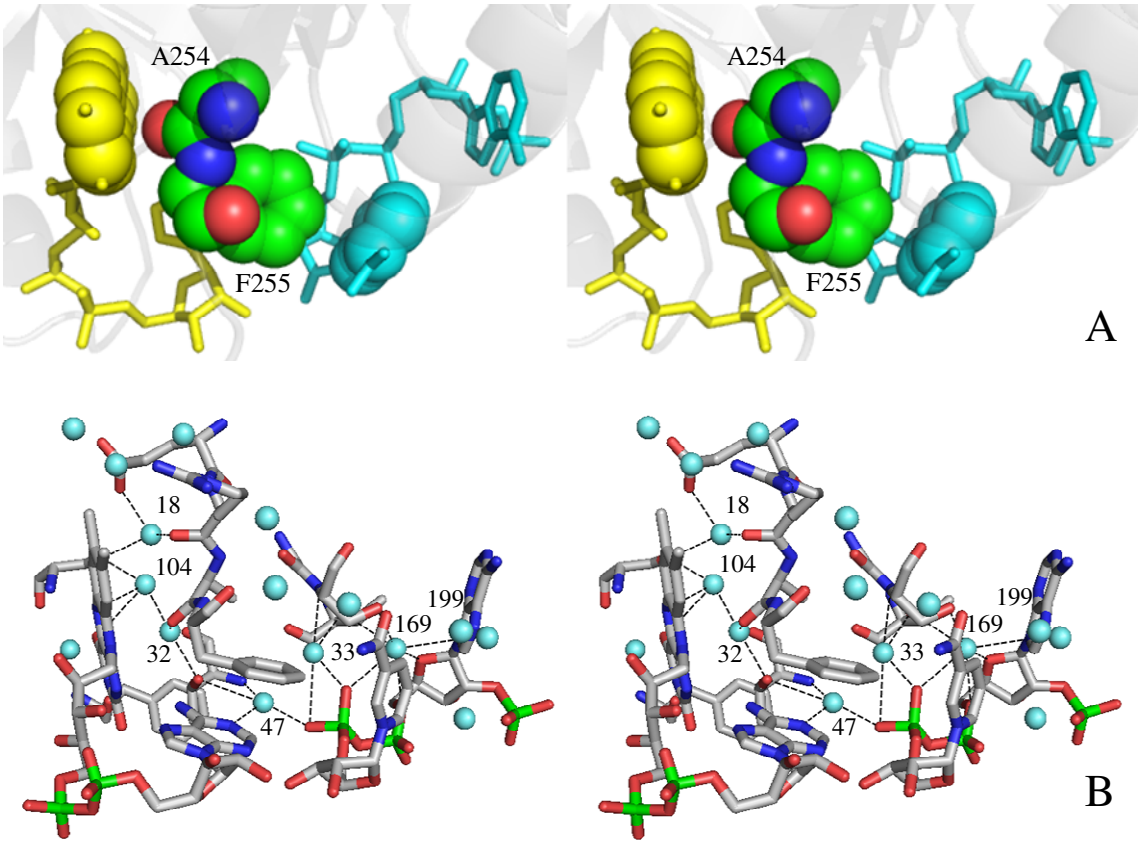

Figure 4-13. Stereoviews of (A) possible "electron tunneling path" which starts with the T-stacking of the nicotinamide ring (cyan) and Phe255 aromatic side chain, continues across the peptide bond into Ala255 and across its carbonyl oxygen into the isoalloxazine ring of FAD (yellow). (B) Several structural waters network the nicotinamide and isoalloxazine reactive sites, which suggest a possible path for proton translocation.

It is important to emphasize that one-electron reduction of $NAD(P)^+$ analogues does not result in an overall hydride ion addition in the same manner in which one-electron oxidation of NAD(P)H triggers a multistep hydride ion release [*53*]. Hence, the proposed mechanism of NADPH oxidation by FPR enzymes is consistent with the fact that these enzymes function by exclusively oxidizing the cofactor, unlike their plastidic counterparts, which function in the "normal" sense by reducing $NADP^+$ via hydride transfer from $FADH_2$ or in the "inverse" sense by oxidizing NADPH. It is therefore possible that the need to reduce $NADP^+$ has placed evolutive pressure on the structure of plastidic FNRs to allow parallel placement of the nicotinamide and isoalloxazine rings for direct hydride transfer and reduction of $NADP^+$. In comparison, the function of FPR enzymes, which is solely the oxidation of NADPH, was acquired with minor modifications of the C'-terminal domain, which makes the direct transfer of hydride ($NADP^+$ reduction) unlikely but permits a multistep hydride transfer (NADPH oxidation) operative. These ideas, which stem from the X-ray crystallographic and NMR spectroscopic observations of the *pa*-FPR-NADP complex, have to be tested experimentally. Their discussion in this report is aimed at providing a frame of ideas consistent with experimental observations and to stimulate future experimentation directed at elucidating the mechanism of NADPH oxidation by FPR enzymes.

6. Protein-Protein Interaction Studies *via* Crystallography and NMR

It has been found that all FNRs interact with their redox proteins *via* mainly electrostatic interaction and its protein complex is transient for efficient electron

transfer purpose [*66*]. In 1995, the spinach FNR and ferredoxin (Fd) protein-protein interaction study by Burns and Karplus suggested that protein interaction interface on FNR is the concave FAD binding domain [*67*]. Also, the protein complex of maize leaves Fd and FNR has been studied by crystallography and NMR [*19*]; it is found that the shortest distance between Fd and FNR is 6Å. The study again confirms that the complex is electrostatic, and the interface is hydrophobic nearing the cofactors [*19*].

In order to study the surprising redox partner proteins *pa*-HO and *pa*-FPR, we take advantage of the available crystal structure of *pa*-HO, *pa*-FPR and *pa*-FPR-NADP$^+$ complex and use Pymol together with APBS program to create the protein electrostatic potential surface views shown below in Figure 4-14, 4-15 and 4-16.

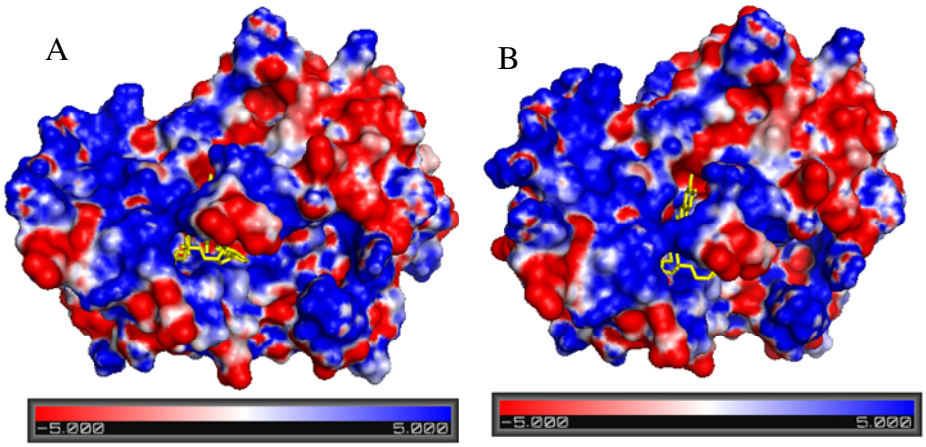

Figure 4-14. *Pa*-FPR electrostatic potential surface views (A) and (B) from different FAD viewing angels. FAD is shown in yellow sticks and NADP in green. Red shows negative charged surface, and blue shows positive charged surface.

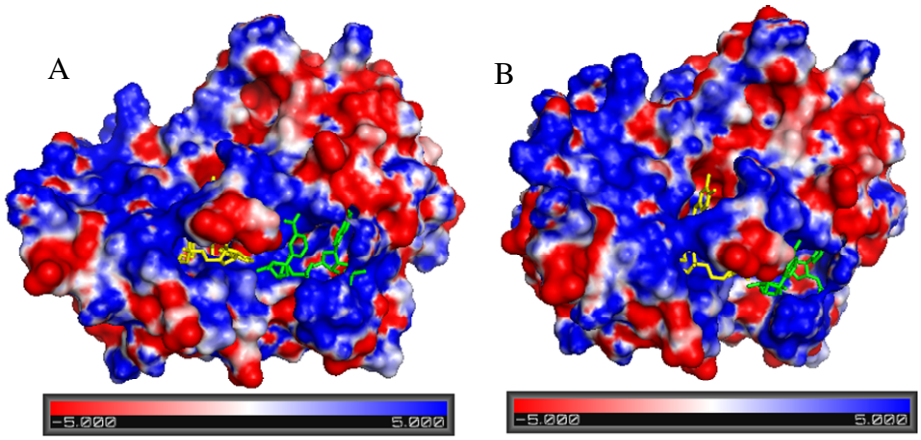

Figure 4-15. *Pa*-FPR-NADP$^+$ electrostatic potential surface views (A) and (B) from different FAD viewing angels. FAD is shown in yellow sticks and NADP$^+$ in green. Red shows negative charged surface, and blue shows positive charged surface.

As shown in above Figure 4-14 and 4-15, the methyl group of FAD's isoallaxozine ring is exposed to solvent. It appears that there is a mostly intense positive charged bowl-shaped concave area on top of the isoallaxazine ring, and only small amount of negative charge besides the methyl group of isoallaxozine ring. Also, the active sites on isoallaxozine ring seem to be exposed at the bottom of this bowl-shaped concave area. As for the cofactors' binding site, there seems to have more positive potential around the NADP$^+$ binding site located down the center "red" negative charged C-terminus on the view after NADP$^+$ binds. While the negative charged c-terminus seems to be quite protruding. In the case of *Av*-FPR as our most similar homolog protein to *pa*-FPR, it has only one intensely positive potential area locates around the FAD binding site which is proposed to interact with *Av*-FdI [*68*]. Therefore, we compared the electrostatic potential surface views for both *pa*-FPR and *pa*-HO, as shown in Figure 4-16 below.

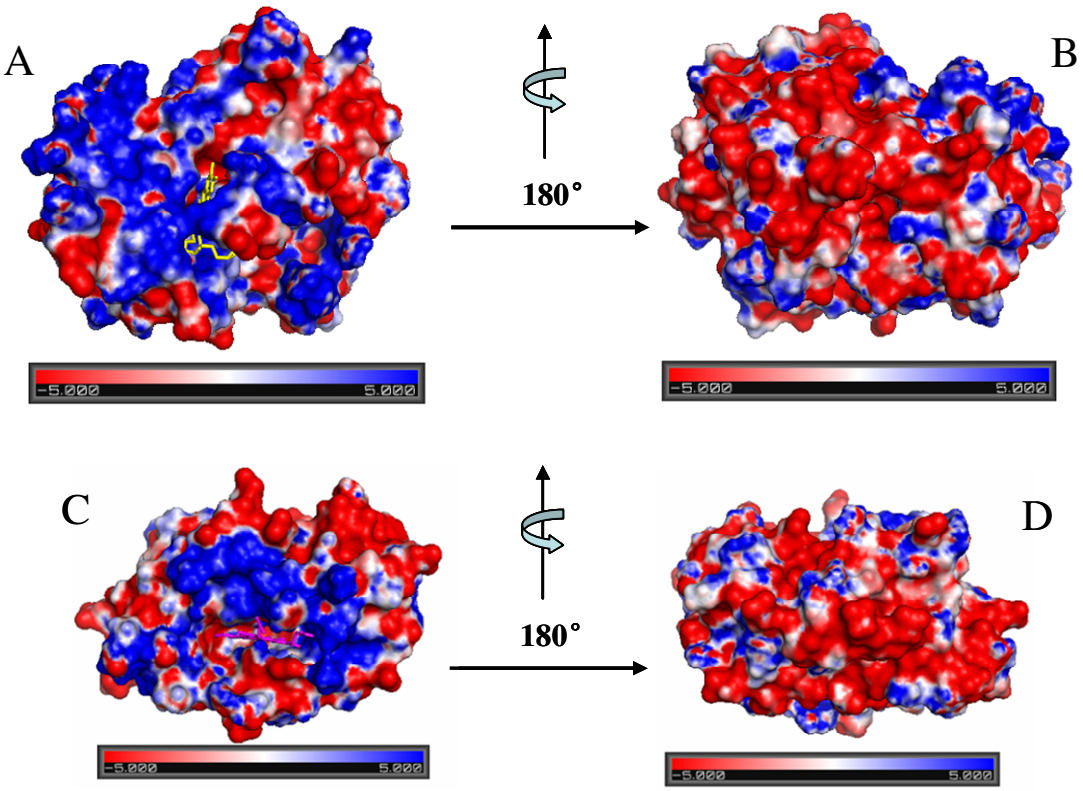

Figure 4-16. *Pa*-FPR electrostatic potential surface views: (A) and (B); *pa*-HO electrostatic potential surface views: (C) and (D). FAD is shown in yellow sticks, $NADP^+$ in green, and heme in magenta. Red shows negative potential and blue shows positive potential.

As for *pa*-HO, shown in above Figure 4-16 (C) and (D), there is largely negative charged area below the heme; and on top of the heme, there is largely positively charged area. The rest of the protein is mostly negatively charged. Therefore, it is very likely that the *pa*-HO interacts with FPR by approaching the heme site toward the concave region of FPR to match up with the opposite charges as shown in Figure 4-17. Again, due to the large positive charge on surface of *pa*-HO, this active sites' interaction is not the only possible electrostatic interaction. Therefore, the chance for protein-protein interaction through the proposed cofactor

binding sites is possibly lowered by the random electrostatic charge interaction between two proteins on other part of protein surfaces. Further investigation by NMR titration is shown below.

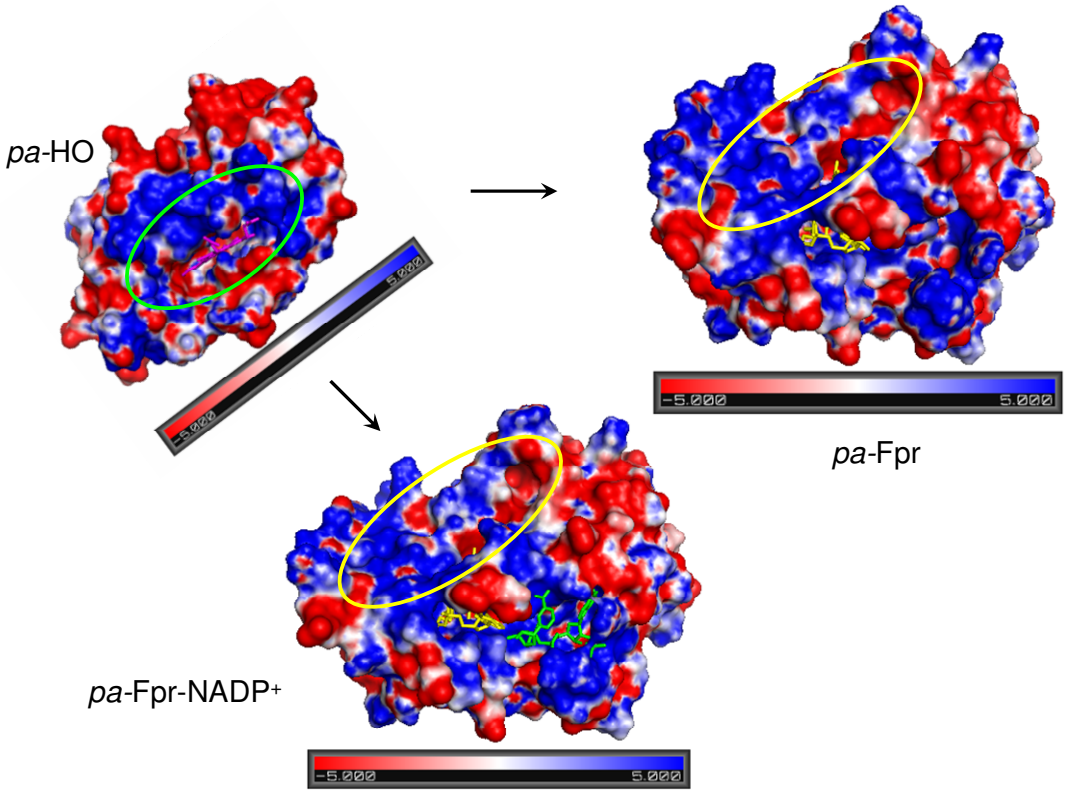

Figure 4-17. Proposed electrostatic protein-protein interaction. *Pa*-HO matches its top positive and bottom negative charges highlighted by green circle around heme with the top negative and bottom positive charges highlighted by yellow circle around FAD isoallaxozine ring in either *pa*-FPR or *pa*-FPR-NADP$^+$. FAD is shown in yellow sticks, NADP$^+$ in green, and heme in magenta. Red shows negative potential and blue shows positive potential.

Protein dissociation constant Kd<10^{-6}M indicates strong protein-protein interaction (PPI), while weak PPI has Kd>10^{-4}M [*69*]. In general, mapping ^{1}H, ^{15}N chemical shift perturbation *via* a ^{1}H-^{15}N HSQC NMR experiment is a very sensitive approach for studying the interface of weak protein binding complex [*70*]. By titrating unlabeled protein into [U-^{15}N] labeled protein using different protein

proportions and tracking the chemical shift pertrubation, not only the binding interface, but also other information like binding specificity, affinity and protein:protein stoichiometry value can be obtained [*71*]. As for ultra-weak protein complex (Kd>10^{-3}M), it is very difficult to detect using conventional methods like coimmunoprecipitation etc, often it is missed as false binding events [*22*]. But, the ultra-weak protein complex with 10 mM Kd has already been reported by this NMR chemical shift perturbation method [*72*].

As for the electrostatic protein-protein complex of *pa*-FPR and *pa*-HO, NMR chemical shift perturbation study using one [U-^{15}N] protein titrated by the other unlabeled protein is carried out with ^{1}H-^{15}N HSQC experiment. This transient *pa*-FPR *pa*-HO protein complex and ultra-weak protein interaction make the chemical shift perturbation extremely small. The observed largest chemical shift change using [U-^{15}N] *pa*-FPR (29.5kD) titrated by unlabeled *pa*-HO (23kD) is negligible. In general, it could suggest either no protein interaction or protein interaction beyond detect limit. As shown in previous chapter, the protein interaction between the two proteins indeed exists. Therefore, we carried out the experiment by titrating unlabeled *pa*-FPR into [U-^{15}N] *pa*-HO which is smaller in protein size. Fortunately, with continuous searching for optimal interaction conditions, we obtained consistent chemical shift perturbation results from many trials. The largest chemical shift change is less than 0.02 or 0.03 ppm, and once again this observation suggests that the protein complex is very weak. By further mapping those perturbed residue onto *pa*-HO protein crystal structure, as shown in Figure 4-18, we found that the largely

perturbed residues due to protein-protein interaction are more or less located around the heme binding site. The observation matches with the predicted protein interaction interface from the previous crystallography study. Currently, this study is continued by Dr. Huili Yao in our lab. Her preliminary data suggest the same result.

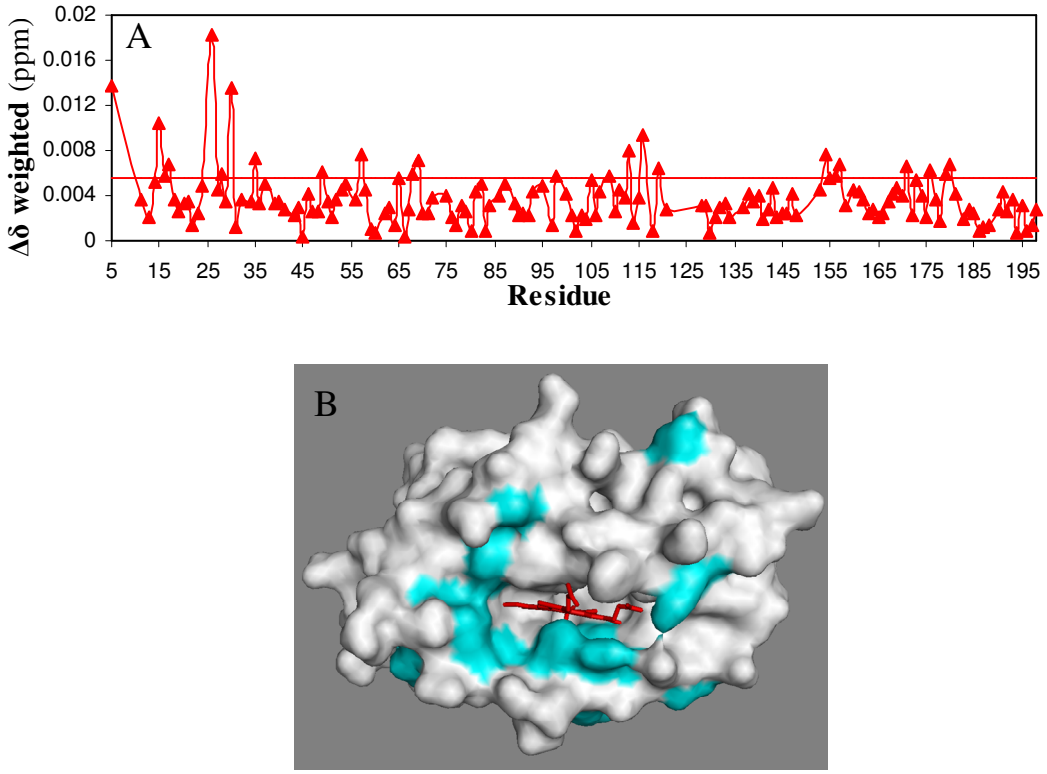

Figure 4-18. (A) Per residue plot of ^{15}N *pa*-HO-N_3 chemical shift perturbation upon titration with 12 equivalents of *pa*-FPR. Red line shows the 1.5 times average. (B) Residues above the 1.5 times average chemical shift change shown by the red line in above plot are mapped onto *pa*-HO crystal structure by cyan color.

These findings shine the light in this ultra-weak PPI that can be commonly missed by many other techniques [*72*]. In general, these ultra-weak PPIs are neglected in many studies due to lack of evidence for interaction. Recently, the ultra-weak PPI has been emphasized in many studies for its important role *in vivo* [*22*].

Yet its study is very difficult, limited, and far from complete. This study is the first example to probe the mysterious ultra-weak protein-protein interaction by analyzing very small change from NMR chemical shift perturbation.

REFERENCES

[1] Arakaki, A. K.; Ceccarelli, E. A.; Carrillo, N. (1997) Plant-Type Ferredoxin $NADP^+$ Reductases: A Basal Structural Framework and a Multiplicity of Functions. *FASEB Journal*, *11*, 133-140.

[2] Shin, M.; Arnon, D. I. (1965) Enzymic Mechanisms of Pyridine Nucleotide Reduction in Chloroplasts. *Journal of Biological Chemistry*, *240*, 1405-1411.

[3] Liochev, S. I.; Hausladen, A.; Beyer, W. F. J.; Fridovich, I. (1994) NADPH:Ferredoxin Oxidoreductase Acts as a Paraquat Diaphorase and is a Member of the *soxRS* Regulon. *Proceedings of the National Academy of Sciences. USA*, *91*, 1328-1331.

[4] Yannone, S. M.; Burgess, B. K. (1998) The Seven-Iron Fdl from Azotobacter vinelandii Regulates the Expression of NADPH:Ferredoxin Reductase vian an Oxidative Stress Response. *Journal of Biological Inorganic Chemistry*, *3*, 253-258.

[5] Bittel, C.; Tabares, L. C.; Armesto, M.; Carrillo, N.; Cortez, N. (2003) The oxidant-Responsive Diaphorase of *Rhodobacter capsulatus* is a Ferredoxin (flavodoxin)-NADP(H) Reductase. *FEBS Letters*, *553*, 408-412.

[6] Wang, A.; Zeng, Y.; Han, H.; Weeratunga, S.; Morgan, B. N.; Moënne-Loccoz, P.; Schönbrunn, E.; Rivera, M. (2007) Biochemical and Structural

Characterization of *Pseudomonas aeruginosa* Bfd and FPR: Ferredoxin $NADP^+$ Reductase and Not Ferredoxin is the Redox Partner of Heme Oxygenase under Iron-Starvation Conditions. *Biochemistry*, *46*, 12198-12211.

[7] Prasad, G. S.; Kresge, N.; Muhlberg, A. B.; Shaw, A.; Jung, Y. S.; Burgess, B. K.; Stout, C. D. (1998) The Crystal Structure of NADPH:Ferredoxin Reductase from *Azotobacter vinelandii*. *Protein Science*, *7*, 2541-2549.

[8] Ingelman, M.; Bianchi, V.; Eklund, H. (1997) The Three-Dimensional Structure of Flavodoxin Reductase from *Escherichia coli* at 1.7 A Resolution. *Journal of Molecular Biology*, *268*, 147-157.

[9] Ceccarelli, E. A.; Arakaki, A. K.; Cortez, N.; Carrilo, N. (2004) Functional Plasticity and Catalytic Efficiency in Plant and Bacterial Ferredoxin-(NADP(H) Reductases. *Biochimica et Biophysica Acta*, *1698*, 155-165.

[10] Karplus, P. A.; Daniels, M. J.; Herriott, D. J. R. (1991) Atomic Structure of Ferredoxin-$NADP^+$ Reductase: Prototype for a Structurally Novel Flavoenzyme Family. *Science*, *251*, 60-66.

[11] Bruns, C. M.; Karplus, P. A. (1995) Refined Crystal Structure of Spinach Ferredoxin Reductase at 1.7 Å Resolution: Oxidized Reduced and 2'phospho-5'AMP Bound States. *Journal of Molecular Biology*, *247*, 125-145.

[12] Hermoso, J. A.; Mayoral, T.; Faro, M.; Gómez-Moreno, C.; Sanz-Aparicio, J.; Medina, M. (2002) Mechanism of Coenzyme Recognition and Binding Revealed by Crystal Structure Analysis of Ferredoxin-$NADP^+$ Reductase Complexed with $NADP^+$. *Journal of Molecular Biology*, *319*, 1133-1142.

[13] Serre, L.; Vellieux, F. M. D.; Medina, M.; Gómez-Moreno, C.; Fontecilla-Camps, J. C.; Frey, M. (1996) X-ray Structure of the Ferredoxin:$NADP^+$ Reductase from the Cyanobacterium *Anabaena* PCC7119 at 1.8 Å Resolution, and Crystallographic studies of $NADP^+$ Binding at 2.25 Å Resolution. *Journal of Molecular Biology*, *263*, 20-39.

[14] Pai, E. F.; Karplus, P. A.; Schulz, G. E. (1988) Crystallographic Analysis of the Binding of NADPH, NADPH Fragments, and NADPH Analogues to Glutathione Reductase. *Biochemistry*, *27*, 4465-4474.

[15] Karplus, P. A.; Schulz, G. E. (1989) Substrate Binding and Catalysis by Glutathione Reductase as Derived from Refined Enzyme: Substrate Crystal Structures at 2 Å Resolution. *Journal of Molecular Biology*, *210*, 163-180.

[16] Deng, Z.; Aliverti, A.; Zanetti, G.; Arakaki, A. K.; Ottado, J.; Orellano, E. G.; Calcaterra, N. B.; Ceccarelli, E. A.; Carrillo, N.; Karplus, P. A. (1999) A Productive NADP+ Binding Mode of Ferredoxin-NADP+ Reductase Revealed by Protein Engineering and Crystallographic Studies. *Nature Structural Biology*, *6*, 847-853.

[17] Shukla, N.; Bhatt, A. N.; Aliverti, A.; Zanetti, G.; Bhakuni, V. (2005) Guanidinium chloride- and urea-induced unfolding of FprA, a Mycobacterium NADPH-ferredoxin reductase. Stabilization of an apo-protein by GdmCl. *FEBS Journal*, *272*, 2216-2224.

[18] Mayoral, T.; Martinlvez, M.; Perez-Dorado, I.; Sanz-Aparicio, J.; Gomez-Moreno, C.; Medina, M.; Hermoso, J. A. (2005) Structural Analysis of Interactions for Complex Formation between Ferredoxin-NADP Reductase and Its Protein Partners. *PROTEINS: Structure, Function, and Bioinformatics*, *59*, 592-602.

[19] Kurisu, G.; Kusunoki, M.; Katoh, E.; Yamazaki, T.; Teshima, K.; Onda, Y.; Kimata-Ariga, Y.; Hase, T. (2001) Structure of the electron transfer complex between ferredoxin and ferredoxin-NADP reductase. *Nature Structural Biology*, *8*, 117-121.

[20] Jenkins, C. M.; Waterman, M. R. (1998) NADPH-Flavodoxin Reductase and Flavodoxin from Escherichia coli: Characteristics as a Soluble Microsomal P450 Reductase. *Biochemistry*, *37*, 6106-6113.

[21] Chen, K.; Hirst, J.; Camba, R.; Bonagura, C. A.; Stout, C. D.; Burgess, B. K.; Armstrong, F. A. (2000) Atomically defined mechanism for proton transfer to a buried redox centre in a protein. *Nature*, *405*, 814-817.

[22] Vaynberg, J.; Fukuda, T.; Chen, K.; Vinogradova, O.; Velyvis, A.; Tu, Y.; Ng, L.; Wu, C.; Qin, J. (2005) Structure of an Ultraweak Protein-Protein Complex and Its Crucial Role in Regulation of Cell Morphology and Motility. *Molecular Cell*, *17*, 513-523.

[23] Morgan, W. D.; Kragt, A.; Feeney, J. (2000) Expression of deuterium-isotope-labelled protein in the yeast Pichia pastoris for NMR studies. *Journal of Biomolecular NMR*, *17*, 337-347.

[24] McIntosh, L. P.; Griffey, R. H.; Muchmore, D. C.; Nielson, C. P.; Redfield, A. G.; Dahlquist, F. W. (1987) Proton NMR measurements of bacteriophage T4 lysozyme aided by 15N isotopic labeling: structural and dynamic studies of larger proteins. *Proceedings of the National Academy of Sciences*, *84*, 1244-1248.

[25] Chen, C. Y.; Cheng, C. H.; Chen, Y. C.; Lee, J. C.; Chou, S. H.; Huang, W.; Chuang, W. J. (2006) Preparation of aminoacid-type selective isotope labeling of protein expressed in pichia pastoris. *PROTEINS: Structure, Function, and Bioinformatics*, *62*, 279-287.

[26] Strauss, A.; Bitsch, F.; Cutting, B.; Fendrich, G.; Graff, P.; Liebetanz, J.; Zurini, M.; Jahnke, W. (2003) Amino-acid-type selective isotope labeling of proteins expressed in Baculovirus-infected insect cells useful for NMR studies. *Journal of Biomolecular NMR*, *26*, 367-372.

[27] Cheng, H.; Westler, W. M.; Xia, B.; Oh, B.-H.; Markley, J. L. (1995) Protein expression, selective isotopic labeling, and analysis of hyperfine-shifted NMR signals of Anabaena 7120 vegetative [2Fe-2S]ferredoxin. *Archives of Biochemistry and Biophysics*, *316*, 619-634.

[28] Rodriguez, J. C.; Wilks, A.; Rivera, M. (2006) Backbone NMR Assignments and H/D Exchange Studies on the Ferric Azide- and Cyanide-Inhibited Forms of Pseudomonas aeruginosa Heme Oxygenase. *Biochemistry*, *45*, 4578-4592.

[29] Wang, A.; Zeng, Y.; Han, H.; Weeratunga, S.; Morgan, B. N.; Moeenne-Loccoz, P.; Schoenbrunn, E.; Rivera, M. (2007) Biochemical and Structural Characterization of Pseudomonas aeruginosa Bfd and FPR: Ferredoxin

NADP+ Reductase and Not Ferredoxin Is the Redox Partner of Heme Oxygenase under Iron-Starvation Conditions. *Biochemistry*, *46*, 12198-12211.

[30] Delaglio, F.; Grzesiek, S.; Vuister, G. W.; Zhu, W.; Pfeifer, J.; Bax, A. (1995) NMRPipe: A Multidimensional Spectral Processing System Based on UNIX pipes. *Journal of Biomolecular NMR*, *6*, 277-293.

[31] Goddard, T. D.; Kneller, D. G. Sparky 3, in *University of California, San Francisco*.

[32] Wishart, D. S.; Bigam, C. G.; Yao, J.; Abildgaard, F.; Dyson, H. J.; Oldfield, E.; Markley, J. L.; Sykes, B. D. (1995) ^{1}H, ^{13}C and ^{15}N Chemical Shift Referencing in Biomolecular NMR. *Journal of Biomolecular NMR*, *6*, 135-140.

[33] Pervushin, K.; Riek, R.; Wider, G.; Wuthrich, K. (1997) Attenuated T2 relaxation by mutual cancellation of dipole-dipole coupling and chemical shift anisotropy indicates an avenue to NMR structures of very large biological macromolecules in solution. *Proceedings of the National Academy of Sciences*, *94*, 12366-12371.

[34] Frueh, D. P.; Sun, Z. Y. J.; Vosburg, D. A.; Walsh, C. T.; Hoch, J. C.; Wagner, G. (2006) Non-uniformly sampled double-TROSY hNcaNH experiments for NMR sequential assignments of large proteins. *Journal of the American Chemical Society*, *128*, 5757-5763.

[35] Cavanagh, J.; Fairbrother, W.; Palmer, I. I. I. A. G.; Skelton, N.; Editors (1995) *Protein NMR Spectroscopy: Principles and Practice*.

[36] Fiaux, J.; Bertelsen, E. B.; Horwich, A. L.; Wuethrich, K. (2004) Uniform and Residue-specific 15N-labeling of Proteins on a Highly Deuterated Background. *Journal of Biomolecular NMR*, *29*, 289-297.

[37] Vanatalu, K.; Paalme, T.; Vilu, R.; Burkhardt, N.; Juenemann, R.; May, R.; Ruehl, M.; Wadzack, J.; Nierhaus, K. H. (1993) Large-scale preparation of fully deuterated cell components. Ribosomes from Escherichia coli with high biological activity. *European Journal of Biochemistry*, *216*, 315-321.

[38] Kabsch, W. (1993) Automatic Processing of Rotation Diffraction Data from Crystals of Initially Unknown Symmetry and Cell Constraints. *Journal of Applied Crystallography*, *26*, 795-800.

[39] Brunger, A. T.; Adams, P. D.; Clore, G. M.; DeLano, W. L.; Gros, P.; Grosse-Kunstleve, R. W.; Jiang, J. S.; Kuszewski, J.; Nilges, M.; Pannu, N. S.; Read, R. J.; Rice, L. M.; Simonson, T.; Warren, G. L. (1998) Crystallography & NMR System: A New Software Suite for Macromolecular Structure Determination. *Acta Crystallographica*, *D54*, 905-921.

[40] Jones, T. A.; Zhou, J. Y. (1991) Improved Methods for Binding Protein Models in Electron Density Maps and the Location of Errors in These Models. *Acta Crystallogr Section A: Foundations of Crystallography*, *A47*, 110-119.

[41] Medina, M.; Luquita, A.; Tejero, J.; Hermoso, J.; Mayoral, T.; Sanz-Aparicio, J.; Grever, K.; Gómez-Moreno, C. (2001) Probing the Determinants of Conezyme Specificity in Ferredoxin $NADP^+$ Reductase by Site-Directed Mutagenesis. *Journal of Biological Chemistry*, *276*, 11902-11912.

[42] Medina, M.; Gómez-Moreno , C. (2004) Interaction of Ferredoxin-NADP+ Reductase with its Substrates: Optimal Interaction for Efficient Electron Transfer. *Photosynthesis Research*, *79*, 113-131.

[43] Permi, P.; Annila, A. (2004) Coherence Transfer in Proteins. *Progress in Nuclear Magnetic Resonance Spectroscopy*, *44*, 97-137.

[44] Rodríguez, J. C.; Zeng, Y.; Wilks, A.; Rivera, M. (2007) The Hydrogen-Bonding Network in Heme Oxygenase Also Functions as a Modulator of Enzyme Dynamics: Chaotic Motions upon Disrupting the H-Bond Network in Heme Oxygenase from *Pseudomonas aeruginosa*. *Journal of the American Chemical Society*, *129*, 11730-11742.

[45] Wishart, D. S.; Sykes, B. D. (1994) Chemical Shifts as a Tool for Structure Determination. *Methods in Enzymology*, *239*, 363.

[46] Wishart, D. S.; Sykes, B. D. (1994) The ^{13}C Chemical-Shift Index: A Simple Method for the Identification of Protein Secondary Structure Using ^{13}C Chemical Shift Data. *Journal of Biomolecular NMR*, *4*, 171-180.

[47] Batie, C. J.; Kamin, H. (1986) Association of Ferredoxin-$NADP^+$ Reductase with NADP(H). Specificity and Oxidation-Reduction Properties. *Journal of Biological Chemistry*, *261*, 11214-11223.

[48] Banci, L.; Bertini, I.; Ciofi-Baffoni, S.; Kandias, N. G.; Robinson, N. J.; Spyroulias, G. A.; Su, X. C.; Tottey, S.; Vanarotti, M. (2006) The delivery of copper for thylakoid import observed by NMR. *Proceedings of the National Academy of Sciences*, *103*, 8320-8325.

[49] Carrillo, N.; Ceccarelli, E. A. (2003) Open Questions in Ferredoxin-$NADP^+$ Reductase Catalytic Mechanism. *European Journal of Biochemistry*, *270*, 1900-1915.

[50] Yuasa, J.; Yamada, S.; Fukuzumi, S. (2008) Detection of a Radical Cation of an NADH Analogue in Two-Electron Reduction of a Protonated *p*-Quinone Derivative by an NADH Analogue. *Angewandte Chemie International Edition*, *47*, 1068-1071.

[51] Fukuzumi, S.; Inada, O.; Suenobu, T. (2002) Direct Detection of Radical Cations of NADH Analogues. *Journal of the American Chemical Society*, *124*, 14538-14539.

[52] Fukuzumi, S.; Inada, O.; Suenobu, T. (2003) Mechanisms of Electron-Transfer Oxidation of NADH Analogues and Chemiluminescence. Detection of the Keto and Enol Radical Cations. *Journal of the American Chemical Society*, *125*, 4808-4816.

[53] Gębicki, J.; Marcinek, A.; Zielonka, J. (2004) Transient Species in the Stepwise Interconversion of NADH and NAD^+. *Accounts of Chemical Research*, *37*, 379-386.

[54] Afanasyeva, M. S.; Taraban, M. B.; Purtov, P. A.; Lashina, T. V.; Grissom, C. B. (2006) Magnetic Spin Effects in Enzymatic Reactions: Radical Oxidation

of NADH by Horseradish Peroxidase. *Journal of the American Chemical Society*, *128*, 8651-8658.

[55] Yuasa, J.; Fukuzumi, S. (2006) Mechanistic Borderline Between One-Step Hydrogen Transfer and Sequential Transfers of Electron and Proton in Reactions of NADH Analogues with Triplet Excited States of Tetrazines and $Ru(bpy)^{2+}$. *Journal of the American Chemical Society*, *128*, 14281-14292.

[56] Fukuzumi, S.; Ohkubo, K.; Tokuda, Y.; Suenobu, T. (2000) Hydride Transfer from 9-Substituted 10-Methyl-9,10-dihydroacridines to Hydride Acceptors via Charge-Transfer Complexes and Sequential Electron-Proton-Electron Transfer. A negative Temperature Dependence. *Journal of the American Chemical Society*, *122*, 4286-4294.

[57] Anne, A.; Hapiot, P.; Moiroux, J.; Neta, P.; Savéant, J. M. (1992) Dynamics of Proton Transfer from Cation Radicals. Kinetic and Thermodynamic Acidities of Cation Radicals of NADH Analogues. *Journal of the American Chemical Society*, *114*, 4694-4701.

[58] Zielonka, J.; Marcinek, A.; Huben, K.; Gębicki, J. (2003) Direct Observation of NADH Radical Cation Generated in Reactions with One-Electron Oxidants. *Journal of Physical Chemistry A*, *107*, 9860-9864.

[59] Marcinek, A.; Adamus, J.; Huben, K.; Gębicki, J.; Bartczak, T. J.; Bednarek, P.; Bally, T. (2000) Hydrogen-Transferred Radical Cations of NADH Model Compounds. 1. Spontaneous Tautomerization. *Journal of the American Chemical Society*, *122*, 437-443.

[60] Almarsson, O.; Sinha, A.; Gopinath, E.; Bruice, T. C. (1993) Mechanism of One-Electron Oxidation of NAD(P)H and Function of NADPH Bound to Catalase. *Journal of the American Chemical Society*, *115*, 7093-7102.

[61] Beratan, D. N.; Betts, J. N.; Onuchic, J. N. (1991) Protein Electron Transfer Rates Set by the Bridging Secondary and Tertiary Structure. *Science*, *252*, 1285-1288.

[62] Beratan, D. N.; Onuchic, J. N.; Betts, J. N.; Bowler, B. E.; Gray, H. B. (1990) Electron-Tunneling Pathways in Ruthenated Proteins. *Journal of the American Chemical Society*, *112*, 7915-7921.

[63] Gray, H. B.; Winkler, J. R. (2005) Long-Range Electron Transfer. *Proceedings of the National Academy of Sciences*, *102*, 3534-3539.

[64] Bhattacharyya, S.; Stankovich, M. T.; Truhlar, D. G.; Gao, J. (2007) Combined Quantum Mechanical and Molecular Mechanical Simulations of One- and Two-Electron Reduction Potentials of Flavin Cofactor in Water, Medium-Chain Acyl-CoA Dehydrogenase, and Cholesterol Oxidase. *Journal of Physical Chemistry*, *111*, 5279-5742.

[65] Ghisla, S.; Massey, V. (1989) Mechanisms of Flavoprotein-Catalyzed Reactions. *European Journal of Biochemistry*, *181*, 1-17.

[66] Carrillo, N.; Ceccarelli, E. A. (2003) Open questions in ferredoxin-NADP+ reductase catalytic mechanism. *European Journal of Biochemistry*, *270*, 1900-1915.

[67] Bruns, C. M.; Karplus, P. A. (1995) Refined crystal structure of spinach ferredoxin reductase at 1.7 .ANG. resolution: oxidized, reduced and 2'-phospho-5'-AMP bound states. *Journal of Molecular Biology*, *247*, 125-145.

[68] Jung, Y.-S.; Roberts, V. A.; Stout, C. D.; Burgess, B. K. (1999) Complex formation between Azotobacter vinelandii ferredoxin I and its physiological electron donor NADPH-ferredoxin reductase. *Journal of Biological Chemistry*, *274*, 2978-2987.

[69] Vaynberg, J.; Qin, J. (2006) Weak protein-protein interactions as probed by NMR spectroscopy. *Trends in Biotechnology*, *24*, 22-27.

[70] Qin, J.; Vinogradova, O.; Gronenborn, A. M. (2001) Protein-protein interactions probed by nuclear magnetic resonance spectroscopy. *Methods in Enzymology*, *339*, 377-389.

[71] Zuiderweg, E. R. (2002) Mapping protein-protein interactions in solution by NMR spectroscopy. *Biochemistry*, *41*, 1-7.

[72] Hall, D. A.; Vander Kooi, C. W.; Stasik, C. N.; Stevens, S. Y.; Zuiderweg, E. R. P.; Matthews, R. G. (2001) Mapping the interactions between flavodoxin and its physiological partners flavodoxin reductase and cobalamin-dependent methionine synthase. *Proceedings of the National Academy of Sciences*, 171168898.

APPENDIX

Table S-4-1. Backbone assignments for *pa*-FPR. Chemical shifts are given in ppm.

No.	AA	N	NH	Cα (i)	Cα (i-1)	C_β (i)	C_β (i-1)	Co (i)	Co (i-1)
1	Met								
2	Ser								
3	Asn								
4	Leu	119.40	7.94	53.93		43.83	38.54	173.97	177.40
5	Tyr	122.40	9.35	57.07	53.98	39.37	43.87	175.72	174.05
6	Thr	116.69	8.58	61.86	57.19	69.54	39.43	177.44	175.72
7	Glu	125.16	9.13	52.96	61.77	31.04	69.56	176.67	177.43
8	Arg	118.10	8.58	53.72	52.86	33.07	31.23	174.99	176.71
9	Val	122.46	9.04	63.69	53.92	31.58	32.92	174.63	174.93
10	Leu	130.79	10.01	55.68	63.69	43.76	31.66	174.74	174.69
11	Ser	110.21	7.53	58.04	55.62	64.17	43.47	179.86	174.87
12	Val	119.92	8.56	61.68	57.66	35.57	64.19	177.13	179.86
13	His	126.77	9.28	56.06	61.68	33.79	35.56	178.17	177.13
14	His	126.93	8.56	55.93	56.06	30.95	33.83	177.10	178.15
15	Trp	126.20	8.29	58.33	55.93	29.45	30.62	174.92	177.09
16	Asn	115.80	8.50	52.81	58.42	36.32	29.85	176.44	174.95
17	Asp								
18	Thr	108.30	8.28	62.24	56.38	70.50	40.23	178.78	174.90
19	Leu	120.81	7.83	54.03	62.28	47.75	70.61	174.64	178.75
20	Phe	122.37	10.52	56.19	54.03	41.64	47.81	180.78	174.58
21	Ser	115.99	9.58	57.69	56.42	67.42	41.75	179.33	180.74
22	Phe	116.76	8.69	55.47	57.23	40.93	67.41	179.16	179.31
23	Lys	117.66	8.41	53.64	55.35	36.40	40.87	174.25	179.12
24	Thr	114.02	9.72	60.17	53.66	72.35	36.47	177.07	174.25
25	Thr	109.60	8.73	63.02	60.13	70.95	72.46	179.52	177.06
26	Arg	117.86	8.03	53.65	62.94	34.48	70.85	176.91	179.55
27	Asn	133.2	9.66	53.81	53.65	38.75	34.13	176.74	176.89
28	**Pro**			64.35		31.52		173.91	
29	Gly	105.00	9.17	44.96	64.35		31.52	177.07	173.91
30	Leu	123.53	8.02	54.50	44.96	39.86		176.92	177.09
31	Arg	128.92	8.42	54.65	54.65	30.74	39.76	177.01	176.91
32	Phe	116.52	7.69	55.57	54.70	41.15	30.73	178.32	177.03
33	Lys	120.43	8.44	54.46	55.58	33.03	41.16	176.56	178.31
34	Thr	119.23	8.15	64.40	54.43	69.18	33.05	178.35	173.80
35	Gly	116.24	8.71	45.50	64.37		69.18	174.78	178.36
36	Gln	116.49	7.89	57.48	45.51	31.01		176.92	174.77
37	Phe	115.07	9.15	55.35	57.49	41.26	31.03	178.02	176.90
38	Val	114.98	8.83	58.97	55.54	35.60	41.28	178.02	178.02

39	Met	118.22	7.93	53.55	59.01	31.71	35.54	175.99	178.02
40	Ile	115.46	8.88	58.72	53.35	41.24	31.63	176.51	175.92
41	Gly	104.55	8.36	46.93	58.54		41.26	180.72	176.48
42	Leu	115.36	7.34	52.01	47.02	46.02		175.92	180.73
43	Glu	121.27	8.69	56.68	52.01	29.48	46.55	176.12	175.92
44	Val	128.47	8.75	61.87	56.71	34.22	29.47	176.09	176.16
45	Asp	127.76	9.36	55.47	61.67	39.33	34.48	175.19	176.03
46	Gly	102.11	8.60	45.24	55.50		39.19	177.77	175.23
47	Arg	122.43	7.95	52.08	45.26	30.58		177.93	177.76
48	**Pro**			63.37		31.50		175.98	
49	Leu	133.00	9.06	55.21	63.37	41.69	31.50	178.00	175.98
50	Met	119.55	8.01	52.04	55.21	33.96	41.53	174.10	178.00
51	Arg	121.07	9.73	52.82	51.88	33.88	33.91	176.55	174.08
52	Ala	124.40	7.77	52.82	52.83	18.30	33.88	175.60	176.57
53	Tyr	122.37	9.25	57.41	52.82	43.46	18.29	176.26	175.54
54	Ser	122.00	8.84	60.67	57.25	64.09	43.32	178.75	176.22
55	Ile	123.91	7.83	63.01	60.63	36.47	64.07	176.34	178.66
56	Ala	129.05	7.98	51.68	63.01	19.01	36.60	175.70	176.33
57	Ser	108.20	7.24	53.61	51.75	61.86	19.01	178.39	175.73
58	**Pro**			60.89		31.55		171.60	
59	Asn	122.01	9.43	55.11	60.89	35.98	31.55	175.27	171.60
60	Tyr	114.26	6.46	55.18	55.18	37.53	36.17	175.28	175.26
61	Glu	121.98	6.83	55.78	55.11	30.07	37.28	174.64	175.29
62	Glu	121.95	8.90	56.02	55.34	28.21	30.00	177.33	174.63
63	His	115.43	7.30	55.25	55.81	32.29	28.24	179.00	177.32
64	Leu	118.57	8.77	53.40	55.77	43.92		176.08	178.99
65	Glu	119.70	7.13	53.94	53.27	33.21	44.18	180.75	176.06
66	Phe	121.18	8.21	56.36	53.83	41.83	32.72	179.00	180.73
67	Phe	125.09	10.51	53.96	56.48	40.08	41.85	178.05	179.01
68	Ser	119.50	9.90	55.81	54.05	65.91	40.04	178.52	177.93
69	Ile	127.99	8.81	57.36	55.86	40.79	66.00	176.38	178.55
70	Lys	121.81	7.59	56.47	57.69	32.56	40.89	176.69	176.46
71	Val	127.48	8.18	59.46	56.42		32.85	175.33	176.77
72	**Pro**							175.17	
73	Asp	118.23	8.54	53.17		33.80		174.92	175.17
74	Gly	113.61	8.23	44.59				177.92	174.93
75	**Pro**			66.36		32.50		174.38	
76	Leu	114.42	9.91	57.17	66.36	41.72	32.50	170.22	174.38
77	Thr	114.34	10.13	67.41	57.31	70.38	41.88	173.77	170.19
78	Ser	118.45	8.77	61.45	67.16	62.74	70.28	175.59	173.84
79	Arg	120.93	7.13	57.52	61.72	30.66	62.79	172.28	175.58
80	Leu	123.41	9.31	56.98	57.56	44.72	30.34	174.73	172.26
81	Gln	108.50	7.51	56.66	56.66	26.48	44.63	176.68	174.74
82	His	119.02	7.04	55.45	56.55	30.55	26.55	176.42	176.67
83	Leu	121.85	7.52	56.04	55.41	43.80	30.56	176.19	176.35
84	Lys	119.58	8.69	53.55	56.01	35.89	43.87	176.46	175.15
85	Glu	119.20	8.64	58.25	53.53	28.70	35.89	174.55	176.46

86	Gly	114.10	9.22	44.87	58.29		28.67	174.54	174.54
87	Asp	121.47	8.03	54.91	44.82	41.36		176.74	177.22
88	Glu	117.15	8.13	55.13	54.95	31.82	41.36	176.31	176.73
89	Leu	123.53	8.78	53.52	55.09	46.56	31.77	176.71	176.23
90	Met	122.75	8.51	55.03	53.43	33.89	46.42	176.17	176.67
91	Val	120.65	8.79	60.95	54.98	36.29	33.51	176.26	176.10
92	Ser	121.89	9.19	58.82	60.96	63.36	36.48	179.85	176.42
93	Arg	109.92	7.52	56.75	58.79	30.94	63.41	174.55	179.84
94	Lys	118.27	7.72	52.82	57.09	33.20	30.90	178.48	174.49
95	**Pro**			62.42		32.02		76.42	
96	Thr	115.28	8.27	59.78	62.42	69.16	32.02	180.93	176.42
97	Gly	106.87	7.47	45.32	59.80		69.18	176.62	180.92
98	Thr	109.81	8.31	61.71	45.33	70.38		174.90	176.61
99	Leu	127.03	9.56	53.64	62.47	38.09	70.42	178.51	174.85
100	Val	107.72	7.08	57.56	53.58	34.15	38.00	174.81	178.49
101	His	119.70	8.66	59.50	57.42	31.25	34.16	172.37	174.81
102	Asp	111.97	8.32	55.87	59.50	40.42	30.99	175.08	172.28
103	Asp	117.20	7.31	54.70	55.89	39.85	40.42	177.80	175.11
104	Leu	118.29	7.43	52.80	54.71	43.27	40.01	173.47	177.82
105	Leu	125.61	8.60	53.52	52.81	40.40	43.28	176.52	173.46
106	**Pro**			63.37		31.42		174.13	
107	Gly	110.96	8.66	45.03	63.37		31.42	181.37	174.13
108	Lys	117.22	8.87	57.78	45.02	35.53		174.94	181.37
109	His	118.42	8.11	52.45	57.75	30.92	35.55	179.21	174.91
110	Leu	123.76	8.14	52.53	52.53	40.92	31.17	178.28	179.14
111	Tyr	126.73	9.37	57.99	52.46	39.26	41.05	178.20	178.28
112	Leu	125.16	9.46	52.52	57.90	39.82	39.06	178.18	178.22
113	Leu	123.22	8.65	54.56	52.59	40.09	39.66	176.96	178.07
114	Ser	116.72	8.44	56.98	54.64	70.70	40.01	175.97	176.98
115	Thr	109.48	7.61	58.66	56.75	71.33	70.70	175.84	175.95
116	Gly	108.74	7.79	47.08	58.78		71.53	174.76	175.77
117	Thr	119.36	9.60	64.50	47.02	67.37		176.33	174.76
118	Gly	109.88	8.87	46.60	64.59		67.46	180.01	176.22
119	Met	114.04	6.80	57.55	46.52	33.03		173.82	180.03
120	Ala	120.96	8.69	56.69	57.89	17.75	33.02	176.15	173.82
121	**Pro**			65.62		30.11		172.30	
122	Phe	118.43	6.91	55.17	65.62	35.65	30.11	173.75	172.30
123	Leu	123.26	7.87	57.71	54.92	40.40	35.73	172.64	173.71
124	Ser	113.74	6.69	62.41	57.76	64.07	40.46	172.75	172.66
125	Val	117.97	7.68	67.18	62.17	31.23	64.33	170.88	173.09
126	Ile	111.62	8.57	64.26	67.48	36.45		176.13	170.80
127	Gln	117.10	7.14	55.02	64.17	31.58	36.60	179.64	176.10
128	Asp	122.17	7.29	50.36	55.12	42.46	31.79	176.19	179.56
129	**Pro**							172.69	
130	Glu	118.28	8.57	58.79		28.88		173.28	172.69
131	Thr	115.94	7.88	65.71	58.76	68.23	28.85	177.80	173.26
132	Tyr	114.98	6.26	59.49	65.20	37.55	68.20	176.03	177.67

133	Glu	117.02	7.35	57.57	59.48	29.57	37.58	172.57	176.04
134	Arg	115.21	7.21	57.81	57.81	32.62	29.51	176.34	172.57
135	Tyr	113.49	6.83	57.86	57.86	41.51	32.63	177.28	176.35
136	Glu	118.75	9.22	57.82	57.82	30.80	41.42	174.18	177.28
137	Lys	113.09	7.67	53.77	57.88	37.39		177.65	174.25
138	Val	124.08	8.88	60.43	53.71	34.01	37.16	179.24	177.63
139	Ile	128.40	9.23	60.34	60.43	39.01	34.02	178.16	179.19
140	Leu	128.53	9.22	53.44	60.34	43.48	39.01	178.12	178.15
141	Val	129.41	9.42	60.96	43.45	32.49	39.01	176.20	178.16
142	His	128.72	7.70		61.04		32.59	178.77	176.24
143	Gly	112.63	8.59	45.61	53.22		33.83	178.66	178.78
144	Val	120.23	8.85	59.02	45.55	34.42		176.29	178.49
145	Arg	117.59	8.21	58.16	58.86	30.71	34.54	176.40	176.31
146	Trp	114.68	7.25	54.36	58.16	32.98	30.91	175.21	176.45
147	Val	123.78	9.79	65.88	54.43	31.45	33.04	172.42	175.21
148	Ser	115.20	8.86	60.10	66.14	62.58	31.79	176.91	172.42
149	Glu	117.36	7.85	55.99	59.99	28.74	62.48	174.27	176.91
150	Leu	122.99	7.46	53.39	55.86	37.98	28.81	174.43	174.28
151	Ala	127.84	8.19	51.91	53.26	19.03	38.02	176.57	174.51
152	Tyr								
153	Ala	121.17	6.88	56.78		19.36		170.93	176.78
154	Asp	118.16	8.59	57.45	57.21	39.49	19.57	173.72	170.93
155	Phe	123.81	8.59	60.97	57.38	38.53	40.04	174.68	173.82
156	Ile	118.33	8.71	65.45	61.42	38.47	38.42	175.45	174.60
157	Thr	104.27	7.60	63.48	65.29	70.96	39.28	175.29	175.45
158	Lys	118.31	8.56	56.99	63.38	33.87	70.88	174.28	175.32
159	Val	121.46	7.32	65.27	57.01	31.79	34.03	173.58	174.26
160	Leu	122.76	8.26	58.85	65.11	38.61	32.00	176.46	173.56
161	**Pro**			64.79		31.03		176.74	
162	Glu	111.30	7.13	53.80	64.79	28.65	31.03	175.05	176.74
163	His	123.35	7.70	59.95	53.68	30.50	28.83	173.47	175.05
164	Glu	127.66	8.52	58.97	60.14	29.40	30.61	174.95	173.48
165	Tyr	119.78	9.88	58.76	58.76		29.98	174.37	174.96
166	Phe	113.97	7.66	56.65	58.40	37.65		175.68	174.29
167	Gly	113.80	8.07	48.21	56.64		37.90	176.69	175.68
168	Asp	118.81	8.59	57.29	48.16	39.25		172.50	176.68
169	Gln	119.11	7.51	58.67	57.35	28.16	39.34	174.08	172.47
170	Val	120.36	7.61	59.65	58.85	31.28	28.48	172.27	174.08
171	Lys	118.03	8.48	59.94	66.12	32.70	31.45	172.54	172.21
172	Glu	115.50	7.40	58.09	59.85	30.81	32.75	173.74	172.59
173	Lys	114.50	8.36	58.73	57.97	36.81	30.76	175.78	173.74
174	Leu	119.36	8.43	55.24	58.73	42.61	36.49	174.91	175.71
175	Ile	131.49	9.78	60.60	55.39	39.45	42.36	178.44	174.87
176	Tyr	128.47	8.62	54.55	60.53	39.97	39.59	178.34	178.47
177	Tyr	134.04	9.67	55.55	54.53	39.27	39.94		178.15
178	**Pro**			61.52		33.44		175.85	
179	Leu	122.53	8.61	54.69	61.52	46.00	33.44	177.79	175.85

180	Val	122.26	7.46	60.09	54.70	35.27	45.97	173.79	177.56
181	Thr	112.90	8.10	63.09	60.14	70.30	35.66	??	173.84
182	Arg	118.87	8.46	56.50	62.97	28.79	70.08	176.90	173.28
183	Glu	116.32	7.09	53.54	56.41	30.84	28.84	179.68	176.87
184	**Pro**			63.72		31.60		175.64	
185	Phe	120.64	7.81	57.65	63.72	41.59	31.60	177.35	175.64
186	Arg								
187	Asn								
188	Gln	123.44	8.42	53.91	51.72	31.92	38.71	175.97	178.19
189	Gly	109.26	7.45	43.61	53.93		31.73	180.70	175.96
190	Arg	116.43	8.41	54.57	43.53	31.15		173.31	180.65
191	Gln								
192	Thr								
193	Asp								
194	Leu								
195	Met								
196	Arg								
197	Ser	110.50	8.24	58.90	59.84	64.07	30.02	175.88	173.13
198	Gly	110.19	7.30	45.15	58.94		64.25	177.86	175.88
199	Lys	125.41	8.12	58.76	45.15	32.43		174.57	177.81
200	Leu	115.85	7.45	58.73	58.84	41.49	32.33	175.26	174.57
201	Phe	112.80	5.61	58.84	58.73	36.41		174.04	175.28
202	Glu	117.68	7.43	52.68	58.84	29.36	36.46	171.62	174.09
203	Asp	119.36	8.66	57.39	53.48	40.72	29.15	172.55	171.61
204	Ile	109.78	7.39	61.59	57.29	38.00	40.66	175.67	172.61
205	Gly	110.38	7.74	46.32	61.62		37.85	177.34	175.63
206	Leu	121.58	7.82	51.97	46.36	41.92		178.25	177.32
207	**Pro**								
208	**Pro**								
209	Met								
210	Asn								
211	**Pro**			64.19		31.51		173.14	
212	Gln	121.30	8.59	59.01	64.19	28.30	31.51	173.85	173.14
213	Asp	115.29	7.74	55.87	58.98	43.86	28.35	174.83	173.86
214	Asp	121.94	8.24	56.24	55.62	44.34	43.83	178.17	174.85
215	Arg	121.06	9.11	51.15	56.20	32.41	44.29	175.84	178.14
216	Ala	118.56	8.10	50.44	50.90	23.22	32.27	176.06	175.81
217	Met	117.22	8.87	54.98	50.54	36.64	23.23	177.96	176.17
218	Ile	121.22	8.81	59.62	54.98	39.71	36.58	177.35	177.96
219	Cys	127.40	8.82	58.73	59.88	28.89	39.83	177.44	177.30
220	Gly	111.22	6.82	45.42	58.43		29.05	179.35	177.58
221	Ser	116.96	7.41	56.06	45.37	62.48			179.36
222	**Pro**								
223	Ser								
224	Met	126.08	7.66	58.72	61.24	31.44	62.38	171.44	174.99
225	Leu	122.94	8.82	58.88	58.88	41.80	31.50	171.28	171.43
226	Glu	119.72	7.64	59.44	58.98	29.35	41.70	172.60	171.24

227	Glu	119.40	7.94	59.01	59.01	29.91	29.50	172.58	172.61
228	Thr	116.20	8.90	67.00	58.78	72.81	29.84	175.07	172.56
229	Ser	118.22	8.23	62.61	67.26			177.33	175.07
230	Ala	120.98	7.09	54.97	62.72	17.33		170.37	177.25
231	Val	119.00	7.34	65.94	54.98	30.69	17.23	173.07	170.37
232	Leu	121.45	7.98	58.97	66.15	38.28	30.42	171.68	173.00
233	Asp	120.71	8.84	56.55	58.97	39.64	38.21	169.77	171.66
234	Ser	119.01	7.70	61.30	56.75	62.47	39.54	176.08	169.76
235	Phe	121.10	7.43	55.99	61.30	38.49	62.40	175.75	176.11
236	Gly	105.96	8.05	44.65	55.99		38.62	177.60	175.72
237	Leu	122.26	7.46	57.36	44.72	42.45		175.18	177.55
238	Lys	121.13	10.25	54.24	57.10	33.67	42.49	176.25	175.21
239	Ile	127.47	8.43	60.90	54.31	38.48	33.63	175.48	176.25
240	Ser	119.29	7.59	56.04	60.85	64.26	38.55	177.09	175.49
241	**Pro**			64.25		32.30		175.03	
242	Arg	112.37	7.31	54.70	64.25	30.68	32.30	178.21	175.03
243	Met	119.64	8.21	57.49	54.73	32.68	30.68	173.87	178.20
244	Gly	116.79	10.12	45.18	57.46		32.75	177.77	173.87
245	Glu	119.19	7.65	52.85	45.26	31.52		178.73	177.76
246	**Pro**			62.47		32.00		174.38	
247	Gly	107.27	8.23	44.36	62.47		32.00	180.10	174.38
248	Asp	119.73	8.81	55.70	44.35	41.42		175.90	180.08
249	Tyr	108.71	7.19	55.64	55.64	41.24	41.24	180.05	175.76
250	Leu	118.74	7.97	52.84	55.46	47.77	41.44	174.96	180.06
251	Ile	111.18	8.32	58.71	52.78	41.74	47.78	176.38	175.01
252	Glu	122.94	8.51	57.17	58.71	33.93	41.68	178.13	176.57
253	Arg	124.62	8.24	56.27	57.09	29.12	34.04	177.22	178.12
254	Ala	121.93	7.64	51.17	56.27	17.68	29.15	176.63	177.20
255	Phe	102.75	6.48	55.19	51.22	37.04	17.71	179.85	176.56
256	Val	114.91	8.60	60.87	55.15	33.77	36.91	175.36	179.85
257	Glu	126.15	8.34	56.13	60.84	30.28	33.63	176.24	175.37
258	Lys	129.26	8.31	57.83	56.19	33.31	30.27	170.28	176.24

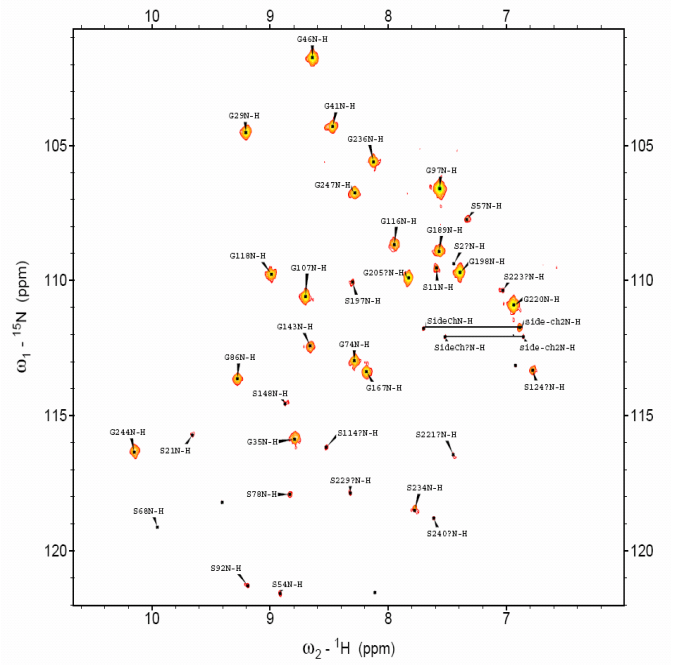

Figure S-4-1. 2D ^{1}H-^{15}N HSQC spectrum of ^{15}N-Gly labeled *pa*-FPR. (Partial scrambling to Serine seen as the weak intensity peak is used to assist assignment work. The black line connects the amide side chain peaks, excluded from analysis)

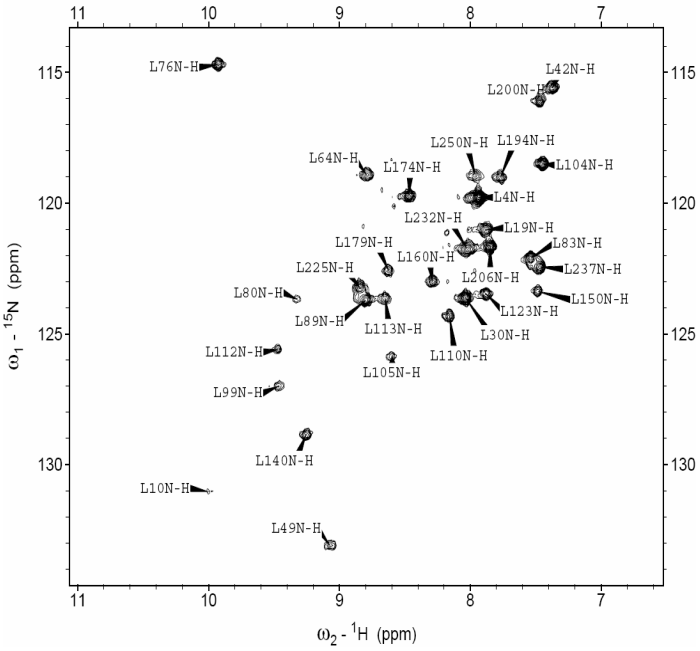

Figure S-4-2. 2D ^{1}H-^{15}N HSQC spectrum of ^{15}N-Leu labeled *pa*-FPR. (Some scrambling to Asp(D) and Val(V) is seen as weak intensity peak.)

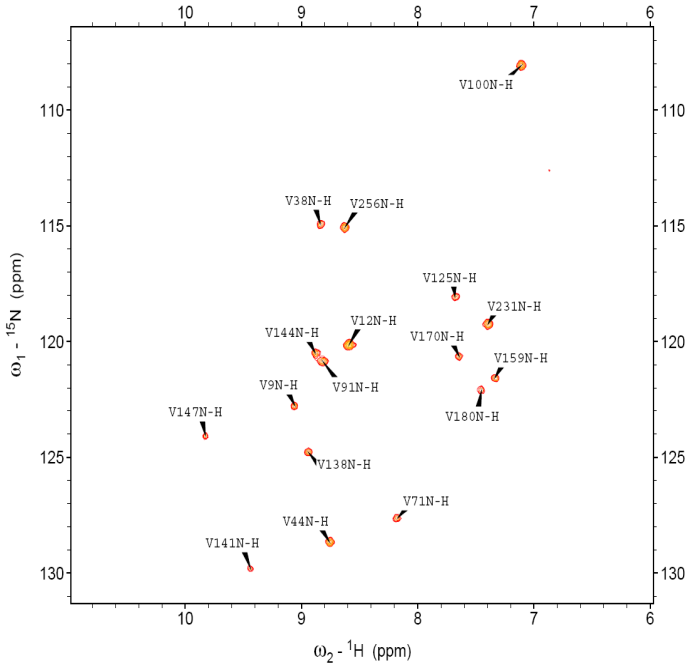

Figure S-4-3. 2D ^{1}H-^{15}N HSQC spectrum of ^{15}N-Val labeled *pa*-FPR. No scrambling.

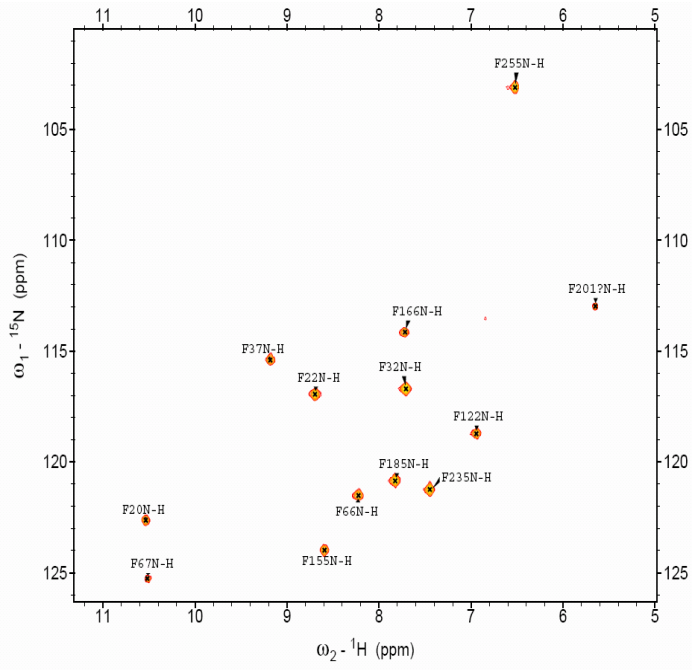

Figure S-4-4. 2D ^{1}H-^{15}N HSQC spectrum of ^{15}N-Phe labeled *pa*-FPR. No scrambling.

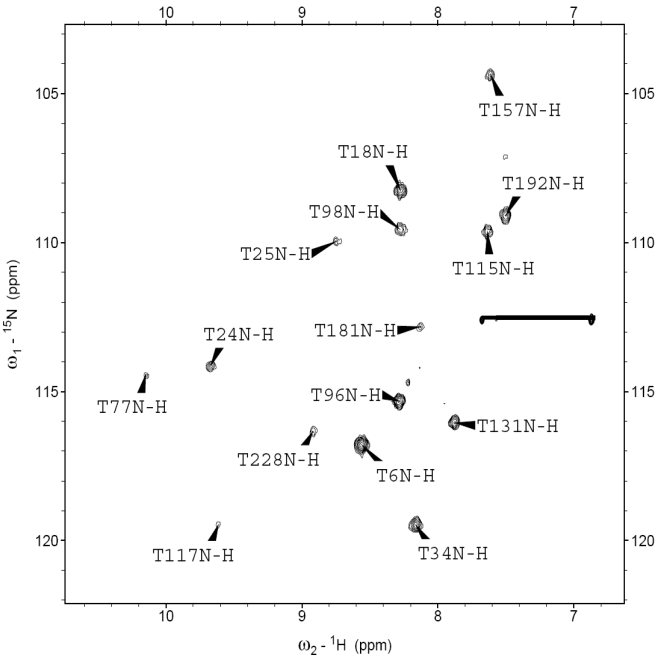

Figure S-4-5. 2D ^{1}H-^{15}N HSQC spectrum of ^{15}N-Thr labeled *pa*-FPR. (A little scrambling to Asp(D) and Gly(G) etc. is seen as very weak intensity peak. The black line connects the amide side chain peaks, excluded from analysis.)

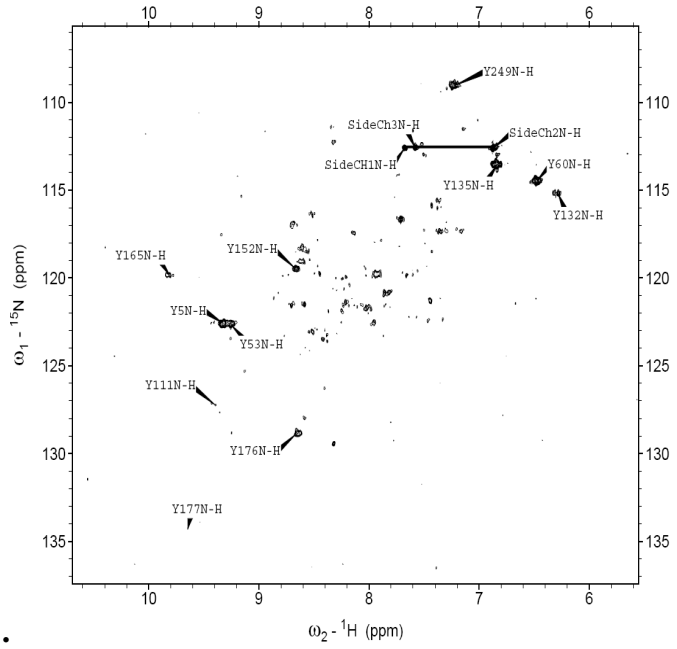

Figure S-4-6. 2D ^{1}H-^{15}N HSQC spectrum of ^{15}N-Tyr labeled *pa*-FPR. (Heavy scrambling to F, D, E, L, V etc. is seen as weak intensity peak. The black line connects the amide side chain peaks, excluded from analysis.)

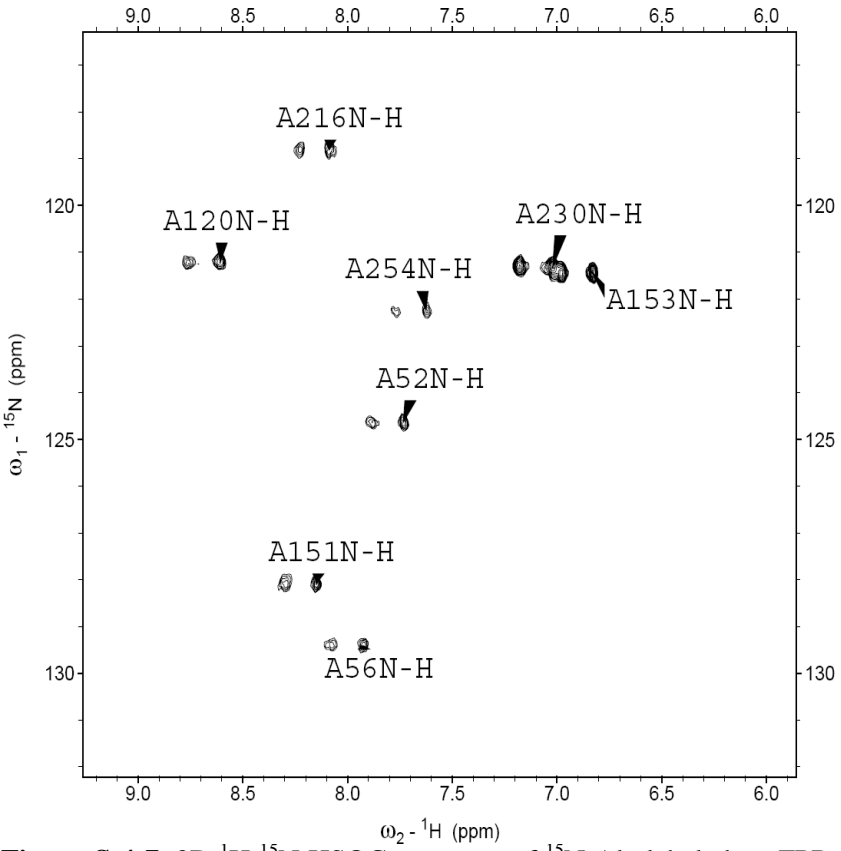

Figure S-4-7. 2D ^{1}H-^{15}N HSQC spectrum of ^{15}N-Ala labeled *pa*-FPR. (No scrambling. Peak doubling is caused by proton decoupling setting in HSQC experiment.)

CHAPTER V: CONCLUSION

The heme oxygenase (*pa*-HO) and ferredoxin NADPH reductase (*pa*-FPR) are two key proteins in the notorious pathogenic bacterium *Pseudomonas aerguinosa*. Unlike any other heme-containing proteins, heme oxygenase has a very unique heme metabolism path. Heme in it is used as both substrate and cofactor for its own degradation to verdoheme together with iron and CO release [*1-6*]. In the process of *P. aerguinosa* initial infection to its host (especially human beings), *pa*-HO is required to degrade heme from host to release iron for its nutrient need [*7-10*]. Therefore, *pa*-HO is the center of the heme-iron acquisition pathway [*11*]. Based on previous intensive study of the protein active site as well as the intriguing heme hydroxylation chemistry [*12-14*], here this study of the phenomenal phenylalanine ring cluster existing in heme oxygenase reveals that not only the crucial heme-protein interaction contributes to the unique catalysis but also the hydrophobic Phenylalanine ring cluster maintains and regulates the protein structure and dynamics, therefore facilitates the protein catalysis through its hydrophobic interaction with the H-bonding network related between amino acids and internal structural water molecules. With the thorough understanding of *pa*-HO protein structure-function relationship, we further searched and studied its potential redox partner proteins in the heme-iron acquisition pathway. A surprising result is discovered that a ferredoxin reductase

protein instead of a ferredoxin protein donates all the electrons required for heme degradation to *pa*-HO [*15*]. Subsequent study is focused on this ferredoxin NADPH reductase protein: *pa*-FPR, the crystal structures and NMR backbone assignments in solution phase for *pa*-FPR protein and its $NADP^+$ bound form were carried out. As the first example of the bacterial FNR-$NADP^+$ complex, we found that the general accepted direct hydride transfer mechanism [*16*] between FNR and NADP(H) is not applicable to *pa*-FPR. Further studies lead us to propose a novel $e^-/H^+/e^-$ step-wise hydride transfer mechanism. At last, with the available NMR assignment and crystal structures, we studied the protein complex between *pa*-FPR and *pa*-HO; the preliminary studies suggest that the complex is weak and transient. In brief, the studies of these two proteins show some intriguing findings and possibly bring some new understanding in protein structure and catalysis relationship, hydride transfer mechanism in ferredoxin reductase protein family and weak protein-protein interaction in redox protein complex.

A cluster of Phe rings exists in HO, and several of them are close to the heme distal pocket and are poised to interact with one another (as shown earlier in Figure 1-5 and 2-3). It can possibly form a hydrophobic cluster and exclude water molecule. The studies of mutagenesis and fluorine labeling to these Phe residues in *pa*-HO revealed decreased heme oxygenase reactivity and increased peroxidase reactivity. While the NMR, UV-vis and CD studies show that protein

overall structure is maintained and only small local disruption mostly around heme binding pocket is observed. Protein dynamics study *via* NMR suggests that either mutation or ortho-^{19}F-Phe labeling increased protein dynamic motion in the large (hrs-days) time scales detected by H/D exchange experiment. These results surprisingly contradict the general belief that ^{19}F-Phe labeling will do very little to influence a protein's structure and function [*17-19*]. With the combination of ortho-^{19}F-Phenylalanine labeling and F45L mutation, the impact is further enhanced on both reactivity and protein dynamics.

It is commonly known that the "active site" in a protein, generally composed of several residues, is directly involved in ligand binding and catalysis. It also has been recognized that protein motion/dynamics are closely related to protein catalysis. Here the interaction between heme and protein active site is crucial in regulating this unique heme oxygenation catalysis. Likely, protein peripheral area also contributes to catalysis through maintaining proper protein conformation as well as sufficient protein motion. Recent NMR studies in human HO-1 done by Lar Mar *et al.* [*20, 21*] and in *pa*-HO done by Dr. Juan Carlos Rodriguez from our lab [*22*] revealed that the influence of a single mutation is propagated to the peripheral area in protein through the hydrogen bonding network and protein dynamics. Here our studies of this Phe ring cluster in *pa*-HO found out that the H-bonding network in the heme binding pocket is likely altered during the protein mutation or/and the ortho-^{19}F-Phe labeling. It

suggests that this hydrophobic cluster not only maintains protein structure, but also fine-tunes protein dynamics to facilitate the channeled H-bonding network from heme binding site to the protein periphery for the unique heme metabolism. Therefore the understanding toward the protein structure and function relationship in *pa*-HO is obtained not only around the active site but also at the protein peripheral area like this phenomenal Phe ring cluster.

Current understanding of the redox partner of bacterial heme oxygenase is lacking. It is believed that cyanobacterial and eubacterial HOs are ferredoxin-dependent. In the study of *pa*-HO redox partner in the heme-iron acquisition pathway, we found a surprising result that a ferredoxin NADPH reductase (*pa*-FPR) by itself can donate all seven electrons to *pa*-HO for heme degradation and iron release without the need of a ferredoxin protein [*15*]. Ferredoxin $NADP^+$ reductases (FNRs) catalyze the reversible electron transfer between NADP(H) and their cognate ferredoxin or flavodoxin partners [*23*]. Spinach leaf FNR, as a typical plastidic FNR, is one of the best characterized enzymes. It reduces $NADP^+$ to produce NADPH necessary for the subsequent photosynthetic paths [*24*]. In contrast, bacterial ferredoxin reductases displace the equilibrium toward the oxidation of the NADPH pool, in order to use this reducing potential in a large number of oxidoreductive processes. *Pa*-FPR is classified as a bacterial subclass I ferredoxin NADPH reductase (FNR) protein [*25*]. We studied *pa*-FPR by X-ray crystallography and spectroscopic methods.

The crystal structure of *pa*-FPR (1.6 Å resolution) revealed very similar protein folding to the structure of *Azotobacter vinelandii* FPR and E. coli flavodoxin reductase. The latter two enzymes interact with distinct redox partners, a ferredoxin and a flavodoxin, respectively. Thus these findings reported here extend the range of redox partners recognized by the fold of *pa*-FPR to include a heme oxygenase (*pa*-HO).

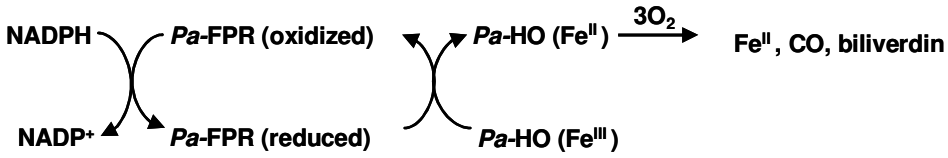

Figure 5-1. Proposed electron transfer from *pa*-FPR to *pa*-HO.

In the reaction between *pa*-FPR and NADPH, *pa*-FPR binds its coenzyme NADPH first, then FAD inside *pa*-FPR is directly reduced to its fully reduced form $FADH_2$, and finally electrons from $FADH_2$ were delivered to *pa*-HO. This $NAD(P)^+$ coenzyme binding process is intensively studied in ferredoxin reductase protein family. The study of electron transfer process of between NADPH and *pa*-FPR protein or $NAD(P)^+$ is the most important step before any further study of protein-protein interaction between *pa*-FPR and *pa*-HO. First, we obtained the NMR backbone assignment in solution phase for *pa*-FPR and co-crystallized *pa*-FPR-$NADP^+$ complex crystal structure as the first example in bacterial subclass FNR group and second example in the whole FNR family.

By comparing bacterial subclass I *pa*-FPR with plastidic FNRs, NMR and crystallography studies revealed that *pa*-FPR has preformed and well-stabilized $NADP^+$ binding site and the conformational change upon $NADP^+$ binding is comparatively small. Therefore, the $NADP^+$ binding process in *pa*-FPR is probably different from the commonly accepted two-step NADP(H) binding in plastidic FNRs: with the first step involving strong interactions between the 2'-adenosyl phosphate and FNR, and the second step requiring displacement of the terminal Tyr to allow the nicotinamide ring to stack parallel to the isoalloxazine ring of FAD [*26*]. In plastidic FNRs, the reaction between FAD and NADPH is generally considered as the result of direct hydride transfer which is facilitated by certain conformational rearrangement placing the nicotinamide and isoalloxazine rings parallel and adjacent to each other. From our studies, there is no large conformational change and dynamic motion observed at the extended C-terminal tail in *pa*-FPR ($AFVEK^{258}$ *vs.* C-terminal Tyrosine in plastidic FNRs). Based on the most recent reported studies in the mechanism of NAD(P)H oxidation, the hydride transfer can also occur in a stepwise manner by sequential electron-proton-electron transfer [*27-36*]. From the study of the *pa*-FPR-$NADP^+$ complex crystal structure, we proposed a novel step-wise $e^-/H^+/e^-$ hydride transfer mechanism for bacterial FNR rather than adopting the conventional direct hydride transfer mechanism for plastidic FNR, as shown in

Equation (5-1). Further study using fast spectroscopic technique can possibly detect the NADPH radicals in Equation (5-1) [*27-36*].

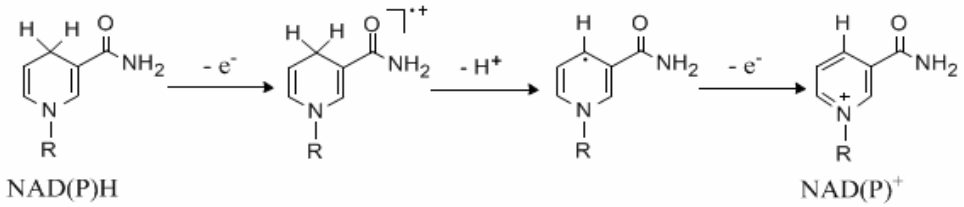

(5-1)

At last, we studied the protein-protein interaction (PPI) between *pa*-FPR and *pa*-HO using the available crystal structures and NMR backbone assignments for both proteins. It has been found that all FNRs interact with their redox proteins via mainly electrostatic interaction and its protein complex is transient for efficient electron transfer purpose [66]. The preliminary data suggests that this PPI is transient, ultra-weak and electrostatic and the interaction interface on *pa*-HO is around the heme binding site. The similar experiments were conducted by Dr. Huili Yao in our lab with possibly optimized conditions. Her data have confirmed the above findings. Further detailed study is ongoing.

Overall, both *pa*-HO and *pa*-FPR proteins are excellent models for protein enzymology studies. Especially, the initial biochemical and structural characterization of *pa*-FPR have brought up several interesting topics, like its redox partnership and protein-protein interaction with *pa*-HO and its unique hydride transfer mechanism as well as the $NADP^+$ binding mode. Still further

studies *via* NMR structure and dynamic experiments (e.g. H/D exchange, CPMG) for understanding the electron transfer and redox chemistry facilitated by *pa*-FPR in complex with *pa*-HO or even other redox partner proteins will be important. All these studies are tremendously informative in revealing the iron acquisition pathway in *Pseudomonas aerguinosa* as well as making potential pharmaceutical applications.

REFERENCES

[1] Yoshida, T.; Noguchi, M.; Kikuchi, G. (1980) Oxygenated Form of Heme-Heme Oxygenase Complex and Requirement for Second Electron to Initiate Heme Degradation from the Oxygenated Complex. *Journal of Biological Chemistry*, *255*, 4418-4420.

[2] Davydov, R. M.; Yoshida, T.; Ikeda-Saito, M.; Hoffman, B. M. (1999) Hydroperoxy-Heme Oxygenase Generated by Cryoreduction Catalyzes the Formation of meso-Hydroxyheme as Detected by EPR and ENDOR. *Journal of the American Chemical Society*, *121*, 10656-10657.

[3] Wilks, A.; Torpey, J.; Ortiz de Montellano, P. R. (1994) Heme Oxygenase (HO-1) Evidence for Electrophilic Oxygen Addition to the Porphyrin Ring in the Formation of α-meso-hydroxyheme. *Journal of Biological Chemistry*, *269*, 29553-29556.

[4] Yoshida, T.; Kikuchi, G. (1978) Features of the Reaction of Heme Degradation Catalyzed by the Reconstituted Microsomal Heme Oxygenase System. *Journal of Biological Chemistry*, *253*, 4230-4236.

[5] Yoshida, T.; Noguchi, M.; Kikuchi, G. (1980) A New Intermediate of Heme Degradation Catalyzed by the Heme Oxygenase System. *Journal of Biochemistry*, *88*, 557-563.

[6] Liu, Y.; Ortiz de Montellano, P. R. (2000) Reaction Intermediates and Single Turnover Rate Constants for the Oxidation of Heme by Human Heme Oxygenase-1. *Journal of Biological Chemistry*, *275*, 5297-5307.

[7] Flo, T. H.; Smith, K. D.; Sato, S.; Rodriguez, D. J.; Holmes, M. A.; Strong, R. K.; Akira, S.; Aderem, A. (2004) Lipocalin 2 Mediates an Innate Immune Response to Bacterial Infection by Sequestering Iron. *Nature*, *432*, 917-921.

[8] Wandersman, C.; Delepelaire, P. (2004) Bacterial Iron Sources: From Siderophores to Hemophores. *Annual Review of Microbiology*, *58*, 611-647.

[9] Genco, C. A.; Dixon, D. W. (2001) Emerging Strategies in Microbial Haem Capture. *Molecular Microbiology*, *39*, 1-11.

[10] Ochsner, U. A.; Johnson, Z.; Vasil, A. I. (2000) Genetics and Regulation of Two Distinct Haem-Uptake Systems, *phu* and *has*, in *Pseudomonas aeruginosa*. *Microbiology*, *146*, 185-198.

[11] Ratliff, M.; Zhu, W.; Deshmukh, R.; Wilks, A.; Stojiljkovic, I. (2001) Homologues of Nisserial Heme Oxygenase in Gram-Negative Bacteria: Degradation of Heme by the Product of the *pigA* Gene of *Pseudomonas aeruginosa*. *Journal of Bacteriology*, *183*, 6394-6403.

[12] Caignan, G. A.; Deshmukh, R.; Zeng, Y.; Wilks, A.; Bunce, R. A.; Rivera, M. (2003) The Hydroxide Complex of Pseudomonas aeruginosa Heme Oxygenase as a Model of the Low-Spin Iron(III) Hydroperoxide Intermediate in Heme Catabolism: 13C NMR Spectroscopic Studies Suggest the Active Participation of the Heme in Macrocycle Hydroxylation. *Journal of the American Chemical Society*, *125*, 11842-11852.

[13] Zeng, Y.; Caignan, G. A.; Bunce, R. A.; Rodriguez, J. C.; Wilks, A.; Rivera, M. (2005) Azide-Inhibited Bacterial Heme Oxygenases Exhibit an S = 3/2 (dxz,dyz)3(dxy)1(dz2)1 Spin State: Mechanistic Implications for Heme Oxidation. *Journal of the American Chemical Society*, *127*, 9794-9807.

[14] Zeng, Y.; Deshmukh, R.; Caignan, G. A.; Bunce, R. A.; Rivera, M.; Wilks, A. (2004) Mixed Regioselectivity in the Arg-177 Mutants of Corynebacterium diphtheriae Heme Oxygenase as a Consequence of in-Plane Heme Disorder. *Biochemistry*, *43*, 5222-5238.

[15] Wang, A.; Zeng, Y.; Han, H.; Weeratunga, S.; Morgan, B. N.; Moeenne-Loccoz, P.; Schoenbrunn, E.; Rivera, M. (2007) Biochemical and Structural Characterization of Pseudomonas aeruginosa Bfd and FPR: Ferredoxin NADP+ Reductase and Not Ferredoxin Is the Redox Partner of Heme Oxygenase under Iron-Starvation Conditions. *Biochemistry*, *46*, 12198-12211.

[16] Deng, Z.; Aliverti, A.; Zanetti, G.; Arakaki, A. K.; Ottado, J.; Orellano, E. G.; Calcaterra, N. B.; Ceccarelli, E. A.; Carrillo, N.; Karplus, P. A. (1999) A Productive NADP+ Binding Mode of Ferredoxin-NADP+ Reductase Revealed by Protein Engineering and Crystallographic Studies. *Nature Structral Biology*, *6*, 847-853.

[17] Sykes, B. D.; Hull, W. E. (1978) Fluorine nuclear magnetic resonance studies of proteins. *Methods in Enzymology*, *49*, 270-295.

[18] Rastinejad, F.; Evilia, C.; Lu, P. (1995) Studies of nucleic acids and their protein interactions by 19F-NMR. *Methods in Enzymology*, *261*, 560-575.

[19] Gettins, P. G. W. (1994) 1H- and 19F-NMR approaches to the study of the structure of proteins larger than 25 kDa. *International Journal of Biological Macromolecules*, *16*, 227-235.

[20] Li, Y.; Syvitski, R. T.; Auclair, K.; Ortiz de Montellano, P. R.; La Mar, G. N. (2003) Solution ^{1}H, ^{15}N NMR Spectroscopic Characterization of Substrate-Bound, Cyanide-Inhibited Human Heme Oxygenase: Water

Occupation of the Distal Cavity. *Journal of the American Chemical Society*, *125*, 13392-13403.

[21] Syvitski, R. T.; Li, Y.; Auclair, K.; Ortiz de Montellano, P. R.; La Mar, G. N. (2002) 1H NMR Detection of Immobilized Water Molecules within a Strong Distal Hydrogen-Bonding Network of Substrate-Bound Human Heme Oxygenase-1. *Journal of the American Chemical Society*, *124*, 14296-14297.

[22] Rodriguez, J. C.; Wilks, A.; Rivera, M. (2006) Backbone NMR Assignments and H/D Exchange Studies on the Ferric Azide- and Cyanide-Inhibited Forms of Pseudomonas aeruginosa Heme Oxygenase. *Biochemistry*, *45*, 4578-4592.

[23] Arakaki, A. K.; Ceccarelli, E. A.; Carrillo, N. (1997) Plant-Type Ferredoxin $NADP^+$ Reductases: A Basal Structural Framework and a Multiplicity of Functions. *FASEB Journal*, *11*, 133-140.

[24] Shin, M.; Arnon, D. I. (1965) Enzymic Mechanisms of Pyridine Nucleotide Reduction in Chloroplasts. *Journal of Biological Chemistry*, *240*, 1405-1411.

[25] Ceccarelli, E. A.; Arakaki, A. K.; Cortez, N.; Carrillo, N. (2004) Functional plasticity and catalytic efficiency in plant and bacterial ferredoxin-NADP(H) reductases. *Biochimica et Biophysica Acta, Proteins and Proteomics*, *1698*, 155-165.

[26] Batie, C. J.; Kamin, H. (1986) Association of Ferredoxin-$NADP^+$ Reductase with NADP(H). Specificity and Oxidation-Reduction Properties. *Journal of Biological Chemistry*, *261*, 11214-11223.

[27] Yuasa, J.; Yamada, S.; Fukuzumi, S. (2008) Detection of a Radical Cation of an NADH Analogue in Two-Electron Reduction of a Protonated *p*-Quinone Derivative by an NADH Analogue. *Angewandte Chemie International Edition*, *47*, 1068-1071.

[28] Fukuzumi, S.; Inada, O.; Suenobu, T. (2002) Direct Detection of Radical Cations of NADH Analogues. *Journal of the American Chemical Society*, *124*, 14538-14539.

[29] Fukuzumi, S.; Inada, O.; Suenobu, T. (2003) Mechanisms of Electron-Transfer Oxidation of NADH Analogues and Chemiluminescence. Detection of the Keto and Enol Radical Cations. *Journal of the American Chemical Society*, *125*, 4808-4816.

[30] Gębicki, J.; Marcinek, A.; Zielonka, J. (2004) Transient Species in the Stepwise Interconversion of NADH and NAD^+. *Accounts of Chemical Research*, *37*, 379-386.

[31] Afanasyeva, M. S.; Taraban, M. B.; Purtov, P. A.; Lashina, T. V.; Grissom, C. B. (2006) Magnetic Spin Effects in Enzymatic Reactions: Radical Oxidation of NADH by Horseradish Peroxidase. *Journal of the American Chemical Society*, *128*, 8651-8658.

[32] Yuasa, J.; Fukuzumi, S. (2006) Mechanistic Borderline Between One-Step Hydrogen Transfer and Sequential Transfers of Electron and Proton in Reactions of NADH Analogues with Triplet Excited States of Tetrazines and $Ru(bpy)^{2+}$. *Journal of the American Chemical Society*, *128*, 14281-14292.

[33] Fukuzumi, S.; Ohkubo, K.; Tokuda, Y.; Suenobu, T. (2000) Hydride Transfer from 9-Substituted 10-Methyl-9,10-dihydroacridines to Hydride Acceptors via Charge-Transfer Complexes and Sequential Electron-Proton-Electron Transfer. A negative Temperature Dependence. *Journal of the American Chemical Society*, *122*, 4286-4294.

[34] Anne, A.; Hapiot, P.; Moiroux, J.; Neta, P.; Savéant, J. M. (1992) Dynamics of Proton Transfer from Cation Radicals. Kinetic and Thermodynamic Acidities of Cation Radicals of NADH Analogues. *Journal of the American Chemical Society*, *114*, 4694-4701.

[35] Zielonka, J.; Marcinek, A.; Huben, K.; Gębicki, J. (2003) Direct Observation of NADH Radical Cation Generated in Reactions with One-Electron Oxidants. *Journal of Physical Chemistry A*, *107*, 9860-9864.

[36] Marcinek, A.; Adamus, J.; Huben, K.; Gębicki, J.; Bartczak, T. J.; Bednarek, P.; Bally, T. (2000) Hydrogen-Transferred Radical Cations of NADH Model Compounds. 1. Spontaneous Tautomerization. *Journal of the American Chemical Society*, *122*, 437-443.